Trinity College Dublin
Coláiste na Tríonóide, Baile Átha Cliath
The University of Dublin

Optimisation of Liquid Heat Exchangers for CPU Thermal Management

Jonathan William Elliott

Supervisor: Dr. Anthony J. Robinson

Department of Mechanical & Manufacturing Engineering

Trinity College Dublin

Ireland

April 2025

A thesis submitted to the University of Dublin in partial fulfilment of the requirements for the degree of *Doctor of Philosophy*

Declaration of Authorship

I declare that this thesis has not been submitted as an exercise for a degree at this or any other university and it is entirely my own work.

I agree to deposit this thesis in the University's open access institutional repository or allow the library to do so on my behalf, subject to Irish Copyright Legislation and Trinity College Library conditions of use and acknowledgement.

I consent to the examiner retaining a copy of the thesis beyond the examining period, should they so wish (EU GDPR May 2018).

Jonathan W Elliott

April 2025

Abstract

The research presented in this thesis addresses critical gaps in the understanding related to electronic cooling with conjugate heat transfer effects, and its integration into practical Central Processing Unit (CPU) architectures, culminating in the development of an automated optimisation framework for liquid jet array impingement heat exchanger design. The work investigates the intricate relationship between heat transfer performance, hydraulic efficiency, and practical constraints, offering novel insights into the design of advanced, energy-efficient cooling solutions tailored to the demands of modern and future electronics.

The first stage of analysis focused on the efficiency of heat spreading in Integrated Heat Spreaders (IHS). While heat spreading efficiency has parallels with fin efficiency in traditional systems, its specific implications for concentrated heat sources with convectively cooled IHSs had not been thoroughly explored. A Genetic Algorithm-based framework was employed to optimise the distribution of convective heat transfer coefficients across the IHS surface. The results demonstrated that non-uniform heat transfer distributions significantly enhanced thermal performance, reducing peak temperatures and minimising gradients across the concentrated heat source. This approach highlighted the potential of using targeted liquid cooling strategies to optimise the conjugate heat transfer, providing a new perspective on managing concentrated heat sources.

Next, the practical application of these theoretical insights to more real-world liquid cooling systems was investigated. An automated multi-objective optimisation workflow was developed to generate high-performance impinging jet array designs optimised for thermal and hydraulic objective functions. Considering CPU-type heat sources with IHSs, the research confirmed that distributed liquid cooling strategies, tailored to specific operational conditions, achieved superior performance, balancing cooling intensity with energy efficiency. This work underscored the practical feasibility of implementing distributed cooling

strategies in commercial applications and further validated the effectiveness of the proposed methodology in achieving optimised cooling solutions.

Finally, the influence of real-life CPU architecture on thermal management strategies was explored. The optimisation framework was adapted to a commercial CPU package, the Intel i5-12600K, to investigate the unique thermal challenges posed by modern high-powered processors. By incorporating discrete and high heat flux cores on the underside of the semiconductor die into the simulation-based optimisation workflow, the research demonstrated that approximately 30% of the total source-to-sink thermal budget could be attributed to the heat transfer in the silicon die. This underscored the importance of considering design architectural influences when designing liquid cooling systems. Experimental verification under realistic operating conditions showed strong agreement between simulation and measured performance, reinforcing the viability and practicality of the developed simulation design approach.

Overall, this research provides a comprehensive framework for optimising liquid jet array impingement heat exchangers, bridging theoretical advancements with practical applications in electronics cooling. By addressing the complexities of heat spreading efficiency, distributed convective cooling, and CPU architectural influences, this research culminates in a robust and experimentally verified simulation design tool for tackling the evolving thermal challenges associated with high-powered CPUs. By validating key hypotheses and providing practical solutions, the findings contribute to the broader field of electronics cooling, offering pathways to more efficient, reliable, and sustainable cooling solutions.

Publications and Conferences

Journal Publications

1. J. W. Elliott, M. T. Lebon, and A. J. Robinson, "Optimising integrated heat spreaders with distributed heat transfer coefficients: A case study for CPU cooling," *Case Studies in Thermal Engineering,* vol. 38, pp. 102354, 2022.

2. J.W. Elliott, A.J. Robinson, “Optimised Liquid Impinging Jet Arrays for Cooling CPU Packages,” *IEEE Transactions on Components, Packaging and Manufacturing Technology*, vol. 15, no. 3, pp. 488-505, 2025.

3. J.W. Elliott, A.J. Robinson, “Optimisation of Liquid Jet Impingement Coldplate for an Overclocked CPU with Multiple Discrete Cores,” *Under Preparation*

Conference Papers

1. G. Murray, J. W. Elliott, R. Jenkins, M. T. Lebon, G. Byrne, and A. J. Robinson, "Thermal-Hydraulic Characterisation of Electronics Cooling Liquids: A Case Study of Jet Impingement Coldplate on Emulated CPU," in *2022 28th International Workshop on Thermal Investigations of ICs and Systems (THERMINIC)*, Dublin, Ireland, pp. 1-4, 2022.

2. J. W. Elliott, G. Byrne, and A. J. Robinson, "Optimising Impinging Microjet Arrays for Varying Heat Source Size in Liquid Cooled Coldplates," in *2023 29th International Workshop on Thermal Investigations of ICs and Systems (THERMINIC)*, Budapest, Hungary, pp. 1-6, 2023.

3. J.W. Elliott, G. Byrne, A.J. Robinson, “Optimising liquid impingement jet arrays for concentrated heat sources,” *Journal of Physics: Conference Series 2766, 9th European Thermal Sciences Conference (Eurotherm)*, Bled, Slovenia, p. 012001, 2024.

Acknowledgments

I would first and foremost like to express my sincere gratitude to my supervisor, Dr. Anthony Robinson, for his continued support and guidance throughout the course of this research project. Additionally, I wish to thank the members of my Doctoral committee, Dr. Séamus O'Shaughnessy and Dr. Tim Persoons, for their feedback on annual reports and providing additional guidance in maintaining a high standard of research.

I would like to thank the AMBER Research Centre, part of Science Foundation Ireland, for providing the funding necessary to support this project, under grant 12/RC/2278, with secondary support from grant 13/RC/2077. Their financial support allowed for the freedom to perform research with access to the necessary tools and facilitate trips overseas to increase research impact.

My gratitude extends to all colleagues in the Department of Mechanical and Manufacturing Engineering, particularly the technical staff in the Parsons Building, from whom much help and support was sought during the construction of the experimental test facilities. A special thanks to Mr. Gerard Byrne for his hands-on assistance in bringing the test apparatus to life, his experience was invaluable in overcoming the many practical challenges encountered in completing this project. I would also like to acknowledge the research and development team at Nexalus Ltd. for their technical support and in-kind contributions towards both the experimental and numerical challenges encountered across the duration of this project.

Thank you to the friends, old and new, who made this process significantly more enjoyable from start to finish, with a particular thanks to those in the Parsons' postgraduate office, where the regular discussion and banter helped to keep the mood light in times of high stress. A massive thank you must also be extended to my family, especially my brother, Daniel, parents, and grandparents, for their constant love and support over the last few years, it has been a constant source of encouragement and motivation to see this through. Finally, thank you to Amy, for being by my side and a shoulder to lean on in the latter years. The completion of this thesis would not have been possible without you all.

Contents

List of Figures

List of Tables

Nomenclature

a	Gaussian curve width indicator
A	Surface area (m^2)
b	Orifice plate thickness (m)
Bi	Biot number
Br	Brinkmann number
C_p	Specific heat capacity (J/kgK)
d	IHS thickness (m)
D	Jet diameter (m)
E	Comparison error
erf	Gauss error function
f	Initial Solution
f	Friction factor
h	Heat transfer coefficient (W/m^2K)
H	Jet-to-target height (m)
j	Chilton-Colburn J-factor
k	Thermal conductivity (W/mK)
L	Length (m)
m	Minimum HTC value of Gaussian distribution (W/m^2K)
N	Number of jets on orifice plate
Nu	Nusselt number
p	Observed order of accuracy
p_{conv}	Order of convergence
P	Pressure (Pa)
P_p	Hydraulic power (W)
Pr	Prandtl number
Q	Thermal power (W)
$Q^{//}$	Heat flux (W/m^2)

r	Displacement from IHS origin (m)
r_r	Arbitrary grid refinement ratio
r_g	Grid convergence ratio
R	Thermal resistance (K/W)
Re	Reynolds number
S	Pitch between successive jets (m)
t	CPU die thickness (mm)
T	Temperature (K)
u	Fluid velocity (m/s)
u'	Velocity fluctuations due to turbulence (m/s)
U	Heat transfer coefficient (W/m^2 K)
Unc	Parameter uncertainty
V_{jet}	Jet nozzle exit velocity (m/s)
$\dot{V}$	Volumetric flow rate (m^3/s)
x	Displacement (m)
$\overline{x}$	Mean value of dataset
y	Displacement (m)

Greek Symbols

β	Non-dimensional heat spreader thickness ratio
δ	p^{th} order error coefficient
ε	Difference between successive meshes for the parameter of interest
η_{IHS}	Fin efficiency (%)
ΔT	Temperature difference (K)
ΔT_{tot}	Thermal Budget (K)
ΔP	Pressure drop (Pa)
θ	Non-dimensional temperature
μ	Dynamic viscosity (Pa s)
ν	Kinematic viscosity (m^2/s)
ρ	Density (kg/m^3)

σ	Standard deviation of dataset
τ	Ratio of HIS thickness to lateral length
ϕ	Ratio of heat source to heat spreader length

Abbreviations

CAD	Computer aided design
CFD	Computational fluid dynamics
CP	Coldplate
CPU	Central processing unit
CTE	Coefficient of thermal expansion
DAQ	Data acquisition system
DLC	Direct liquid cooling
DTS	Digital thermal sensor
FC	Forced convection
FoS	Factor of safety
FS	Accuracy of full scale
FEA	Finite element analysis
GA	Genetic algorithm
GCI	Grid convergence index
GPU	Graphics Processing Unit
HEEDS	Hierarchical Evolutionary Engineering Design System
HEX	Heat exchanger
HTC	Heat transfer coefficient
IC	Integrated circuit
IGBT	Insulated gate bipolar transistor
IHS	Integrated heat spreader
MOO	Multi-objective optimisation
NC	Natural convection
OC	Overclocking

OFE	Oxygen-free electronic copper
RANS	Reynolds-Averaged Navier-Stokes
RD	Accuracy of reading
RSS	Root sum of squares
RMS	Root mean square
RTD	Resistance temperature detector
SOO	Single objective optimisation
SST	Shear-stress transport
STIM	Solder-based thermal interface material
TIM	Thermal interface material
TDP	Thermal design power
TTV	Thermal test vehicle

Subscripts

atm	Ambient atmospheric temperature
avg	Average
b	Bottom-most
BHEX	Brazed heat exchanger
c	Coolant
CPHEX	Coldplate heat exchanger
conv	Convective
core	Single CPU core
eff	Effective
exact	Exact solution
f	Fluid
hs	Heat source
HT	Heat transfer
in	Inlet
j	Junction Temperature
jet	Impinging jet
m	Measured parameter uncertainty
max	Maximum

min	Minimum
nozzle	Orifice jet nozzle
pred	Predicted
r	Area ratio
s	Solid
stag	Stagnation point
t	Top-most
Z	Derived parameter
∞	Average liquid temperature

Chapter 1

Introduction

1.1. Background and Context

1.1.1. Data Centres and the Electronics Cooling Problem

The information and communications technology (ICT) sector, which includes data centres, is responsible for approximately 2% of global Carbon Dioxide (CO_2) emissions annually, with data centres exhibiting the most rapid growth in carbon footprint within this sector [1-3]. This surge can be attributed to the escalating demand for online cloud computing and internet usage, leading to an exponential increase in energy requirements over recent decades. Currently, the ICT sector is estimated to account for approximately 7% of total global electricity consumption, a figure projected to rise to nearly 13% by 2030 [4]. In Ireland, data centres are poised to become the largest energy consumers. Between 2015 and 2022, the total electricity consumption by data centres in Ireland saw a fourfold increase, with a 31% increase occurring between 2021 and 2022 alone [5].

The considerable thermal waste generated by high-power computing and storage applications leads to cooling systems accounting for up to 40% of a data centre's average energy consumption. This figure can vary significantly, ranging from ~25% for highly efficient systems to as much as ~60% for the least efficient, depending on the application and level of sophistication [6]. The high temperatures experienced by the numerous servers in data centres necessitate a substantial portion of this power consumption to be allocated specifically for cooling individual electrical components, ensuring long-term operation and reliability. Consequently, a thermal management issue arises, whereby a significant percentage of power is consumed solely to maintain suitable operating temperatures for active servers. However, this issue presents an opportunity to repurpose the substantial thermal waste generated for use in other applications. Notably, data centres operate as heat-producing engines, generating large quantities of low-grade thermal energy as waste heat. The capture and redistribution of this waste, through the likes of heat recovery, could lead to reduced monetary and environmental costs across this sector, thereby decreasing the ever-expanding carbon footprint.

Addressing the high energy consumption of data centres and similar high-power applications necessitates tackling the thermal management challenges inherent to integrated circuit (IC) components, with thermal management having emerged as one of the most significant challenges in advanced microelectronics in recent decades [7]. As microelectronic components continue to evolve, particularly in terms of device miniaturisation and design complexity, it has become increasingly apparent that these advancements are often accompanied by non-uniform power distributions within high-power processors [8]. Consequently, the power densities of these components are seeing significant increase [4], elevating the risk of hot spot formation across the surface of IC components. The presence of hot spots can result in elevated chip temperatures and exacerbate the presence of substantial temperature gradients across the component's heat transfer surface. Such thermal non-uniformities significantly compromise both performance and reliability, further diminishing the efficiency of cooling systems. It has been estimated that the power density of a hot spot can be three to eight times greater than the average power density of the chip [9-11].

This growing power density of electronics aligns with Moore’s Law, which posits that the number of transistors in IC circuits approximately doubles every 18 to 24 months [12]. Since its introduction in 1965, Moore’s Law has largely held true [13], with transistor density consistently increasing with each new generation of hardware. As it stands today, there is a pressing need for enhanced cooling techniques capable of achieving higher rates of heat dissipation with improved system efficiency that extends product lifespan [6, 8]. Failure to manage heat generation effectively may necessitate unwanted performance throttling to reduce power and safeguard critical IC components [14]. Moreover, the design of the cooling system is constrained by practical considerations, including spatial limitations and a factor of safety relative to the heat dissipation capability [15].

Historically, air cooling has been the preferred solution for electronic cooling systems, largely due to the general ease and cost of implementation. However, for high-power applications, such as modern CPU and GPU processors, air cooling has reached its limit in terms of thermal management, constrained by air's poor thermophysical properties [16]. To put this into perspective, Saini and Webb [17] theoretically showed that for fan-fin type cooling of typical Central Processing Units (CPUs), the heat flux limit is as low as 40 W/cm^2, and this was recently confirmed experimentally by Naduvilakath-Mohammed et al. [18]. To manage this, for example, data centres have had to employ non-ideal strategies such as redistributing computational loads across multiple servers to manage elevated processor temperatures more effectively and prevent thermal throttling, though this ultimately has limited benefit in terms of improving overall data centre performance [19]. Additional drawbacks of air cooling include excessive fan power, noise and size [20] alongside potential airflow restrictions in larger-scale applications [21]. It is evident that a shift in cooling technology is required to facilitate better thermal management, particularly in data centres where the power utilisation efficiency sees only marginal gains with conventional cooling strategies [22].

In recent years, direct liquid cooling (DLC) has emerged as a more advantageous solution for effectively managing high heat flux applications, offering significantly higher overall heat transfer coefficients and thus overall cooling intensity [23, 24]. The reduced mechanical work required for liquid circulation contributes to a notably lower energy consumption compared to air-cooled systems [25, 26]. Water is among the most widely utilised working fluids in liquid cooling systems, owing to its superior thermal and physical properties [27]. When compared to alternative coolants such as air or engineered solutions (e.g., glycol-water mixtures), water demonstrates significantly enhanced heat transfer performance. However, its application is not without limitations. Key challenges include its electrical conductivity and vulnerability to freezing, which can restrict its suitability for certain environments or use cases. To address these challenges, alternative coolants or water-based solutions augmented with specific additives are often employed to mitigate these drawbacks [28]. The selection of an appropriate working fluid must be tailored to align with the thermal management objectives, environmental conditions, and reliability requirements of the system.

Table 1.1 provides a comparative analysis of water and other potential working fluids discussed in the literature, outlining their respective advantages and limitations. This highlights the multifaceted considerations required when choosing a coolant, emphasising the balance between competing priorities necessary for optimal performance in microelectronic cooling applications.

Table 1.1: Properties of suitable working fluids for liquid cooling applications [29-32]

Property	**Water**	**Air**	**50% Ethylene Glycol-Water Mixture**	**3M Fluorinert FC-72**
Thermal Conductivity (W/mK)	~0.6	~0.025	~0.35	~0.1 - 0.15
Density (kg/m^3)	~997 (20°C)	~1.2 (20°C)	~1060	~1700
Kinematic Viscosity [$x10^{-6}$] (m^2/s)	~0.89	~15.6	~2–3	~1.5 - 2.5
Specific Heat Capacity (kJ/kg·K)	~4.18	~1.005	~3.8	~1.1 - 1.5
Electrical Conductivity	Moderate (depends on purity)	Very low (insulator)	Moderate	Extremely low (non-conductive)
Environmental Impact	Minimal	Minimal	Moderate (toxic glycol)	Low to Moderate (chemically inert)
Freezing Point	0°C (adjustable with additives)	N/A	~ -37°C	Variable (typically below -40°C)

To date, the most widely studied and commercially deployed liquid heat sink design is that of microchannels. The concept of the microchannel heat exchanger for high heat flux electronics was first explored by Tuckerman and Pease [33], with a large body of subsequent research building upon their foundational work. However, the predominant focus of much of the microchannel heat exchanger literature has been on the reduction of the maximum chip temperature. Another critical, yet less frequently addressed issue is the reduction of temperature gradients across the semiconductor die. Significant temperature gradients within the IC component can lead to increased thermal stresses at the interfaces with the heat sink due to large differences in coefficients of thermal expansion. Additionally, larger temperature gradients can induce differential ageing across the system, potentially resulting in circuit imbalances and further reliability concerns [34]. Regardless, this illustrates that when developing cooling solutions for semiconductor electronic packages, there are often more aspects to consider than simply the overall cooling intensity.

Extensive reviews have been carried out in the literature, exploring the thermal hydraulics of laminar flow type microchannel heat sinks [35-37], along with investigations focused on optimising channel geometry to enhance heat transfer through various modifications, such as alterations to the convective surface geometry [38-42], adjustments to channel cross sections [43, 44], channel bifurcation [45-47], the incorporation of fins and similar geometric surface features [48-52] and channel stacking [53-55]. Despite the extensive research on channel designs, several challenges persist that underscore the diminishing effectiveness of microchannel type heat sinks as power density levels in IC components continue to escalate beyond manageable limits. Notable drawbacks of microchannel heat sinks include high pressure drops relative to thermal performance [56], the necessity for high-cost micro-manufacturing techniques, and the technique being a global surface cooling strategy, in that they provide a relatively uniform cooling intensity across the entire heat transfer surface. As alluded to earlier, this latter point is important in the context of cooling hot spots, which are better addressed by targeted cooling solutions.

1.1.2. Liquid Impinging Jet Cooling

1.1.2.1. Overview

Jet impingement cooling is an emerging technology that demonstrates a marked superiority in electronic cooling capabilities when compared to conventional microchannel heat sinks. This is underpinned by the fact that jet arrays can achieve significantly higher convective heat transfer coefficients than microchannels [57]. This technology has been effectively employed in various commercial applications, including turbine blade cooling and metal quenching [58, 59]. Notably, jet impingement cooling is well known to possess one of the highest known heat transfer coefficient capabilities for single-phase flow [60]. Additionally, it offers the advantage of maintaining a relatively low pressure drop and associated pumping power compared to microchannel-type cooling systems, while delivering equivalent heat transfer performance [57, 61].

Further to the high convective cooling intensity, jet impingement cooling facilitates the direct application of coolant to regions of higher heat flux, thereby enabling a more localised and targeted cooling approach. This capability can be achieved by simple location of the jet arrays without the necessity for intricate surface geometries and manufacturing, thus reducing design and manufacturing complexity and costs [7]. A critical aspect of jet impingement heat transfer is the high sensitivity of the thermal-hydraulic performance to a manageable set of geometric design parameters, such as jet diameter, jet-to-jet spacing and jet-to-target spacing, each of which being focussed on the orifice plate. This affords impinging jet arrays a high degree of design freedom, allowing for customisation of the size, shape and profile of the jets by simply altering the geometric design of the orifice plate of the heat sink. By focussing the design to the orifice plate, designers can significantly simplify the overall design process for different electronics packages, whilst maintaining low manufacturing costs.

1.1.2.2. Jet Mechanics

It has been well documented across the literature that impinging jets hydrodynamically evolve across distinct regions, which change as the flow is redirected radially outwards from the point of impact on the target surface [62]. Since this work is focussed on cooling of highly integrated electronic packages, the discussion will be limited to confined jets, being a specific category where there is interaction with a confining surface, usually the orifice plate that houses the jet nozzles.

Figure 1.1(a) illustrates the main profile features of a confined submerged impinging jet, highlighting key aspects such as the potential core and shear layer. As depicted, the impinging jet is generated by forcing fluid through a nozzle, resulting in a high-speed jet that issues into the confined gap region to strike the target surface. The impinging jet profile can be separated into three distinct regions, as detailed by Martin [63] and illustrated in Figure 1.1(b). These are;

1. *Free-Jet Region*: Immediately following exit from the jet nozzle, this region contains the jet's potential core, where the flow velocity equals that at the nozzle exit. Surrounding this core is a mixing layer due to flow entrainment of the stagnant fluid within the channel, leading to velocity gradients and a shear flow zone at the periphery of the jet profile. The entrainment within the shear flow region experiences a reduction in velocity from that of the potential core, though acts to increase to overall width and mass flow rate of the jet. Given a high enough jet-to-target spacing, the potential core diminishes in width with distance from the nozzle, as illustrated in Figure 1.1, as the mixing layer penetrates deeper into the jet. For submerged jets the potential core typically extends approximately five times the nozzle diameter [64]. Prior to striking the surface, the developing free jet can be subdivided into an initial developing zone and a fully developed zone, during which it transitions from a constant velocity profile at nozzle exit to a Gaussian velocity profile due to the increased penetration of the shear layer [65]. The development profile of the free-jet depends on the relative magnitudes of the dimensionless jet-to-target distance, H/D. When this ratio is less than approximately

two, jet development is influenced by the elevated static pressure in the stagnation region, which changes the overall profile of the jet compared with that illustrated in Figure 1.1 [63].

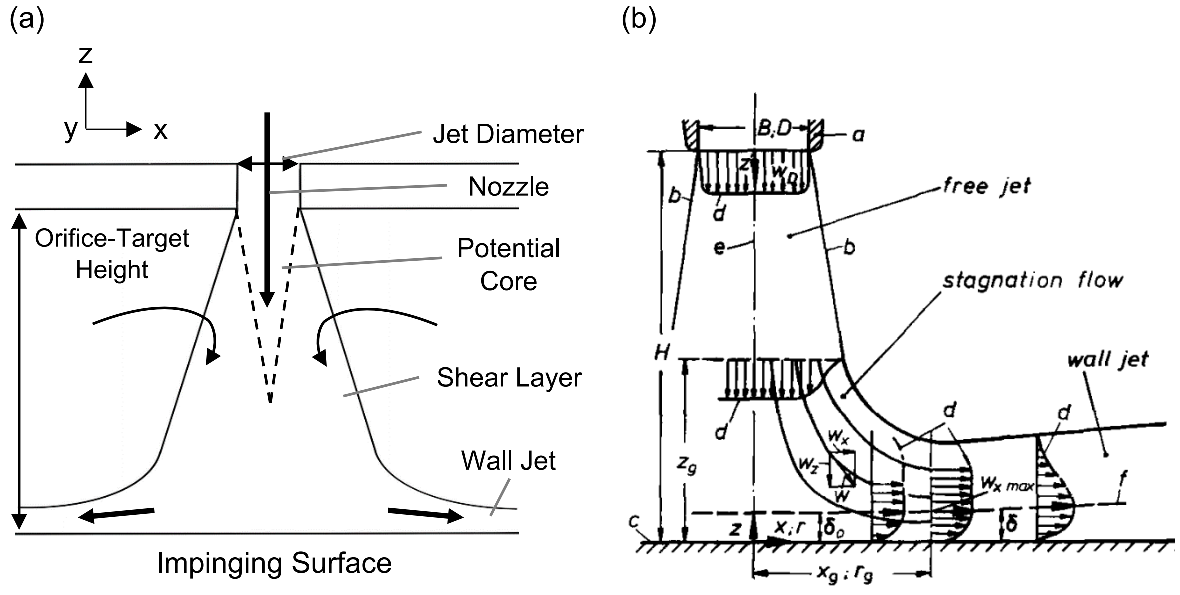

Figure 1.1: (a) Flow regions of a confined submerged impinging jet, adapted from Womac et al. [66], and (b) Flow field and velocity profiles of a single, submerged impinging jet [63].

2. *Stagnation Region*: As the flow approaches the target surface, it experiences a loss of axial velocity and a transition from vertical to radial motion, and this is defined as the stagnation region. In this zone, flow deceleration occurs, and the loss of kinetic energy causes an increase in static pressure above the impinging surface, thus affecting the upstream flow. This directional change results in substantial normal and shear stresses, increased vorticity, stretching the vortices, and increasing turbulence intensity. Observations suggest that the stagnation region can extend up to 1.2 jet diameters for circular impinging jets [63]. Unsurprisingly, convective heat transfer intensity is very high in this region due to the thin thermal and hydraulic boundary layers.
3. *Wall Jet Region*: The high pressure in the stagnation region creates a horizontal pressure gradient within the channel. This pressure gradient establishes the wall jet region (Figure 1.1) which flows along the surface radially outward from the stagnation

zone. Typically, this region maintains a low boundary layer thickness (order of 1% of the jet diameter) within three jet diameters off the jet axis, after which it gradually increases in thickness due to entrainment [67]. Similar to the normal free jet, the wall jet develops and draws in additional fluid from the surroundings, and thus increases in thickness and reduces in velocity. While heat transfer remains high in the early wall jet region, it tends to diminish rapidly with increased radial distance from the stagnation zone due increasing thermal and hydraulic boundary layer thicknesses [68]. This is of course an important feature when arranging jets in arrays, where inter-jet interactions occur.

The heat transfer to impinging jets is sensitive to both the steady nozzle velocity profile and temporal velocity fluctuations. The primary source of jet turbulence is the shear flow at the jet's periphery, which initiates at the sharp nozzle edge and subsequently expands as the jet develops. At higher Reynolds numbers, this shear layer instigates instabilities akin to the Kelvin–Helmholtz instability, resulting in flow oscillations dependent on axial position and velocity profile, with large-scale eddies developing downstream [69]. For large enough jet-to-target spacings, the largest eddies may approach the scale of the jet diameter, remaining active in the flow until interaction with other downstream features occurs [70]. The rapid deceleration of the jet within the high pressure stagnation region generates normal strains and stresses, causing existing eddies and vortices to stretch and distort, further enhancing turbulence intensity [71]. Numerical models developed by Abe and Suga [72] highlighted that heat and mass transport in free jets is predominantly governed by large-scale eddies, whereas shear strain is the primary transport mechanism in the developed wall jet. Flow field turbulence in transitional and turbulent jets exhibit large velocity fluctuations acting normal to the wall, distinguishing it from shear flows acting parallel to the wall [73].

The large turbulent structures present in the free jet significantly influence the convective heat transfer coefficients in both stagnation and wall jet regions. Principally, the generated vortices can penetrate the boundary layers, facilitating the exchange of fluids with differing kinetic energy levels and temperatures. As these vortices disrupt the boundary layers along the wall, they enhance local intensity of convective heat transfer. The presence of turbulence in the wall jet regions is attributed to increased shear forces within the thin, developing region of accelerating flow immediately beyond the stagnation region of the jet [74]. Secondary vortices may also form along the wall jet due to the turbulent characteristics of the wall flow field, where flow reversals can occur, particularly in response to pressure gradient fluctuations. These secondary vortices cause localised increases in heat and mass transfer rates, despite the overall loss of kinetic energy [75].

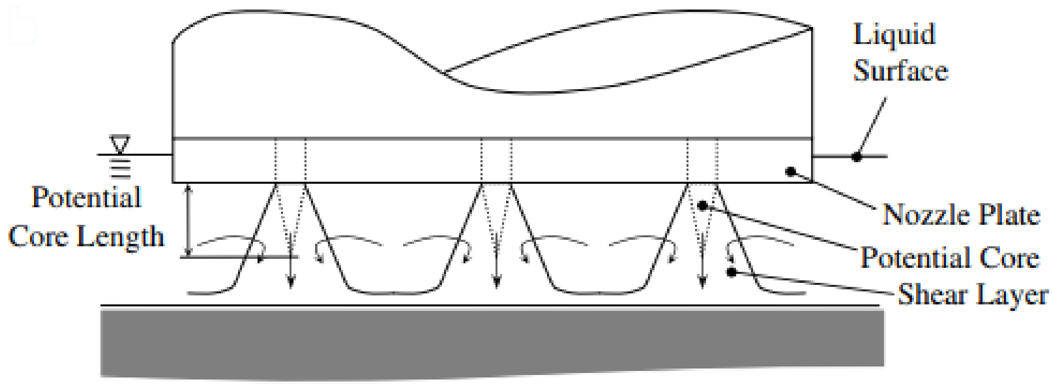

Figure 1.2: Flow regions of confined submerged impinging jet arrays [64].

Since impinging jets create high convective heat transfer intensity in localised regions around their stagnation zones, they must be used in arrays when larger areas are to be cooled. Figure 1.2 shows a simplified schematic of a jet array, where the jet-to-jet spacing is sufficiently large that neighbouring jets do not interact prior to impact with the surface. Compared with isolated single jets, the key differences when considering arrays is the interaction of the neighbouring wall jets, non-stagnant flow in the inter-jet regions, and potential cross flow effects. Like isolated jets, the heat and mass transfer behaviours are sensitive to the jet Reynolds number and jet-to-target spacing. However, now the influence of both the jet-to-jet spacing and the overall number of jets become important.

1.1.2.3. Key Geometric Design Parameters

The local and average heat transfer coefficient as well as the pressure drop associated with jet array impingement heat transfer is intricately linked to several design parameters, since they define the resulting fluid flow characteristics. Key design factors, including the shape, size, and distribution of jet nozzles across the orifice plate, significantly influence the heat transfer and hydraulic behaviour [76, 77].

It is evident that the physical attributes of an impinging jet are determined by several geometric design parameters, with the high sensitivity to jet shape, jet population (N), jet-to-jet spacing (S), jet-to-target spacing (H), and jet array configuration (e.g. in-line versus staggered) all being influenced by the jet Reynolds number, which characterises the flow regime and is a primary factor affecting heat transfer performance in jet impingement systems, being defined as [78],

$$Re = \frac{\rho V D}{\mu} \tag{1.1}$$

where ρ is the fluid density, V is the characteristic velocity (e.g., jet exit velocity) in m/s, D is the jet nozzle diameter, and μ is the dynamic viscosity.

To comprehensively assess the geometric and operational parameters influencing jet impingement cooling systems, several additional dimensionless and derived metrics are integral to understanding their performance characteristics. The Nusselt number is a fundamental parameter representing the ratio of convective to conductive heat transfer at the solid-fluid interface. For jet impingement, established correlations between the Nusselt and Reynolds numbers enable the prediction of heat transfer rates. The Nusselt number can be further characterised based on stagnation heat transfer or as an average performance metric across the entire impingement surface, providing a nuanced understanding of localised and global cooling efficiency. These correlations are given as [64, 79],

$$Nu_{stag} = 0.0304 Re^{0.8} Pr^{\frac{1}{3}} \tag{1.2}$$

$$Nu_{avg} = \frac{hD}{k} = 1.485Re^{0.46}\left(\frac{S}{D}\right)^{-0.442}\left(\frac{H}{D}\right)^{-0.00716}Pr^{0.4} \tag{1.3}$$

where h is convective heat transfer coefficient, k is the thermal conductivity of the fluid, and Pr is the Prandtl number. The Prandtl Number is defined as the ratio of momentum diffusion to thermal diffusion and is calculated as,

$$\mathrm{Pr} = \frac{C_p\mu}{k} \tag{1.4}$$

where C_p is the specific heat of the fluid. The total heat transfer rate, Q, represents the thermal energy exchanged between the system and its environment, serving as a direct indicator of cooling performance. It is defined as,

$$Q = hA\Delta T \tag{1.5}$$

where ΔT is the temperature difference between the solid surface and fluid. The friction factor, f, is a dimensionless parameter that characterises the resistance to fluid flow arising from frictional forces within the system. It provides a quantitative measure of pressure losses attributable to both viscous shear forces and flow separation. In the context of jet impingement cooling systems, the friction factor encompasses the cumulative effects of fluid acceleration through the nozzle, interaction with the impingement surface, and subsequent downstream flow dynamics. It is given as; [80],

$$f = \frac{\Delta P}{(0.5\rho \mathrm{V}^2)\left(\frac{b}{D}\right)} \tag{1.6}$$

where ΔP is the pressure drop across the system and *b* is the thickness of the orifice plate.

Pumping power (P_p) quantifies the energy required to drive the fluid through the system and is calculated as the product of pressure drop (ΔP) and volumetric flow rate ($\dot{V}$). This metric is crucial for evaluating the energy efficiency of the cooling system. Derived metrics offer additional insights into system performance. The Coefficient of Performance (COP), defined as the ratio of heat transfer rate (Q) to pumping power (P_p), provides a measure of the system's thermal efficiency. Another valuable tool is the Chilton-Colburn J-factor analogy, which links heat transfer, friction, and mass transfer processes through dimensionless parameters [81, 82]. The Colburn J-factor for heat transfer is given as,

$$j_{HT} = \frac{Nu}{Re\ Pr^{\frac{1}{3}}} \tag{1.7}$$

This analogy also indicates that the Colburn J-factor for friction ≈ $0.5f$, underscoring the interdependence of these transport phenomena, particularly in turbulent flows dominated by eddy diffusion. Integrating these metrics and correlations establishes a robust analytical framework for the evaluation and comparison of jet impingement cooling systems, enabling a detailed investigation of their thermal-hydraulic performance within the scope of this thesis.

Building upon the established metrics and correlations associated with direct liquid cooling techniques, a comparative evaluation of impinging jet arrays and microchannels highlights the superior suitability of jet impingement for high-performance thermal management applications. Table 1.2 provides a detailed analysis based on the geometric ranges reported by Robinson [83], who conducted a direct comparison of microchannel and impinging jet heat sinks representative of typical configurations. The data reveals that impinging jet arrays consistently achieve higher Nusselt numbers, underscoring their enhanced convective heat transfer capabilities relative to microchannels.

Table 1.2: Comparative analysis between microchannels and impinging jets using geometric inputs provided by [47].

Parameter	Microchannel Heat Sink	Impinging Jet Array Heat Sink
Reynolds Number (Re)	200 - 800	500 - 2000
Nusselt Number (Nu)	3 - 6	20 - 50
Pressure Drop (ΔP)	20 - 80 kPa	5 - 20 kPa
Colburn j-Factor (j)	0.005 - 0.008	0.01 - 0.02

Additionally, the narrower flow passages in microchannels contribute to a significantly higher pressure drop, resulting in greater pumping power requirements. Moreover, the elevated Colburn j-factor observed in impinging jet arrays indicates a more advantageous balance between heat transfer enhancement and hydraulic performance. This makes jet impingement a more efficient and effective cooling solution for applications requiring optimal thermal-hydraulic performance.

A concise review is provided in Table 1.3 to summarise some of the key findings with regard to design parameters explored for impinging jet arrays. Looking in detail at the influence of physical geometric attributes of an impinging jet array, in terms of the jet nozzle shape, a crucial factor affecting jet array thermal-hydraulic behaviour is the formation of an edge shear layer around the jet core within the nozzle. The intensity of the vorticity of this shear layer not only incurs a high pressure drop penalty, but also impacts the jet profile at the nozzle exit, influencing the mixing layer's development in the free jet zone and consequently affecting the size and stability of the potential core. Nozzle geometry thus emerges as a pivotal element in dictating the jet's flow profile during its initial transition to a free jet state, which subsequently influences the heat transfer behaviour. For example, it has been found that, for submerged circular jets, chamfered or contoured inlets diminished the heat transfer performance, the extent of which varies with the chamfer or contour angle [84]. However, chamfered or contoured inlets disproportionately reduce pressure drop and pumping power across the nozzle compared with the heat transfer deterioration.

The influence of nozzle shape is further highlighted by the work of Koseoglu and Baskaya [85] who investigated the heat transfer influence of three distinct jet nozzle geometries: circular, elliptical and rectangular. Their results revealed that elliptical jet nozzles facilitated enhanced flow entrainment resulting in a shorter potential core region compared to circular nozzles, ultimately resulting in reduced stagnation point heat transfer. However, overall heat transfer improved for certain cases of high aspect ratio jets due to higher levels of flow mixing from the larger spreading rate relative to circular jets. Additionally, findings have suggested that converging jet nozzles tend to enhance local heat transfer by promoting increased turbulence and reducing recirculation zones close to the target surface. Conversely, diverging nozzles, while reducing pressure drop, achieve reduced heat transfer performance compared to straight nozzles [86].

Overall, the findings provided further evidence that nozzle shape and its influence of the flow dynamics is highly influential on the heat transfer, with high aspect ratio elliptical jets occasionally outperforming uniform circular jets under specific conditions, contingent on nozzle-to-target distance, flow rate, and aspect ratio [87, 88]. The work of Caliskan et al. [89] further supported the preference for circular and elliptical jet nozzles, particularly asserting that high aspect ratio jet nozzles could serve as passive enhancement techniques for localised cooling solutions. Additionally, irregular jet shapes, such as high aspect ratio elliptical jets or oblique cross-shaped jet nozzles [90], have shown some limited evidence of enhancing heat transfer between adjacent jets. However, this must be considered in the context of the overall impact and practical manufacturing implications of irregular nozzle geometries.

The heat transfer coefficient of impinging jet arrays has been found to diminish with decreasing nozzle lengths, L/D, as shorter nozzles allow less distance for flow development before transitioning to a free jet at the nozzle exit [91]. However, when $L/D < 1$, separation bubbles forms at the nozzle inlet, preventing flow reattachment within the nozzle before exiting into the lower volume. This scenario severely constricts the flow, causing it to behave as a jet with a smaller diameter, thus producing a higher exit velocity jet that can improve the heat transfer, though this incurs a significant pressure drop penalty. Notably, Royne and Dey [92] observed that thin orifice plates resulted in superior jet array impingement heat transfer performance for a fixed flowrate, while a thicker orifice plate yielded better heat transfer for a fixed pumping power. Again, this highlights the need to consider both the heat transfer and pressure drop characteristics on the overall engineering design of an impinging jet array heat sink.

The heat transfer coefficient of impinging jets are typically maximised near the central impingement zone, whilst rapidly diminishing radially outward from the jet centreline [93].

This spatial distribution indicates that increasing the inter-jet spacings, (S/D), will decrease the overall average heat transfer coefficient due to the increasing distance between stagnation regions. This was well demonstrated by Pan and Webb [94] who found that for low jet population arrays (i.e. low cross flow effects), the heat transfer coefficient at the stagnation point remains relatively independent of inter-jet spacing. However, decreasing S/D led to improvement in the average convective heat transfer along the surface. As the proximity of jet stagnation zones became closer, it tended to mitigate the drop-off in heat transfer intensity within the inter-jet regions. Moreover, smaller S/D ratios increases the intensity and influence of neighbouring wall jet interactions. The collision of adjacent wall jets induces another region of boundary layer separation, diverting flow upward from the surface, resulting in increased local convective heat transfer coefficients [95]. However, if S/D is too small, the developing free jets can intersect and entrain coolant into the jet streams, creating a complex distribution of the heat transfer coefficient across the impinging surface [96]. For a sufficiently small S/D, neighbouring free jet shear layers merge, reducing velocity in the jet periphery regions. This further decreases the overall jet turbulence by interfering with the formation of larger-scale eddies and vortices. Testing various inter-jet spacings has, overall, demonstrated that decreasing S/D improved the heat transfer due to a higher density of stagnation zone and neighbouring wall jet interactions. However, there is a point at which the spacing is so small that the free jets intersect and merge, and can lead to heat transfer degradation.

Another critical geometric design parameter for impinging jet arrays is the distance between the nozzle exit and the target surface, often expressed as the dimensionless jet-to-target distance, (H/D). Remembering that developing free jets experience a reduction in velocity as they spread, it is unsurprising that much of the literature has determined that increasing H/D results in a general decrease in convective heat transfer intensity, especially beyond H/D ~ 5, as this is approximately beyond the length of the potential core region of the free jet [64, 97, 98]. Within the potential core region, the heat transfer is less sensitive to H/D [64]. However, other influencing factors must be taken into account when considering

H/D in a jet array design, in particular crossflow within the channel [99]. Depending on the total jet population and/or the jet Reynolds number, which both influence the net flow rate in the channel, a sufficiently small H/D can increase the velocity and associated inertia of the horizontally directed crossflow in the lower channel in such a way as to deflect and weaken jets in the array before impingement. Typically, an optimal H/D value exists for any given jet array and volumetric flow configuration, and illustrates the complexity of jet array impingement heat exchanger design owing to the interdependence of the various parameters on the flow mechanics and subsequent heat transfer. This is further highlighted by the fact that the intensity of the crossflow is dictated by the configuration of the exit flow from the channel, as illustrated in Figure 1.3 from Obot and Trabold [100]. Here it was found the single exit channel configuration was the worst performing in terms of heat transfer owing to the maximum crossflow effects (Figure 1.3(c)). Conversely, the quad-exit design that minimised crossflow (Figure 1.3(a)) exhibited the best heat transfer performance owing to the reduced overall crossflow velocity within the channel and subsequent interference with the jets in the array.

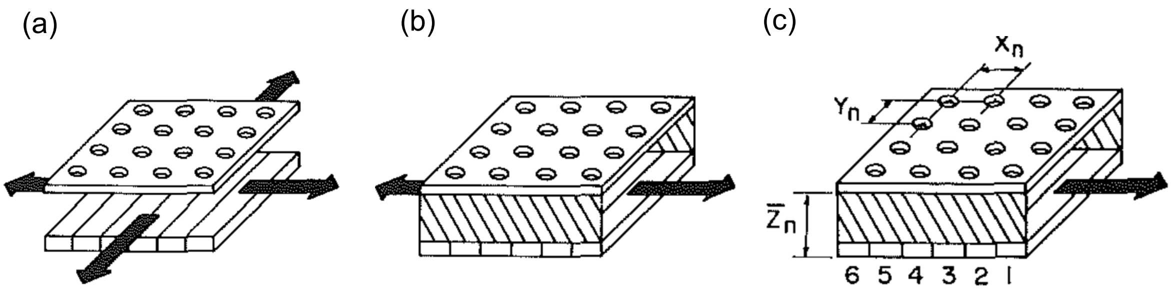

Figure 1.3: Crossflow configurations for an impinging jet array representing (a) minimum, (b) intermediate and (c) maximum crossflow exit channel designs [100].

Inevitable trade-offs exist between improved heat transfer performance and the associated pressure drop and pumping power hydraulic penalties. In the simplest scenario, increasing the jet Reynolds number will increase the convective heat transfer coefficient, though with a disproportionate increase in the pressure drop and hydraulic power. Numerous studies have focused on understanding the overall thermal-hydraulic behaviour of jet arrays, considering both thermal and hydraulic performance indicators. As the discussion above reveals, impinging jet array thermal-hydraulics are sensitive to simple geometric variations such as jet shape, jet population, jet-to-jet spacing, jet to target spacing, and exit channel configuration, and their relative influence depends on the jet Reynolds number. Complicating this is the fact that there is interdependence between these design parameters, in that design interventions that tend to increase the heat transfer tend to come at the expense of increased hydraulic penalties. Considering the complex nature of this type of heat exchanger design, rigorous optimisation strategies must include a fairly broad range of design parameters, and may also need to consider both thermal and hydraulic performance simultaneously. As it stands, impinging jet array optimisation is a developing field and the relevant work to date is discussed below.

1.1.2.4. Literature Review Summary

Table 1.3: Impinging Jet Literature Review Summary

Publication	Num. / Exp.	Jet Shape	Jet Diameter, D (mm)	Jet Population, N	Nozzle Length, L/D	Jet Spacing, S/D	Jet Distance, H/D	Re_{jet}	Main Findings
Goldstein and Timmers (1982) [101]	Exp. (Air)	Circular	10	1 - 7	1	4	2 - 6	40000	- For large jet array, crossflow influences flow distribution at outer jets so heat transfer coefficient maxima occur away from geometrical centre of the jet. - With large arrays, flow interaction causes mixing-induced turbulence to penetrate further towards centre of individual jets. More profound with higher jet populations and smaller H/D values.
Goldstein and Franchett (1988) [102]	Exp. (Air)	Circular (Oblique: 30°, 45°, 60°, 90°)	10	1	1	-	4 - 10	10000 – 35000	- Oblique jets displace the peak heat transfer from intersection of geometric axis. - Heat transfer is reduced in all cases of oblique jets compared to the jets normal to the target.
Womac et al. (1993) [66]	Exp. (Water/ FC-55)	Circular	0.978 - 6.55	4 - 9	2.77 - 18	5 - 20	1 - 10	500 – 20000	- Higher heat transfer coefficients achieved for submerged jet impingement compared with free jets illustrating importance of shear layer turbulence. - Heat transfer coefficient is influenced by the location of the surface relative to the position of the jet potential core, with notable decrease observed at higher H/D values.
Pan and Webb (1995) [94]	Exp. (Water)	Circular	1 - 3	7 - 9	0.67 - 6	2 - 6	2 - 5	5000 – 22000	- Central jet stagnation Nusselt number found to be independent of inter-jet spacing. - Strong Nusselt number dependence on H/D. - Secondary stagnation heat transfer zones of significant magnitude observed midway between jets due to inter-jet flow interaction.

Garimella and Nenaydykh (1996) [91]	Exp. (FC-77)	Circular	0.79 - 6.35	1	0.12 – 48.23	-	1 - 14	4000 – 23000	- HTC peaks at nozzle length-to-diameter ratio <1, with sharp drop between 1 - 4 and gradual recovery between 8 - 12. Due to flow separation and reattachment in nozzle, dependant on Re_{jet}. - Effect of nozzle aspect ratio on heat transfer less pronounced as H/D increases.
Dhir and Fabbri (2004) [103]	Exp. (Water/ FC-40)	Circular	0.069 – 0.25	61 - 397	2 - 7.25	4 – 26.1	40 - 145	73 – 3813	- Nusselt number significantly improves with increasing Re_{jet} and decreasing S/D.
Royne and Dey (2006) [92]	Exp. (Water)	Circular (straight and converging)	1.4	4	0.7 - 1.43	≈7.1	≈3.6	1000 – 7700	- Pressure drop performance linked to formation of separation bubbles, with contracted effective nozzle areas being created at shorter developing lengths. - This results in sensitivity of pressure drop to L/D being greater than sensitivity of heat transfer coefficient, making longer nozzles preferable on pumping power basis when risk of separation bubbles at nozzle entry are high.
Sleiti and Kapat (2006) [97]	Exp. (PAO)	Circular	1 - 2	22 - 39	N/A	1.1 – 2.2	1.5 - 26	200 – 800	- Heat transfer showed dependence on N and Re_{jet} flows. - Heat transfer coefficient increases with H/D up to about 1200 W/m^2K then decreases.
Robinson and Schnitzler (2007) [64]	Exp. (Water)	Circular	1	21 - 121	3	3 - 7	2 - 30	650 – 6500	- Submerged jets offer superior hydraulic performance over free jets. - Heat transfer decreases monotonically with increasing H/D. - Increasing S/D has detrimental impact on heat transfer for fixed Re_{jet}. - Heat transfer has stronger dependence on S/D for smaller H/D values.
Whelan and Robinson (2009) [84]	Exp. (Water)	Circular (straight and contoured inlet)	1	45	3	5	2 (sub) 20 (free)	800 - 10000	- Submerged jets offer superior hydraulic performance over free jets. - Contoured inlets reduce pressure drop across jet nozzles, whilst contoured outlets have adverse effect.

Koseoglu and Baskaya (2010) [85]	Num. (Air)	Circular Elliptical Rectangular	10 (Asp. ratios of 1, 2 & 4)	1	0.3	-	2 - 12	10000	- Stagnation region heat transfer increases with increasing elliptical aspect ratio, though lower average heat transfer rates were predicted. - The effect of aspect ratio on heat transfer decreases with increasing H/D.
Bhunia and Chen (2011) [104]	Exp. (Water/ HFE7200)	Circular	0.2	441	2.3	32.7	35 (sub) 125 (free)	1118 – 3555 (Water) 2368 – 5263 (HFE7200)	- Heat transfer coefficient magnitude has weak dependency on heat source length scale, instead showing strong dependence on jet impingement and adjacent wall jet collision fronts. - Fundamental mechanics of inter-jet interactions for large N align with previous literature investigating substantially smaller populations.
Kim et al. (2012) [105]	Num. (Water)	Circular	≥ 0.5	1 - 16	≥ 2	≥ 3.2	1.8 - 5	N/A	- Pressure drop proportional to Re_{jet} and inversely proportional to N. - H/D and geometry of upper manifold cavity shown to have strong influence on heat transfer characteristics of jet.
Husain et al. (2013) [106]	Num. (Water)	Circular	0.05 – 0.1	4 - 16	3 - 6	32 - 80	1.5 - 4	1000	- D and H/D were found to have the most significant influence on thermal-hydraulic performance. - Staggered jet arrays offer superior heat transfer performance over in-line arrays. - Temperature uniformity increases with higher flow rate, but at expense of higher pressure drop.
Yamane and Yamamoto (2013) [90]	Exp. (Air)	Circular Cross Oblique-cross	4	9	1.67	6	2 - 6	4680	- Cross-shaped jets enhance heat transfer in region between central-diagonal jets and increase Nusselt number uniformity, though stagnation heat transfer is reduced. - Local flow fluctuations due to wall jet interference can significantly affect heat transfer.
Marzec and Kucaba-Piętal (2014) [76]	Num. (Air)	Circular (straight and converging)	0.8	6	N/A	8	8	4800	- Heat transfer coefficient has high dependency on direction of flow entering the jet nozzle. - Outer jets of an array most susceptible to flow deflection at nozzle exit. This is enhanced with chamfered inlets.

Caliskan et al. (2014) [89]	Num. (Air)	Circular Elliptical Rectangular	5 (Asp. ratios of 0.5 & 2)	15	1	6	2 - 10	2000 – 10000	- Circular/elliptic jets provide higher heat transfer coefficients compared to rectangular jets. - Stagnation heat transfer proportional to aspect ratio of jet. - H/D and Re_{jet} have most significant influence on overall heat transfer performance for a given jet array.
Marzec and Anna (2017) [77]	Num. (Air)	Circular (straight and contoured inlet)	0.8	10	N/A	8	8	4800	- Straight jets offer the highest jet Nusselt numbers. - Improvement in average Nusselt Number performance with straight jets of at least 28% compared to convergent and divergent jets tapered to 30°
Yu and Zhu (2017) [107]	Exp. (Air)	Circular	5	1	1.2	-	0.2 - 2	20000 – 60000	- Flow field is highly dependent on H/D. - Decreasing H/D increases heat transfer at stagnation point but decreases heat transfer at jet periphery. - Heat transfer uniformity is greatest at higher H/D.

1.1.3. Heat Sink Geometric Optimisation

A limited number of studies have endeavoured to optimise the geometric configurations of impinging jet arrays, tailoring designs to specific target goals and/or operational scenarios. For simple circular straight jets, Dhir and Fabbri [103] employing a Design of Experiments (DOE) methodology across various orifice array design configurations and demonstrated that, for a constant net flow rate, the optimal jet arrangement for achieving the highest heat removal capacity was with a densely populated array of minimum diameter jets with reduced inter-jet spacings. Later, Husain et al. [106] undertook a multi-objective optimisation approach of jet array orifice designs utilising Kriging meta-modelling in conjunction with an evolutionary algorithm. Their findings indicated that the parameters exerting the most substantial influence on the cooling intensity were the jet-to-target spacing (H/D) and the inter-jet spacing (S/D). This analysis culminated in an optimal configuration featuring a highly populated array of irregularly positioned jets, which effectively mitigated some of the disadvantages linked to stagnation zone interactions at lower jet spacings, with an overall 18% enhancement in overall cooling intensity and reduction in thermal gradients by approximately 25%. Similarly, Kim et al. [105] utilised the Kriging meta-modelling approach to develop an optimisation methodology encompassing only two design variables: the jet-to-target spacing, (H/D), and the height of the cavity between the jet nozzle and the impinging surface, expressed as the length-to-height ratio of the flow outlet channel. Consistent with other studies [108, 109], this result indicated a notable enhancement in cooling performance when multiple objective functions were considered for optimisation and underscores the importance of carefully selecting these variables.

When conducting optimisation calculations, particularly those involving multiple objective functions, there exists a significant risk of solutions becoming ensnared in local optima, thereby eluding the true optimum. To circumvent this challenge and maintain a comprehensive exploration of the design space, it is often imperative to implement strategies that capitalise on the global distribution of data. This approach helps ensure that potential global maxima and minima are not overlooked. To this end, Qidwai et al. [110]

recently employed a Particle Swarm Optimisation (PSO) strategy to optimise a 3 x 3 impinging jet array to minimise thermal resistance and temperature gradients for a non-uniform heat flux distribution at the base of a heat sink. The PSO operates by sampling a subset of solutions otherwise too large to be completely enumerated with available computation resources. As such, with multiple simulations, it is adept at traversing the full design space within an acceptable timeframe, minimising the risk of convergence on localised optima and facilitating the identification of true optimal design solutions. The position of each jet nozzle was optimised independently within a given constrained area, resulting in different flow behaviours from each jet depending on the distance from the neighbouring wall jets. However, the variable inputs were more focused towards the optimisation strategy than the geometric features of the jet array, such as number of particles and number of iterations. Consequently, while the optimisation yielded a jet configuration that successfully targeted regions of higher heat flux to mitigate large temperature gradients, the result from the algorithm varied slightly for each complete optimisation run, requiring experimental verification for each combination of PSO input parameters.

Optimising individual geometric features of an impinging jet array heat sink has been shown to yield substantial improvements in thermal performance. For instance, Brakmann et al. [111] demonstrated that numerical optimisation of a fixed 9 x 9 impinging jet array, combined with surface enhancement features such as pin fins, increased the heat flux by up to 142% [112]. However, this improvement came at the cost of a 14% rise in pressure drop across the system. These findings highlight the pronounced sensitivity of thermal-hydraulic performance to variations in geometric design parameters, underscoring the importance of carefully balancing enhancements in heat transfer against the associated hydraulic penalties. Furthermore, Rachdi et al. [113] conducted a numerical investigation into the effects of various geometric parameters on the heat transfer performance of impinging jet arrays, focusing on their individual impacts on the impingement surface. Their findings revealed that for a fixed jet population (N) increasing the inter-jet spacing (S) by a factor of four resulted in a 21% increase in the stagnation Nusselt number, highlighting enhanced cooling intensity at the stagnation zones. Conversely, when S was held constant, doubling N led to a near 25% increase in the Nusselt number along the lateral zones of the target surface, thereby improving peripheral heat transfer. This study, and similar [114, 115], underscore the significance of optimising geometric parameters, emphasising that each parameter influences jet flow dynamics and thermal performance in distinct ways. Importantly, it also highlights the limitations of investigating these parameters in isolation, as such an approach fails to capture the complex interplay between variables. To fully understand and maximise the global thermal-hydraulic performance of an impinging jet array, a more comprehensive optimisation approach is necessary, considering the combined influence of all geometric parameters on the system.

Clearly, the prior optimisation work on impinging jet array heat exchangers is quite limited, both in scope of the optimisation and in the design parameters which have been investigated. This can largely be attributed to the inherent complexity and interdependence of the parameters involved, which make such problems particularly suited to CFD-based analyses. However, from an optimisation standpoint, CFD simulations impose substantial computational demands, requiring advanced software capabilities and significant computing resources. Realistically speaking, it is only in recent years that advancements in computational tools and hardware have enabled the effective exploration of such complex optimisation problems. Despite these advancements, a notable gap persists in the comprehensive understanding of the interplay among all geometric parameters associated with jet array impingement. Most existing studies focus on isolated parameters or narrow groupings of design variables, typically prioritising those with the most significant impact on heat transfer. While this approach has yielded valuable insights, it overlooks the potential contributions of less influential geometric features. Although their individual effects may be less pronounced, these secondary parameters could play a critical role in shaping the overall thermal-hydraulic performance of the system. Investigating these interactions offers the potential to uncover additional findings that could inform the development of next-generation heat sink designs, emphasising the need for a more holistic approach to optimisation in this domain.

1.1.4. Conjugate Heat Transfer

For the specific topic of the present research, which considers electronics cooling, the heat transfer becomes even more complex when concentrated heat sources are fitted with a heat spreader, since it now includes conjugate heat transfer effects. Concisely, high heat flux electronics can often be of such a small area that there is insufficient surface area for practical convective cooling to achieve safe operating temperatures. To address this, it is essential to spread the generated heat across a larger convective surface area in order to reduce the convective thermal resistance for a given convective heat transfer intensity. This is achieved by a heat spreader material, typically referred to as an Integrated Heat Spreader (IHS), which is generally a high thermal conductivity material placed between the heat source and convective heat sink. Including an IHS transforms the electronics cooling challenge into a conjugate heat transfer problem, incorporating both axial and lateral conduction, which are themselves influenced by the intensity and distribution of the fluid convection. Although it is well known that an IHS adds thermal resistance between the source and sink, if designed correctly it can distribute the heat over a large enough convective surface area that the reduced convective resistance more than offsets this additional conductive resistance of the IHS [116]. The end result is a net decrease in source-to-sink thermal resistance.

The performance of heat spreading systems can be assessed using the Biot number $(\mathrm{Bi} = \mathrm{hd/k})$, which compares the internal thermal resistance of a solid of thickness *d* to the external convective resistance [117]. Integrated Heat Spreaders are typically constructed from materials with high thermal conductivity, such as copper ($k \approx 400$ W/mK) or aluminium ($k \approx 230$ W/mK), enabling efficient heat distribution from the heat source to a larger surface area for enhanced convective cooling. However, this process often induces significant thermal gradients within the spreader. For instance, at heat fluxes ranging from 50 to 300

W/cm², temperature gradients can reach up to 50 K/cm, depending on the material properties and geometry [118]. These thermal gradients introduce challenges such as differential thermal expansion, which can lead to mechanical stresses at material interfaces. For example, in typical CPU configurations, copper exhibits a coefficient of thermal expansion (CTE) of approximately 16.5 x10^{-6} K^{-1}, compared to 2.6 x10^{-6} K^{-1} for silicon. This disparity can result in substantial mechanical stresses, potentially leading to material fatigue or interface delamination under repeated thermal cycling [119].

Mitigating these issues requires careful optimisation of the IHS's thickness and lateral dimensions. Robinson et al. [116] demonstrated that increasing the base dimensions of the heat spreader significantly reduces the net source-to-sink thermal resistance, enhancing overall thermal performance and reducing the risks associated with thermal gradients and mechanical stress. However, these gains diminish beyond a certain size, at which point the rate of decrease in thermal resistance becomes disproportionately small compared to the additional material added. Thus, exceeding this threshold offers minimal performance enhancement. Moreover, when optimising the geometry with fixed lateral dimensions of the spreader, an optimal thickness exists since there are conflicting effects between the axial resistance across the spreader and lateral spreading through the material [120, 121].

In microelectronic cooling applications, heat sinks are often modelled using a thermal resistance network, which represents the heat transfer pathways from the heat source through intermediate layers, such as a heat spreader, to the convective cooling medium. This network typically encompasses conductive heat transfer within solid layers and convective transfer at the fluid interface. Lee et al. [122] developed a detailed model for thermal spreading resistance within a heat spreader, capturing the effects of lateral heat conduction as thermal energy transitions from the smaller footprint of the heat source to the larger surface area of the spreader. The spreading resistance, R_s, is expressed as,

$$R_s = \frac{\psi}{kA_{IHS}} \tag{1.8}$$

with

$$\psi = \frac{\phi}{\tanh(\phi\tau)} \tag{1.9}$$

where k is the conductivity of the spreader material, A_{IHS} is the surface area of the spreader, ϕ is the ratio of the heat source size to the spreader size and τ is the ratio of IHS thickness to the lateral length (d/L). The total thermal resistance across the thermal stack is then determined by summing the individual resistances of each layer, incorporating both conductive and convective resistances. This comprehensive approach provides a robust framework for evaluating and optimising the thermal performance of heat spreaders within microelectronic cooling systems [123].

In the context of jet impingement heat transfer, Awad et al. [124] recently investigated the integration of a heat spreading plate into a microjet heat sink, revealing that the employment of a heat spreader as a passive cooling technique effectively distributes heat across a broader area, thereby improving the overall heat removal process. The inclusion of the spreader was shown to reduce thermal gradients across the heat transfer surface by up to 20%, allowing inlet flow rates to decrease by as much as 40% while maintaining the same cooling effect for a given heat flux. Such reductions underscore the dual impact of conjugate heat transfer and fluid mechanics on thermal management. Considering the earlier discussion regarding the sensitivity of jet array impingement heat transfer to several design parameters, together with the influence of conjugate heat transfer within an IHS, this preliminary study strongly suggests that an optimal cooling solution for thermal management of concentrated heat sources should consider both the heat spreading within the IHS and the jet array design, which adds another layer of complexity on an already complex optimisation problem.

1.1.5. Brief Synthesis

The above concise review of the literature highlights that the fluid mechanics and associated heat transfer and hydraulic penalties associated with impinging jet arrays are quite complex. The thermal-hydraulics are sensitive to a set of largely interdependent design parameters, ranging from the jet nozzles themselves, through the nozzle population and layout on the orifice plate, to the method by which the flow exits the system. Complicating this is the requirement of an Integrated Heat Spreader when concentrated heat sources are considered, since this couples the convective problem with the conduction problem via conjugate heat transfer. Altogether, the design problem is somewhat overwhelming, in particular when considering potential approaches to optimise the heat exchanger. Beyond this, electronic packages are wide ranging in their design architectures and tend to evolve rapidly, meaning that what is optimal for one design will unlikely be optimal for another, and this will change quickly over time. Considering these points, the objectives of the present work are outlined below.

1.2. Thesis Objectives and Contribution

The overarching objective of this research is to develop an automated simulation-based optimisation design strategy for liquid jet array impingement heat exchangers, specifically focussing on scenarios whereby concentrated and high heat flux sources require heat spreaders to achieve cooling targets. The work focusses on Central Processing Units (CPUs), which contain more concentrated thermal loads and thus experience higher thermal gradients and localised hotspots compared to similar components such as Graphics Processing Units (GPUs), and implements a Computational Fluid Dynamics (CFD) approach, aiming to develop an optimisation methodology that is accurate, versatile in terms different CPU package layouts, and capable of multi-objective optimisation - specifically considering both cooling intensity and hydraulic performance. To achieve this primary research objective, the following specific sub-objectives were required:

1. To gain a fundamental understanding of conjugate heat transfer in heat spreaders and subsequently develop a mathematical optimisation model for convectively cooled heat spreaders with concentrated heat sources.
2. To develop a Computational Fluid Dynamics (CFD) based simulation model for impinging jet array heat exchangers for cooling concentrated heat sources with Integrated Heat Spreaders.
3. To design and fabricate necessary experimental facilities to verify the veracity of the CFD simulations.
4. To develop an automated optimisation strategy and workflow for heat exchanger design optimisation capable of both maximising cooling and minimising hydraulic penalties for a range of practical CPU designs.
5. To demonstrate the developed simulation-based methodology to the design of optimised heat exchanger designs for a commercial CPU package, and to verify performance by testing manufactured heat sinks on a live CPU under high computing workload conditions.

1.3. Thesis Structure

This thesis is presented in the format of a "Thesis by Publications" comprising chapters designed to function as standalone publications suitable for submission to research journals. As such, the forthcoming chapters include two published journal articles and one prepared for submission. The final chapter synthesises the overarching conclusions derived from the collective works presented in the preceding chapters. Chapters 2 through 4 are organised in accordance with standard journal publication conventions, featuring the typical section headings of Abstract, Introduction, Theory and Methodology, Results, Discussion, and Conclusions. Each chapter begins with an introduction that offers a relevant and concise literature review, highlighting evident gaps in existing knowledge and outlining the specific aims and objectives of the chapter. As the journal papers making up each individual chapter are included in their entirety within this thesis, it is acknowledged that some repetition is present. Nevertheless, each chapter reports different standalone contributions to knowledge, with different aims, objectives, results, discussions, and conclusions. The upcoming contents of the thesis are outlined as follows:

Chapter 2

The second chapter of this thesis presents the work entitled; "Optimising Integrated Heat Spreaders with Distributed Heat Transfer Coefficients: A Case Study for CPU Cooling," [125] published in *Case Studies in Thermal Engineering.* This chapter examines concentrated heat sources and the impact of imposing a non-uniform heat transfer coefficient across the convective surface of an Integrated Heat Spreader, specifically in the context of commercial CPU packages. To investigate this phenomenon, a finite element model of a copper heat spreader was developed in MATLAB, utilising a Gaussian function to define the profile of the heat transfer coefficient distribution across the convective surface. A Genetic Algorithm-based optimisation code was implemented to ascertain the prioritisation of objective functions that yielded the most effective heat transfer coefficient distribution for a predetermined set of fixed inputs. The results demonstrated that, compared to a uniform heat transfer coefficient distribution, realistic reductions in junction temperature could be achieved by optimising the non-uniform convective heat transfer boundary condition on the IHS, and proved the concept that conjugate heat transfer could be leveraged in such a way as to improve overall cooling effectiveness.

Chapter 3

The third chapter presents the work entitled; “Optimised Liquid Impinging Jet Arrays for Cooling CPU Packages,” [126] published in *IEEE Transactions on Components, Packaging and Manufacturing Technology*. This chapter overviews the jet array impingement CFD model development as well as the experimental test facility designed to generate the data used to verify the simulations. Additionally, it details the development of an automated workflow for geometric optimisation of the heat exchanger. To achieve this, an integrated feedback-type workflow was developed across three separate software packages. The work then implements the simulation-based tool to investigate the design implications across varying degrees of concentration of the heat source, mimicking a range of CPU dies, and different optimisation goals, specifically the minimisation of the heat source temperature and the overall hydraulic pumping power across the heat exchanger. The subsequent analysis compares and contrasts the optimal jet array designs across the range of heat source sizes for both the single and multiple objective optimisation cases, identifying the key geometric differences in the designs and physical interpretation of the heat and fluid flow that is responsible for the observed thermal-hydraulic performance.

Chapter 4

The fourth chapter presents the work entitled; “Optimisation of Liquid Jet Impingement Coldplate for an Overclocked CPU with Multiple Discrete Cores,“ currently ready for submission to *IEEE Transactions on Components, Packaging and Manufacturing Technology*. This chapter further progresses the simulation-based optimisation workflow outlined in the preceding chapter to a commercial CPU package, specifically an Intel i5 12th generation processor. Importantly, this real-life case includes the influence of the individual

CPU cores as discrete and very high heat flux sources, together with 3D conduction heat transfer effects in the semiconductor die and Thermal Interface Material. Consistent with Chapter 2, an experimental apparatus was designed and fabricated that allowed for live testing of the test CPU and production of data suitable for verification of the more advanced simulation model. Subsequently, the automated optimisation workflow was implemented to generate optimal heat exchanger designs for the test CPU, targeting maximum cooling of the non-centred and discrete cores, as well as maximum cooling of the cores with minimum hydraulic power consumption. Overall, this chapter concludes that the developed automated workflow is a powerful design tool for optimising liquid impinging jet array heat exchangers for cooling of commercial CPU packages.

Chapter 5

The final chapter summarises the major findings of the thesis and the contributions to knowledge, followed by suggestions for potential future work.

Appendix

The thesis appendices report additional results and information not included in the published papers, including but not limited to full code text, function derivations, equipment calibration information, and additional visuals to those presented in the main body of the thesis.

References

[1] B. Whitehead, D. Andrews, A. Shah, and G. Maidment, "Assessing the environmental impact of data centres part 1: Background, energy use and metrics," *Building and Environment,* vol. 82, pp. 151-159, 2014, doi: 10.1016/j.buildenv.2014.08.021.

[2] C. Freitag, M. Berners-Lee, K. Widdicks, B. Knowles, G. S. Blair, and A. Friday, "The real climate and transformative impact of ICT: A critique of estimates, trends, and regulations," *Patterns,* vol. 2, no. 9, p. 100340, 2021, doi: 10.1016/j.patter.2021.100340.

[3] J. Malmodin, N. Lövehagen, P. Bergmark, and D. Lundén, "ICT sector electricity consumption and greenhouse gas emissions – 2020 outcome," *Telecommunications Policy,* vol. 48, no. 3, p. 102701, 2024, doi: 10.1016/j.telpol.2023.102701.

[4] M. Avgerinou, P. Bertoldi, and L. Castellazzi, "Trends in Data Centre Energy Consumption under the European Code of Conduct for Data Centre Energy Efficiency," *Energies,* vol. 10, p. 1470, 2017, doi: 10.3390/en10101470.

[5] C. S. O. Ireland. "Data Centres Metered Electricity Consumption 2022." https://www.cso.ie/en/releasesandpublications/ep/p-dcmec/datacentresmeteredelectricityconsumption2022/keyfindings/ (accessed 22/07/2024).

[6] H. Zhang, S. Shao, H. Xu, H. Zou, and C. Tian, "Free cooling of data centers: A review," *Renewable and Sustainable Energy Reviews,* vol. 35, pp. 171-182, 2014, doi: 10.1016/j.rser.2014.04.017.

[7] G. Laguna *et al.*, "Numerical parametric study of a hotspot-targeted microfluidic cooling array for microelectronics," *Applied Thermal Engineering,* vol. 144, pp. 71-80, 2018, doi: 10.1016/j.applthermaleng.2018.08.030.

[8] H. Lee, Y. Jeong, J. Shin, J. Baek, M. Kang, and K. Chun, "Package embedded heat exchanger for stacked multi-chip module," *Sensors and Actuators A: Physical,* vol. 114, no. 2, pp. 204-211, 2004, doi: 10.1016/j.sna.2003.12.026.

[9] G. Sery, S. Borkar, and V. De, "Life is CMOS: why chase the life after?," in *Proceedings 2002 Design Automation Conference (IEEE Cat. No.02CH37324)*, 10-14 June 2002, pp. 78-83, doi: 10.1109/DAC.2002.1012598.

[10] M. Yu and J. Zhu, "Hotspot thermal management of silicon-based high power hetero-integration," *International Journal of Heat and Mass Transfer,* vol. 203, p. 123790, 2023, doi: 10.1016/j.ijheatmasstransfer.2022.123790.

[11] J. Zhang, S. Sadiqbatcha, M. O'Dea, H. Amrouch, and S. X. D. Tan, "Full-Chip Power Density and Thermal Map Characterization for Commercial Microprocessors Under Heat Sink Cooling," *IEEE Transactions on Computer-Aided Design of Integrated Circuits and Systems,* vol. 41, no. 5, pp. 1453-1466, 2022, doi: 10.1109/TCAD.2021.3088081.

[12] R. K. Cavin, P. Lugli, and V. V. Zhirnov, "Science and Engineering Beyond Moore's Law," *Proceedings of the IEEE,* vol. 100, no. Special Centennial Issue, pp. 1720-1749, 2012, doi: 10.1109/JPROC.2012.2190155.

[13] G. E. Moore, "Cramming More Components Onto Integrated Circuits," *Proceedings of the IEEE,* vol. 86, no. 1, pp. 82-85, 1998, doi: 10.1109/JPROC.1998.658762.

[14] A. L. Moore and L. Shi, "Emerging challenges and materials for thermal management of electronics," *Materials Today,* vol. 17, no. 4, pp. 163-174, 2014, doi: 10.1016/j.mattod.2014.04.003.

[15] I. Mudawar, "Assessment of high-heat-flux thermal management schemes," *IEEE Transactions on Components and Packaging Technologies,* vol. 24, no. 2, pp. 122-141, 2001, doi: 10.1109/6144.926375.

[16] A. C. Kheirabadi and D. Groulx, "Cooling of server electronics: A design review of existing technology," *Applied Thermal Engineering,* vol. 105, pp. 622-638, 2016, doi: 10.1016/j.applthermaleng.2016.03.056.

[17] M. Saini and R. L. Webb, "Heat rejection limits of air cooled plane fin heat sinks for computer cooling," *IEEE Transactions on Components and Packaging Technologies,* vol. 26, no. 1, pp. 71-79, 2003, doi: 10.1109/TCAPT.2003.811465.

[18] F. M. Naduvilakath-Mohammed, R. Jenkins, G. Byrne, and A. J. Robinson, "Closed loop liquid cooling of high-powered CPUs: A case study on cooling performance and energy optimization," *Case Studies in Thermal Engineering,* vol. 50, p. 103472, 2023, doi: 10.1016/j.csite.2023.103472.

[19] Y. Fulpagare and A. Bhargav, "Advances in data center thermal management," *Renewable and Sustainable Energy Reviews,* vol. 43, pp. 981-996, 2015, doi: 10.1016/j.rser.2014.11.056.

[20] Z. Wang and H. Hu, "Development of an Ultra-Quiet Fan for Computer Cooling Applications," in *ASME 2014 12th International Conference on Nanochannels, Microchannels, and Minichannels*, 2014, vol. 1A, doi: 10.1115/fedsm2014-21324.

[21] A. Capozzoli and G. Primiceri, "Cooling Systems in Data Centers: State of Art and Emerging Technologies," *Energy Procedia,* vol. 83, pp. 484-493, 2015, doi: 10.1016/j.egypro.2015.12.168.

[22] T. Persoons and J. A. Weibel, "Foreword: Special Section on Data Center Cooling," *IEEE Transactions on Components, Packaging and Manufacturing Technology,* vol. 7, no. 8, pp. 1189-1190, 2017, doi: 10.1109/TCPMT.2017.2729698.

[23] M. Tański *et al.*, "A System for Cooling Electronic Elements with an EHD Coolant Flow," *Journal of Physics: Conference Series,* vol. 494, 2014, doi: 10.1088/1742-6596/494/1/012010.

[24] B. Watson and V. K. Venkiteswaran, "Universal Cooling of Data Centres: A CFD Analysis," *Energy Procedia,* vol. 142, pp. 2711-2720, 2017, doi: 10.1016/j.egypro.2017.12.215.

[25] Y. Hadad *et al.*, "Three-objective shape optimization and parametric study of a micro-channel heat sink with discrete non-uniform heat flux boundary conditions,"

Applied Thermal Engineering, vol. 150, pp. 720-737, 2019, doi: 10.1016/j.applthermaleng.2018.12.128.

[26] S. Alkharabsheh, B. Ramakrishnan, and B. Sammakia, "Pressure drop analysis of direct liquid cooled (DLC) rack," in *2017 16th IEEE Intersociety Conference on Thermal and Thermomechanical Phenomena in Electronic Systems (ITherm)*, 30 May-2 June 2017, pp. 815-823, doi: 10.1109/ITHERM.2017.7992570.

[27] L. Yuan, Y. Wang, R. Kosonen, Z. Yang, Y. Zhang, and X. Wang, "Comparative Study on Heat Dissipation Performance of Pure Immersion and Immersion Jet Liquid Cooling System for Single Server," *Buildings,* vol. 14, no. 9, p. 2635, 2024, doi: 10.3390/buildings14092635.

[28] A. Roslan, N. Tukiman, N. N. Ibrahim, A. R. Juanil, and M. Arbanah, "The Effects of Ethylene Glycol to Ultrapure Water on Its Specific Heat Capacity and Freezing Point," *Journal of Applied Environmental and Biological Sciences,* vol. 7, pp. 56-60, 2017.

[29] J. V. Sengers and J. T. R. Watson, "Improved International Formulations for the Viscosity and Thermal Conductivity of Water Substance," *Journal of Physical and Chemical Reference Data,* vol. 15, no. 4, pp. 1291-1314, 1986, doi: 10.1063/1.555763.

[30] K. Stephan and A. Laesecke, "The Thermal Conductivity of Fluid Air," *Journal of Physical and Chemical Reference Data,* vol. 14, no. 1, pp. 227-234, 1985, doi: 10.1063/1.555749.

[31] F. Kreith and M. S. Bohn, *Principles of heat transfer*. West Publishing Company, Eagan, Minnesota, United States, 1986.

[32] "3M™ Fluorinert™ Electronic Liquid FC-72." https://multimedia.3m.com/mws/media/64892O/3m-fluorinert-electronic-liquid-fc-72.pdf (accessed 03/05/2025).

[33] D. B. Tuckerman and R. F. W. Pease, "High-performance heat sinking for VLSI," *IEEE Electron Device Letters,* vol. 2, no. 5, pp. 126-129, 1981, doi: 10.1109/EDL.1981.25367.

[34] JEDEC, "Failure mechanisms and models for semiconductor devices," *JEDEC,* pp. 1-9, 68-72, 2010.

[35] I. Hassan, P. Phutthavong, and M. Abdelgawad, "Microchannel heat sinks: An overview of the state-of-the-art," *MTE,* vol. 8, pp. 183-205, 2004, doi: 10.1080/10893950490477338.

[36] J. F. Tullius, R. Vajtai, and Y. Bayazitoglu, "A Review of Cooling in Microchannels," *Heat Transfer Engineering,* vol. 32, no. 7-8, pp. 527-541, 2011, doi: 10.1080/01457632.2010.506390.

[37] A. Adham, N. Mohd-Ghazali, and R. Ahmad, "Thermal and hydrodynamic analysis of microchannel heat sinks: A review," *Renewable and Sustainable Energy Reviews,* vol. 21, pp. 614-622, 2013, doi: 10.1016/j.rser.2013.01.022.

[38] J. Benner and P. T. Lin, "Design and Optimization of Multiple Microchannel Heat Transfer Systems," *Journal of Thermal Science and Engineering Applications,* vol. 6, p. 011004, 2013, doi: 10.1115/1.4024706.

[39] V. Leela Vinodhan and K. S. Rajan, "Computational analysis of new microchannel heat sink configurations," *Energy Conversion and Management,* vol. 86, pp. 595-604, 2014, doi: 10.1016/j.enconman.2014.06.038.

[40] Z. Dai, D. Fletcher, and B. Haynes, "Impact of tortuous geometry on laminar flow heat transfer in microchannels," *International Journal of Heat and Mass Transfer,* vol. 83, 2015, doi: 10.1016/j.ijheatmasstransfer.2014.12.019.

[41] M. Ruiz and V. P. Carey, "Experimental Study of Single Phase Heat Transfer and Pressure Loss in a Spiraling Radial Inflow Microchannel Heat Sink," *Journal of Heat Transfer-transactions of The Asme,* vol. 137, p. 071702, 2015, doi: 10.1115/1.4029821.

[42] J. Rostami, A. Abbassi, and M. Saffar-Avval, "Optimization of conjugate heat transfer in wavy walls microchannels," *Applied Thermal Engineering,* vol. 82, pp. 318-328, 2015, doi: 10.1016/j.applthermaleng.2015.02.069.

[43] A. A. Alfaryjat, H. A. Mohammed, N. M. Adam, M. K. A. Ariffin, and M. I. Najafabadi, "Influence of geometrical parameters of hexagonal, circular, and rhombus microchannel heat sinks on the thermohydraulic characteristics," *International Communications in Heat and Mass Transfer,* vol. 52, pp. 121-131, 2014, doi: 10.1016/j.icheatmasstransfer.2014.01.015.

[44] J. Zhang, Y. H. Diao, Y. H. Zhao, and Y. N. Zhang, "An experimental study of the characteristics of fluid flow and heat transfer in the multiport microchannel flat tube," *Applied Thermal Engineering,* vol. 65, no. 1, pp. 209-218, 2014, doi: 10.1016/j.applthermaleng.2014.01.008.

[45] G. Xie, F. Zhang, B. Sunden, and W. Zhang, "Constructal design and thermal analysis of microchannel heat sinks with multistage bifurcations in single-phase liquid flow," *Applied Thermal Engineering,* vol. 62, pp. 791-802, 2014, doi: 10.1016/j.applthermaleng.2013.10.042.

[46] Y. Li, F. Zhang, B. Sunden, and G. Xie, "Laminar thermal performance of microchannel heat sinks with constructal vertical Y-shaped bifurcation plates," *Applied Thermal Engineering,* vol. 73, no. 1, pp. 185-195, 2014, doi: 10.1016/j.applthermaleng.2014.07.031.

[47] S. Riera, J. Barrau, M. Omri, L. G. Fréchette, and J. I. Rosell, "Stepwise varying width microchannel cooling device for uniform wall temperature: Experimental and numerical study," *Applied Thermal Engineering,* vol. 78, pp. 30-38, 2015, doi: 10.1016/j.applthermaleng.2014.12.012.

[48] J. F. Douglas, *Fluid Mechanics*. Pearson Education, 2005.

[49] C. A. Rubio-Jimenez, S. G. Kandlikar, and A. Hernandez-Guerrero, "Numerical Analysis of Novel Micro Pin Fin Heat Sink With Variable Fin Density," *IEEE*

Transactions on Components, Packaging and Manufacturing Technology, vol. 2, no. 5, pp. 825-833, 2012, doi: 10.1109/TCPMT.2012.2189925.

[50] Y. J. Lee, P. S. Lee, and S. K. Chou, "Enhanced Thermal Transport in Microchannel Using Oblique Fins," *Journal of Heat Transfer,* vol. 134, no. 10, 2012, doi: 10.1115/1.4006843.

[51] Y. J. Lee, P. S. Lee, and S. K. Chou, "Hotspot Mitigating With Obliquely Finned Microchannel Heat Sink—An Experimental Study," *IEEE Transactions on Components, Packaging and Manufacturing Technology,* vol. 3, no. 8, pp. 1332-1341, 2013, doi: 10.1109/TCPMT.2013.2244164.

[52] Y. J. Lee, P. Singh, and P. S. Lee, "Fluid flow and heat transfer investigations on enhanced microchannel heat sink using oblique fins with parametric study," *International Journal of Heat and Mass Transfer,* vol. 81, 2014, doi: 10.1016/j.ijheatmasstransfer.2014.10.018.

[53] B. Lu, W. Meng, and F. Mei, "Experimental investigation of Cu-based, double-layered, microchannel heat exchangers," *Journal of Micromechanics and Microengineering,* vol. 23, p. 035017, 2013, doi: 10.1088/0960-1317/23/3/035017.

[54] K.-C. Wong and F. Muezzin, "Heat transfer of a parallel flow two-layered microchannel heat sink," *International Communications in Heat and Mass Transfer,* vol. 49, pp. 136–140, 2013, doi: 10.1016/j.icheatmasstransfer.2013.09.004.

[55] C. Leng, X.-D. Wang, and T.-H. Wang, "An improved design of double-layered microchannel heat sink with truncated top channels," *Applied Thermal Engineering,* vol. 79, pp. 54-62, 2015, doi: 10.1016/j.applthermaleng.2015.01.015.

[56] T. Hou and Y. Chen, "Pressure drop and heat transfer performance of microchannel heat exchanger with different reentrant cavities," *Chemical Engineering and Processing - Process Intensification,* vol. 153, p. 107931, 2020, doi: 10.1016/j.cep.2020.107931.

[57] S. H. Kim, H.-C. Shin, and S.-M. Kim, "Numerical study on cooling performance of hybrid micro-channel/micro-jet-impingement heat sink," *Journal of Mechanical*

Science and Technology, vol. 33, no. 7, pp. 3555-3562, 2019, doi: 10.1007/s12206-019-0649-7.

[58] G. J. Michna, E. A. Browne, Y. Peles, and M. K. Jensen, "The effect of area ratio on microjet array heat transfer," *International Journal of Heat and Mass Transfer,* vol. 54, no. 9, pp. 1782-1790, 2011, doi: 10.1016/j.ijheatmasstransfer.2010.12.038.

[59] M. Shin, S. Senguttuvan, and S. Kim, "Investigations of Flow and Heat Transfer Characteristics in a Channel Impingement Cooling Configuration with a Single Row of Water Jets," *Energies,* vol. 14, no. 14, p. 4327, 2021, doi: 10.3390/en14144327.

[60] S. D. Barewar *et al.*, "Optimization of jet impingement heat transfer: A review on advanced techniques and parameters," *Thermal Science and Engineering Progress,* vol. 39, p. 101697, 2023, doi: 10.1016/j.tsep.2023.101697.

[61] Y. Fan and I. Hassan, "Numerical Simulation of a Novel Jet-Impingement Micro Heat Sink With Cross Flow Under Non Uniform Heating Condition," in *ASME 2011 9th International Conference on Nanochannels, Microchannels, and Minichannels*, 2011, vol. ASME 2011 9th International Conference on Nanochannels, Microchannels, and Minichannels, Volume 1, pp. 441-449, doi: 10.1115/icnmm2011-58002.

[62] X. Liu, J. H. Lienhard, V, and J. S. Lombara, "Convective Heat Transfer by Impingement of Circular Liquid Jets," *Journal of Heat Transfer,* vol. 113, no. 3, pp. 571-582, 1991, doi: 10.1115/1.2910604.

[63] H. Martin, "Heat and Mass Transfer between Impinging Gas Jets and Solid Surfaces," *Advances in Heat Transfer,* vol. 13, pp. 1-60, 1977, doi: 10.1016/S0065-2717(08)70221-1.

[64] A. J. Robinson and E. Schnitzler, "An experimental investigation of free and submerged miniature liquid jet array impingement heat transfer," *Experimental Thermal and Fluid Science,* vol. 32, no. 1, pp. 1-13, 2007, doi: 10.1016/j.expthermflusci.2006.12.006.

[65] R. Viskanta, "Heat transfer to impinging isothermal gas and flame jets," *Experimental Thermal and Fluid Science,* vol. 6, no. 2, pp. 111-134, 1993, doi: 10.1016/0894-1777(93)90022-B.

[66] D. J. Womac, S. Ramadhyani, and F. P. Incropera, "Correlating Equations for Impingement Cooling of Small Heat Sources With Single Circular Liquid Jets," *Journal of Heat Transfer,* vol. 115, no. 1, pp. 106-115, 1993, doi: 10.1115/1.2910635.

[67] Y. Liu, M. Wei, T. Zhang, H. Qiao, and H. Li, "Overview on the development and critical issues of water jet guided laser machining technology," *Optics & Laser Technology,* vol. 137, p. 106820, 2021, doi: 10.1016/j.optlastec.2020.106820.

[68] S. V. Garimella and R. A. Rice, "Confined and Submerged Liquid Jet Impingement Heat Transfer," *Journal of Heat Transfer,* vol. 117, no. 4, pp. 871-877, 1995, doi: 10.1115/1.2836304.

[69] L. Yang, P. Ligrani, J. Ren, and H. Jiang, "Unsteady Structure and Development of a Row of Impingement Jets, Including Kelvin–Helmholtz Vortex Development," *Journal of Fluids Engineering,* vol. 137, no. 5, 2015, doi: 10.1115/1.4029386.

[70] N. Zuckerman and N. Lior, "Jet Impingement Heat Transfer: Physics, Correlations, and Numerical Modeling," *Advances in heat transfer,* vol. 39, pp. 565-631, 2006, doi: 10.1016/S0065-2717(06)39006-5.

[71] C. J. Hoogendoorn, "The effect of turbulence on heat transfer at a stagnation point," *International Journal of Heat and Mass Transfer,* vol. 20, pp. 1333-1338, 1977, doi: 10.1016/0017-9310(77)90029-1.

[72] K.-i. Abe and K. Suga, "Large eddy simulation of passive scalar in complex turbulence with flow impingement and flow separation," *Heat Transfer Research,* vol. 30, pp. 402-418, 2001, doi: 10.1002/htj.1027.

[73] R. Gardon and J. C. Akfirat, "The role of turbulence in determining the heat-transfer characteristics of impinging jets," *International Journal of Heat and Mass Transfer,* vol. 8, no. 10, pp. 1261-1272, 1965, doi: 10.1016/0017-9310(65)90054-2.

[74] M. Behnia, S. Parneix, Y. Shabany, and P. A. Durbin, "Numerical study of turbulent heat transfer in confined and unconfined impinging jets," *International Journal of Heat and Fluid Flow,* vol. 20, pp. 1-9, 1999, doi: 10.1016/j.ijheatmasstransfer.2015.12.022.

[75] J. M. Khodadadi, T. M. Nguyen, and N. S. Vlachos, "Laminar Forced Convective Heat Transfer in a Two-Dimensional 90° Bifurcation," *Numerical Heat Transfer,* vol. 9, no. 6, pp. 677-695, 1986, doi: 10.1080/10407788608913501.

[76] K. Marzec and A. Kucaba-Pietal, "Heat transfer characteristic of an impingement cooling system with different nozzle geometry," *Journal of Physics Conference Series,* vol. 530, no. 1, p. 8, 2014, doi: 101088/1742-6596/530/1/012038.

[77] K. Marzec and K.-P. Anna, "Numerical investigation of local heat transfer distribution on surfaces with a non-uniform temperature under an array of impinging jets with various nozzle shapes," *Journal of Theoretical and Applied Mechanics,* vol. 55, pp. 1313-1324, 2017, doi: 10.15632/jtam-pl.55.4.1313.

[78] R. Gharraei, A. Vejdani, S. Baheri, and A. A. Davani D, "Numerical investigation on the fluid flow and heat transfer of non-Newtonian multiple impinging jets," *International Journal of Thermal Sciences,* vol. 104, pp. 257-265, 2016, doi: 10.1016/j.ijthermalsci.2016.01.012.

[79] K. B. Girish, D. S H, B. S. Dayananda, and T. Rajashekaraiah, "Experimental investigation of turbulent flow behavior in an air to air double pipe heat exchanger using novel para winglet tape," *Case Studies in Thermal Engineering,* vol. 22, pp. 1-8, 2020, doi: 10.1016/j.csite.2020.100791.

[80] O. E. Turgut, M. Asker, and M. T. Çoban, "A review of non iterative friction factor correlations for the calculation of pressure drop in pipes," *Bitlis Eren University Journal of Science and Technology,* vol. 4, no. 1, pp. 1-8, June 2014, doi: 10.17678/beujst.90203.

[81] F. P. Incropera and D. P. DeWitt, *Fundamentals of Heat and Mass Transfer*. John Wiley & Sons, Inc., 111 River Street, Hoboken, NJ, United States, 2006.

[82] T. H. Chilton and A. P. Colburn, "Mass Transfer (Absorption) Coefficients Prediction from Data on Heat Transfer and Fluid Friction," *Industrial & Engineering Chemistry,* vol. 26, pp. 1183-1187, 1934.

[83] A. J. Robinson, "A Thermal–Hydraulic Comparison of Liquid Microchannel and Impinging Liquid Jet Array Heat Sinks for High-Power Electronics Cooling," *IEEE Transactions on Components and Packaging Technologies,* vol. 32, no. 2, pp. 347-357, 2009, doi: 10.1109/TCAPT.2008.2010408.

[84] B. P. Whelan and A. J. Robinson, "Nozzle geometry effects in liquid jet array impingement," *Applied Thermal Engineering,* vol. 29, no. 11, pp. 2211-2221, 2009, doi: 10.1016/j.applthermaleng.2008.11.003.

[85] M. F. Koseoglu and S. Baskaya, "The role of jet inlet geometry in impinging jet heat transfer, modeling and experiments," *International Journal of Thermal Sciences,* vol. 49, no. 8, pp. 1417-1426, 2010, doi: 10.1016/j.ijthermalsci.2010.02.009.

[86] Y. Zhong, C. Zhou, and Y. Shi, "Effect of the Nozzle Geometry on Flow Field and Heat Transfer in Annular Jet Impingement," *Energies,* vol. 15, no. 12, p. 4271, 2022, doi: 10.3390/en15124271.

[87] U. Allauddin, Naeemullah, and P. G. Verdin, "Effect of Nozzle Shape on Fluid Flow and Heat Transfer characteristics of an Impinging Jet System – A Numerical Study," *MATEC Web Conf.,* vol. 398, p. 01004, 2024, doi: 10.1051/matecconf/202439801004.

[88] O. Yalçınkaya and U. Durmaz, "Numerical analysis of jet impingement cooling with elongated nozzle holes on a curved surface roughened with V-shaped ribs," *Journal of Thermal Analysis and Calorimetry,* vol. 149, no. 8, pp. 3453-3470, 2024, doi: 10.1007/s10973-024-12965-4.

[89] S. Caliskan, S. Baskaya, and T. Calisir, "Experimental and numerical investigation of geometry effects on multiple impinging air jets," *International Journal of Heat and Mass Transfer,* vol. 75, pp. 685-703, 2014, doi: 10.1016/j.ijheatmasstransfer.2014.04.005.

[90] Y. Yamane, M. Yamamoto, M. Motosuke, and S. Honami, "Effect of Jet Shape of Square Array of Multi-Impinging Jets on Heat Transfer," in *ASME Turbo Expo 2013: Turbine Technical Conference and Exposition*, 2013, vol. 3A: Heat Transfer, doi: 10.1115/gt2013-94452.

[91] S. V. Garimella and B. Nenaydykh, "Nozzle-geometry effects in liquid jet impingement heat transfer," *International Journal of Heat and Mass Transfer,* vol. 39, no. 14, pp. 2915-2923, 1996, doi: 10.1016/0017-9310(95)00382-7.

[92] A. Royne and C. J. Dey, "Effect of nozzle geometry on pressure drop and heat transfer in submerged jet arrays," *International Journal of Heat and Mass Transfer,* vol. 49, no. 3, pp. 800-804, 2006, doi: 10.1016/j.ijheatmasstransfer.2005.11.014.

[93] B. W. Webb and C. F. Ma, "Single-Phase Liquid Jet Impingement Heat Transfer," *Advances in Heat Transfer,* vol. 26, pp. 105-217, 1995, doi: 10.1016/S0065-2717(08)70296-X.

[94] Y. Pan and B. W. Webb, "Heat Transfer Characteristics of Arrays of Free-Surface Liquid Jets," *Journal of Heat Transfer,* vol. 117, no. 4, pp. 878-883, 1995, doi: 10.1115/1.2836305.

[95] S. J. Slayzak, R. Viskanta, and F. P. Incropera, "Effects of interaction between adjacent free surface planar jets on local heat transfer from the impingement surface," *International Journal of Heat and Mass Transfer,* vol. 37, no. 2, pp. 269-282, 1994, doi: 10.1016/0017-9310(94)90098-1.

[96] S. Nawani and M. Subhash, "A review on multiple liquid jet impingement onto flat plate," *Materials Today: Proceedings,* vol. 46, pp. 11190-11197, 2021, doi: 10.1016/j.matpr.2021.02.393.

[97] A. Sleiti and J. Kapat, "An Experimental Investigation of Liquid Jet Impingement and Single-Phase Spray Cooling Using Polyalphaolefin," *Experimental Heat Transfer,* vol. 19, pp. 149-163, 2006, doi: 10.1080/08916150500479349.

[98] C. Kistak, A. Taskiran, and N. Celik, "Experimental analysis of transient and steady-state heat transfer from an impinging jet to a moving plate," *Heat and Mass Transfer,* vol. 60, no. 10, pp. 1713-1729, 2024, doi: 10.1007/s00231-024-03517-5.

[99] A. H. Untuç and S. O. Unverdi, "Heat Transfer Enhancement by Mitigating the Adverse Effects of Crossflow in a Multi-Jet Impingement Cooling System in Hexagonal Configuration by Coaxial Cylindrical Protrusion—Guide Vane Pairs," *Applied Sciences,* vol. 13, no. 20, p. 11260, 2023, doi: 10.3390/app132011260.

[100] N. T. Obot and T. A. Trabold, "Impingement Heat Transfer Within Arrays of Circular Jets: Part 1—Effects of Minimum, Intermediate, and Complete Crossflow for Small and Large Spacings," *Journal of Heat Transfer,* vol. 109, no. 4, pp. 872-879, 1987, doi: 10.1115/1.3248197.

[101] R. J. Goldstein and J. F. Timmers, "Visualization of heat transfer from arrays of impinging jets," *International Journal of Heat and Mass Transfer,* vol. 25, no. 12, pp. 1857-1868, 1982, doi: 10.1016/0017-9310(82)90108-9.

[102] R. J. Goldstein and M. E. Franchett, "Heat Transfer From a Flat Surface to an Oblique Impinging Jet," *Journal of Heat Transfer,* vol. 110, no. 1, pp. 84-90, 1988, doi: 10.1115/1.3250477.

[103] M. Fabbri and V. K. Dhir, "Optimized Heat Transfer for High Power Electronic Cooling Using Arrays of Microjets," *Journal of Heat Transfer,* vol. 127, no. 7, pp. 760-769, 2004, doi: 10.1115/1.1924624.

[104] A. Bhunia and C. L. Chen, "On the Scalability of Liquid Microjet Array Impingement Cooling for Large Area Systems," *Journal of Heat Transfer,* vol. 133, no. 6, 2011, doi: 10.1115/1.4003532.

[105] S.-M. Kim, A. Husain, and K.-Y. Kim, "Optimization of an Indirect Micro-Jet Impingement Cooling System," 2012, doi: 10.2514/6.2012-5638.

[106] A. Husain, S.-M. Kim, and K.-Y. Kim, "Performance analysis and design optimization of micro-jet impingement heat sink," *Heat and Mass Transfer,* vol. 49, no. 11, pp. 1613-1624, 2013, doi: 10.1007/s00231-013-1202-3.

[107] P. Yu, K. Zhu, Q. Shi, N. Yuan, and J. Ding, "Transient heat transfer characteristics of small jet impingement on high-temperature flat plate," *International Journal of Heat and Mass Transfer,* vol. 114, pp. 981-991, 2017, doi: 10.1016/j.ijheatmasstransfer.2017.06.112.

[108] H. C. Cui, C. Y. Shi, M. J. Yu, Z. K. Zhang, Z. C. Liu, and W. Liu, "Optimal parameter design of a slot jet impingement/microchannel heat sink base on multi-objective optimization algorithm," *Applied Thermal Engineering,* vol. 227, p. 120452, 2023, doi: 10.1016/j.applthermaleng.2023.120452.

[109] P. Martínez-Filgueira, E. Zulueta, A. Sánchez-Chica, U. Fernández-Gámiz, and J. Soriano, "Multi-Objective Particle Swarm Based Optimization of an Air Jet Impingement System," *Energies,* vol. 12, no. 9, p. 1627, 2019, doi: 10.3390/en12091627.

[110] M. O. Qidwai, I. A. Badruddin, N. Z. Khan, M. A. Khan, and S. Alshahrani, "Optimization of Microjet Location Using Surrogate Model Coupled with Particle Swarm Optimization Algorithm," *Mathematics,* vol. 9, no. 17, p. 2167, 2021, doi: 10.3390/math9172167.

[111] R. Brakmann, L. Chen, B. Weigand, and M. Crawford, "Experimental and Numerical Heat Transfer Investigation of an Impinging Jet Array on a Target Plate Roughened by Cubic Micro Pin Fins," *Journal of Turbomachinery,* vol. 138, no. 11, 2016, doi: 10.1115/1.4033670.

[112] Z. Ren, X. Yang, X. Lu, X. Li, and J. Ren, "Experimental Investigation of Micro Cooling Units on Impingement Jet Array Flow Pressure Loss and Heat Transfer Characteristics," *Energies,* vol. 14, no. 16, p. 4757, 2021, doi: 10.3390/en14164757.

[113] Z. Rachdi, N. Hnaien, A. Eladeb, B. M. Alshammari, L. Kolsi, and H. Dhahri, "CFD analysis of heat transfer enhancement in impinging jet array by varying number of jets and spacing," *Scientific Reports,* vol. 15, no. 1, p. 3023, 2025, doi: 10.1038/s41598-025-86360-w.

[114] P. Chandra, P. Panda, and P. Dutta, "An augmented swirling and round jet impinging on a heated flat plate and its heat transfer characteristics," *International Communications in Heat and Mass Transfer,* vol. 149, p. 107121, 2023, doi: 10.48550/arXiv.2211.08059.

[115] H. Zhen, B. Du, X. Liu, Z. Liu, and Z. Wei, "Experimental Investigation on the Heat Flux Distribution and Pollutant Emissions of Slot LPG/Air Premixed Impinging Flame Array," *Energies,* vol. 14, no. 19, p. 6255, 2021, doi: 10.3390/en14196255.

[116] A. J. Robinson, J. Colenbrander, R. Kempers, and R. Chen, "Solid and Vapor Chamber Integrated Heat Spreaders: Which to Choose and Why," *IEEE Transactions on Components, Packaging and Manufacturing Technology,* vol. 8, no. 9, pp. 1581-1592, 2018, doi: 10.1109/TCPMT.2018.2822400.

[117] R. L. McMasters, F. d. Monte, G. D'Alessandro, and J. V. Beck, "The Effect of Biot Number on a Generalized Heat Conduction Solution," *ASME Journal of Heat and Mass Transfer,* vol. 145, no. 9, 2023, doi: 10.1115/1.4062637.

[118] K. Karabulut, "Heat transfer improvement study of electronic component surfaces using air jet impingement," *Journal of Computational Electronics,* vol. 18, no. 4, pp. 1259-1271, 2019, doi: 10.1007/s10825-019-01387-3.

[119] S. Li *et al.*, "Thermal expansion coefficients of high thermal conducting BAs and BP materials," *Applied Physics Letters,* vol. 115, no. 1, 2019, doi: 10.1063/1.5103166.

[120] G. Maranzana, I. Perry, D. Maillet, and S. Raël, "Design optimization of a spreader heat sink for power electronics," *International Journal of Thermal Sciences,* vol. 43, no. 1, pp. 21-29, 2004, doi: 10.1016/S1290-0729(03)00107-8.

[121] J. Deepak, "Heat spreading characteristics of heat sink for cooling a concentrated heat source," presented at the National Conference on Progress, Research and Innovation in Mechanical Engineering, SCET, Surat, Gujarat, India, 2017.

[122] S. Lee, S. Song, V. Au, and K. P. Moran, "Constriction/Spreading Resistance Model for Electronics Packaging," in *ASME/JSME Thermal Engineering*, 1995, vol. 4, pp. 199-206.

[123] Y. S. Muzychka, J. Culham, and M. Yovanovich, "Thermal Spreading Resistance of Eccentric Heat Sources on Rectangular Flux Channels," *Journal of Electronic Packaging,* vol. 125, no. 2, pp. 178-185, 2003, doi: 10.1115/1.1568125.

[124] M. Awad, A. Radwan, O. Abdelrehim, M. Emam, A. N. Shmroukh, and M. Ahmed, "Performance evaluation of concentrator photovoltaic systems integrated with a new jet impingement-microchannel heat sink and heat spreader," *Solar Energy,* vol. 199, pp. 852-863, 2020, doi: 10.1016/j.solener.2020.02.078.

[125] J. W. Elliott, M. T. Lebon, and A. J. Robinson, "Optimising integrated heat spreaders with distributed heat transfer coefficients: A case study for CPU cooling," *Case Studies in Thermal Engineering,* vol. 38, p. 102354, 2022, doi: 10.1016/j.csite.2022.102354.

[126] J. W. Elliott and A. J. Robinson, "Optimised Liquid Impinging Jet Arrays for Cooling CPU Packages," *IEEE Transactions on Components, Packaging and Manufacturing Technology,* vol. 15, no. 3, pp. 488-505, 2025, doi: 10.1109/TCPMT.2024.3485478.

Chapter 2

Optimising Integrated Heat Spreaders with Distributed Heat Transfer Coefficients

Abstract

Increasing power densities of modern CPUs has led to regions of high temperature on the semiconductor die which can lead to performance and reliability problems. In this case study, the effect of imposing a non-uniform heat transfer coefficient profile across the convective surface of the CPU's integrated heat spreader was investigated as a potential enhanced cooling concept. A finite element model of a copper heat spreader of 40 x 40 mm^2 area and 2.5 mm thickness with a centred 13 x 13 mm^2 heat source at 100 W/cm^2 heat flux was considered to approximate typical modern high-powered CPUs. Both uniform and Gaussian distributions of the heat transfer coefficient were then considered. For the latter, both single and multi-objective Genetic Algorithm optimisations were carried out for three source temperature objectives: average temperature, maximum temperature and maximum temperature difference. The analysis showed that the multi-objective optimisation strategy produced the best overall heat transfer coefficient distribution, with almost 5 K reduction in both the maximum temperature and temperature gradient across the heat source relative to a baseline design case with a uniform heat transfer coefficient distribution applied across the convective surface of the heat spreader. This chapter corresponds to the publication [1].

2.1. Introduction

The increasing power densities of central processing units (CPUs) has led to regions of high heat flux on the semiconductor die. The concentration of thermal power can negatively influence CPU performance, to the point that thermal management can dictate the design power. Practically, if cores on the CPU die exceed the maximum specified temperature threshold, it causes the performance of the CPU to be throttled in order to reduce power and prevent damage [2]. Typically, the exact measurement technique used to monitor CPU temperature for both the die and individual cores vary between CPU architecture and manufacturer. However, these most commonly take the form of Digital Thermal Sensors (DTS) built directly into the die, with an accuracy of ± 5 K, or analogue thermal diodes that measure voltage changes which correlate with temperature [3, 4]. The exact nature of measurement technique used for each CPU is difficult to ascertain as this information is rarely provided by the manufacturer. Furthermore, while these measurement techniques do not provide a full power breakdown across the active cores of a CPU, they do, at least in the case of DTSs, allow for a breakdown of temperatures for each core, which can be advantageous during observation under high loading conditions of which cores generate a higher heat flux and hence require greater cooling.

In multicore processors, uneven distribution of compute activity can lead to an uneven heat flux distribution, which can exacerbate cooling challenges [5]. Therefore, it is imperative that adequate cooling is available, specifically for the hottest and most problematic core(s) on the silicon die. Further to this, aggressive global cooling to target the problem core(s) may overcool neighbouring cores, leading to significant temperature gradients on the die, which presents its own reliability problems, particularly when considering the different coefficients of thermal expansion of neighbouring components [6]. As such, advanced cooling of CPUs must consider a balance that enables adequate cooling of the hottest core(s), yet not induce unacceptable thermal gradients along the die. Inadequate cooling effectiveness of electronic devices can lead to significant issues such as performance degradation, reduced reliability, and shortened lifespan, in addition to problems such as degradation of Thermal Interface Materials (TIM), thermal runaway, throttling and reduced signal fidelity [7-9].

The cooling effectiveness of a concentrated heat source can be improved by spreading the thermal energy to a larger convective cooling area, effectively increasing the area of convective heat transfer with associated reduction in its thermal resistance. In CPU packages, this is facilitated by incorporating an Integrated Heat Spreader (IHS) between the die and the convective heat sink. Thermal management of the electronic package thus requires accurate determination of individual thermal resistances present between contacting surfaces for the system in question, including the IHS [10]. Robinson et al. [11] determined that, for a concentrated heat source, increasing the size of the IHS lateral dimension can indeed decrease the convective and overall resistance. However, this decreasing trend plateaus such that little benefit is achieved for high IHS sizes. Similarly, if the lateral dimension of the spreader is fixed, an optimal IHS thickness exists which minimises the characteristic temperature (maximum or average) of the heat source [12]. Although increased thickness tends to improve lateral conduction, it simultaneously increases the transverse conduction resistance. It is therefore vital that, for a given heat source, the IHS dimensions are considered critically and optimised, with the aim of minimising the spreader thermal resistance or maximising its effective conductance [13]. If designed correctly, the additional resistance associated with the IHS system will be more than offset by the reduced convective resistance, leading to an overall reduction in the source-to-sink thermal resistance, facilitating cooler die temperatures or potentially reduced coolant flow rates for the same cooling effectiveness [14, 15].

In order to optimise an IHS system, prediction of the thermal resistance associated with a concentrated source on a heat spreader with a convective boundary condition on the opposite face is required. Most cooling strategies can be well approximated as a uniform convective resistance on the cooled surface, which is a sufficient simplification to allow analytic modelling of the three-dimensional heat flow problem. Exact and approximate analytic solutions have been put forth by several authors, including but not limited to [16-22], with a detailed review provided by Razavi et al. [23]. Of the available analytic solutions, the model proposed by Lee at al. [24] is the most convenient, owing to the leading order approximation eliminating the infinite series terms, and has been shown to be very accurate [18]. In the context of aggressive cooling of high-powered CPUs, the analytic models show that increasing the effective heat transfer coefficient decreases the source-to-sink thermal resistance. Although this is unsurprising, it is noted that this is a conjugate heat transfer problem, so the optimum IHS dimensions will also be sensitive to the imposed convective boundary condition.

As CPU heat fluxes escalate, cooling with air becomes less feasible owing to issues around fan power, noise, compactness and inadequate cooling effectiveness. In applications such as data centres, which can host thousands of CPUs, the infrastructure energy associated with conditioning and handling air, along with the low potential for heat recovery, also become problematic [25, 26]. The practical limitations of air cooling have motivated an emerging shift to liquid cooling of CPUs, owing to its superior thermophysical properties [27]. A large body of work has been published on advanced liquid cooling technologies that include though is not limited to microchannels [28], pin fins [29], microjets [30, 31], and hybrid solutions [32]. As mentioned, however, aggressive liquid cooling will influence the heat flow in the IHS owing to the conjugate nature of the problem. Liquid cooling solutions and concepts that specifically target concentrated heat sources are less common. The works of Kim et al. [13], Nikolić et al. [33], Lee at al. [34], Sharma et al. [35], Laguna et al. [36], Wu et al. [37], Wiriyasart & Naphon [38] and Kong et al. [39], are examples of liquid cooling studies that consider concentrated heat sources and both the convection and conduction problem simultaneously. An important conclusion that can be drawn from these studies is that clever design of the liquid cooled heat sink can positively influence the source-to-sink resistance of the package, including targeted cooling of hot spots.

It is evident from the literature that the concepts of heat spreading and high-performance liquid cooling have been extensively investigated. The preponderance of knowledge is associated with the scenario whereby the heat transfer coefficient across the heat spreader is uniform. Less work has been conducted on the combined conductive-convective problem, though there is evidence that hot spot mitigation occurs when concentrating the convective heat transfer in regions of high heat flux. In other words, when a concentrated heat source is dissipating heat through an IHS, providing a heat transfer coefficient that is non-uniform on the cooled face is likely to be advantageous.

The aim of this case study is to investigate the effect of aggressive cooling solutions which incorporate non-uniform heat transfer coefficient distributions on the convective surface of an IHS in order to determine if a significant improvement in thermal performance is realised compared with a uniform distribution. To achieve this, a realistic case study scenario, typifying modern CPUs, has been chosen. A non-uniform Gaussian distribution function of the convective heat transfer coefficient was then optimised by considering different temperature objectives to determine the best thermal performance. Although this case study targets a single CPU architecture with uniform thermal loading at the source and specific functional form of the convective heat transfer coefficient, the mathematical process developed can be adapted to broader and more complex scenarios, including different geometric configurations, non-uniform heat loading and multi-chip modules. The fluid dynamics associated with this type of cooling problem are not considered within this study, instead focusing on the thermal conduction present across a solid heat spreader for an applied convective boundary condition of both uniform and variable distributions.

2.2. Heat Spreaders in Modern CPU Packages

2.2.1. Why are heat spreaders required in modern CPUs?

The embedded table in Figure 2.1 presents an example list of modern high heat flux CPUs available from Intel and AMD, where the appropriate die characteristic dimension has been determined from the die area ($L_{hs} = \sqrt{A_{hs}}$) [40] and the heat flux determined from A_{hs} and the manufacturer-recommended Thermal Design Power ($Q''_{hs} = Q_{hs}/A_{hs}$). The heat fluxes of the selected CPUs range between around 50 W/cm^2 to over 110 W/cm^2, and this can be considered conservative, since the CPU cores occupy only a region of the total lower die surface. For illustrative purposes in this case study, the average characteristic size of L_{hs} = 13 mm will be used for a square die as representative of high heat flux CPUs.

Figure 2.1 illustrates how the required heat transfer coefficient, $\left(h = Q''_{hs}/\Delta T_{j-c}\right)$ varies with the heat flux, Q''_{hs}, when a source-to-sink temperature difference of $\Delta T_{j-c} = T_j - T_c = 55$ K must be maintained. This corresponds with a maximum allowable junction temperature of $T_j = 90$°C at the source, typical of modern CPUs, and a coolant temperature of $T_c = 35$°C, which is the suggested heat sink design temperature for CPUs [3]. The figure also compares the approximate achievable heat transfer coefficient magnitudes of different direct contact natural convection (NC) and forced convection (FC) types, for air and a typical dielectric liquid (here HFE7000), with that required to sufficiently cool the bare CPU die. As shown, even with boiling of a refrigerant on the die, direct cooling is clearly incapable of achieving sufficient heat transfer coefficients to cool modern CPUs [41]. Consequently, engineering solutions must be implemented to decrease the thermal resistance and thus facilitate cooling with air and dielectrics, or potentially allow use of more effective heat transfer fluids, like water.

(a)

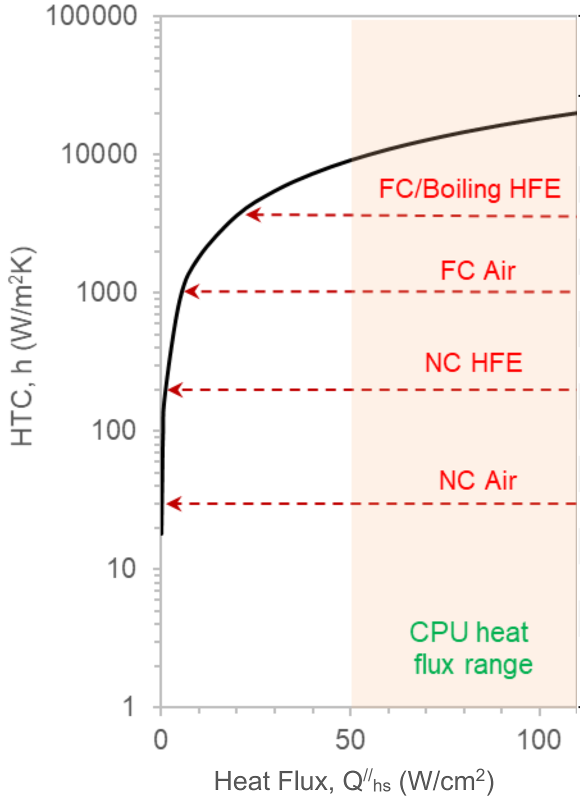

CPU	L_{hs} (mm)	TDP (W)	Q''_{hs} (W/cm^2)
Intel i5-12600KF (Turbo)	14.7	150	69.7
Intel i7-7740X	11.2	112	88.9
Intel i7-8700K	12.4	95	61.8
Intel i7-8809G	11.2	100	79.4
Intel i7-9700K	13.3	95	53.4
Intel i9-9900K	13.4	95	52.7
Intel i9-9900KS	13.2	127	73.0
Intel i9-10900K	14.4	125	60.7
Intel i9-12700K (Turbo)	14.7	190	88.3
Intel i9-12900K (Turbo)	14.7	241	112.0
Intel Xeon E-2274G	11.2	83	65.9
Intel Xeon E-2286G	12.2	95	63.5
AMD Ryzen 9 3900X	12.2	105	70.9
AMD Ryzen 9 5950X	12.8	105	64.0
AMD Ryzen Threadripper 3960X	17.2	280	94.6
Average:	13.3	133.2	73.2

(b)

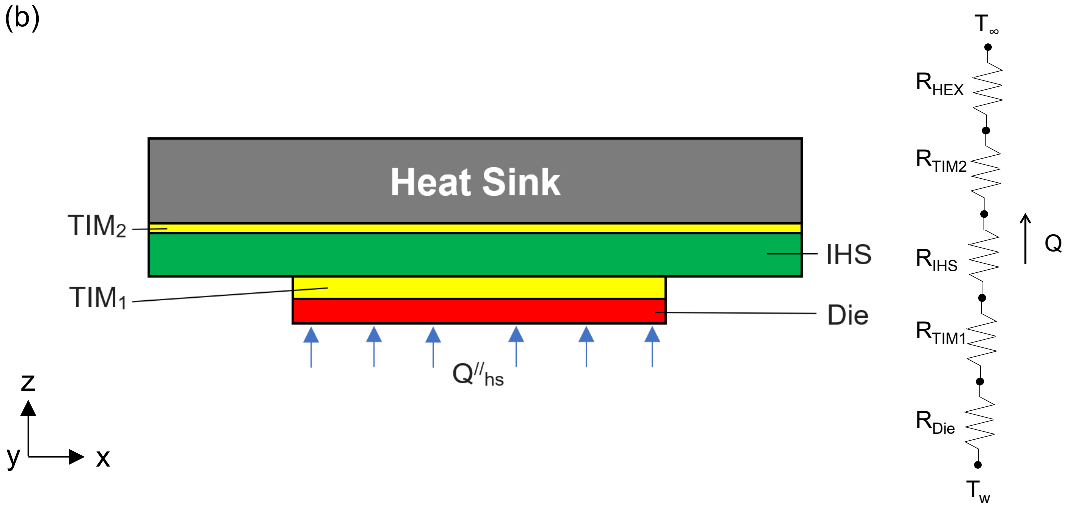

Figure 2.1 : (a) Required convective heat transfer coefficient versus heat flux for a 13 mm square die and required source-to-sink temperature difference of $\Delta T_{j\text{-}c} = 55$ K, along with approximate magnitudes of direct contact convection of insulating coolants [42, 43]. Inset table provides list of typical modern high heat flux CPUs. (b) Illustration of the thermal stack with associated thermal resistance diagram of a CPU package.

The relationship for convective thermal resistance, $R_{conv} = (hA_{IHS})^{-1}$, indicates that the thermal resistance is inversely proportional to the surface area. Consequently, for a given convective heat transfer intensity, R_{conv} can be decreased by increasing the total surface area upon which convection acts. In modern CPUs packages, this is facilitated via the introduction of an Integrated Heat Spreader (IHS), as depicted in Figure 2.1(b). An IHS functions by adding additional surface area between the heat source and the heat sink, allowing the heat to spread laterally. Hence, for an otherwise insufficient convective heat transfer coefficient, *h*, there can be enough surface area, A_{IHS}, to allow the target thermal resistance to be achieved. Practically, however, implementing an IHS requires the stack package depicted in Figure 2.1(b), and involves the penalties of adding further resistances to the thermal network, namely the Thermal Interface Materials and the IHS itself. The balance, when adding these elements to improve the heat transfer, should always be to ensure that the net resistance is lower than if direct cooling occurred on the bare die. The inclusion of an IHS can be of further benefit as it acts as a protective barrier between the die and the coolant. Consequently, this allows the use of high-performance coolants, i.e. liquids like water, and high-performance thermal hardware, such as microchannels and microjet coldplates.

Several analytical estimates exist in literature for determining the thermal spreading resistance within a heat spreader. For example, Lee et al. [24] proposed a model that accounts for a single-layer heat spreader and heat source geometry, where the spreading resistance is defined as,

$$R_s = \frac{\psi}{kA_{IHS}} \tag{2.1}$$

with

$$\psi = \frac{\phi}{\tanh(\phi\tau)} \tag{2.2}$$

where k is the conductivity of the spreader material, A_{IHS} is the surface area of the spreader, ϕ is the ratio of the heat source size to the spreader size and τ is the ratio of IHS thickness to the lateral length (d/L). This model builds of the single 45-degree rule for thermal spreading resistance, which states that $R_s \approx d/(kA_{IHS})$, which assumes that heat spreads uniformly at a 45-degree angle from a localised source into a spreader. Lee's analytical model is widely used in practical design because it balances simplicity and accuracy.

Additionally, Muzychka et al. [44] extended this analytical framework to address multi-layered structures where heat conduction occurs through multiple layers of differing materials. The model is especially relevant in modern electronics with complex thermal stacks between the heat source and coolant. Muzychka's model uses Bessel functions to account for multi-layer heat spreading and variations in thermal conductivity across layers, as well as non-uniform heat source locations. This approach considers lateral spreading resistances for each layer, with the contributions summed to calculate total resistance. However, this model considers complex calculations and requires numerical methods to reach a solution.

2.2.2. Integrated Heat Spreader Thermal Resistance

With the integration of an IHS into the package and its potential to facilitate a wide range of cooling options, a question then arises around how large R_{IHS} is in proportion to the thermal resistances that can be achieved by different practical heat sinks for various CPUs. To address this question, a straight-forward numerical model has been developed as a case study that is representative of modern high heat flux CPUs. Figure 2.2 presents the geometry used for this IHS model, with area of 40 x 40 mm^2, thickness *d*, and a centrally located CPU die of 13 x 13 mm^2. No symmetry conditions were applied to this geometry, taking into account potential future applications of this analysis where non-uniform and non-centralised head sources could be considered. Additionally, omitting symmetry conditions simplified the optimisation code development and allowed for less complex code regarding the extraction of temperature data at the interface between the heat source and heat spreader.

When modelling the IHS, copper was selected as the material, with an isotropic thermal conductivity of *k* = 400 W/mK. This selection was made owing to the excellent thermophysical properties of copper and widespread adoption in industry for high-performance electronic packaging. This relevance ensures that research findings can be effectively translated into practical applications. While not considered in this study, it would be expected that if a non-isotropic heat spreader material were to be employed, i.e. thermal conductivity is non uniform in all directions, that a higher level of lateral heat spreading would be encouraged if lateral conductivity were greater than axial conductivity, mitigating high heat fluxes on the convective surface of the IHS and requiring less intense targeted cooling to deal with high heat flux concentrations. As a result, it would be expected that heat spreader efficiency would be higher in this case than if an isotropic spreader material were used. This would also be expected to be the case if the axial dimension of the heat spreader was increased, which increases thermal resistance in the axial direction, encouraging better lateral spreading, though this comes at the cost of adding material and may not be suitable when under certain practical limitations such as material availability and spacial considerations.

The parameter ranges investigated were; effective heat sink conductance of 1,000 W/m^{2}K ≤ h_{eff} ≤ 50,000 W/m^{2}K, and IHS thickness between 1.0 mm ≤ d ≤ 5.0 mm. These cases, where the convective heat transfer coefficient is uniform, can be considered the baseline to which the non-uniform scenarios will be compared in a later section. The thermal model used to simulate the case study was based upon the steady state three-dimensional heat conduction equation, which assumes a constant thermal conductivity in the solid domain,

$$\frac{\delta^2 T}{\delta x^2} + \frac{\delta^2 T}{\delta y^2} + \frac{\delta^2 T}{\delta z^2} = 0 \tag{2.3}$$

where T is the temperature within the solid. This governing equation was subject to the following boundary conditions;

$$\frac{\delta T}{\delta x}\Big|_{x=-\frac{L_{IHS}}{2}} = \frac{\delta T}{\delta x}\Big|_{x=\frac{L_{IHS}}{2}} = \frac{\delta T}{\delta x}\Big|_{y=-\frac{L_{IHS}}{2}} = \frac{\delta T}{\delta y}\Big|_{y=\frac{L_{IHS}}{2}} = 0 \tag{2.4}$$

$$-k\frac{\delta T}{\delta x}|_{z=d} = h(T - T_{\text{atm}}) \tag{2.5}$$

$$k\frac{\delta T}{\delta x}|_{z=0} = \begin{cases} Q"_{hs} \quad (x,y) \in \left(-\frac{L_{hs}}{2}, \frac{L_{hs}}{2}\right) \\ 0 \quad (x,y) \in \left(-\frac{(L_{IHS} - L_{hs})}{2}, \frac{(L_{IHS} - L_{hs})}{2}\right) \end{cases} \tag{2.6}$$

Here, h is the uniform convective heat transfer coefficient applied to the top surface, $Q^{//}_{hs}$ is the uniform heat flux applied to the smaller area on the lower surface, $\frac{1}{2}L_{IHS}$ is half the length of the heat spreader and $\frac{1}{2}L_{hs}$ is the half the length of the heat source, where the geometric model is constructed such that the centre of the square heat source is the origin.

The model used to simulate the heat transfer in the IHS was solved in the MATLAB Finite Element solver using the Partial Differential Equation Toolbox. The MATLAB solver used triangular mesh elements, as depicted in Figure 2.2(b), and mesh independence was verified by increasing the mesh density for a high heat flux ($Q^{//}_{hs}$ = 100 W/cm^2) until the percentage error between successive simulations was less than 1% for the parameter of interest, in this case the average temperature across the contact face between source and spreader. The final mesh selected for the optimisation study was approximately 12,000 mesh elements. The mesh independence study is detailed below in Table 2.1, which also details the Grid Convergence Index (GCI), defined as [45],

$$GCI = \frac{1.25\varepsilon_{12}}{r_r{}^{p_{conv}} - 1} \tag{2.7}$$

where ε is the difference in parameter of interest between successive meshes, labelled here as grid 1 and grid 2 respectively. r_r is the ratio of grid spacing between two successive grids, which for a 3D problem is defined as the cubic root of the ratio of the number of cells used between successive meshes, and p_{conv} is the order of convergence, quantifying how quickly the numerical solution approaches the true solution as the grid is refined, defined as,

$$p_{conv} = \frac{ln\left(\frac{\varepsilon_{32}}{\varepsilon_{12}}\right)}{ln(r_r)} \tag{2.8}$$

A GCI of less than unity implies grid independence, with a decreasing GCI with increasing mesh density indicates convergence towards the true solution.

Table 2.1: Mesh independence study of MATLAB FEA model

Mesh cell density (no. of cells)			ε_{21}	ε_{32}	r_r	p_{conv}	GCI (course)	GCI (fine)
Course	*Medium*	*Fine*						
2916	6090	12550	0.01	0.06	1.26	8.42	0.013	0.0018

The numerical simulation outputs the non-uniform temperature distribution in the solid domain. The average net thermal resistance is typically presented as the sum of those associated with the heat spreader and convective heat transfer from the top face [10, 21, 46];

$$R_{net,avg} = \frac{\bar{T}_{hs} - T_{\mathrm{atm}}}{Q} = R_{IHS} + \frac{1}{hA_{IHS}} \tag{2.9}$$

where $\bar{T}_{hs}$ is the average temperature of the heat source area, A_{hs}, and R_{IHS} is the overall resistance associated with the addition of the heat spreader. Albeit convenient from a simplified calculation standpoint to some degree it masks the true influence of the heat spreader by lumping it into the R_{IHS} term, where in fact both the conductive and convective heat transfer are influenced by the presence of the spreader. This is clearly observable in the investigation of Lee et al. [21] though not discussed explicitly.

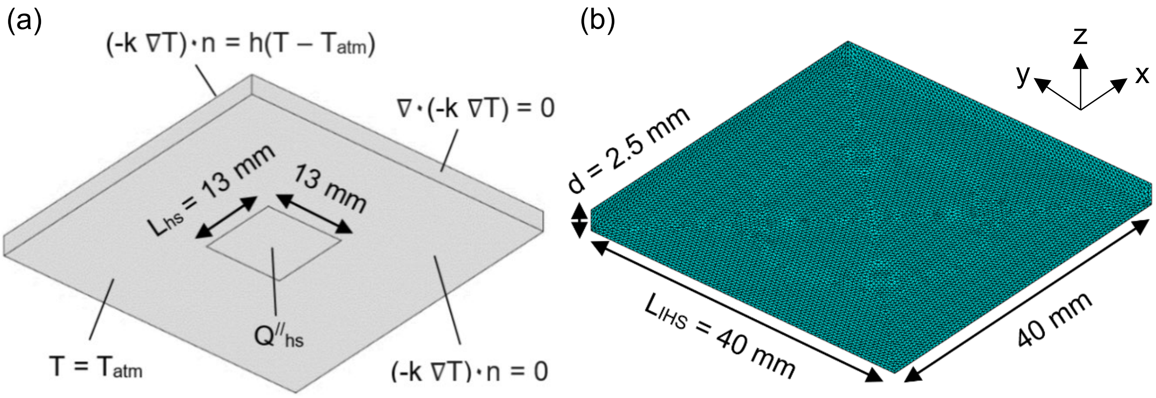

Figure 2.2: (a) 3D geometry of IHS and heat source with associated boundary conditions and coordinate system, (b) 3D mesh of IHS geometry with dimensions.

Heat spreaders are, in principle, lateral fins since they are intended to increase the heat transfer surface area, precisely the function of traditional fins, though in a different orientation in relation to the heat source. However, they are not historically considered in the same manner as fins. Fins themselves are a classical scenario of conjugate heat transfer, where the solid phase conductive heat transfer is strongly dependant on the convective heat transfer that acts on the solid boundaries. This is also the case for heat spreaders and is an important consideration since, like fins, a heat spreader's purpose is to increase the surface area for convection to act. Therefore, considering the heat spreader as a fin can provide a more effective means to describe the conjugate heat transfer problem being considered.

The efficiency of the heat spreader can be defined in the same manner as the fin efficiency, which compares the thermal resistance to one of an infinite thermal conductivity.

$$\eta_{IHS} = \frac{R_{net,avg}}{\left(\frac{1}{hA_{IHS}}\right)} \tag{2.10}$$

where A_{IHS} is the surface area of the convective surface on the spreader. The spreader efficiency, η_{IHS}, thus provides a representation of the heat spreading performance, where the closer η_{IHS} is to unity, the more effective area of the spreader's top surface is active for convection to act. Consequently, the source-to-sink thermal resistance can be given by,

$$R_{net,avg} = \frac{1}{(\eta_{IHS}A_{IHS})h} \tag{2.11}$$

Figure 2.3(a) illustrates the relationship between the fin efficiency and the lateral Biot number $(Bi = hd/k)$ for different non-dimensional heat spreader thickness ratios, $\beta = d/L_{IHS}$. As this case study considers a fixed thermal conductivity, decreasing Bi is associated with decreasing convective heat transfer coefficient and vice versa. In terms of the analogy with traditional fins, this is the same behaviour with respect to heat transfer coefficient and fin efficiency. This is clearly depicted in Figure 2.3(b), which plots distributions of the non-dimensional temperature, θ, for three different Biot numbers and β = 0.05, where,

$$\theta = \frac{\mathrm{T(x,y,z)} - \mathrm{T_{atm}}}{\mathrm{T_{max}} - \mathrm{T_{atm}}} \tag{2.12}$$

It is clear from Figure 2.3(b) that the active area on the convective side of the IHS decreases with increasing magnitude of Bi, consistent with the lower calculated spreader efficiency. It is also clear from Figure 2.3(a) that decreasing the thickness of the spreader, which restricts the lateral heat transfer, decreases the overall spreader efficiency, in the same manner as traditional fins. Also shown in Figure 2.3(a) is the comparison between the present FEA numerical model and the approximate analytical model of Lee et al. [24]. The figure indicates that the numerical model is capable of adequately reproducing the analytical data and gives confidence in the efficacy of both modelling approaches.

The key point here is that, like traditional fins, the conductive heat transfer in solid heat spreaders is highly coupled with the convective heat transfer. When implementing aggressive cooling that globally cools the top surface, such as with water-cooled coldplates, the drop in spreader efficiency means that the effective area of convective cooling is small. This is not ideal and brings into question whether global-cooling the surface of the IHS is the best option. Pumped water-cooling loops in computing systems have constraints on pressure drop and flow rate. It thus seems better engineering judgement to deploy the limited coolant resource to the portions of the heat sink that are more actively heated. However, this being a conjugate heat transfer problem, focussing the convective heat transfer will influence the conductive heat transfer, requiring a full conjugate heat transfer analysis to explore the overall impact on the cooling effectiveness, combined with an optimisation strategy to find the best overall operating condition. This can be defined as the operating condition that provides the best heat transfer performance that is able to mitigate high temperature gradients by reducing the temperature difference across the surface of the heat source whilst also minimising both the average and maximum temperatures located across this surface.

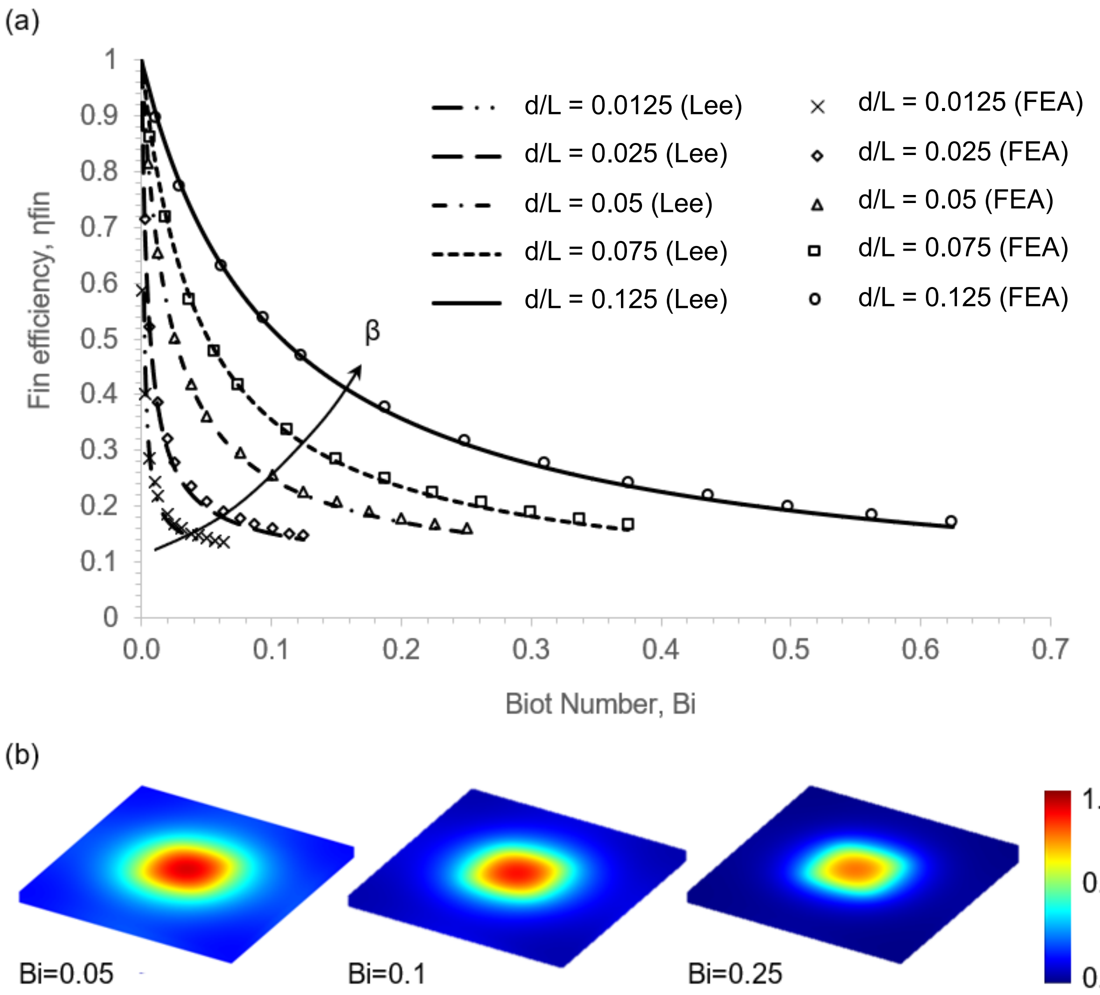

Figure 2.3: (a) Comparison between fin efficiency versus Biot number for varying β = d/L. Also shown is the comparison between the current numerical simulations and the analytic solution of Lee et al. [24]. (b) Non-dimensional temperature distributions at different Biot numbers for β = 0.05.

2.3. Distributed Heat Transfer Coefficient Distribution and Optimisation Strategy

2.3.1. Heat Transfer Coefficient Distribution

Based on the position of the heat source relative to the spreader, the aim when considering the distribution of the heat transfer coefficient was to have a continuous function that contained a maximum located at the centre of the IHS convective surface, which would decrease to a non-zero value at the outer edges of the IHS. This would be similar to the behaviour of the temperature fields on the IHS convective surface as seen in the previous section. This concentration of the heat transfer coefficient at the centre would enable better lateral spreading across the IHS and help produce a more uniform temperature distribution across the convective surface.

Based on this logic, a Gaussian distribution was determined to be a suitable function, as it produces a centrally located maximum which decreases to a minimum on either side of the peak. The associated mathematical form of this function contains inputs which can be used to control the steepness of the peak region of the curve and the minimum value to which it decreases. These variables could therefore be tailored accordingly based on the heat flux applied at the source. The Gaussian function was specified as:

$$f(x) = \frac{1}{\sigma\sqrt{2\pi}} e^{-\frac{1}{2}\left(\frac{x-\bar{x}}{\sigma}\right)^2} \tag{2.13}$$

where $\bar{x}$ is the mean value of the data set and σ is the standard deviation. To maintain a certain level of control over the optimisation, a limit was introduced into the function that specifies the average heat transfer coefficient across the whole convective surface of the IHS. This allows the function to remain within practical limits of achievable convective heat transfer coefficients. To facilitate this, the Gaussian function was amended as,

$$f(x) = \left(Z\, e^{-\frac{1}{2}\left(\frac{x^2+y^2}{a^2}\right)}\right) + m \tag{2.14}$$

Here, *m* is the minimum heat transfer coefficient that the curve asymptotically approaches in the far-field, and *a* is a multiplier that controls the width of the peak curve, which falls within the limits of 0.001 to 0.01. The expression for *Z* is specified as[1],

$$Z = \frac{2\sqrt{2}\left(h_{avg} - m\right)}{\sqrt{\pi}\, a\, \left(\mathrm{erf}\left(\frac{r}{\sqrt{2}\, a}\right)\right) - \mathrm{erf}\left(\frac{-r}{\sqrt{2}\, a}\right)} \tag{2.15}$$

where h_{avg} is the specified average heat transfer coefficient magnitude across the entire convective surface, and r is the displacement from the origin, here the centre of the IHS. The inclusion of h_{avg} as a constraint allows for an added element of control over the convective intensity, in conjunction with the existing variables 'a' and 'm.' This allows for the convective profile to be contained within known achievable intensities by practical cooling mediums. To omit this constraint would mean that the optimum distribution would be unrestricted in terms of maximum cooling intensity and therefore provide a distribution with peaks that are unobtainable without incurring significant penalties elsewhere in a practical cooling system, such as hydraulic restrictions. The Gauss error function is defined as [47],

$$erf\colon x| \rightarrow \frac{2}{\sqrt{\pi}} \int_0^x e^{-v^2}\ dv \tag{2.16}$$

Figure 2.4 illustrates how the variable inputs *a* and *m* affect the overall Gaussian distribution, where an increasing value of *a* produces a broader curve and reduces the maximum value of the peak to maintain the specified average, while increasing *m* increases the minimum value reached by the asymptotes in the far-field. An increase in *m* also contributes to a reduction in the maximum peak value, again to maintain the convective surface average heat transfer coefficient condition.

[1] For function derivation, see Appendix A1

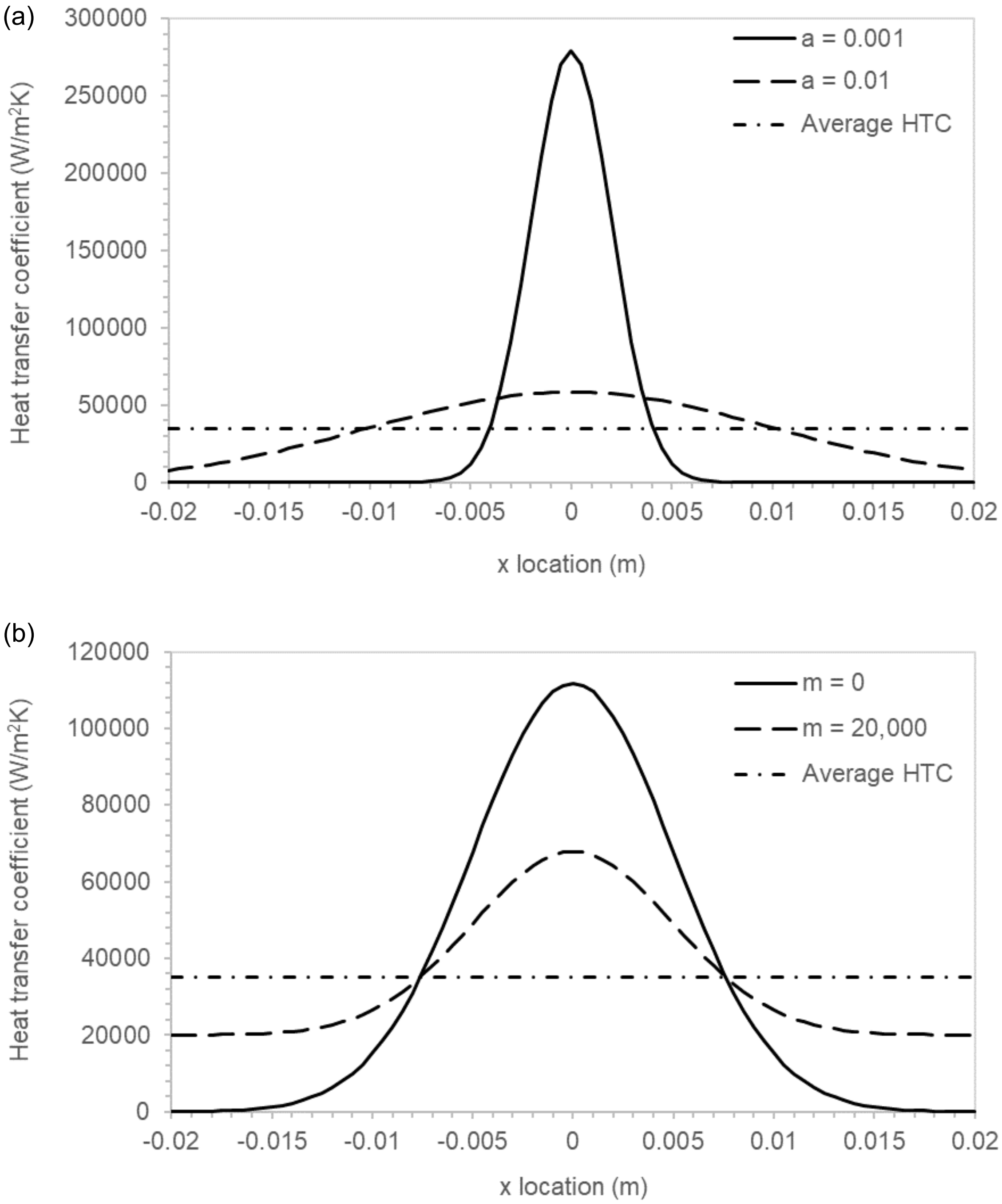

Figure 2.4: Gaussian convective heat transfer coefficient distribution profiles showing the effects of changing the inputs a and m with a surface average of h_{avg} = 35,000 W/m^{2}K. (a) Constant m = 0 W/m^{2}K for different values of a, (b) Constant a = 0.05 for varying m.

2.3.2. Heat Transfer Coefficient Optimisation

2.3.2.1. Objective functions and variable inputs parameters

For this case study, the main area of concern was the contact area between the heat source and solid heat spreader, since this is the location where the CPU die interfaces with the IHS and is the location where the highest temperatures are located. The temperature profile of the heat source region can be characterised by three different temperatures,

- Maximum temperature, T_{max}
- Average temperature, T_{avg}
- Temperature difference, $\Delta T_{max\text{-}min}$

These three temperatures were considered as the objective functions for the optimisation study. The maximum temperature indicates the most problematic region of the source, the average temperature represents the overall effectiveness of the cooling solution and the temperature difference is indicative of the temperature gradients and thus thermal stresses which would be present across the die-IHS interface.

Two inputs were set as variable parameters during optimisation: the minimum far field heat transfer coefficient, m, and the peak curve width indicator, a. The input for the former was confined to a range of $0 \leq m \leq 30{,}000\ W/m^2K$, whereas the latter was set between $0.001 \leq a \leq 0.01$. The other geometric parameters, physical properties and boundary conditions were considered to be constant for this example case study: $Q''_{hs} = 100\ W/cm^2$, $A_{hs} = 13 \times 13\ mm^2$, $A_{IHS} = 40 \times 40\ mm^2$, $b = 2.5\ mm$, and $k = 400\ W/mK$. The lateral dimensions of the IHS surface area used in this study are consistent with those commonly found in CPU packages for desktops and high-performance servers [48]. For this investigation, the IHS dimension is fixed to simplify the existing optimisation problem. While varying this parameter could provide additional insights, it would considerably increase computational complexity and runtime without offering proportional advantages to the study's objectives. The average heat transfer coefficient condition was set at a constant value of $h_{avg} = 35{,}000\ W/m^2K$. In terms of overall heat transfer coefficient, this magnitude is in line with those achievable by both microjet impingement and microchannel based heat exchangers [27].

2.3.2.2. Genetic algorithm

An in-house Genetic Algorithm (GA) program was written using the Matrix Laboratory R2022a optimisation toolbox in MATLAB[2]. GA utilises an optimisation strategy based on natural selection evolution via genetic reproduction, mutation and crossover. The algorithm uses the individuals from the previous generation to create the children that make up the current generation. This iterative process is run until a global optimum for the specified objective function(s) is found [49]. The rate of mutation for this case study was set as *adaptive*, implying that during the optimisation process, each iteration randomly combines genes of individuals from the previous iteration to form new children. This process then adapts with each successive generation based on the results of the last. For a multi-objective problem, this helps to ensure that the true global optimum is located as opposed to a localised optimum, which can miss sections of the test range [50]. Table 2.2 presents the GA parameters employed for the case study, with the initial simulation parameters configured following the recommendations provided in the MATLAB GA user guide [39] for this class of optimisation problem.

Table 2.2: Genetic algorithm operating parameters

Operating parameter	Value
Objective Functions	T_{max}, T_{avg}, $\Delta T_{max\text{-}min}$
Variable Inputs	*a, m*
Initial population size	50
Max. Generations	1000
Crossover fraction	0.8
Mutation	Adaptive

[2] For the full MATLAB GA optimisation code, see Appendix A2

A sensitivity analysis was conducted to evaluate the influence of initial conditions on the optimisation outcome. The results indicated that variations in the initial parameter values had no effect on the final optimised solution, influencing only the computational time required for convergence.

2.4. Results and Discussion

For a case study, the methodology and potential impact of the type of design intervention are presented for a specific design scenario. In a real-world context, a case study is performed in preference to investigating all the possible scenarios that could be encountered, as these would be too numerous. Thus, an ‘average CPU’ is considered, in the sense that the fixed parameters listed in Table 2.3 used in this case study were informed by existing commercial CPU packages (Figure 2.1(a)).

Table 2.3: Case study fixed parameter values

Parameter	Symbol	Value	Unit
Heat source length	L_{hs}	13	mm
IHS length	L_{IHS}	40	mm
IHS thickness	d	2.5	mm
Thermal conductivity	k	400	W/mK
Average heat transfer coefficient	h_{avg}	35,000	W/m^2K
Heat flux	Q''_{hs}	100	W/cm^2
Coolant temperature	T_c	35	°C

2.4.1. Baseline Global Cooling Case

In order to provide context for later comparisons, Figures 2.5(b) and (c) presents the local and distribution of the temperatures across the IHS associated with the baseline case, where a uniform heat transfer coefficient of h_{avg} = 35,000 W/m^2K was applied across the convective surface of the IHS (Figure 2.5(a)). For this case, Bi = 0.219 and β = 0.0625. In this case study, the dimensions of the IHS were held constant to focus exclusively on the effects of varying convective intensity on the heat transfer surface. Introducing changes to the heat spreader's dimensions would complicate the optimisation process and obscure the isolated assessment of the convective intensity distribution. Simultaneously varying the geometric properties of the heat spreader would require a more extensive analysis beyond the scope of this investigation.

Although the influence of heat spreader dimensions is not explored here, insights into the effects of varying Biot number can be drawn from the numerical comparison presented in Figure 2.3. Changes in the axial dimension of the heat spreader, which alter both the Biot number and β, would influence spreading efficiency by modifying the axial thermal resistance. For a thinner heat spreader, a reduction in spreading efficiency would likely result in thermal energy remaining concentrated near the geometric footprint of the heat source. Conversely, a thicker spreader, characterised by higher spreading efficiency, would enable a greater portion of the convective surface to actively participate in heat transfer.

The maximum temperature for this baseline case, T_{max} = 87.4°C, occurs at the geometric centre of the heat source on the bottom surface, as clearly illustrated in Figure 2.5(b). The temperature differential across the heat source/IHS contact area is $\Delta T_{max\text{-}min}$ = 11.7 K and the average temperature of the heat source was calculated to be T_{avg} = 83.3°C. The top and bottom temperature profiles are such that the temperature decreases monotonically from the geometric centre of the spreader. It can be seen from Figure 2.5(b) that an inflection point occurs at the approximate location of the heat source edge (x/L = 0.325) on the bottom surface of the IHS, as the curves change from being concave to convex beyond this point. This prompts high temperature gradients, and subsequent lateral heat conduction, in this location, which diminish to zero at the edge of the IHS.

For this baseline case, the spreading efficiency of the IHS was found to be η_{IHS} = 21%, implying that only a fifth of the available heat spreader surface area was effectively active for convective heat transfer. Considering the 2D temperature distributions displayed in Figure 2.5(c), it is evident that this low efficiency is due to the lack of lateral heat spreading across the IHS. Conversely, the thermal energy remains concentrated directly above the heat source, with most of the heat flowing transversely in the region of the heat source.

Since the convective heat flux at the top surface is proportional to the difference in wall and coolant temperature at the surface, $Q''_{conv} \propto T(x,y,b) - T_c$, the distribution in the top image of Figure 2.5(c) is indicative of the convective heat flux distribution, which is clearly localised.

Despite Figure 2.5(b) illustrating that the footprint of the heat transfer coefficient distribution closely aligns with that of the heat source, the presence of the heat spreader mitigates the severity of temperature gradients across the heat source. This is evident in the temperature distribution on the convective surface, which suggests that some degree of lateral heat spreading is still achieved even under a uniform convective intensity. Consequently, the inclusion of the spreader enables the tailoring of convective intensity to enhance heat spreading, ultimately minimising critical temperature objective functions. The forthcoming optimisation study will further demonstrate how this approach can enhance the thermal performance of the system.

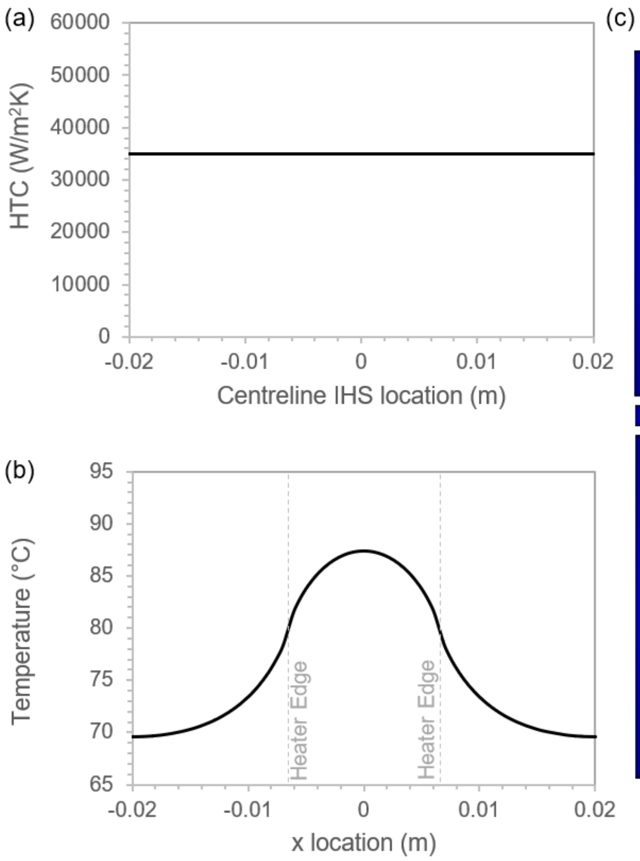

Figure 2.5: (a) Plot of convective heat transfer coefficient distribution on top surface, (b) plot of centreline temperature distribution on bottom surface, and (c) non-dimensional temperature distribution (Top) convective side, (Middle) centreline cross-section, (Bottom) heat source side.

2.4.2. Optimised Convective Cooling Cases

As shown in Figure 2.6(a), the optimal convective heat transfer distributions for T_{max} and each T_{avg}, T_{max} and $\Delta T_{max\text{-}min}$ (cases (ii) and (iii)) are broadly similar and fall in between the more extreme profiles of cases (iv) and (v) that optimised for the T_{avg} and $\Delta T_{max\text{-}min}$ objective functions respectively. Consequently, the temperature distributions for case (ii) and (iii) are very similar, as shown qualitatively in Figure 2.6(b) and more qualitatively in the centreline temperature plots in Figure 2.7. It should be noted that the temperature scale used in Figure 2.6(b) is normalised relative to the maximum temperature. As a result, the improvements in the performance metrics over the baseline case, (T_{avg}-$T_{avg,case\ (i)}$), (T_{max}-$T_{max,case\ (i)}$), ($\Delta T_{max\text{-}min}$-$\Delta T_{max\text{-}min,\ case\ (i)}$), shown in Figure 2.8, do not differ significantly whether T_{max} or each ΔT_{avg}, T_{max} and $\Delta T_{max\text{-}min}$ are chosen as the objective functions. Importantly, the concept proposed here, that a distributed heat transfer coefficient can provide superior cooling performance of heat spreaders of otherwise low spreading efficiency, is proven. Table 2.4 presents the overall results of the GA optimisation study, highlighting the objective functions considered for each case and the key results.

Table 2.4: Summary of findings for GA optimisation

Parameter	**(i)**	**(ii)**	**(iii)**	**(iv)**	**(v)**
Objective Functions	N/A	T_{max}, T_{avg}, $\Delta T_{max\text{-}min}$	T_{max}	T_{avg}	$\Delta T_{max\text{-}min}$
a	N/A	0.0047	0.0045	0.0073	0.0036
m	N/A	4798.05	5592.73	2895.45	2.99
Max. Temperature (K)	360.41	356.78	356.81	357.16	361.70
Avg. Temperature (K)	356.29	355.09	355.18	354.45	360.75
Temperature Difference	11.71	6.49	6.44	8.52	2.33

While no weightings were assigned within the code itself for the objective functions of the multi-objective case, i.e. (ii), a virtual weighting exists given the influence that maximum temperature exerts over the other two thermal objectives, i.e. when maximum temperature is reduced across a surface, inevitably average temperature and the severity of the temperature gradients reduce also. As such, the optimised convective intensity profile for T_{max}, case (iii), results in a similar distribution to that of the combined multi-objective optimisation of case (ii).

Furthermore, although the average source temperature is only reduced by T_{avg}-$T_{avg,case\ (i)}$ = -1.2 K for the multi-objective optimisation case (ii), the maximum temperature is decreased by T_{max}-$T_{max,case\ (i)}$ = -3.6 K, and the temperature gradient diminished by $\Delta T_{max\text{-}min}$ - $\Delta T_{max\text{-}min,\ case\ (i)}$ = -5.2 K, which are significant. It is clear from Figures 2.6(a) and (b) that a higher, and subsequently more focused, distribution of the heat transfer coefficient in the central region leads to a more uniform temperature across the IHS. Focussing the heat transfer coefficient acts to mitigate the lateral temperature gradients which would otherwise promote conduction from the centre of the IHS to the outer edges. This is apparent in Figure 2.7, particularly for the $\Delta T_{max\text{-}min}$ optimisation case (v), which has the most focused heat transfer coefficient profile with the highest peak magnitude and subsequent most uniform non-dimensional temperature, θ, distribution that is comparatively closest to unity throughout most of the domain. Closer inspection of Figure 2.7(a) reveals that the highly focussed heat transfer coefficient of this case has the effect of creating a local minimum in θ at the centre of the heat source, and a local maximum of slightly higher magnitude in the region of the heat source's edge (x/L = 0.325). This is the only case where the maximum temperature is not located at the geometric centre of the heat source. Similarly for the top surface of the IHS plotted in Figure 2.7(b), the temperature gradients for case (v) are positive, i.e., directed inwards, denoting lateral conduction inward towards the centre. Consequently, to create a uniform temperature distribution on the localised heat source, such as the one considered here, requires sufficiently intense and focussed convective cooling in the source region to cause the lateral flow of heat in the solid to be directed inward towards the central region.

An interesting observation can be made by comparing case (v) to the baseline case (i) which is the non-focussed, uniform heat transfer coefficient scenario. Case (i) has the steepest temperature gradients which are directed outwards from the centre. This indicates that there is high lateral conduction across the IHS, where the spreader is conducting heat across the full extent of the spreader, since convection is occurring to the edge of the spreader in this scenario. Conversely, for case (v), the optimum convective heat transfer coefficient distribution ostensibly insulates the spreader over a large portion of the area (Figure 2.6(a)), forcing the heat to be dissipated in the central region. Here, $dT/dx \sim 0$ in the outer regions of the IHS on both the top and bottom surfaces, as seen in Figure 2.7, such that minimal lateral conduction is occurring to the peripheral region, since there is no convective means to dissipate the heat. The consequence, however, is that the most uniform temperature gradient at the heat source ($\Delta T_{max\text{-}min}$ - $\Delta T_{max\text{-}min,\ case\ (i)}$ = -9.4 K) is attained at the sacrifice of having increased T_{avg} and T_{max} levels compared to the baseline, as shown in Figure 2.8. Here, T_{max}-$T_{max,case\ (i)}$ = 1.3 K, and T_{avg}-$T_{avg,case\ (i)}$ = 4.5 K, both being detrimental in terms of overall performance.

Of the four optimisation cases studied, minimising T_{avg} (case (iv)) results in the least concentrated convective heat transfer coefficient distribution. Like the baseline case (i), the top and bottom temperature profiles are such that the slope is continuously negative and decreases monotonically from the geometric centre of the spreader to a slope of zero at the edge, owing to the adiabatic boundary condition imposed there. Unlike the baseline, the top surface temperature for case (iv) is suppressed in the central region owing to the elevated heat transfer coefficient, whilst both the top and bottom temperatures are sustained to a higher magnitude of θ in the far field, owing to the diminishing, yet non-zero, heat transfer coefficient. Thus, minimising T_{avg} requires a balance between increasing the convective heat transfer in the heated zone of the source whilst maintaining a degree of lateral conduction and subsequent convective cooling to the edge of the spreader. Overall, performance improvement over the baseline is reasonably good, with a 1.8 K drop in average temperature, with the added benefit of the maximum temperature and temperature gradient both improving by about 3.2 K.

Based on the evidence provided in Figures 2.6 - 2.8, case (ii), the multi-objective optimisation case which minimises each of the objective functions ΔT_{avg}, T_{max} and $\Delta T_{max\text{-}min}$, can be said to be the best performing scenario. For this specific distribution function and under the prescribed conditions and constraints defined here, it strikes the best balance across all criteria for minimising temperatures across the heat source. The associated heat transfer coefficient distribution depicted in Figure 2.6(a) is between the extremes cases (iv) and (v) i.e. the least and most concentrated respectively. Apparent from the non-zero temperature gradients in Figure 2.7, lateral spreading is occurring to the edge of the spreader which remains heated, with $0.3 \lesssim \theta \lesssim 0.8$, in the far-field. This acts to sustain convective cooling over the entire spreader and subsequently lower the overall magnitude of the heat source temperature, consistent with case (iv) discussed above. Additionally, the distribution peak remains concentrated enough to maintain high convective heat flux directly above the heat source region, to the extent that the temperature gradient is slightly positive on the top surface above the source (Figure 2.7(b)), signifying a reversal in the heat flow direction in this region. This aids in mitigating excessive temperature gradients across the source, consistent with case (v) discussed earlier. Figure 2.6(b) illustrates these points, showing that the temperature distribution for case (ii) is reasonably concentrated in the region where the heat transfer coefficient is high, promoting high convective heat flux, yet sustains heating and associated convective heat flux, to the edge of the spreader. Figure 2.8 reinforces how the improvement of all three temperature objectives over the baseline for case (ii) falls between the results for the T_{max} and T_{avg} optimised cases, cases (iii) and (iv) respectively, indicating that the multi-objective optimisation scenario results in the best balance of criteria to provide the optimum cooling performance.

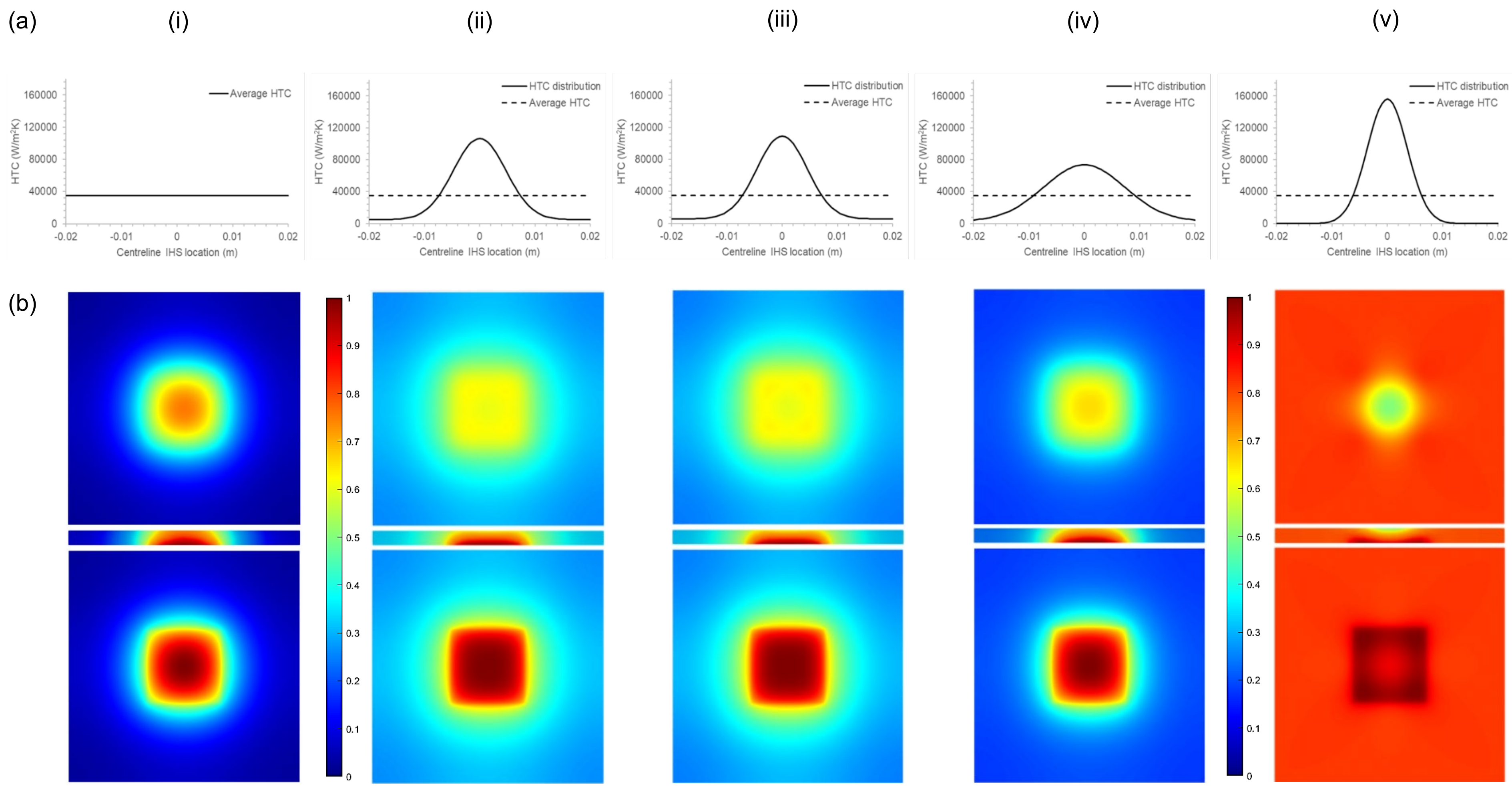

Figure 2.6: (a) Plot of convective heat transfer coefficient distribution on top surface, (b) non-dimensional temperature distribution (Top) convective side, (Middle) centreline cross-section, (Bottom) heat source side. From left to right; (i) baseline global cooling case, (ii) multi-objective optimised for T_{avg}, T_{max}, $\Delta T_{max\text{-}min}$, and single objective optimised for (iii) T_{max}, (iv) T_{avg}, and (v) $\Delta T_{max\text{-}min}$.

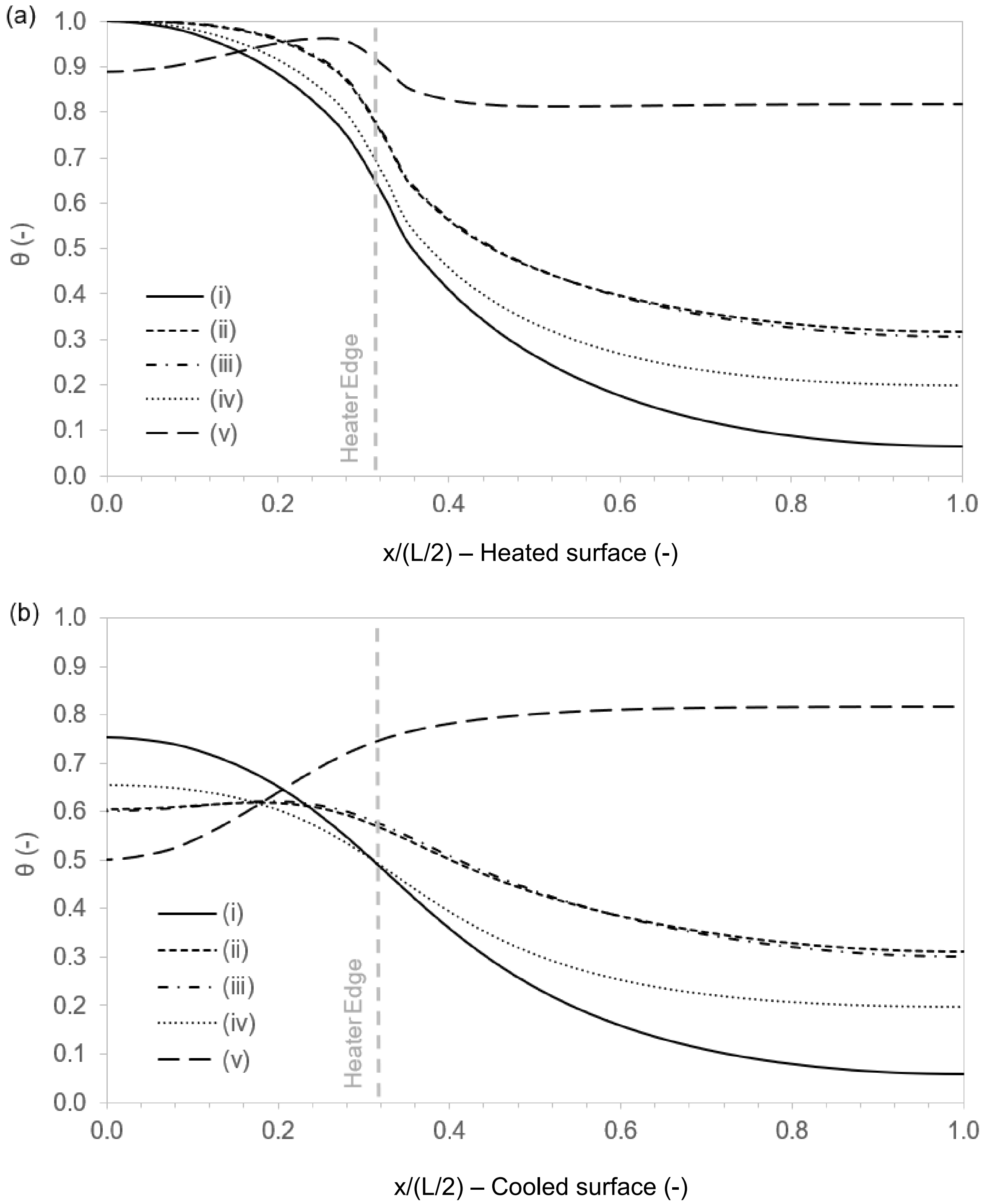

Figure 2.7: Comparison of non-dimensional temperature profiles between the optimisation cases across; (a) the heated surface and (b) the cooled surface for half the length of the IHS.

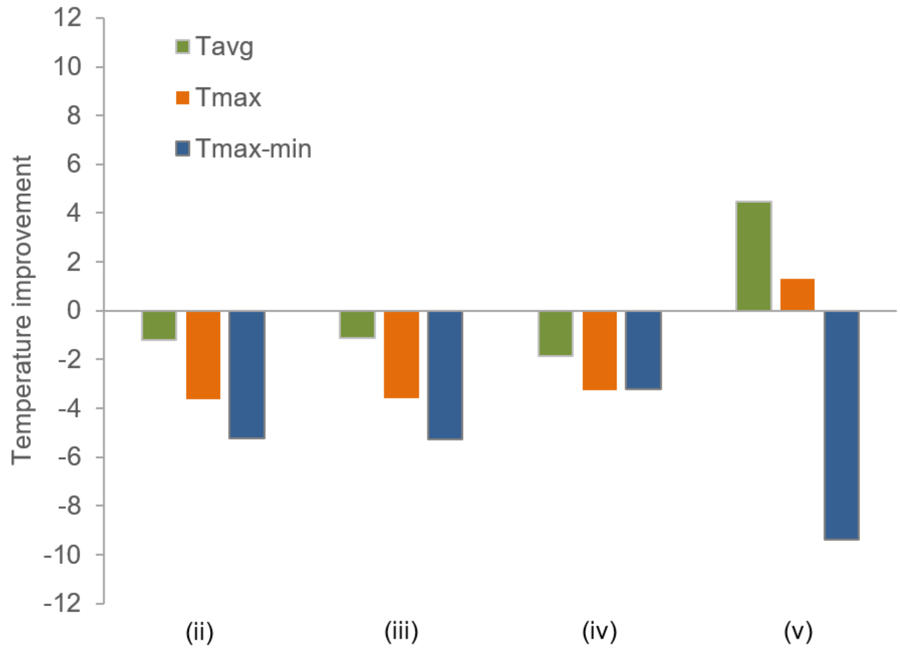

Figure 2.8: Improvement or detriment in temperature performance metrics for each optimisation case compared to the baseline.

2.5. Conclusions

This case study has showed that the optimised non-uniform heat transfer coefficient function can realise significant reductions in both the operating temperature and the temperature gradients across the heat source compared with a uniform distribution. Other key findings from this investigation were as follows:

1. The steepest heat transfer coefficient profile occurred when minimising $\Delta T_{max\text{-}min}$ and produced the lowest temperature gradient across the heat source for the given heat flux, but at the cost of having overall higher average and maximum temperatures. The steeper and narrower profile discouraged outward lateral flow of heat, forcing transverse heat flow directly above the heat source. In fact, the lateral flow of heat was directed inward towards the centreline of the IHS in this case.
2. An optimum distribution of the heat transfer coefficient occurred for the multi-objective optimisation case where the objective functions T_{max}, T_{avg} and $\Delta T_{max\text{-}min}$ were minimised simultaneously. This provided a single result that balanced the gains achieved by each objective function individually.

3. Of the three single objective optimisation cases considered, minimising the maximum temperature of the heat source, T_{max}, was the best performing. Here, the resulting heat transfer coefficient distribution and performance enhancement were quite similar to the multi-objective optimum case. This potentially simplifies the mathematical optimisation process.

Given the findings of this case study, subsequent chapters will focus on investigating the practical means to produce the non-uniform distributions of the heat transfer coefficient discussed in this case study via impinging liquid microjet array cooling, as it is capable of achieving the magnitudes of local heat transfer coefficient as calculated by this study [51]. The arrangement of microjets can be configured as such to approximate the ideal Gaussian style distribution of the convective intensity on the heat transfer surface of the IHS. Concentrating jets around the centre of the IHS would generate a high convective intensity, though the profile may be less smooth than the ideal case specified in this study due to the high rate of cooling intensity drop off between successive jets in an array, resulting in significant peaks and troughs. The inclusion of surface features such as pin fins or wells may allow for the profile to be smoothed out and bring the distribution of convective intensity closer to the ideal profiles illustrated in Figure 2.6. The following chapter will introduce thermal hydraulics into the existing conjugate heat transfer analysis to develop a viable CFD optimisation tool, with subsequent work applying this to a practical design case utilising real-world CPU architectures to test the applicability of the developed workflow.

References

[1] J. W. Elliott, M. T. Lebon, and A. J. Robinson, "Optimising integrated heat spreaders with distributed heat transfer coefficients: A case study for CPU cooling," *Case Studies in Thermal Engineering,* vol. 38, p. 102354, 2022, doi: 10.1016/j.csite.2022.102354.

[2] A. L. Moore and L. Shi, "Emerging challenges and materials for thermal management of electronics," *Materials Today,* vol. 17, no. 4, pp. 163-174, 2014, doi: 10.1016/j.mattod.2014.04.003.

[3] Intel. "Intel Xeon Processor Scalable Family Thermal Mechanical Specifications and Design Guide." https://www.intel.com/content/dam/www/public/us/en/documents/guides/xeon-scalable-thermal-guide.pdf (accessed 06/04/2022).

[4] M. Yan and M. Onabajo, "An offset calibration scheme for on-chip thermal profiling with differential temperature sensors," *Analog Integrated Circuits and Signal Processing,* vol. 120, no. 1, pp. 83-91, 2024, doi: 10.1007/s10470-024-02285-w.

[5] L. S. Maganti, P. Dhar, T. Sundararajan, and S. K. Das, "Mitigating non-uniform heat generation induced hot spot(s) in multicore processors using nanofluids in parallel microchannels," *International Journal of Thermal Sciences,* vol. 125, pp. 185-196, 2018, doi: 10.1016/j.ijthermalsci.2017.11.015.

[6] Y. Zhang, H. Wang, Z. Wang, Y. Yang, and F. Blaabjerg, "Simplified Thermal Modeling for IGBT Modules With Periodic Power Loss Profiles in Modular Multilevel Converters," *IEEE Transactions on Industrial Electronics,* vol. 66, no. 3, pp. 2323-2332, 2019, doi: 10.1109/TIE.2018.2823664.

[7] A. R. Dhumal, A. P. Kulkarni, and N. H. Ambhore, "A comprehensive review on thermal management of electronic devices," *Journal of Engineering and Applied Science,* vol. 70, no. 1, p. 140, 2023, doi: 10.1186/s44147-023-00309-2.

[8] Z. Zhang, X. Wang, and Y. Yan, "A review of the state-of-the-art in electronic cooling," *e-Prime - Advances in Electrical Engineering, Electronics and Energy,* vol. 1, p. 100009, 2021, doi: 10.1016/j.prime.2021.100009.

[9] A. Shanmuga Sundaram and V. Ramalingam, "Thermal management of electronics: A review of literature," *Thermal Science,* vol. 12, no. 2, pp. 5-26, 2008, doi: 10.2298/TSCI0802005A.

[10] T. Q. Feng and J. L. Xu, "An analytical solution of thermal resistance of cubic heat spreaders for electronic cooling," *Applied Thermal Engineering,* vol. 24, no. 2, pp. 323-337, 2004, doi: 10.1016/j.applthermaleng.2003.07.001.

[11] A. J. Robinson, J. Colenbrander, R. Kempers, and R. Chen, "Solid and Vapor Chamber Integrated Heat Spreaders: Which to Choose and Why," *IEEE Transactions on Components, Packaging and Manufacturing Technology,* vol. 8, no. 9, pp. 1581-1592, 2018, doi: 10.1109/TCPMT.2018.2822400.

[12] G. Maranzana, I. Perry, D. Maillet, and S. Raël, "Design optimization of a spreader heat sink for power electronics," *International Journal of Thermal Sciences,* vol. 43, no. 1, pp. 21-29, 2004, doi: 10.1016/S1290-0729(03)00107-8.

[13] M. Kim, K. H. Lee, D. I. Han, and J. H. Moon, "Numerical case study and modeling for spreading thermal resistance and effective thermal conductivity for flat heat pipe," *Case Studies in Thermal Engineering,* vol. 31, p. 101803, 2022, doi: 10.1016/j.csite.2022.101803.

[14] M. Awad, A. Radwan, O. Abdelrehim, M. Emam, A. N. Shmroukh, and M. Ahmed, "Performance evaluation of concentrator photovoltaic systems integrated with a new jet impingement-microchannel heat sink and heat spreader," *Solar Energy,* vol. 199, pp. 852-863, 2020, doi: 10.1016/j.solener.2020.02.078.

[15] A. Ali, "Thermal performance and stress analysis of heat spreaders for immersion cooling applications," *Applied Thermal Engineering,* vol. 181, p. 115984, 2020, doi: 10.1016/j.applthermaleng.2020.115984.

[16] T. S. Fisher, F. A. Zell, K. K. Sikka, and K. E. Torrance, "Efficient Heat Transfer Approximation for the Chip-on-Substrate Problem," *Journal of Electronic Packaging,* vol. 118, no. 4, pp. 271-279, 1996, doi: 10.1115/1.2792163.

[17] M. Yovanovich, Y. S. Muzychka, and J. Culham, "Spreading Resistance of Isoflux Rectangles and Strips on Compound Flux Channels," *Journal of Thermophysics and Heat Transfer,* vol. 13, pp. 495-500, 1999, doi: 10.2514/2.6467.

[18] G. N. Ellison, "Maximum thermal spreading resistance for rectangular sources and plates with nonunity aspect ratios," *IEEE Transactions on Components and Packaging Technologies,* vol. 26, no. 2, pp. 439-454, 2003, doi: 10.1109/TCAPT.2003.815088.

[19] K. Alam, X. Shen, and R. Taposh, "Design considerations for heat spreader in high heat flux systems," in *2012 28th Annual IEEE Semiconductor Thermal Measurement and Management Symposium (SEMI-THERM)*, 18-22 March 2012, pp. 283-287, doi: 10.1109/STHERM.2012.6188861.

[20] S. M. Thompson and H. B. Ma, "Thermal Spreading Analysis of Rectangular Heat Spreader," *Journal of Heat Transfer,* vol. 136, no. 6, 2014, doi: 10.1115/1.4026558.

[21] J. Lee, S. M. Thompson, and T. E. Lacy, "Thermal spreading analysis of a transversely isotropic heat spreader," *International Journal of Thermal Sciences,* vol. 118, pp. 461-474, 2017, doi: 10.1016/j.ijthermalsci.2017.05.009.

[22] H. A. Guo, K. F. Wiedenheft, and C. H. Chen, "Hotspot Size Effect on Conductive Heat Spreading," *IEEE Transactions on Components, Packaging and Manufacturing Technology,* vol. 7, no. 9, pp. 1459-1464, 2017, doi: 10.1109/TCPMT.2017.2704419.

[23] M. Razavi, Y. Muzychka, and S. Kocabiyik, "Review of Advances in Thermal Spreading Resistance Problems," *Journal of Thermophysics and Heat Transfer,* vol. 30, pp. 1-17, 2016, doi: 10.2514/1.T4801.

[24] S. Lee, S. Song, V. Au, and K. P. Moran, "Constriction/Spreading Resistance Model for Electronics Packaging," in *ASME/JSME Thermal Engineering*, 1995, vol. 4, pp. 199-206.

[25] S. Zimmermann, M. K. Tiwari, I. Meijer, S. Paredes, B. Michel, and D. Poulikakos, "Hot water cooled electronics: Exergy analysis and waste heat reuse feasibility," *International Journal of Heat and Mass Transfer,* vol. 55, no. 23, pp. 6391-6399, 2012, doi: 10.1016/j.ijheatmasstransfer.2012.06.027.

[26] S. Zimmermann, I. Meijer, M. K. Tiwari, S. Paredes, B. Michel, and D. Poulikakos, "Aquasar: A hot water cooled data center with direct energy reuse," *Energy,* vol. 43, no. 1, pp. 237-245, 2012, doi: 10.1016/j.energy.2012.04.037.

[27] B. Watson and V. K. Venkiteswaran, "Universal Cooling of Data Centres: A CFD Analysis," *Energy Procedia,* vol. 142, pp. 2711-2720, 2017, doi: 10.1016/j.egypro.2017.12.215.

[28] T. Dixit and I. Ghosh, "Review of micro- and mini-channel heat sinks and heat exchangers for single phase fluids," *Renewable and Sustainable Energy Reviews,* vol. 41, pp. 1298-1311, 2015, doi: 10.1016/j.rser.2014.09.024.

[29] A. Mohammadi and A. Kosar, "Review on Heat and Fluid Flow in Micro Pin Fin Heat Sinks under Single-phase and Two-phase Flow Conditions," *Nanoscale and Microscale Thermophysical Engineering,* vol. 22, pp. 1-45, 2018, doi: 10.1080/15567265.2018.1475525.

[30] B. W. Webb and C. F. Ma, "Single-Phase Liquid Jet Impingement Heat Transfer," *Advances in Heat Transfer,* vol. 26, pp. 105-217, 1995, doi: 10.1016/S0065-2717(08)70296-X.

[31] A. J. Robinson and E. Schnitzler, "An experimental investigation of free and submerged miniature liquid jet array impingement heat transfer," *Experimental Thermal and Fluid Science,* vol. 32, no. 1, pp. 1-13, 2007, doi: 10.1016/j.expthermflusci.2006.12.006.

[32] R. Kempers, J. Colenbrander, W. Tan, R. Chen, and A. J. Robinson, "Experimental characterization of a hybrid impinging microjet-microchannel heat sink fabricated using high-volume metal additive manufacturing," *International Journal of Thermofluids,* vol. 5-6, p. 100029, 2020, doi: 10.1016/j.ijft.2020.100029.

[33] D. Nikolic, M. Hutchison, P. T. Sapin, and A. J. Robinson, "Hot spot targeting with a liquid impinging jet array waterblock," in *2009 15th International Workshop on Thermal Investigations of ICs and Systems*, 7-9 Oct 2009, pp. 168-173.

[34] Y. J. Lee, P. S. Lee, and S. K. Chou, "Hotspot Mitigating With Obliquely Finned Microchannel Heat Sink—An Experimental Study," *IEEE Transactions on Components, Packaging and Manufacturing Technology,* vol. 3, no. 8, pp. 1332-1341, 2013, doi: 10.1109/TCPMT.2013.2244164.

[35] C. S. Sharma, G. Schlottig, T. Brunschwiler, M. K. Tiwari, B. Michel, and D. Poulikakos, "A novel method of energy efficient hotspot-targeted embedded liquid cooling for electronics: An experimental study," *International Journal of Heat and Mass Transfer,* vol. 88, pp. 684-694, 2015, doi: 10.1016/j.ijheatmasstransfer.2015.04.047.

[36] G. Laguna *et al.*, "Numerical parametric study of a hotspot-targeted microfluidic cooling array for microelectronics," *Applied Thermal Engineering,* vol. 144, pp. 71-80, 2018, doi: 10.1016/j.applthermaleng.2018.08.030.

[37] R. Wu, Y. Fan, T. Hong, H. Zou, R. Hu, and X. Luo, "An immersed jet array impingement cooling device with distributed returns for direct body liquid cooling of high power electronics," *Applied Thermal Engineering,* vol. 162, p. 114259, 2019, doi: 10.1016/j.applthermaleng.2019.114259.

[38] S. Wiriyasart and P. Naphon, "Heat spreading of liquid jet impingement cooling of cold plate heat sink with different fin shapes," *Case Studies in Thermal Engineering,* vol. 20, p. 100638, 2020, doi: 10.1016/j.csite.2020.100638.

[39] D. Kong *et al.*, "A holistic approach to thermal-hydraulic design of 3D manifold microchannel heat sinks for energy-efficient cooling," *Case Studies in Thermal Engineering,* vol. 28, p. 101583, 2021, doi: 10.1016/j.csite.2021.101583.

[40] C. J. M. Lasance, "How to Estimate Heat Spreading Effects in Practice," *Journal of Electronic Packaging,* vol. 132, no. 3, 2010, doi: 10.1115/1.4001856.

[41] A. Suszko and M. S. El-Genk, "Thermally anisotropic composite heat spreaders for enhanced thermal management of high-performance microprocessors," *International Journal of Thermal Sciences,* vol. 100, pp. 213-228, 2016, doi: 10.1016/j.ijthermalsci.2015.09.018.

[42] S. Wongwises, S. Disawas, J. Kaewon, and C. Onurai, "Two-phase evaporative heat transfer coefficients of refrigerant HFC-134a under forced flow conditions in a small horizontal tube," *International Communications in Heat and Mass Transfer,* vol. 27, no. 1, pp. 35-48, 2000, doi: 10.1016/S0735-1933(00)00082-8.

[43] A. N. Khalifa, "Natural convective heat transfer coefficient – a review: I. Isolated vertical and horizontal surfaces," *Energy Conversion and Management,* vol. 42, no. 4, pp. 491-504, 2001, doi: 10.1016/S0196-8904(00)00042-X.

[44] Y. S. Muzychka, J. Culham, and M. Yovanovich, "Thermal Spreading Resistance of Eccentric Heat Sources on Rectangular Flux Channels," *Journal of Electronic Packaging,* vol. 125, no. 2, pp. 178-185, 2003, doi: 10.1115/1.1568125.

[45] P. J. Roache, "Quantification of Uncertainty in Computational Fluid Dynamics," *Annual Review of Fluid Mechanics,* vol. 29, no. 1, pp. 123-160, 1997, doi: 10.1146/annurev.fluid.29.1.123.

[46] D. Lee, S. J. Lee, and J. H. Lee, "Heat transfer from a flat plate to a fully developed axisymmetric impinging jet," (in English), *Journal of Heat Transfer,* vol. 117, pp. Medium: X; Size: pp. 772-776, 1995, doi: 10.1115/1.2822647.

[47] S. Chevillard, "The functions erf and erfc computed with arbitrary precision and explicit error bounds," *Information and Computation,* vol. 216, pp. 72-95, 2012, doi: 10.1016/j.ic.2011.09.001.

[48] C. Kuo, K. Liu, T. Li, D. Wu, and B. Lin, "Numerical simulation and optimization of fine-blanking process for copper alloy sheet," *The International Journal of Advanced Manufacturing Technology,* vol. 119, 2022, doi: 10.1007/s00170-021-08225-6.

[49] J. H. Holland, *Adaptation in Natural and Artificial Systems: An Introductory Analysis with Applications to Biology, Control, and Artificial Intelligence*. University of Michigan Press, Ann Arbor, Michigan, United States, 1975.

[50] "The MathWorks Inc. Global Optimization Toolbox User's Guide 2022a." https://uk.mathworks.com/help/gads/ (accessed 01/04/2022).

[51] A. J. Robinson, "A Thermal–Hydraulic Comparison of Liquid Microchannel and Impinging Liquid Jet Array Heat Sinks for High-Power Electronics Cooling," *IEEE Transactions on Components and Packaging Technologies,* vol. 32, no. 2, pp. 347-357, 2009, doi: 10.1109/TCAPT.2008.2010408.

Chapter 3

Optimised Liquid Impinging Jet Arrays for Cooling CPU Packages

Abstract

This study investigates the optimisation of the thermal-hydraulic performance of liquid impinging jet arrays for cooling of concentrated heat sources with an integrated heat spreader, mimicking a typical high-powered CPU package. Three heat source sizes were investigated, namely 10 x 10 mm^2, 15 x 15 mm^2, and 20 x 20 mm^2, all with a 1.3 mm thick copper heat spreader. An automated optimisation workflow was developed in a CFD-based environment to determine the ideal geometric design parameters of the impinging jet array heat exchangers, with the objective functions chosen to minimise hydraulic power consumption and/or minimise the overall thermal resistance, representing both single and multi-objective optimisation strategies. The analysis showed that for maximising the heat transfer performance only, the design tended to favour fewer closely spaced and higher velocity jets that targeted a concentrated region within the footprint on the heat spreader that was commensurate with the heat source. This focussed the high convective intensity of the impinging jets on the central region of the heat spreader where the highest heat flux levels exist. However, the high jet velocities incurred a comparatively high hydraulic pumping power penalty. Conversely, when minimising both thermal resistance and hydraulic power consumption simultaneously, the design favoured a much higher population of lower velocity jets in order to mitigate the pressure drop and reduce the hydraulic power. Here, despite the lower convective cooling intensity of the lower velocity jets, the designs leveraged a much larger surface area of the heat spreader, which tended to maintain high heat transfer performance with disproportionately lower hydraulic penalties. This chapter corresponds to the publication [1].

3.1. Introduction

The decrease in size and increasing power density of transistors and other integrated circuit (IC) components and devices [2] has led to the need for improved cooling techniques to achieve more effective heat dissipation and improved cooling system efficiency [3-5]. Thermal management has indeed become one of the major challenges facing microelectronics packaging [6], since it ultimately impacts their overall performance and reliability [7, 8]. Historically the main heat sink technology used for cooling higher-powered electronic components is the forced air heat sink. However, as power and heat flux levels continue to escalate, air cooling has and will continue to reach its limit. For example, Saini and Webb [9] theoretically showed that for fan-fin type cooling of typical Central Processing Units (CPUs), the heat flux limit is as low as 40 W/cm^2, and this was recently confirmed experimentally by Naduvilakath-Mohammed et al. [10]. As detailed in the author's previous work [11], commercial CPUs have already breached this limit, and there is no indication that this trend will reverse. Furthermore, as air cooling is pushed towards its limit, other undesirable characteristics such as excessive heat sink size, high levels of acoustic noise, and increased fan power consumption become problematic [12-14]. Considering these, there is increased motivation to move towards liquid cooled heat sinks, which are more compact, operate quietly, are capable of significantly higher cooling intensities, and overall consume significantly less energy [15, 16].

To date, microchannels remain the most investigated and commercially deployed liquid cooling technology [17-20]. Microchannels direct fluid flow through parallel arrays of channels, typically of widths between 0.25 mm - 0.5 mm. They can produce very low thermal resistances owing to the high convective heat transfer coefficients associated with liquids in low hydraulic diameter channels, together with the high surface area density created by the channel walls. Some main disadvantages of microchannels are the limited choice of low-cost micro-fabrication techniques, fouling and clogging, and high pressure drops, with the latter also influencing the hydraulic power penalty.

In practical high-power applications, such as CPUs, the semiconductor die area is sufficiently small that Integrated Heat Spreaders (IHS) are required to increase the convective surface area to achieve the required cooling performance. This creates a conjugate heat transfer situation, where the convective and conductive heat transfer mechanisms are coupled. Elliott et al. [11] recently showed that in typical CPU packages, the concentration of the heat source on the underside of an IHS results in a comparable concentration on the convection-side of the IHS, and this becomes progressively more so as the convective cooling intensifies. Thus, despite the addition of a heat spreader, its overall spreading efficiency is low, in the same way that classical fin efficiency deteriorates with increased convective heat transfer coefficients. However, this work also showed that conjugate heat transfer can indeed be leveraged to reduce the overall source-to-sink thermal resistance with a non-uniform convective cooling intensity, ostensibly targeting regions where the heat is concentrated [11]. Since microchannel heat sinks are a global surface cooling technique, they are not well suited for this targeting of regions of high heat concentration. Conversely, jet array impingement is ideal for hot spot targeting, since concentrated cooling can be achieved simply by arranging the jets over areas of higher heat flux [6]. In this way, the available coolant flow is utilised in the region where maximum cooling is required.

Jet impingement cooling, whether single jets or arranged in arrays, can achieve exceptionally high single-phase convective heat transfer coefficients [21, 22]. Compared with microchannel-type designs, jet arrays rely on the fluid mechanics of the coolant delivery to the surface, opposed to the use of surface features, to enhance the heat transfer. Furthermore, jet arrays offer a broad design space, since the thermal-hydraulics are sensitive to several geometric design parameters including jet population, jet diameter, inter-jet spacing, and jet-to-target spacing [23-26]. A large body of work exists in the literature addressing the sensitivity to these design variables in scenarios with uniform heating of the target surface. However, to the best of knowledge, target cooling in a CPU-type conjugate heat transfer scenario, whereby a concentrated heat source with attached heat spreader is considered, is relatively unexplored despite being alluded to [27]. Like all heat exchanger designs, it requires careful balancing between the heat transfer and the hydraulic penalties, such as pressure drop and pumping power [27, 28].

Designing thermal management systems for electronics packages requires that the cooling system achieves or exceeds the required cooling target in order maintain safe junction temperatures [29], whilst not requiring unnecessarily high energy consumption to do so [21, 30]. This creates two interesting optimisation problems: one where maximum cooling is achieved at an acceptable power consumption, and one where maximum cooling and minimum power consumption are achieved simultaneously. For the problem considered here, which involves targeted cooling of a high-powered CPU-type package with a concentrated heat source with an IHS, the optimisation problem has the additional complexities brought about by the interplay between the fluid mechanics, non-uniform convective heat transfer, and conduction heat transfer in the IHS; all being sensitive to the geometric design parameters of the jet array impingement heat sink. Furthermore, it is unlikely that the design which maximises cooling will be the same as that which simultaneously minimises the required hydraulic power consumption, and this adds another level of complexity to the design problem. This is further exacerbated by the fact that there is a diverse range of CPU package design architectures, including but not limited to different die sizes, locations, shapes, and power levels. All these add up to a commensurately broad range of optimum jet impingement array heat exchanger designs, in the sense that there is no 'one-size-fits-all' optimal solution to address the range of commercial CPUs, and the same can be said about other high-powered electronics packages such as IGBTs. Considering the above discussion, it is clear that advanced simulation-based approaches are best suited for this type of heat exchanger design problem, in particular if an automated optimisation workflow can be developed that enables customisable input geometries for different electronics packages.

The objective of the present investigation is to deploy a simulation-driven design workflow for the optimisation of liquid jet array impingement heat exchangers for the cooling of concentrated heat sources requiring Integrated Heat Spreaders (IHS). To demonstrate the optimisation design process, a range of heat source sizes typical of commercial CPUs is investigated, all with a copper IHS. The objective functions of interest for this optimisation problem are the maximisation of cooling intensity and minimisation of hydraulic pumping power. The sole thermal objective function considered in this study is the minimisation of the maximum temperature. This decision is informed by the findings of Elliott et al. [11], which demonstrate that minimising the maximum temperature across a surface inherently leads to concurrent reductions in both the average temperature and temperature gradients. This relationship simplifies the optimisation process by reducing the total number of objective functions required in a single study, thereby decreasing complexity and the associated computational effort. To illustrate the design method, both single (cooling intensity) and multiple objective (cooling intensity and hydraulic power) optimisation processes are compared and contrasted, both in terms of the overall thermal-hydraulic performance and underlying fluid mechanics and heat transfer, since they result in distinct heat exchanger designs.

3.2. Experimental Study

3.2.1. The Baseline Cold Plate

This study aims to optimise jet array impingement heat transfer for concentrated heat sources using a Computational Fluid Dynamics (CFD) approach. In order to verify the accuracy of the CFD model, experiments were performed to emulate a CPU package with a semiconductor die as the single concentrated heat source, an Integrated Heat Spreader as the lid, and a liquid cooled impingement jet array coldplate. As noted by the author's previous work [11], a centralised heat source is most effectively cooled by having a higher concentration of the heat transfer coefficient directed towards the projected region of the heat source. Considering this, the standard baseline orifice design selected for experimental verification was one which approximately covered the heat source projected area.

The basis for the heat exchanger used in this study utilised a modified Nexalus Enflux^{TM} manifold, which contains an integrated orifice plate that can be interchanged to allow for testing of different jet array designs. The coldplate design of the TTV was similarly taken from the Enflux^{TM} design, as this is a commercially available heat exchanger with applications on data centre servers and similar, therefore provided an excellent bassline for this optimisation case given the projected application of this workflow being in CPU thermal management in such applications as data centre servers. Table 3.1 presents all key geometries present on the cold plate heat exchanger used for the experimental study, which subsequently influence the geometry of the CFD model. Figure 3.1 presents the baseline jet orifice plate used for testing, sectioned and housed within the full coldplate heat exchanger assembly.

The cold plate element of the heat exchanger consisted of a 50 x 50 x 1.3 mm^3 base as per the commercial design, which here doubled as a heat spreader, with an attached heated meter bar neck to extrapolate junction temperature via three thermocouples spaced at equidistant intervals across the vertical height of the neck. The orifice plate was positioned between the manifold and the Thermal Test Vehicle (TTV) and was fabricated using a 3D printing process. Consequently, the sharp-edged nozzle inlets incorporated into the subsequent CFD simulations were subject to manufacturing constraints, resulting in an edge radius of approximately 20 μm. This limitation was dictated by the resolution of the Elegoo Saturn 3 resin printer employed for producing the orifice plates.

The baseline orifice design consisted of an array of 49 circular jets, of nozzle length 1.8 mm, arranged in a 7 x 7 inline square array, with a constant diameter of 1.0 mm which were equally spaced with an inter-jet pitch, S, of 2.25 mm, with a jet-to-target distance, H, of 1.7 mm. The inlet/outlet channels of the manifold had an internal diameter of 10 mm, in line with the internal diameter of the piping used to connect the flow loop.

Table 3.1: Baseline cold plate heat exchanger key dimensions

Geometric Parameter	Abbreviation	Value	Units
Jet nozzle diameter	D	1.0	mm
Nozzle length	L_{nozzle}	1.8	mm
Manifold inlet diameter	D_{inlet}	10	mm
Jet pitch	S	2.25	mm
Jet-to-target height	H	1.7	mm
IHS surface area	A_{IHS}	50 x 50	mm^2
IHS thickness	d	1.3	mm
Number of jets	N	49	-

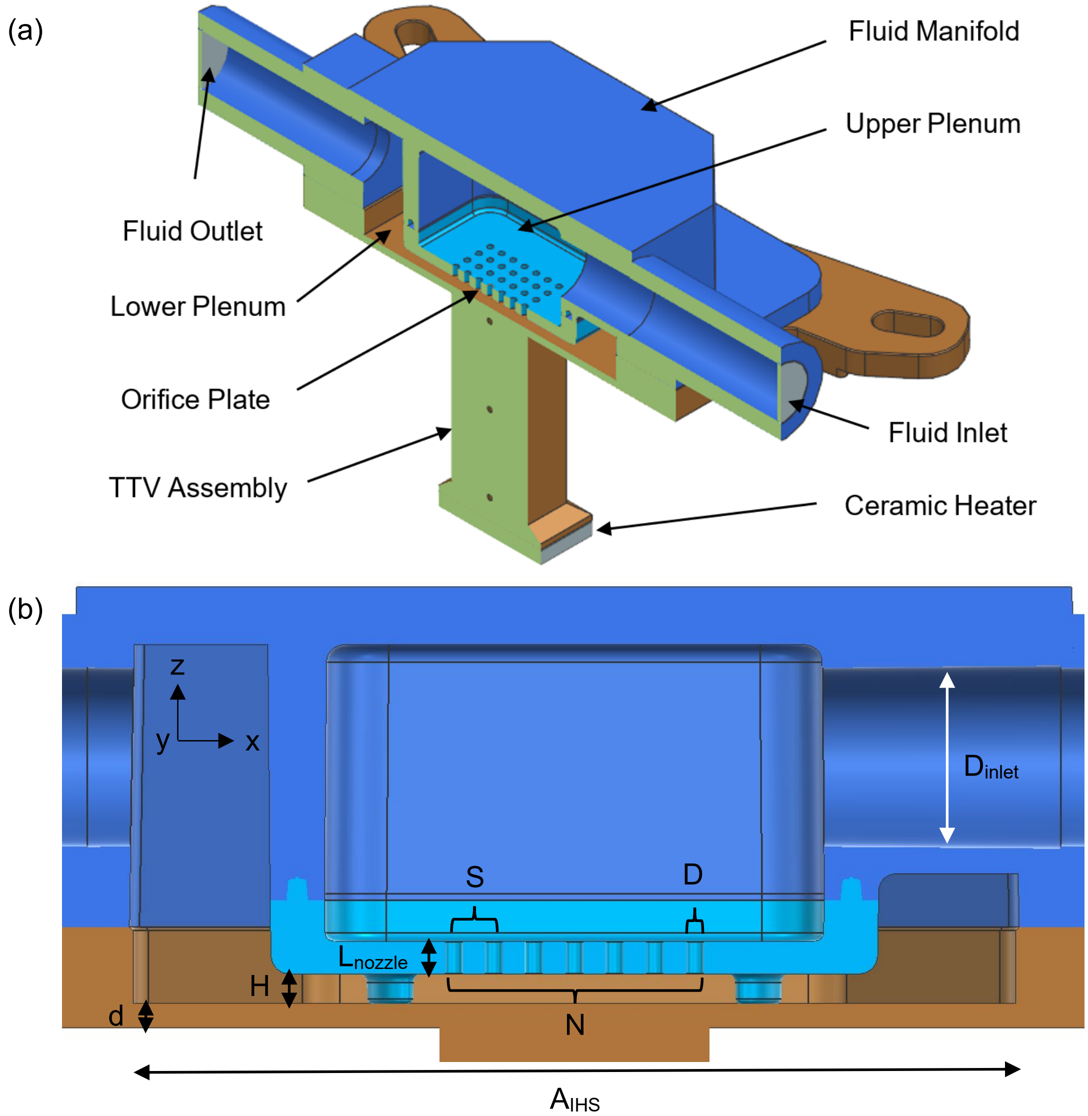

Figure 3.1: (a) Sectioned view of TTV and attached liquid coldplate heat exchanger assembly, (b) cross-sectional view of fluid manifold, highlighting key geometric parameters.

3.2.2. Experimental Apparatus

As depicted in Figure 3.2, the main features of the test facility are a pumped liquid flow loop, a liquid coldplate heat exchanger, and the Thermal Test Vehicle (TTV). The TTV, shown in Figure 3.1, was designed to approximate the design and thermal loading of a typical CPU. It consisted of an ultra-pure OFE copper (k ≈ 395 W/mK) heated meter bar with a lower neck region with square cross-sectional areas emulating a semiconductor die, expanding to a 1.3 mm thick and 50 x 50 mm^2 wetted area top overhanging section, typical of a CPU IHS. The TTV was made from a single piece of OFE copper to remove the TIM between the cold plate and heated meter bar neck, thus simplifying the thermal stack, as TIMs can significantly contribute to the uncertainty of the thermal resistance. Therefore, having the TTV as a single piece increases the confidence in the experimental verification of the CFD simulation by removing additional sources of uncertainty.

In Figure 3.1, the 15 x 15 mm^2 meter bar is depicted, though both of the 10 x 10 mm^2 and 20 x 20 mm^2 TTVs were also fabricated and tested. Fixed to the base of each meter bar was a 20 x 20 mm^2 ceramic heater. For the current experiments, the TTV assembly could provide the target maximum power of Q_{hs} = 250 W to the attached liquid coldplate heat exchanger. To measure the heat flux and temperature at the intersection of the meter bar and IHS (representing the top of a CPU die), three 1.0 mm diameter sheathed T-type thermocouples (±0.5°C) were spaced at equal intervals along the length of the meter bar section of the TTV, inserted into holes that extended midway through the neck. To minimise heat loss to the surrounding ambient air, insulation was applied around the TTV neck region, positioned between the base of the TTV bracket, which secures the heat source in place, and the cold plate base. Since the junction temperature was the sole thermal parameter recorded in this investigation, heat losses to the outer regions of the heat spreader and the bracket beneath the heat source were deemed negligible. This assumption was validated by the subsequent CFD optimisation results, which showed no measurable influence from these losses on the recorded performance metrics.

As depicted in Figure 3.1, the liquid coldplate heat exchanger consisted of an upper plastic manifold with an inlet port that supplied the coolant to an upper plenum. The pressurised coolant was forced through a lower nozzle plate which contained the array of jet orifices. The jets impinged directly on the top surface of the IHS and subsequently flowed laterally in a lower channel region into a skirt-type outer plenum, and then exited through the outlet port.

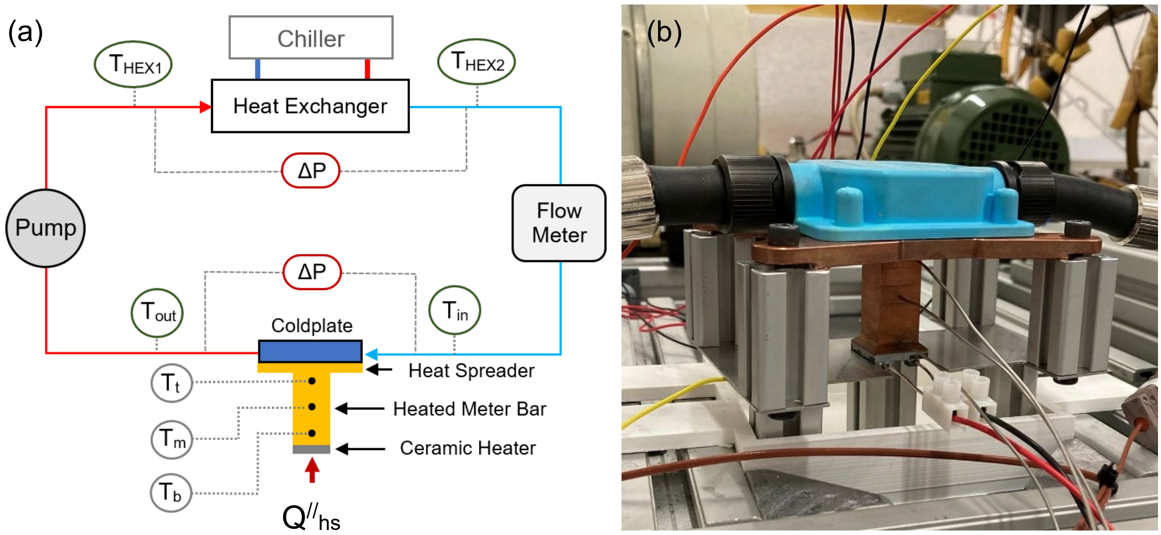

Figure 3.2: (a) Schematic of experimental test facility and (b) close up of practical TTV assembly.

Distilled water was used as the working fluid and was circulated through the flow loop with a TCS M3000 micropump connected to a 2 Litre reservoir. The flow rate was controlled by varying the voltage to the pump in tandem with a control valve for finer control when appropriate, with the flow rate being measured by a Sensata Cynergy3 UF series ultrasonic flow meter (10 L/min ± 3% RD). Omega PX26-015DV wet/wet differential pressure meters (100 kPa ± 0.25% FS) were used for pressure drop measurements, indicated in Figure 3.2. To account for any drift experienced during this study, the pressure sensor calibration was checked before each series of tests. It was found during the experimental tests performed for this study that no offset correction was required.

For this investigation, a fixed liquid inlet temperature to the coldplate of 35°C was used, which was controlled using a compact brazed heat exchanger connected to a Julabo Presto

A40 microprocessor-controlled chiller. The water temperature measurements indicated in Figure 3.2 were measured using sheathed T-type thermocouples inserted into the flow via compression fittings. All temperatures in the test facility were calibrated against an ASL F100 RTD reference probe (±0.2°C)[3]. A National Instruments Data Acquisition (DAQ) system was used to record the temperature, pressure and flow rate readings, used in conjunction with the National Instruments LabVIEW software. The experimental procedure involved allowing sufficient time to achieve steady state conditions and subsequently recording the temperature, pressure and flow rate measurements. The heat source boundary conditions involved a test range of 50 - 250 W input heater powers in 50 W intervals. Tests were conducted across a flow rate range of 1 to 6 L/min, in increments of 1 L/min, corresponding to inlet velocities into the manifold between 0.21 m/s and 1.2 m/s (Re ≈ 3000 - 17600) for a 10 mm diameter inlet. For the baseline configuration comprising 49 jets, the jet nozzle exit velocities ranged from 0.43 m/s to 2.6 m/s, translating to jet Reynolds numbers between 600 and 3600. These Reynolds numbers indicate turbulent inlet flow conditions, with the presence of vortical structures in the inlet manifold being likely. Consequently, asymmetric inflow to the jet nozzles is anticipated, with potential flow separation occurring in some nozzles due to the sharp-edged inlet geometry.

3.2.3. Data Reduction

As discussed, the heated meter bar technique [31] used here allowed for the measurement of both the thermal power, Q_{hs}, and temperature at the intersection of the meter bar and base of the IHS, here denoted as the junction temperature, T_j. Assuming one-dimensional conduction, Q_{hs} can be determined from,

$$Q_{hs} = -kA_{hs}\frac{dT}{dx} \tag{3.1}$$

where k is the thermal conductivity of the ultra-pure OFE copper, A_{hs} is the cross-sectional area of the neck section, and dT/dx is the measured temperature gradient, determined by

[3] For information on the experimental apparatus calibration, see Appendix B

linear regression of the three temperature measurements along the length of the meter bar. The junction temperature was calculated by linear extrapolation of the temperature gradient, such that,

$$T_j = T_t + \left(x_t - x_j\right)\left(\frac{dT}{dx}\right) \tag{3.2}$$

where T_t is the temperature of the thermocouple closest to the IHS of the copper block, and $x_t - x_j$ is the vertical distance from the T_t measurement location to the meter bar – IHS intersection. The value for each measured parameter was taken from the average of the dataset collected for each thermocouple, taken over 5 minutes intervals, following an initial 20 minute settling period at the beginning of each test to allow for temperature stabilisation. Thermal steady state was assumed when the variation in temperature measurements was no greater than 0.5°C after 50 readings. Following thermal stabilisation, readings were recorded at one second intervals, i.e. a sampling frequency of 1 Hz, resulting in a sample size of 300 for each thermocouple after each test run.

The overall die-to-coolant heat transfer coefficient, U, was calculated using the Log-Mean Temperature method suggested by Webb [32] for these electronics cooling type scenarios,

$$Q_{hs} = UA_{hs}\left[\frac{\Delta T_2 - \Delta T_1}{\ln\left(\frac{\Delta T_2}{\Delta T_1}\right)}\right] = UA_{hs}\Delta T_{LM} \tag{3.3}$$

such that,

$$U = \frac{Q_{hs}}{A_{hs}\Delta T_{LM}} \tag{3.4}$$

where ΔT_{LM} is the Log-Mean Temperature Difference assuming a uniform surface temperature; $\Delta T_1 = T_j - T_{in}$, and $\Delta T_2 = T_j - T_{out}$. The overall heat transfer coefficient thus includes the contributions of heat spreader and the convective heat transfer to the overall thermal conductance between the heat source and heat sink. The average exit velocity of the flow through each jet, V_{jet}, and hence the jet Reynold's Number, Re_{jet}, are defined as [26]:

$$V_{jet} = \frac{4\dot{V}}{N\pi D^2} \tag{3.5}$$

$$Re_{jet} = \frac{V_{jet}D}{\nu} \tag{3.6}$$

where $\dot{V}$ is the volumetric flow rate of the fluid entering the cold plate manifold, ν is the kinematic viscosity of the fluid and N is the number of jets on the orifice plate. The hydraulic power of the coldplate heat exchanger can this be determined as,

$$\mathrm{P}_p = \dot{V}\Delta P \tag{3.7}$$

where ΔP is the pressure drop across the coldplate.

3.2.4. Uncertainty Analysis

The method described by Kempers and Robinson [31] for determining the uncertainty on the heat flux and junction temperature when using the heated meter bar was used in this work. This method uses a Monte Carlo technique to combine the uncertainties associated with the spatial and temperature errors for multiple readings that are combined into a single parameter by regression analysis, specifically here the temperature gradient, dT/dx used in Eqs (3.1) and (3.2). To perform a Monte Carlo analysis, probability distributions are assigned to all of the measured quantities with associated uncertainties required for calculating the temperature gradient which, in this case, are the positional and temperature measurements of the thermocouples located within the TTV neck. Random sampling is employed to generate a dataset of input values spanning the uncertainty ranges of the measured parameters. For this study, a total of 10,000 input data points were generated, ensuring comprehensive coverage across the defined uncertainty ranges of each parameter. The statistical outputs, including the mean, standard deviation, and confidence intervals, were subsequently determined for each parameter. A confidence level of 95% was adopted for this analysis, aligning with the standard interpretation of uncertainties under a Gaussian normal distribution framework.

The uncertainty in each derived quantity (Eq. (3.1), (3.4) - (3.7)) was calculated using the method of Kline and McClintock [33]. Denoting each measurement by x_i and the uncertainty in the measurement Unc_i, the uncertainty on derived parameter Z is Unc_z, calculated by,

$$Unc_z = \sqrt{\left(\sum_{i=1}^{n}\left[\frac{\partial Z}{\partial x_i}Unc_i\right]^2\right)} \tag{3.8}$$

Experimental uncertainties on all measurements are listed in Table 3.2, whilst uncertainties on derived parameters are presented in Table 3.3 for a range of flow rates and a fixed heat transfer rate of 250 W[4]. It is worth noting that the relative error on the overall heat transfer coefficient increases with increased flow rate, and this is primarily due to the diminishing difference in temperature between T_j and the coolant. Regardless, the uncertainty remains acceptably low even at the highest flow rate.

Table 3.2: Measurement errors

Error (Absolute)	1 LPM	3 LPM	6 LPM
T_j (°C)	0.6	0.6	0.6
ΔT (°C)	0.9	0.9	0.9
$\dot{V}$ (L/min)	0.03	0.09	0.18
ΔP (Pa)	17.5	85.0	250.0

Table 3.3: Relative uncertainty on derived parameters

Relative Error (%)	1 LPM	3 LPM	6 LPM
Q_{hs}	2.5	2.5	2.5
U	3.7	4.5	5.0
V_{jet}	3.7	3.7	3.7
Re_{jet}	4.1	4.1	4.1
P_p	6.8	4.6	4.0

[4] For an example of the propagation of errors for a derived parameter, see Appendix C

3.3. Numerical Simulations

3.3.1. Computational Domain and Governing Equations

A representation of the computational domain for the 15 x 15 mm^2 simulation case is depicted in Figure 3.3, showing both the fluid and solid subdomains. In this example it is geometrically the same as the system shown in Figure 3.1, except the region where heat is applied is shortened to reduce computation time. For the CFD verification study, the heat source material was copper, whereas for the optimisation study it was silicon. It is noted however that for the optimisation study discussed, the orifice plate design varies since the number of jets, jet diameter, jet-to-jet spacing, and jet-to-target spacing are the chosen design parameters.

The simulation model developed in STAR-CCM+ employed a steady-state, coupled implicit solver to manage pressure-velocity coupling, ensuring robust and efficient computation, with a second-order upwind discretisation scheme implemented to enhance accuracy in resolving flow gradients, particularly in regions of steep variations. The convergence criterion for iterative solvers was defined by a residual threshold of 10^{-6}, ensuring a high level of solution precision. Automatic initialisation was utilised to establish the initial solver conditions, streamlining the setup process and providing a consistent starting point for all simulations. The maximum iteration count for the simulations was set to 1500 steps, ensuring sufficient room for convergence while maintaining computational efficiency. Simulations were programmed to terminate upon reaching this iteration limit if convergence of all residuals was not achieved. This measure was implemented to prevent excessive delays in completing the optimisation process across all feasible design points. Non-convergent cases were anticipated primarily for extreme orifice geometries, which were unlikely to fall within the optimal design regions for either of the objective functions considered in this study. Such geometries would likely induce significant pressure drops across the manifold, prolonging convergence and rendering these configurations impractical within the scope of the optimisation analysis.

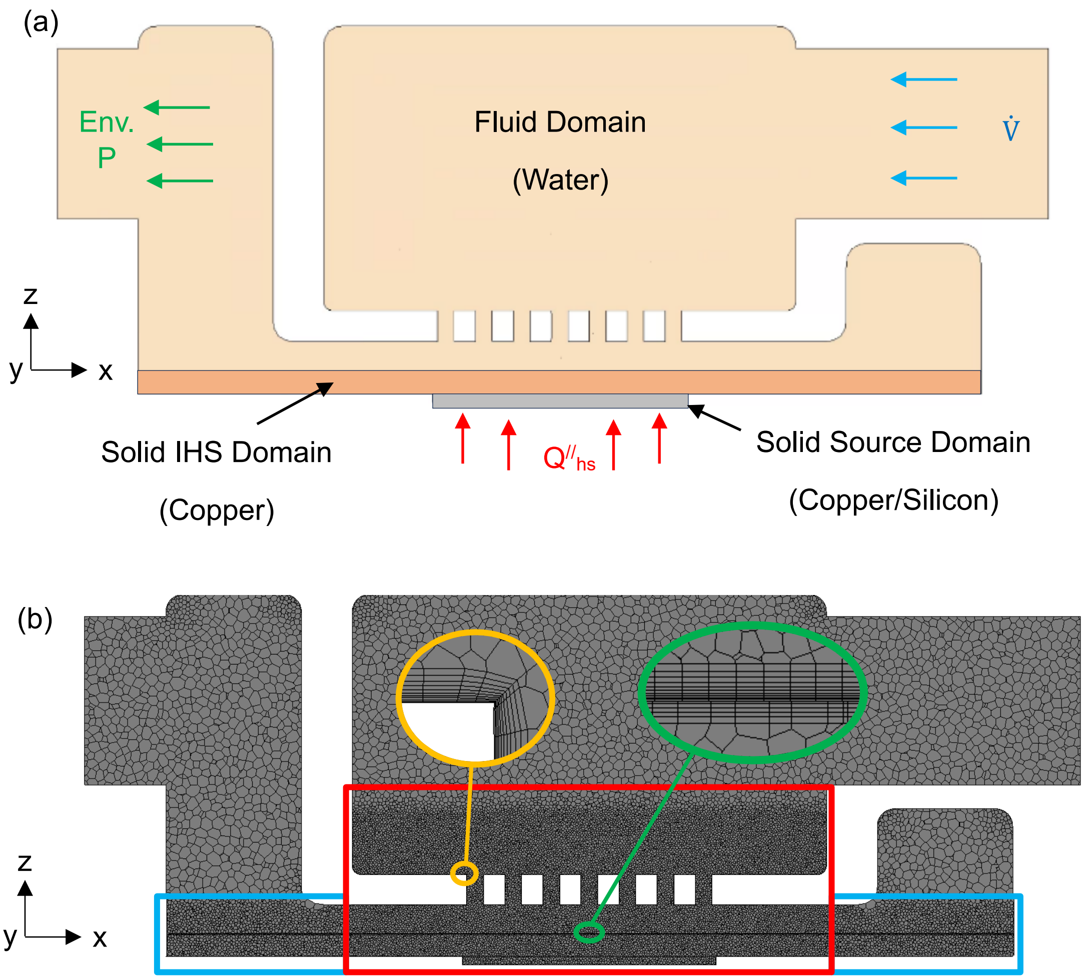

Figure 3.3: (a) Sectioned view of computational domain, depicting both fluid and solid subdomains, (b) Illustration of computational mesh with highlighted localised mesh regions and insert of boundary layer meshing.

Within the fluid domain, the steady-state conservation equations for mass, momentum, and energy are solved using the commercial software package STAR-CCM+. These are expressed as follows [34-36]:

Conservation of mass:

$$\nabla . u = 0 \tag{3.9}$$

Conservation of Momentum:

$$u \cdot \nabla u = -\frac{\nabla P}{\rho} + \frac{1}{\rho}(\nabla \cdot \mu \nabla u) - (\overline{u'} \cdot \nabla \overline{u'}) \tag{3.10}$$

Conservation of Energy (Fluid):

$$\mathrm{u}\,.\,\nabla\mathrm{T} = \frac{1}{\rho}\left[\nabla\cdot\left(\frac{k_f\nabla T}{C_p}\right)\right] \tag{3.11}$$

Conservation of Energy (Solid):

$$\nabla\cdot\left(\frac{k_s\nabla T}{C_p}\right) = 0 \tag{3.12}$$

where u refers to the velocity of the fluid, u' is the velocity fluctuation component due to turbulence, ρ is the fluid density, P is the pressure, μ is the dynamic viscosity and T is the temperature. Additionally, k is thermal conductivity, and C_p is specific heat capacity. Owing to the turbulent nature of the flow it is imperative to use an adequately accurate turbulence model when applying the Reynolds-Averaged Navier-Stokes (RANS) approximation. For this investigation, the SST (Shear-Stress Transport) k-ω turbulence model was found to be adequate and will be discussed in more detail in a following section. Viscous heating was not considered, as for the expected range of impinging jet arrays, the Brinkmann number remained less than unity. The Brinkmann number is defined as the ratio of viscous heat generation to conductive heat transfer within a fluid flow [37], and is given as,

$$Br = \frac{\mu u^2}{k\Delta T} \tag{3.13}$$

where ΔT is the temperature difference between the heat transfer surface and the inlet fluid temperature.

The boundary conditions for the CFD model are as follows; a uniform heat transfer rate, representative of the heat produced from the cores of a CPU, was applied to the heat source base. The input heat transfer rate was held at 250 W (111 W/cm^2), representing the maximum power tested during the experimental testing. An environmental pressure boundary condition was applied at the outlet nozzle, whilst a volumetric flow rate was applied at the inlet, which was extended by 25 mm at both the inlet and outlet of the manifold to ensure developed flow, with an applied turbulence intensity of 5% and a turbulence length scale of equal magnitude to the inlet diameter. For the verification study, the flow rates were varied between fixed flows of 1 - 6 L/min to replicate the flows investigated during the physical experiments. For the optimisation study, the flow rate was dictated by a fan/pump boundary condition within STAR-CCM+, dictated by a pump curve typical to that of pumps used in closed-loop liquid cooling systems, specifically here the TCS M500 series micropump. This boundary condition dictated the flow rate for each orifice design, dependent on the pressure drop across the fluid manifold, which varied for each new jet configuration i.e. the specific orifice design dictated the operating point on the pump curve from which the flow rate is determined. For the chosen pump, the pump curve is adequately described by the following function;

$$\Delta P = -8.65\dot{V} + 69.13 \tag{3.14}$$

where the flow rate is in L/min and pressure drop in kPa. Thus, the maximum static pressure of the pump is 69.13 kPa and the maximum flow rate is 8 L/min. The maximum hydraulic power of this pump is $P_{p,max}$ = 2.34 W, which occurs at an operating point of ΔP = 35.4 kPa and $\dot{V}$ = 4.0 L/min. No-slip boundary conditions were applied to all other contact surfaces of the fluid domain. No conditions of symmetry were applied to the model as this approach also anticipates the evaluation of non-uniform and/or non-centred heat sources in future studies.

3.3.2. Meshing and Mesh Independence

STAR-CCM+ utilises both surface and volume meshing strategies, and in this instance a main polyhedral mesh was used with an underlying tetrahedral layer, which are better suited for heat transfer and swirling flow regimes compared to a purely tetrahedral mesh [38]. Advanced layer meshing was also utilised which generates prismatic cell layers next to wall boundaries, which are of particular benefit for capturing boundary layers at the solid/fluid interfaces [39].

In order to ensure maximum accuracy around the impinging jets, a localised mesh region was created to better capture the turbulence and high gradients in the region where the jets impinged on the target surface. Two regions of localised mesh were created. The first covered the volume immediately surrounding the jets. This region had the highest mesh density with cells being no larger than 0.125 mm. The second, less dense region covered the source/spreader assembly at a sufficient height from the wall into the fluid domain to ensure adequate accuracy in the fluid boundary layers and maintain a y^+ value of approximately 1, with the solid-fluid interface boundary mesh consisting of 10 layers for a total height of 0.15 mm, with prism layer stretching set at 120%. This results in . The localised volumes were positioned centrally and considered the underside of the heat source as the origin point (see Figure 3.3), providing ample room to model all possible jet configurations within the optimisation range and the immediate downstream flow region. Due to the variable jet nozzle diameters considered for optimisation, the boundary mesh surrounding the nozzles needed to be tighter to the nozzle walls, as for the smallest diameters these boundary prism layers could result in non-conformal mesh cell generation within the nozzle if the boundaries occupied too much volume within the nozzle. Consequently, the prism layers within the nozzle were reduced to a maximum total height of 0.10 mm across 10 layers, again with 120% prism layer stretching, to maintain the y^+ value required for sufficient accuracy at the nozzle boundaries.

A mesh independence study was carried out by incrementally increasing the mesh density until the key variables converged adequately. The mesh independence study was carried out using the baseline design depicted in Figure 3.3 for the highest flow rate of 6 L/min. Table 3.4 indicates that a mesh of approximately 3.4 million cells was sufficiently dense, since the difference between tracked variables (overall pressure drop and junction temperature shown here) was less than 1% with the next highest mesh count. The Grid Convergence Index is also included, as defined in the previous chapter using [40]. The consistent decrease in GCI across mesh levels supports asymptotic convergence, with grid independence confirmed with the GCI dropping below unity.

Table 3.4: Mesh independence study

Parameter	I	II	III	IV	V	VI	VII
No. of elements (x10^6)	0.50	1.09	1.74	2.25	2.56	3.02	3.40
T_j diff. (%)	-	4.50	4.32	3.93	3.47	1.81	0.08
ΔP diff. (%)	-	16.75	2.41	2.81	1.10	0.86	0.82
GCI	-	-	27.01	17.03	15.44	1.45	2.6 x10^{-5}

3.3.3. Simulation Model Verification

The first stage of the CFD simulation model verification was to independently determine the correctness of implementing the SST k-ω turbulence model. Simulations were thus conducted to compare against the CFD study of Yang et al. [41], who themselves verified their simulations against the experimental results provided by Goldstein and Behbahani [42]. Figure 3.4 illustrates the STAR-CCM+ model developed using these boundary conditions, highlighting the jet's flow velocity profile under crossflow conditions. These works considered a single, free, turbulent air jet entering a crossflow channel and impinging onto a heated surface, with data presented in terms of the local Nusselt number distribution. The jet was characterised by an inlet Reynolds number of 78,300 and a jet-to-crossflow velocity ratio of 5.8, corresponding to a crossflow velocity of 16.6 m/s. The jet nozzle diameter was 12.7 mm. The computational domain represented a wind tunnel with a rectangular cross-section, measuring 20.32 cm in width, 15.24 cm in height, and 114 cm in length. Centrally positioned on the tunnel's top wall, the jet nozzle created a jet-to-target height-to-diameter ratio (H/D) of 12. The impingement surface at the tunnel base was heated with a uniform heat flux of 1200 W/m².

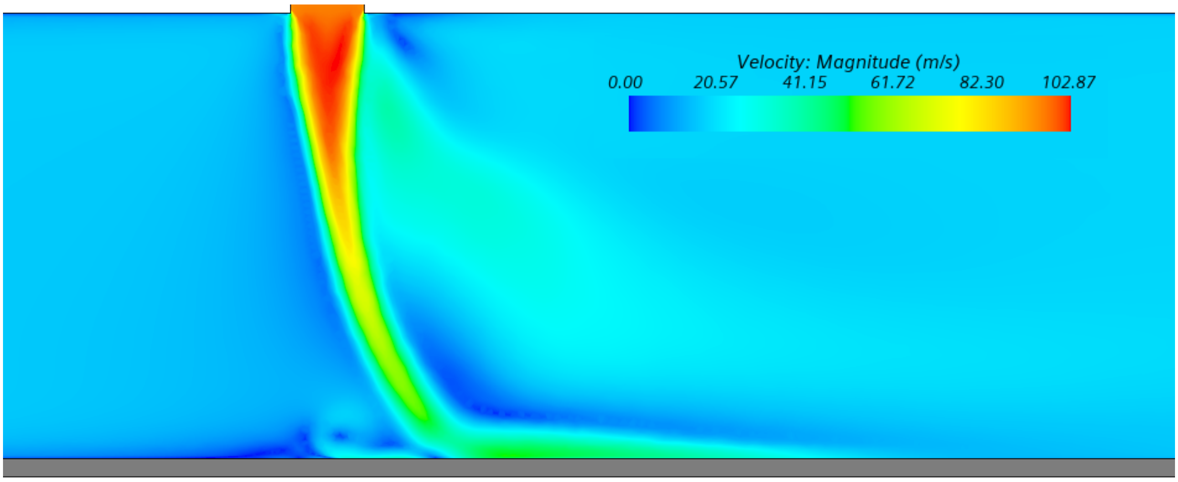

Figure 3.4: Flow velocity contour of Goldstein & Behbahani [39] impinging jet in crossflow.

Although the jet Reynolds number in this example significantly exceeds those anticipated in the current study, the works of [41] and [42] were selected for turbulence model validation. These studies uniquely address the combined challenges of a turbulent impinging jet under crossflow conditions and a heated target surface, providing the only comprehensive example of this type in existing literature. Most other cases focus on isolated aspects of the problem. Therefore, this dataset was deemed the most suitable reference for validating the CFD tool, ensuring alignment with the expected flow behaviours pertinent to the present investigation.

The STAR-CCM+ simulation results adequately agree with both earlier simulation and experimental studies when the SST k-ω turbulence model is implemented. To illustrate the importance of modelling the turbulence correctly, identical simulations were carried out using the k-ε turbulence model. As seen in Figure 3.5, this strategy did a poor job at predicting the published data, particularly showing an unrealistically weak influence of the crossflow on the heat transfer. Overall, these findings are consistent with previous literature [43-45] giving further evidence to support the conclusion that the SST k-ω turbulence model is appropriate for modelling jet impingement heat transfer[5].

[5] For additional detail on numerical verification, see Appendix D.

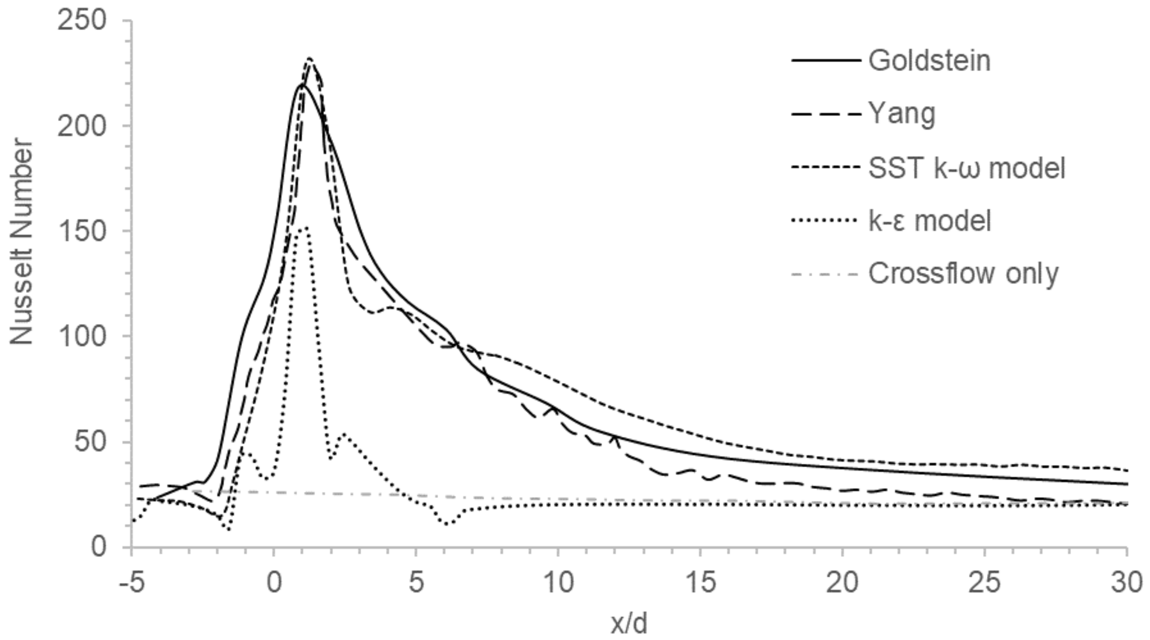

Figure 3.5: Comparison of average Nusselt number vs horizontal displacement for a single impinging jet in crossflow between present work and previous literature [41, 42] for both the SST k-ω and k-ε turbulence models.

The second stage of the simulation verification was to compare the numerical predictions against experimental data for the baseline impinging jet orifice configuration as detailed previously. Considering the discussion above, only the SST k-ω turbulence model was implemented. Both the junction temperature and pressure drop experimental and simulation results are shown in Figure 3.6 for a heat transfer rate of 250 W and flow rates between 1 - 6 L/min. Experimental data was gathered for the three investigated heat source concentrations. Table 3.5 provides the specifics of experimental versus CFD deviation across the range of investigated heat source concentrations, as well as the absolute mean average deviation. Clearly, the simulation model accurately predicts both the thermal and hydraulic experimental data, with a maximum 2.6% discrepancy for the junction temperature and a maximum 8.2% for the pressure drop. Overall, it is concluded that the CFD simulation model is sufficiently accurate and can be used with confidence in the forthcoming optimisation study.

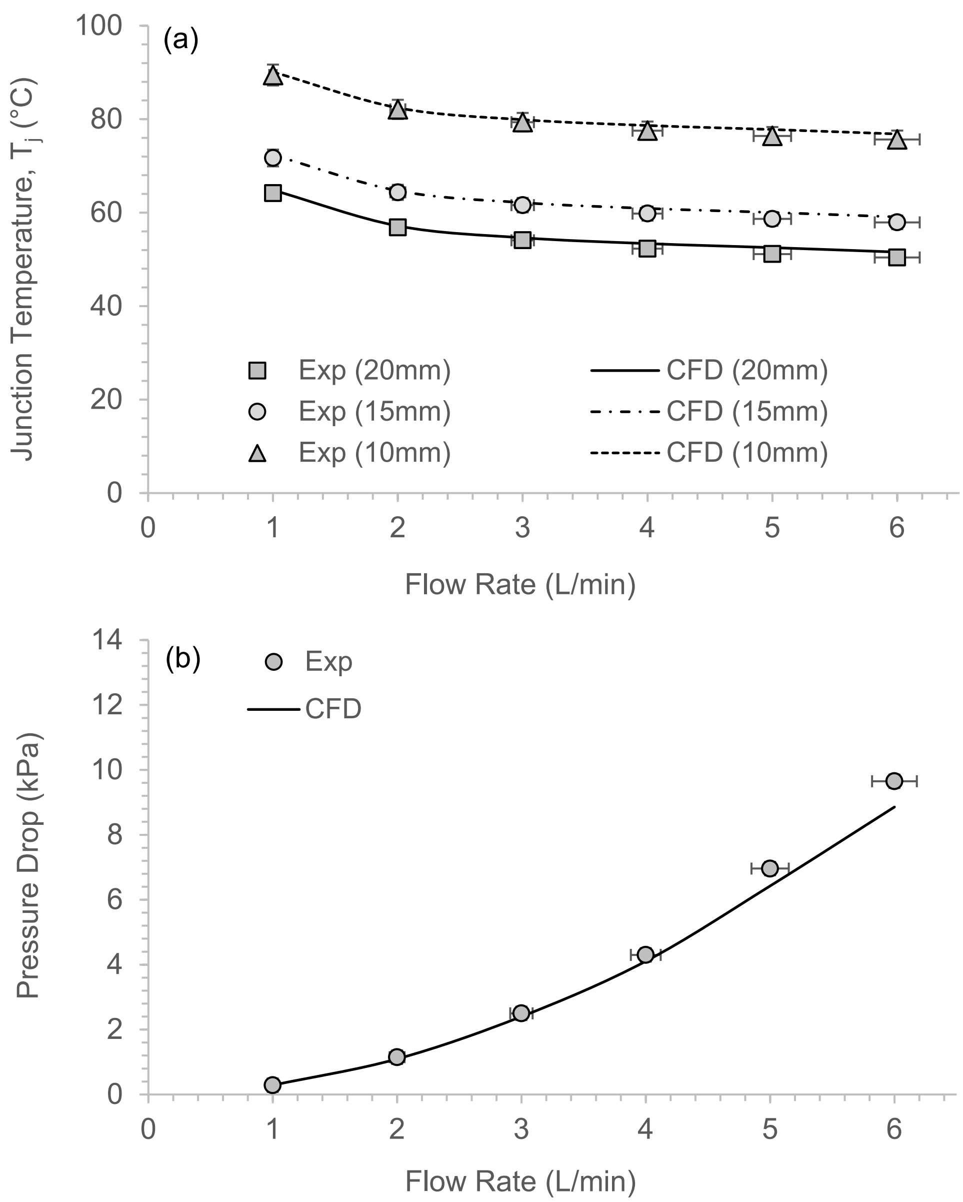

Figure 3.6: Comparison between numerical and experimental data for (a) junction temperature and (b) pressure drop.

Table 3.5: CFD deviation from experimental data

Deviation (%)		Minimum	Maximum	Mean Average
T_j	10 x 10 mm^2	0.59	2.81	1.32
	15 x 15 mm^2	0.90	2.56	1.16
	20 x 20 mm^2	0.40	1.78	0.90
ΔP		-4.31	8.22	5.19

3.3.4. Multi-Objective Optimisation

An automated optimisation workflow process was established in Siemens NX which integrated three separate software packages: NX CAD for modelling the variable design geometries, STAR-CCM+ for the CFD simulations, and the Hierarchical Evolutionary Engineering Design System (HEEDS) for the optimisation. The embedded CAD feature of Siemens NX enabled the creation of 3D geometries with variable geometric features, which was imported automatically into STAR-CCM+ to perform the CFD simulations. HEEDS acted as the optimisation interface, whereby it imported and post-processed simulation data based on the selected optimisation goals. HEEDS then updated the geometric parameter information in NX CAD which initiates the next CFD simulation in STAR-CCM+.

In this investigation, the automated process was utilised to optimise the jet array impingement heat exchanger for the concentrated heat source with the integrated heat spreader. Specifically, Figure 3.7 shows the geometric variables investigated during the optimisation; the jet-to-jet spacing ratio (S/D), the jet-to-target ratio (H/D), the total jet population (N), the jet diameter (D) and the heat source area (A_{HS}). These variables were assigned the designations of A, B, C, D and E respectively and Table 3.6 presents the investigated ranges for each. It is reminded here that the achieved flow rate for each design, and subsequently the heat transfer performance, depended on the pressure drop characteristic since the inlet flow boundary condition was subject to the selected pump curve. The thickness of the IHS remained constant throughout this optimisation analysis, as its inclusion did not change the outcome of developing an optimisation design workflow for a heat exchanger, in addition to adding computation time and effort to existing optimisation. However, the CFD model was constructed so that this parameter could be easily added to the existing optimisation workflow. This is also the case for other elements that may be of use in the future to investigate as part of a multi-objective optimisation, such as variable jet spacings and diameters, as well as material properties such as non-isotropic thermal conductivity of the solid heat spreader. As such, the arrangement of jet nozzles on the orifice pate were confined to equidistant square arrays for this study.

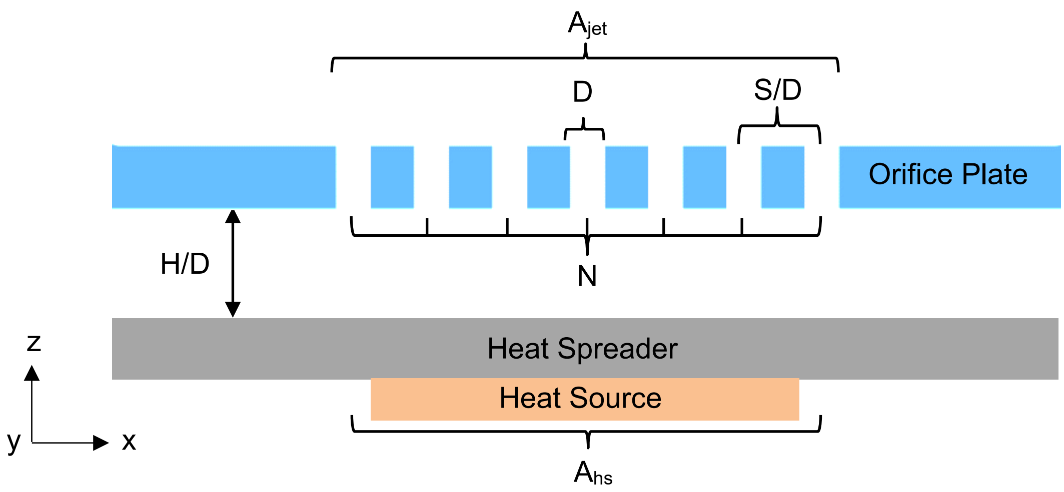

Figure 3.7: Sectioned baseline orifice plate, highlighting geometric variables for optimisation.

A key goal of the present study was to develop and deploy an automated Multi-Objective Optimisation (MOO) design process for jet array impingement coldplate heat exchangers. The optimisation targets were to generate the designs that simultaneously maximised the cooling effectiveness and minimised the energy consumption. To realise this, two objective functions were selected, specifically the maximum junction temperature, T_j, and the pumping power, P_p, with the goal being to minimise both. The junction temperature, defined at the interface between the heat source and heat spreader, was selected as the thermal boundary condition for this study as this approach allows for direct measurement from the CFD simulations, thereby streamlining the optimisation process by eliminating the need to compute a derived parameter with each design iteration. With the objectives selected, the HEEDS optimisation software coordinated the parameter optimisation process with the SHERPA hybrid and adaptive algorithm.

The SHERPA (Simultaneous Hybrid Exploration that is Robust, Progressive, and Adaptive) algorithm represents a hybrid optimisation methodology specifically designed to efficiently navigate complex, high-dimensional design spaces. By dynamically adjusting its search strategy in response to the characteristics of the problem, SHERPA achieves adaptability throughout the optimisation process. The algorithm integrates multiple optimisation techniques to effectively balance the exploration of the search space with the exploitation of identified promising regions. SHERPA employs a combination of stochastic methods for broad exploration, gradient-based techniques for local refinement, evolutionary algorithms to manage multimodal landscapes and maintain diversity, and response surface models to approximate objective functions that are computationally expensive to evaluate. During the optimisation process, SHERPA adapts the relative contributions of these constituent methods based on their observed performance, ensuring efficient allocation of computational resources [46].

One of SHERPA's key advantages is its ability to evaluate multiple candidate solutions concurrently, leveraging parallel computing capabilities to accelerate the search process. By progressively refining its exploration based on intermediate results, the algorithm demonstrates an enhanced capability to converge effectively towards optimal or near-optimal solutions. Notably, the adaptive framework of SHERPA requires minimal user-defined inputs beyond the specification of design parameters and objective functions, as it autonomously adjusts its internal variables to optimise performance. This feature simplifies its application while maintaining robust optimisation capabilities across diverse and challenging design problems.

Table 3.6: Optimisation geometric variables

Parameter	Description	Unit	Range
A: S/D	Jet spacing ratio	-	1.17 - 6.5
B: H/D	Jet-target ratio	-	0.17 - 5.5
C: N	Jet population	-	9 - 169
D: D	Jet diameter	mm	0.5 - 1.5
***E**: A_{hs}	Heat source area	mm^2	100 - 400

* The surface area of the heat source is a non-independent variable, and not a parameter for optimisation.

3.4. Results and Discussion

3.4.1. Thermal-Hydraulics of Baseline Design

As mentioned earlier, jet array impingement thermal-hydraulics in this CPU-type scenario that includes a concentrated heat source and IHS is relatively unexplored. To illustrate the behaviour as well as to provide a scenario to which other design configurations can be compared and contrasted, the baseline design for the mid-concentration A_{hs} = 15 x 15 mm^2 heat source will be described in some detail. As listed in Table 3.7, this design results in an overall source-to-sink heat transfer coefficient of U = 46,879 W/m^{2}K with a flow rate of 6.67 L/min.

Figure 3.7 illustrates the sectioned profiles of fluid velocity, heat spreader temperature, pressure, and vorticity fields respectively. As can be seen from Figure 3.8, fluid enters the upper manifold of the heat exchanger through the inlet port as a moderate velocity (1.4 m/s) jet and decelerates within the chamber. The moderate velocity and deceleration as it expands in the upper chamber is sufficient to pressurise the manifold above the jet orifice, and Figure 3.7 shows that the chamber pressure is relatively uniform. This equalisation of pressure above the jet orifices ensures a relatively unform distribution of flow across the jets, with average velocities in the region of 3 m/s for the baseline case considered here.

Considering the central jet in Figure 3.8, the flow above the orifice is nearly stagnant and a near ideal symmetrical jet issues into the lower gap region. It is clear from Figure 3.8 that the constriction of the flow at the orifice entrance is the primary contributor to the total pressure drop, which is ΔP = 10.8 kPa for the baseline design. The sharp edges of nozzle contribute to this, evidenced by the high vorticity generated in this region (Figure 3.8), which creates a mixing layer along the wall region within the nozzle, as discussed by Davis et al. [47].

Table 3.7: Baseline numerical simulation results

Parameter	**Value**	**Orifice CAD**
S/D	2.25	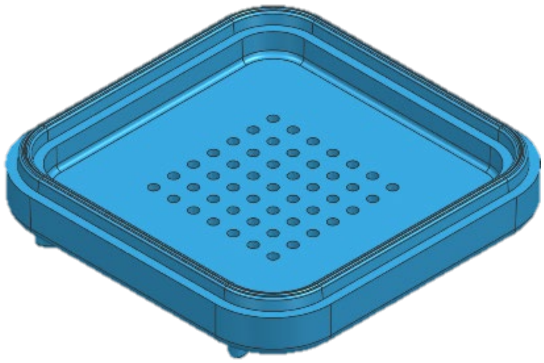
H/D	1.70	
N	49	
D (mm)	1.00	
V_{jet} (m/s)	2.89	
Re_{jet}	3,990	
A_r	0.93	
T_j (°C)	58.70	
ΔP (Pa)	10,815	
$\dot{V}$ (L/min)	6.67	
P_p (W)	1.20	
U (W/m^2K)	46,879	

Upon exiting the nozzle, the jet is issued into the lower gap region at an average jet exit velocity of 2.9 m/s. The associated Reynolds number is Re_{jet} = 3990, signifying fully turbulent flow. Upon entering into the confined lower chamber, the jet-to-target spacing of H/D = 1.7 is low enough for there to be low entrainment and subsequent spreading of the jet prior to impact on the surface. The higher vorticity observed at the outer edge of the issued jet in Figure 3.8 is primarily from the shear layer formed within the nozzle, which subsequently impacts the region encompassing the impingement zone on the surface. The end result is that the potential core of the jet remains intact upon impact with the surface, clearly defining the impingement zone of approximate diameter of the jet nozzle, as signified by the high stagnation pressure region in Figure 3.8. The rise in pressure in the stagnation region creates a horizontal pressure gradient to form the wall jet, which spreads radially outward along the surface, as seen in the Figure 3.8. Here, the flow accelerates and the rapid directional change of the flow results in high near-wall vorticity. Owing to the relatively close spacing of the jets, at S/D = 2.25, the wall boundary layer of the central jet impacts that of its neighbours with enough inertia to create the up-washing fountain effect seen in Figure 3.8. This forms a region of flow recirculation at the approximate midpoint between the jets.

As the central impinging jet contacts the solid surface of the heat spreader, it generates a distribution of convective heat flux that correlates to the intensity of the convective heat transfer (Figure 3.9). This associates with the different fluid flow zones of the impinging jet, and thus varies in the outward direction from the central stagnation point. However, this is a conjugate heat transfer problem, where the intensity of the convective heat transfer influences the conduction in the solid, which together determine the net local convective heat flux at the surface. To illustrate this, Figure 3.9 shows the ratio of convective heat flux at the upper surface ($Q^{//}_{t}$) to the applied uniform heat flux at the lower surface ($Q^{//}_{hs}$ = 111.1 W/cm^2). This highlights regions where the fluid mechanics influence change in the local convective heat transfer intensity, including conjugate heat transfer effects. Generally speaking, if $Q^{//}_{t}$ / $Q^{//}_{hs}$ decreases, it signifies a transition to a region of lower convective heat transfer intensity. Since this causes the local solid temperature to increase, it creates a temperature gradient and lateral heat flow in the solid phase towards the higher convective intensity region of lower temperature.

Figure 3.9 shows that the distribution of heat flux for the central symmetric jet is similarly symmetrical. The central stagnation zone is characterised by an extremely thin thermal boundary layer where the high velocity potential core impacts the surface and results in a high convective heat transfer intensity region, which is well known in the literature, e.g. [48]. The observed heat flux at the central stagnation point approaches that of the applied heat flux at the source, though remains less than the surrounding region for reasons to be discussed. Beyond the central stagnation region, a thin outer ring of proportionately high convective intensity ($Q^{//}_{t}$ / $Q^{//}_{hs}$ > 1) exists, located approximately between one third and half the diameter of the nozzle. This region coincides with the point of minimum flow velocity, which signifies the leading edge of the wall jet. Pamadi and Belov [49] observed such peaks outside of the central stagnation point for high confinement (low H/D) jets, and attributed it to the development of the wall jet causing thinning of the thermal boundary layer, which is consistent to what is observed here. It has also been shown in other studies, e.g. [50], that this peak is not present for jets with low confinement (high H/D), indicating that the level of confinement is a contributing factor. In the context of conjugate heat transfer, the high convective intensity where the wall jet is forming causes a local depression in solid temperature giving rise to horizontal temperature gradients in the solid near the surface. This induces lateral conduction from the adjacent regions of lower convective intensity, including the stagnation zone, which explains why Q''_t / Q''_{hs} < 1 here.

Moving outward from the peak heat transfer region of the central jet, the wall jet is forming and is doing so symmetrically, as depicted in Figure 3.8. Here, the hydraulic and thermal boundary layers develop and the convective heat transfer intensity diminishes as expected [51]. However, the wall jet boundary layer development is occurring within the projected area of the jet orifice, and is thus subject to the influence of the downward flow of the main jet, including the mixing associated with the high vorticity shear layer. This moderates the rate of boundary layer growth and heat transfer deterioration. Although lower than the stagnation and peak zones, Figure 3.8 shows that high convective intensity is still sustained, only to drop notably once the wall jet is beyond that of the main vertical jet. This transition region is clear from Figure 3.8, where the near wall pressure drops sharply. Beyond this, the wall jet boundary layer develops at a more rapid rate resulting in the expected decay of the convective heat transfer intensity [52]. However, as seen in Figure 3.8, for this relatively low S/D scenario, the decay is stunted early owing to the wall jet interaction with that of its neighbouring jets. As Figure 3.8 shows, the colliding wall jets create the discussed up-washing of the fluid, resulting in the observed increase in the convective heat flux in this region.

Moving outward from the centre jet, the flow profiles of the jets become progressively less symmetric (Figure 3.8) and the resulting convective heat transfer intensity progressively diminishes (Figure 3.9). Since the mass flow rate in the lower channel increases with relative distance of the jets from the geometric centre of the array, so does the crossflow velocity. The escalating crossflow progressively deflects the jets, making them more oblique at the impact zone. As expected, Figure 3.8 shows that the convective heat transfer intensity deteriorates as the degree of obliqueness increases, which is well known in the archived literature [53, 54]. It is also worth noting here that despite having similar pressure above all of the jets in the array (Figure 3.8), the flow within the upper manifold chamber has some influence on the jet formation of the outer most jets in the array, in particular for the row furthest from the manifold inlet. As shown in Figure 3.8, the circulation of the flow in the upper chamber creates a non-negligible crossflow at the jet orifice inlet here. This produces a Venturi-type effect within the nozzle, causing the maximum flow velocity to be larger as well as possessing a curved outlet profile, which accentuates the jet deflection and convective heat transfer deterioration.

The overall thermal-hydraulic performance of this baseline design is summarised in Table 3.7. Of particular relevance are the achieved junction temperature, T_j = 58.7°C, for the required hydraulic pumping power penalty of P_p = 1.2 W. In what is to follow, an attempt has been made to understand the improvement achieved by the optimum designs by comparing the thermal-hydraulics to the above-described baseline design.

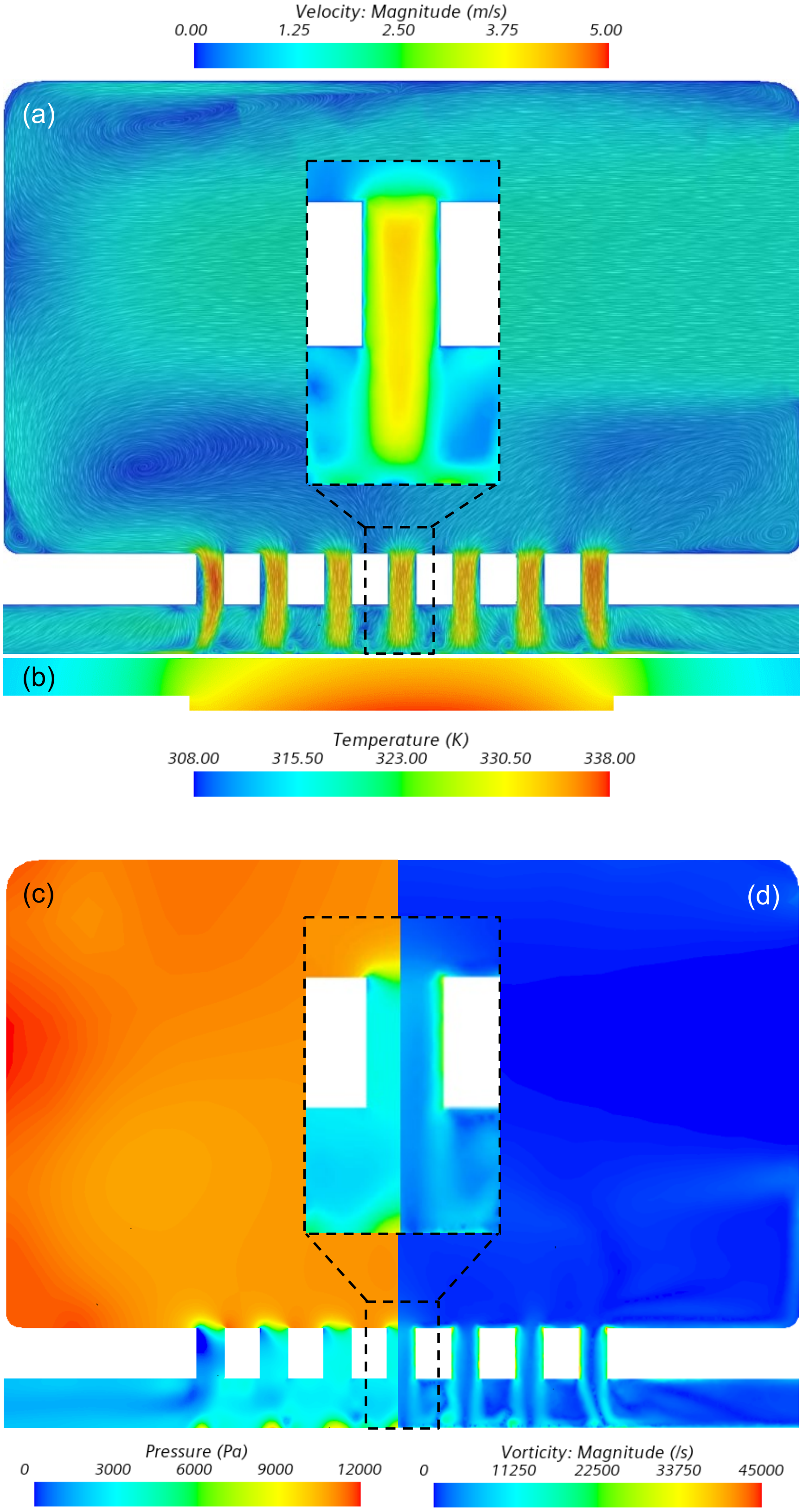

Figure 3.8: Sectioned baseline model plots of (a) velocity, (b) temperature, (c) pressure and (d) vorticity contours.

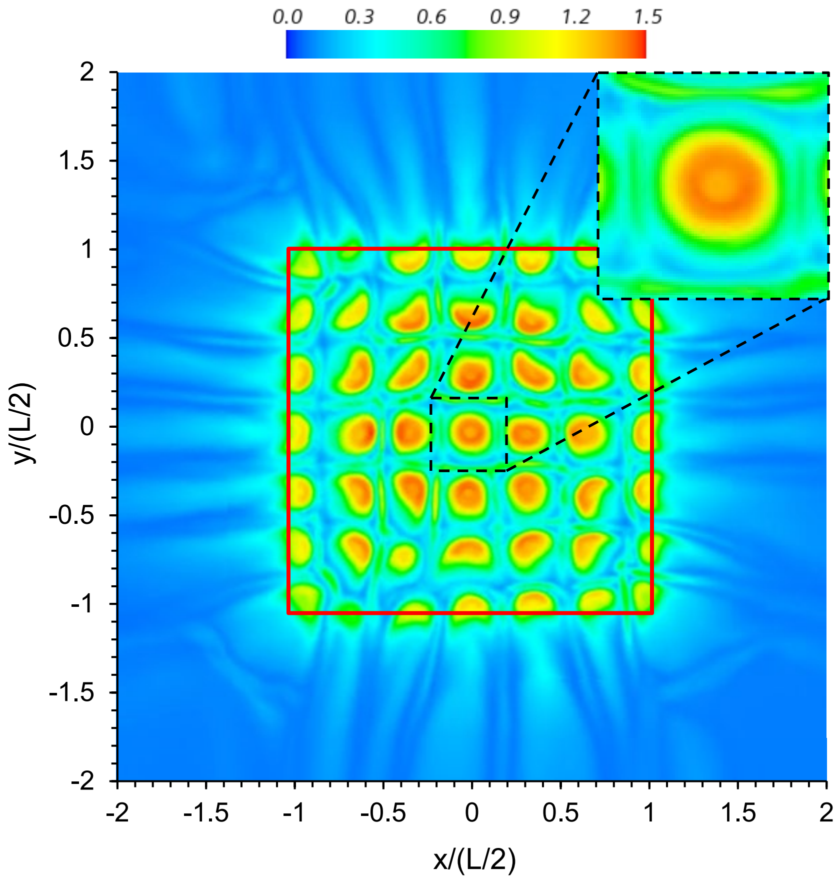

Figure 3.9: Baseline ratio of surface heat flux to applied heat flux (111.1 W/cm^2) contour with heat source footprint highlighted.

3.4.2. Optimisation Pareto Plot

The CFD-based optimisation workflow produces a set of feasible solutions which are compiled into a series of Pareto Plots in Figure 3.10 representing the individual heat source concentrations investigated. Here, the Pareto Plot axes are the two objective functions (T_j and P_p) and the data points represent the feasible solutions that implemented a specific set of geometric design variables within the ranges defined in Table 3.6, remembering that the pressure drop and resulting flow rate are determined by the operating point on the imposed pump curve. The adaptive nature of the HEEDS algorithm is clear from the data points tending to merge towards the Pareto Front, which is the curve that separates the feasible and non-feasible solution spaces. Marked on the Pareto Front are the optimum solutions associated with minimising the junction temperature (Single-Objective Optimisation, SOO) and minimising both the junction temperature and pumping power (Multi-Objective

Optimisation, MOO). The MOO optima are found via the data points located closest to the ideal point at T_j = 35°C and P_p = 0 W. Min(x) illustrates the data point at minimum displacement from this point. For reference, the baseline solution is also indicated in Figure 3.10.

All data points situated near the Pareto Front successfully achieved residual convergence within the specified maximum iteration limit. Conversely, certain geometrically extreme designs, characterised by significant pressure drops that impeded the rate of convergence, did not fully converge before reaching the iteration cap. However, these cases were located far from the Pareto Front and were consequently excluded from further analysis. For the optimal configurations evaluated in this study, including the baseline and both optimisation scenarios, all simulations reached full convergence, ensuring the reliability of the results used in the analysis.

Looking more closely at the SOO and MOO optimums, it is evident that some clustering of data points was determined. This indicates that more than one orifice design existed that achieves very similar heat transfer and hydraulic performance. Some similarities and differences in these designs will be discussed in the ensuing discussion, since it is relevant to understanding the overall impact of the geometric design parameters and combinations thereof. Observing the overall global trends across all three heat source concentrations, it is evident from the Pareto Plots that the junction temperature generally increased with increased heat source concentration. This is expected since the associated source heat flux increased with the power being 250 W for each case. Furthermore, the junction temperature range of the feasible solutions decreases with decreasing heat source concentration, highlighting the influence of conjugate heat transfer within the IHS. Conversely, the range of pumping power was not sensitive to source concentration, since these are associated with the operating points on the pump curve, and the same pump was used for each heat source.

Although not included in this study for the reasons previously outlined, incorporating additional geometric modifications into the optimisation process would likely yield diminishing returns. For instance, contoured nozzle inlets, while effective in reducing hydraulic penalties, particularly pressure drop at the nozzle entrance, would also decrease turbulence generation within the nozzle. This reduction in turbulence would adversely affect the development of the jet shear layer, a critical factor in enhancing heat transfer at the impinging surface. Consequently, although the reduction in pressure drop might produce a higher velocity jet, the diminished post-nozzle turbulent mixing would likely result in a noticeable decline in overall heat transfer performance.

A similar trade-off would apply to other geometric adjustments, such as incorporating flow conditioners at the manifold inlet, altering the nozzle angle, or using alternative nozzle shapes. Each of these modifications might improve hydraulic performance by reducing pressure drop but would simultaneously hinder the formation of turbulent eddies and vortices that are essential for effective flow mixing and, by extension, heat transfer enhancement. While these parameters could offer valuable insights in a broader optimisation analysis for impinging jet cold plate heat exchangers, their inclusion is not critical to achieving the primary objective of this study: developing an automated, simulation-driven optimisation workflow. To ensure the validity and feasibility of the optimisation tool within the scope of this work, these parameters were deliberately excluded, thereby simplifying the design problem. However, provisions were made during the development process to accommodate the integration of such parameters in future studies, depending on specific user requirements.

Moreover, as the optimisation workflow simplifies the thermal stack by removing the TTV neck, thus enabling direct contact between the heat source and heat spreader, experimental validation of the optima generated was not pursued, as the absence of the TTV's heated meter bar neck poses significant challenges in accurately extracting junction temperature data. It is anticipated that future applications of this optimisation methodology to commercial CPU architectures will provide more appropriate opportunities for experimental validation. These real-world scenarios are expected to offer a better alignment between the simulation-based optimisation process and practical testing conditions, thereby facilitating comprehensive verification of the developed design tool.

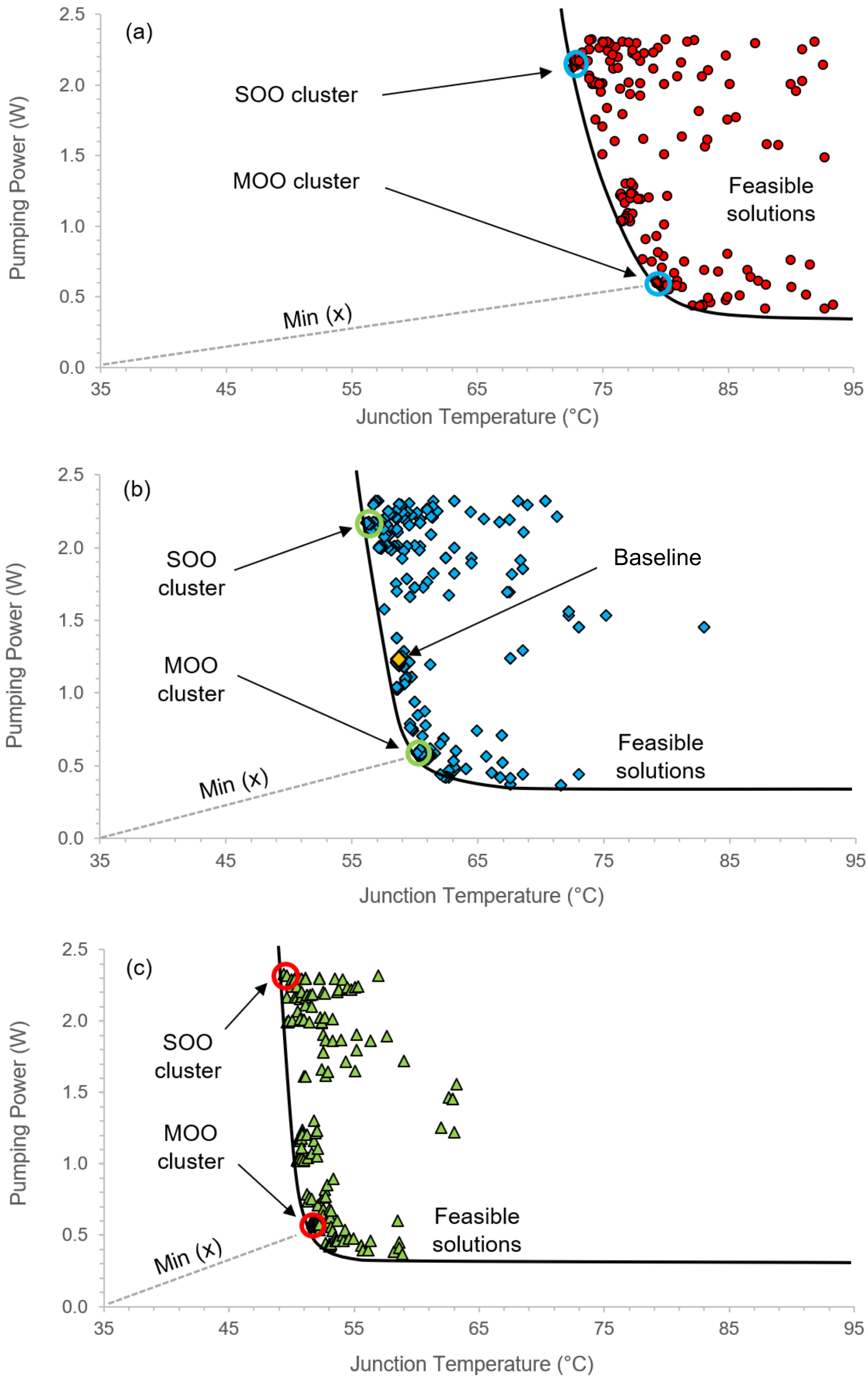

Figure 3.10: HEEDS optimisation Pareto plot of all design points for (a) 10 x 10 mm^2, (b) 15 x 15 mm^2 and (c) 20 x 20 mm^2 heat sources.

3.4.3. Multi-Objective Optima

The true optimum and those very close in overall performance are included in Table 3.8 for the MOO design cluster. For this optimisation scenario the variation between orifice configurations is small. The three representative cases shown have the same jet diameter and population, with only small differences in S/D and H/D differentiating them. Since there is low deviation of design options that minimise both the junction temperature and pumping power, only the true optimum will be discussed here.

Compared with the baseline, the general features of the MOO design are that the jet population is the same (N = 49) and the jet diameters are larger (D = 1.5 mm). Similar relative inter-jet spacing (S/D) is retained, though the larger diameter increases the overall area of the jet array compared with the baseline, causing them to extend well beyond the footprint of the heat source. Defining the Area Ratio, A_r, as the ratio of the jet array area to the heat source area (see Figure 3.7),

$$A_r = \frac{A_{jet}}{A_{hs}} = \frac{\left(D(\sqrt{N}) + \left((\sqrt{N}-1)(S-D)\right)\right)^2}{A_{hs}} \tag{3.15}$$

$A_r \sim 2$ for the MOO array compared with $A_r \sim 1$ for the baseline, such that the jets now tend to populate most of the available area of the orifice plate.

In terms of the hydraulics, compared with the baseline the larger jet diameters offer lower hydraulic resistance such that the operating point on the pump curve is shifted to a lower pressure drop and thus higher net volumetric flow rate, from 4.8 kPa to 7.4 L/min. Hence, the MOO optimum design reduces the hydraulic power penalty primarily by using larger diameter jets to decrease jet velocity and associated pressure drop, despite a moderate increase in the flow rate. Compared to the baseline, Figure 3.11 shows that the general flow and heat transfer features are similar, with some visible differences. Comparing Figures 3.9 and 3.12, it is clear that the overall convective intensity is diminished, and this is unsurprising considering that the jet velocity has nearly halved.

Table 3.8: MOO optimum orifice design and results

Parameter	Value	Orifice CAD
S/D	2.17	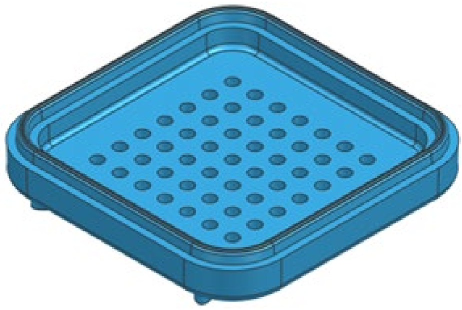
H/D	1.83	
N	49	
D (mm)	1.50	
V_{jet} (m/s)	1.42	
Re_{jet}	2,938	
A_r	1.96	
T_j (°C)	60.15	
ΔP (Pa)	4,774	
$\dot{V}$ (L/min)	7.37	
P_p (W)	0.59	
U (W/m^{2}K)	44,173	

	MOO Design II	MOO Design III
	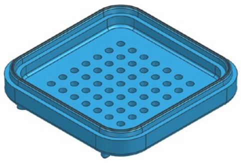	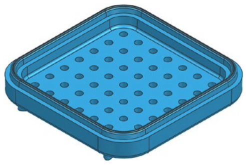
S/D	2.17	2.50
H/D	0.83	1.83
N	49	49
D (mm)	1.50	1.50

However, the jet impingement zone is larger owing to the increased jet diameter. Furthermore, since the active jet area overhangs the projected area of the heat source, the MOO design maintains high convective intensity over a larger overall area of the heat spreader. Thus, despite the lower jet velocities, the MOO design sustains a high overall heat transfer coefficient of U = 44,173 W/m^{2}K by utilising more effective surface area of the IHS to moderate the general decrease in convective heat transfer intensity. This is notwithstanding the fact that the Venturi-type effect discussed earlier is more pronounced for the larger diameter jets, and over a higher proportion of the jets. The effective surface area of the IHS can be defined as the surface area occupied by high convective intensity on account of the jet configuration. On the whole, compared with the baseline the overall heat transfer coefficient decreases by only about 7% (~1.5 K increase in T_j) with a disproportionately large drop in hydraulic pumping power of ~50%.

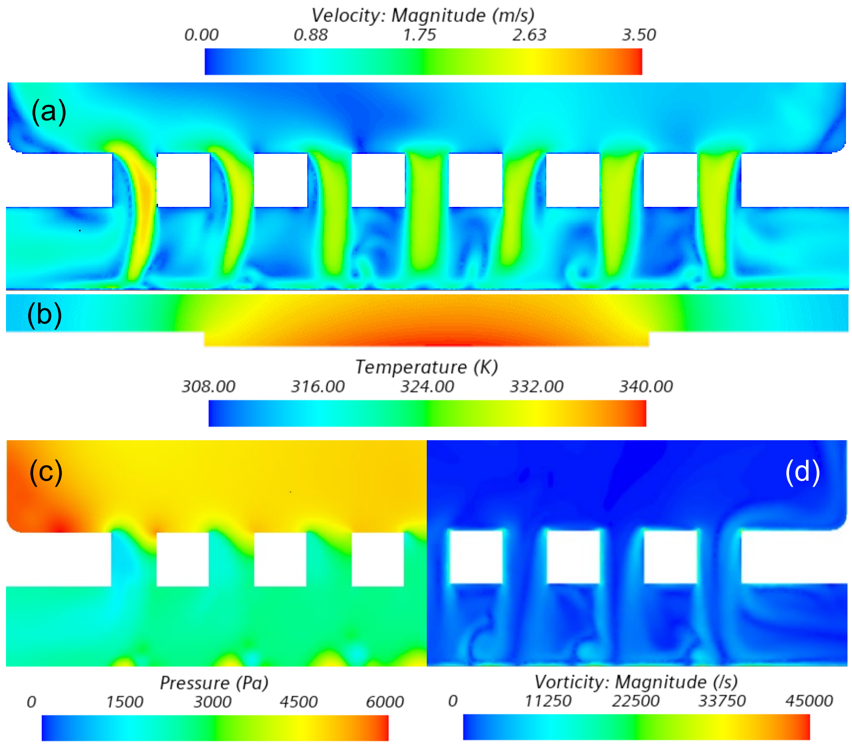

Figure 3.11: Sectioned MOO model plots of (a) velocity, (b) temperature, (d) pressure, and (c) vorticity.

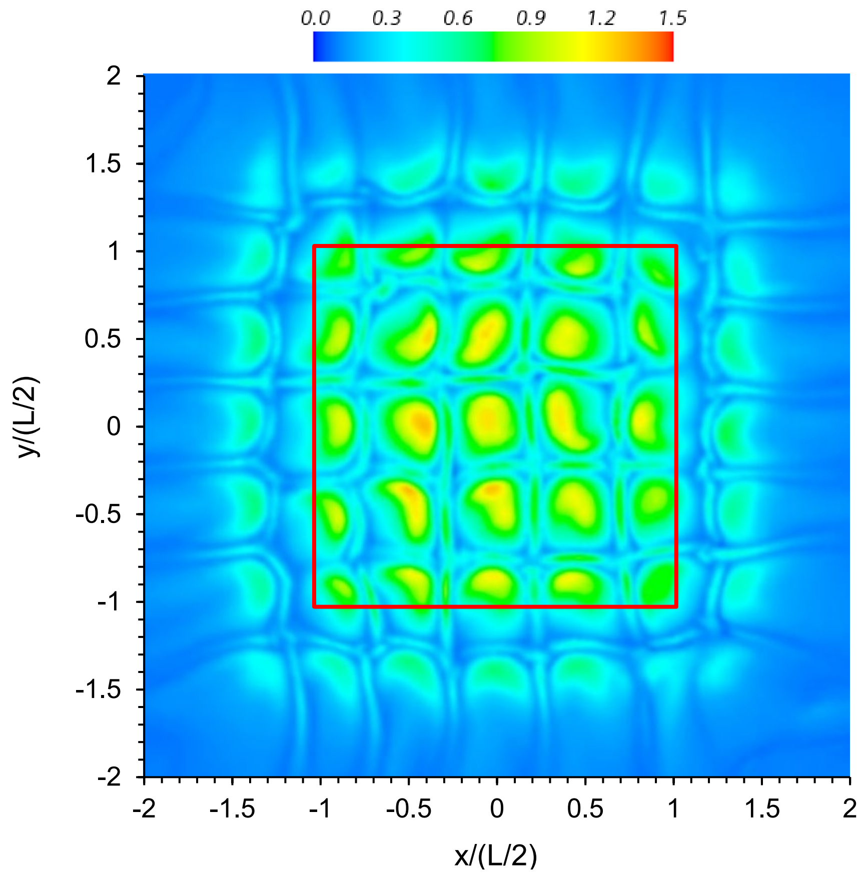

Figure 3.12: MOO ratio of surface heat flux to applied heat flux (111.1 W/cm^2) contour with heat source footprint highlighted.

3.4.4. Single Objective Optima

Unlike the MOO optimised jet orifices, Table 3.9 shows that quite different orifice designs can result in similar minimisation of the junction temperature for the SOO study. The consistent features of the three different designs shown are the sub-unity Area Ratio (i.e. the jet array area is contained within the projected heater area) and the jets are comparatively high velocity (4.12 m/s - 5.17 m/s) relative to the baseline (2.89 m/s) and MOO optimum (1.42 m/s) designs. Design I is the true optimum and achieves a 2.5 K reduction in junction temperature below the baseline design, and 4 K below the MOO optimal design. Here, the low population of N = 9 large diameter (D = 1.5 mm) jets shifts the operating point on the pump curve to a location of much higher pressure drop (~26 kPa, Figure 3.13) with a less severe reduction in the volumetric flow rate (~5 L/min). The resulting pumping power is 3.7 times higher than the MOO optimal design and almost 2 times higher than the baseline.

Table 3.9: SOO optimum orifice cluster designs and results

Parameter	I	II	III
Orifice layout	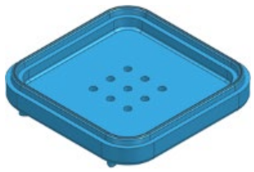	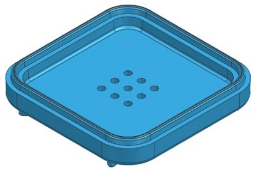	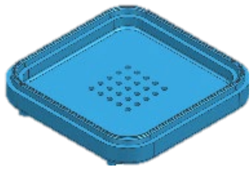
S/D	2.83	2.17	2.25
H/D	1.17	0.17	0.25
N	9	9	25
D (mm)	1.50	1.50	1
V_{jet} (m/s)	5.17	4.12	3.11
Re_{jet}	10,712	8,541	4,276
A_r	0.44	0.28	0.44
T_j (°C)	56.16	56.90	56.75
ΔP (Pa)	26,385	35,019	36,913
$\dot{V}$ (L/min)	4.93	3.87	3.59
P_p (W)	2.17	2.23	2.21
U (W/m²K)	52,510	50,737	51,090

As Figure 3.13 shows, the higher jet velocity of the SOO optimal design (due to the reduced jet population for a still reasonably high volumetric flow rate) produces straight and symmetrical jets across the whole array i.e. the outer jets are largely unaffected by the cross-flow in the channel nor the non-fully stagnant flow in the upper chamber. This is ideal for sustaining high convective heat transfer intensity in the impingement and wall jet regions across the whole jet array area, as shown in Figure 3.14. Furthermore, compared with the baseline, the larger jet diameters with moderate S/D ~ 2.8 has the same benefit discussed for the MOO optimum design, in that it sustains high convective intensity over the large inter-jet area. It is also noticed in Figure 3.13 that the higher velocity creates higher vorticity in the shear layer within the nozzle, with commensurate higher vorticity flow impinging on the developing wall jet. This likely influences the convective heat transfer intensity positively, though is difficult to quantify.

Overarchingly, for the SOO design the jet array area is much smaller than the heat source area, concentrating the jets within an Area Ratio of only $A_r = 0.44$. In contrast to the MOO design, with $A_r = 1.96$, this illustrates that in terms of overall source-to-sink thermal resistance for this conjugate heat transfer scenario, there is a trade-off between convective intensity and effective surface area. This is critical, considering that the SOO overall heat transfer coefficient is only 16% higher than that of the MOO design, though with almost 4-fold increase in pumping power.

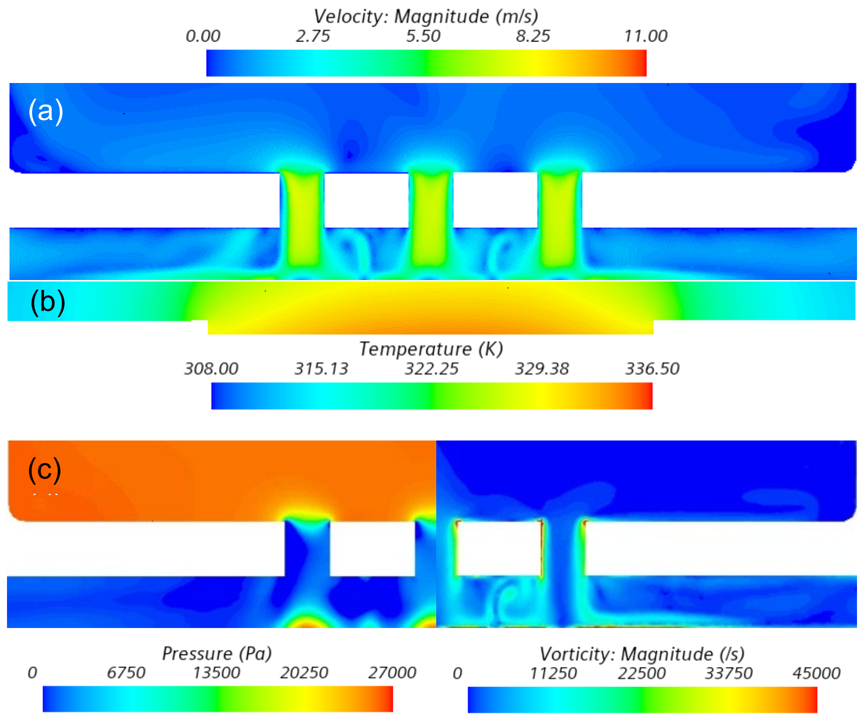

Figure 3.13: Sectioned SOO Design I plots of (a) velocity, (b) solid temperature, (p) pressure, and (c) vorticity.

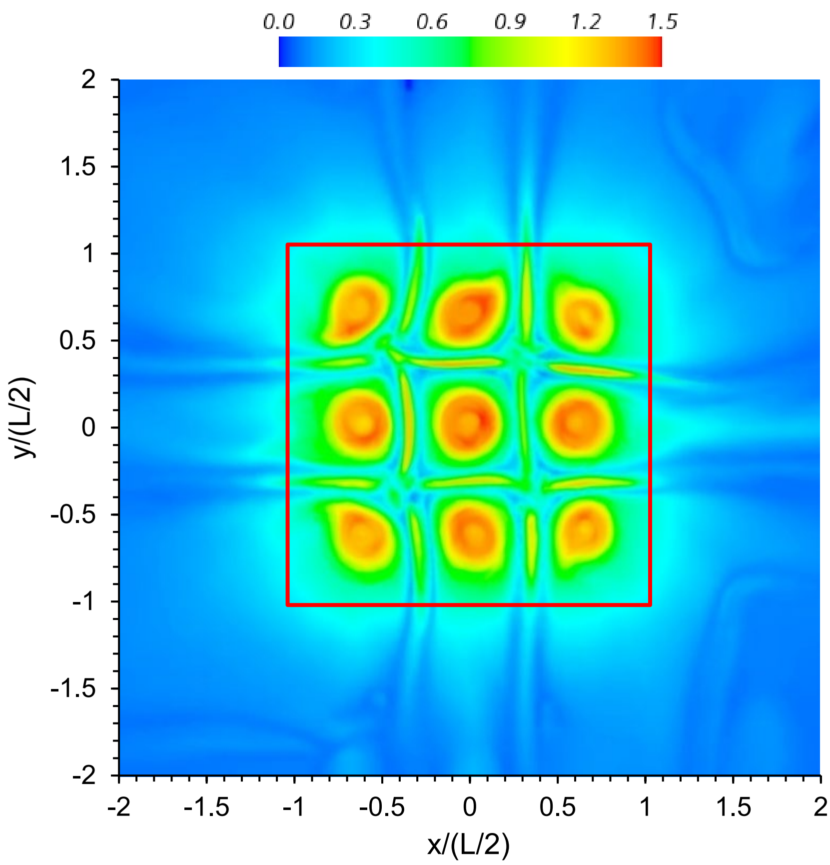

Figure 3.14: SOO Design I ratio of surface heat flux to applied heat flux (111.1 W/cm^2) contour with heat source footprint highlighted.

The Design II orifice plate and associated data is listed in Table 3.9 and is interesting because it produces very similar thermal-hydraulic behaviour to Design I (only 0.15 W increase in P_p and 0.7 K increase in T_j), but for different reasons. The key differences are that this design implements a very low jet-to-target spacing of H/D = 0.17 combined with a more compact jet array, with A_r = 0.28. As shown in Figure 3.15, the low H/D changes the hydraulics considerably compared with the cases discussed thus far. In particular, the central jet is of lower velocity compared to the outer ones due to the lateral pressure gradient in the lower channel. Furthermore, the low channel height sustains high velocity in the downstream region beyond the jet array in the thin gap region. Overall, the thin lower channel creates flow resistance which increases the overall pressure drop to over 35 kPa. With regard to the influence on the heat transfer, as indicated in Figure 3.16, the key difference in the convective cooling profile is mainly associated with a higher convective heat transfer intensity of the outer jets, along with the sustained intensity within the thin lower channel once outside the perimeter of the jet array. As Figure 3.15 clearly shows, these regions of increased cooling intensity are those associated with high vorticity, which is indicative of intense fluid mixing.

Design III possesses similar geometric traits to Design II, with a low H/D = 0.25 which again results in the highest convective heat transfer intensity occurring in the outer jets and as well as sustained intensity in the thin exit channel. The key difference is the higher jet population of N = 25, an increase of over 150 % compared to the other two designs. In order to maintain a comparable level of convective cooling intensity for an area ratio similar to Design I (A_r = 0.44), the jet diameter is decreased (D = 1.0 mm) to maintain a relatively high jet exit velocity (3.1 m/s) and, like Designs I and II, tend to be relatively straight over the entire population (Figure 3.17). With the similar S/D = 2.25 and higher jet population, Figure 3.18 shows that this design generates high convective intensity over the approximate region of the heat source, consistent with the previous two designs, despite a noticeable reduction in the jet Reynold's number attributed to the higher jet population (see Table 3.9).

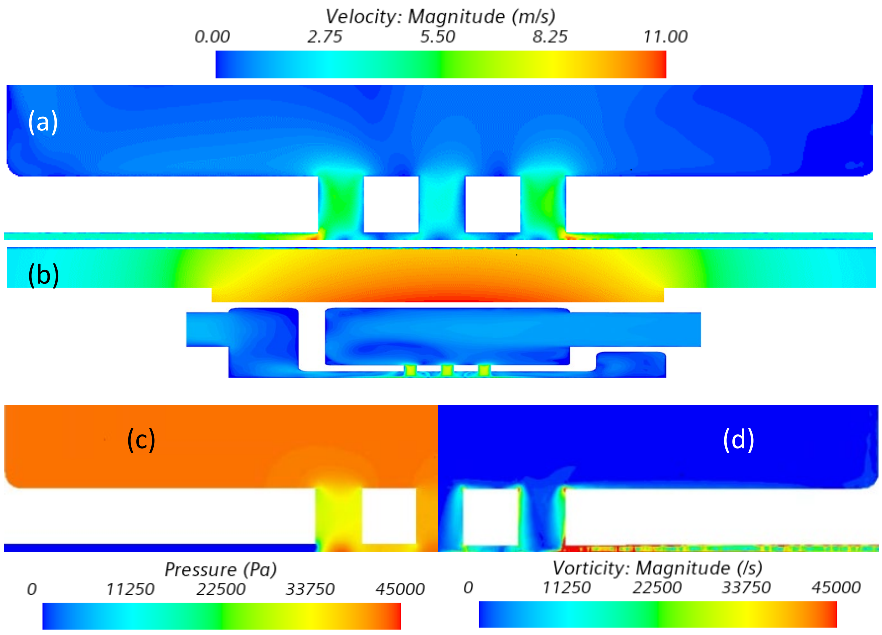

Figure 3.15: Sectioned SOO Design II plots of (a) velocity, (b) solid temperature, (c) pressure, and (c) vorticity.

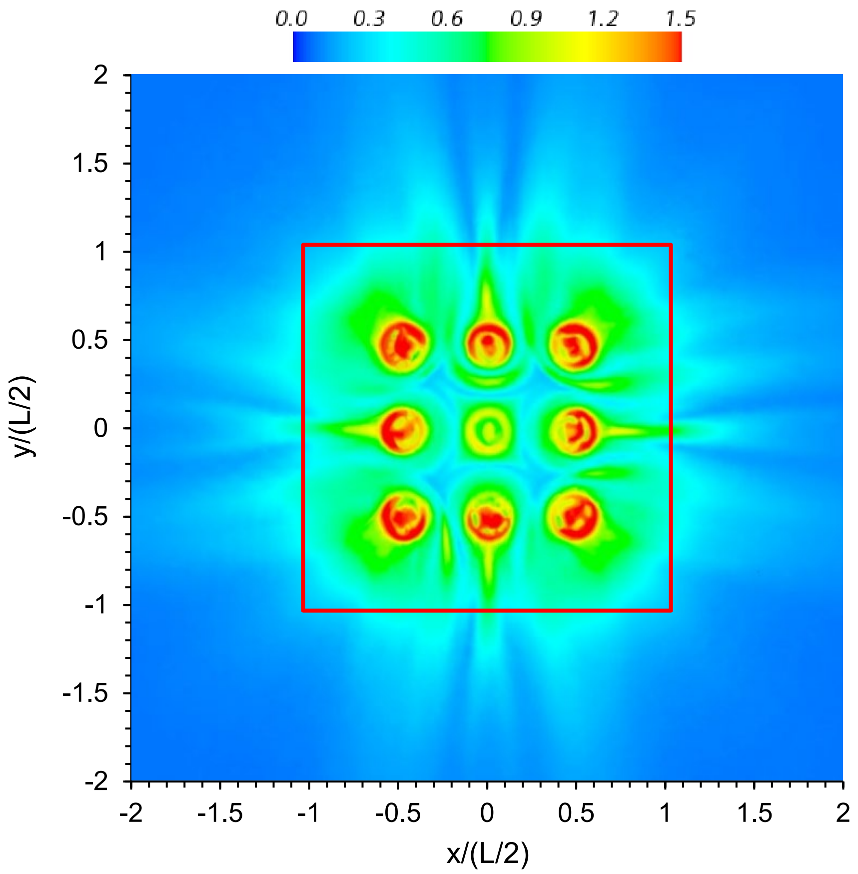

Figure 3.16: SOO Design II ratio of surface heat flux to applied heat flux (111.1 W/cm^2) contour with heat source footprint highlighted.

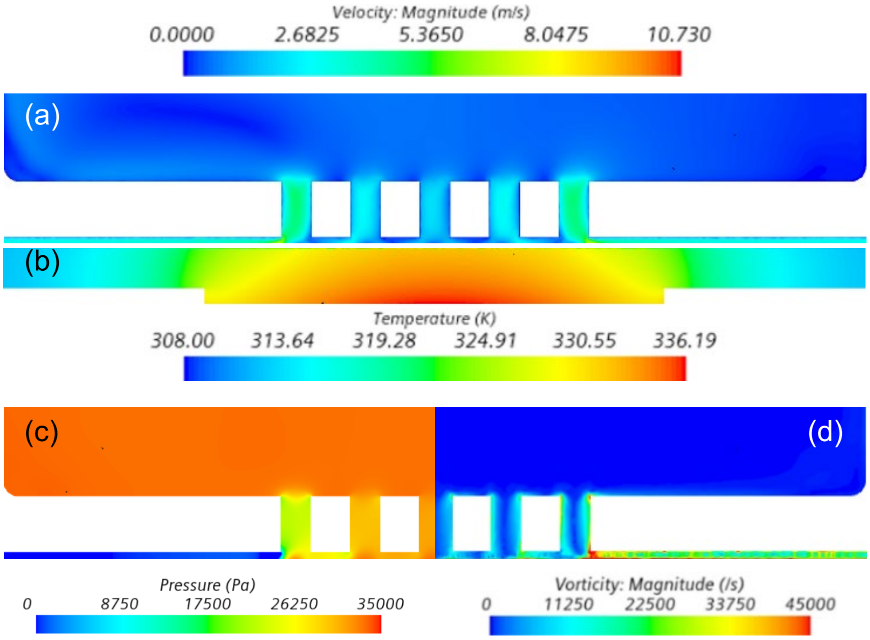

Figure 3.17: Sectioned SOO Design III plots of (a) velocity, (b) solid temperature, (c) pressure, and (c) vorticity.

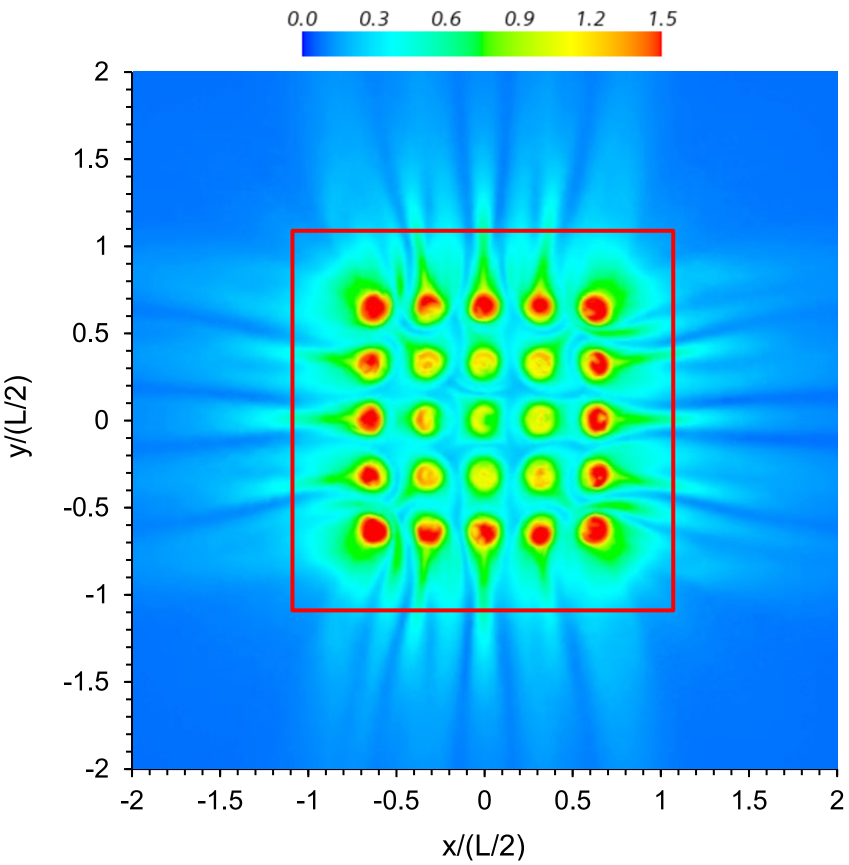

Figure 3.18: SOO design III ratio of surface heat flux to applied heat flux (111.1 W/cm^2) contour with heat source footprint highlighted.

Overall, the SOO study has revealed some key differences with respect to the jet impingement heat exchanger design for maximising cooling of a concentrated heat source with an Integrated Head Spreader, compared with the MOO design which simultaneously maximised cooling and minimised the energy consumption. In particular, the jets are more concentrated and within the projected heater area, are high velocity, and do not impinge obliquely in comparison. Despite producing lower net volumetric flow rates, the trade-off for the better cooling performance is that the higher velocities incur higher pressure drop, to the extent that the pumping power penalty is about four times larger.

3.4.5. Influence of Heat Source Concentrations

Figure 3.19 plots the optimised thermal-hydraulic results for both the SOO and MOO designs across all three heat source concentrations. For both scenarios, the influence of the heat source size is clear from the increase in T_j owing to the rise in the source heat flux, shown in Figure 3.20. However, the rise in T_j is not in-step with the escalation in heat flux, which increases 3-fold between the lowest and highest source concentration. As shown in Figure 3.19, this is due to an improvement in the overall heat transfer coefficient, U, as the heat source size decreases, which will be discussed in more detail below. In terms of the hydraulic power penalty, there is a very low sensitivity to heat source concentration.

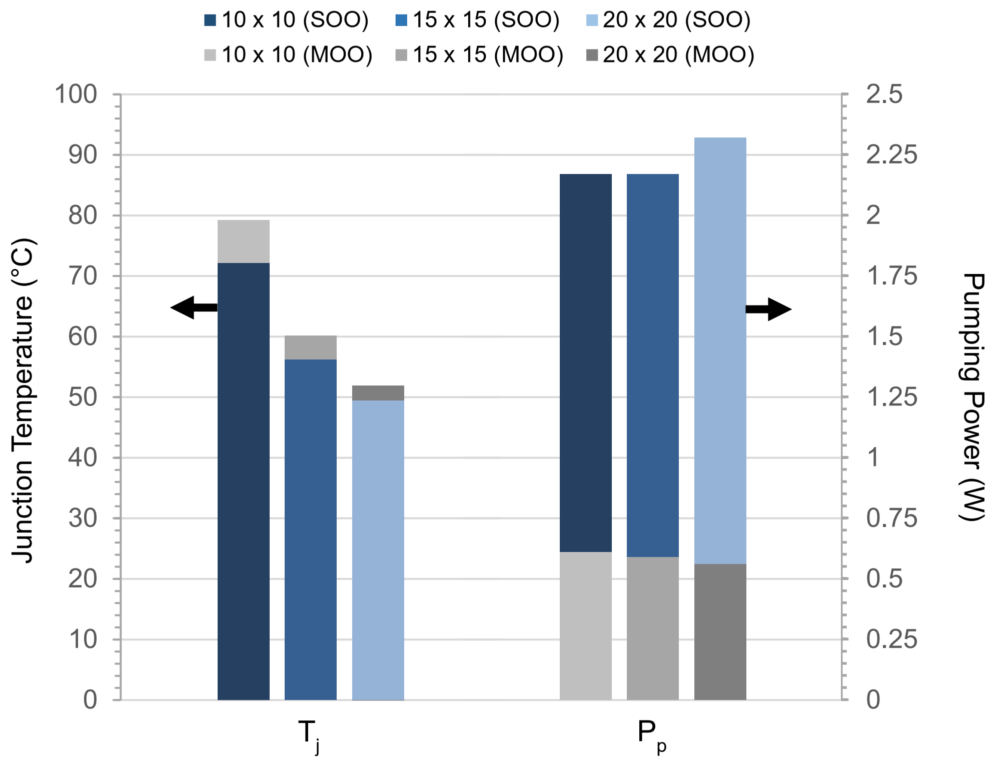

Figure 3.19: Comparison between MOO and SOO results for optimisation objective functions across span of heat source concentrations.

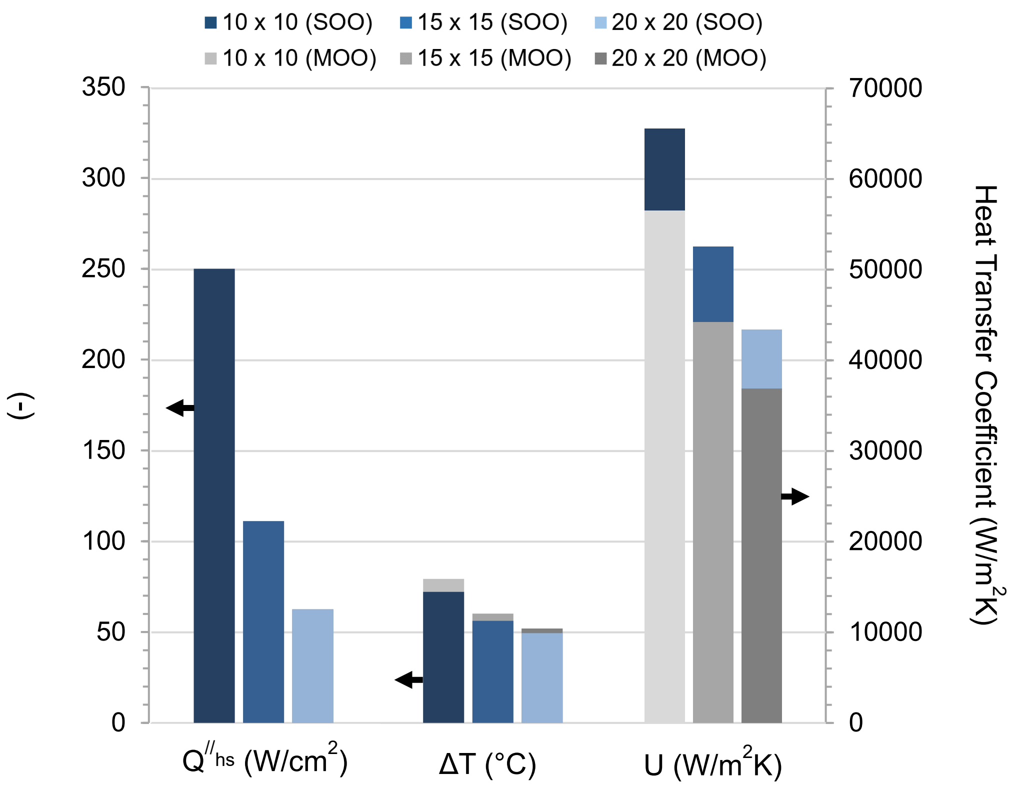

Figure 3.20: Comparison between MOO and SOO thermal performance results across span of heat source concentrations.

3.4.5.1. SOO Design Comparison

The pertinent design and thermal hydraulic performance data for all three heat source concentrations for the SOO study are listed in Table 3.10, with the geometric design features plotted in Figure 3.21. Since the A_{hs} = 15 x 15 mm^2 case has been detailed above, comparisons here will be made with respect to this mid-source case. Referring to Figure 3.21, the A_{hs} = 10 x 10 mm^2 case retains the same jet diameter, jet population, jet-to-target spacing as the mid-source case. Unsurprisingly, the hydraulics of this design (flow rate, jet velocity, Reynolds number, pressure drop and pumping power) are about the same as the mid-source case. However, as noted above, the overall heat transfer coefficient, U, has increased. This tends to moderate the escalation in T_j with increased source heat flux. Defining the source-to-sink thermal resistance as,

$$R = (UA_{hs})^{-1} \tag{3.16}$$

it only increases by 80% for a 125% increase in Q''_{hs}. The smaller increase in thermal resistance relative to the applied heat flux is due to the closer inter-jet spacing, S/D, the only notably different design parameter compared with the mid-source case (Figure 3.21). This is highlighted in the heat flux ratio plot in Figure 3.22 which shows that, consistent with the earlier discussion, the SOO optimised jet array focusses the high convective intensity over the projected heat source area. However, for the smaller heat source, the jet array can be more tightly packed in this area resulting in a higher proportion of the area being exposed to high intensity convective cooling. This is further evidence to support the earlier observation that, when maximising cooling performance, the best design focusses the jets over the heat source, despite the IHS being in place to support heat spreading. To achieve this, an Area Ratio, which is a function of D, N and S/D (see Eq. 3.15), should maximise the convective intensity within the footprint of the heat source.

Table 3.10: SOO optima for different heat source concentrations

Parameter	**10 x 10 mm^2**	**15 x 15 mm^2**	**20 x 20 mm^2**
Orifice layout	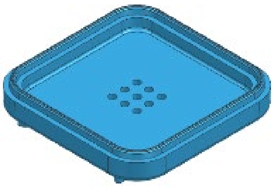	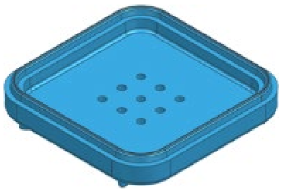	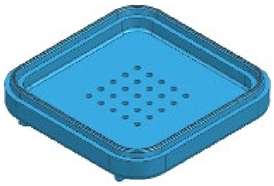
Q''_{hs} (W/cm^2)	250.0	111.1	62.5
S/D	1.83	2.83	2.75
H/D	1.17	1.17	1.25
N	9	9	25
D (mm)	1.50	1.50	1.00
V_{jet} (m/s)	5.16	5.17	3.33
Re_{jet}	10,688	10,712	4,600
A_r	0.49	0.44	0.36
T_j (°C)	72.13	56.16	49.40
ΔP (Pa)	26450	26385	35531
$\dot{V}$ (L/min)	4.92	4.93	3.92
P_p (W)	2.17	2.17	2.32
U (W/m^{2}K)	65,559	52,510	43,415
R (K/W)	0.15	0.08	0.06
h_{pred} (W/m^{2}K)	61,986	51,175	52,671

To support this claim, the predicted average heat transfer coefficient, h_{pred}, was calculated using the Nusselt Number correlation detailed by Robinson and Schnitzler [26] for confined jet arrays,

$$Nu_{jet} = \frac{h_{pred} D}{k_f} = 1.485 Re^{0.46} \left(\frac{S}{D}\right)^{-0.442} \left(\frac{H}{D}\right)^{-0.00716} Pr^{0.4} \tag{3.17}$$

and are included in Table 3.10. For the more concentrated 10 x 10 mm^2 and 15 x 15 mm^2 cases, U and h_{pred} are in very close agreement indicating targeted cooling of the source region, with S/D being the term which accounts for the difference observed between the two.

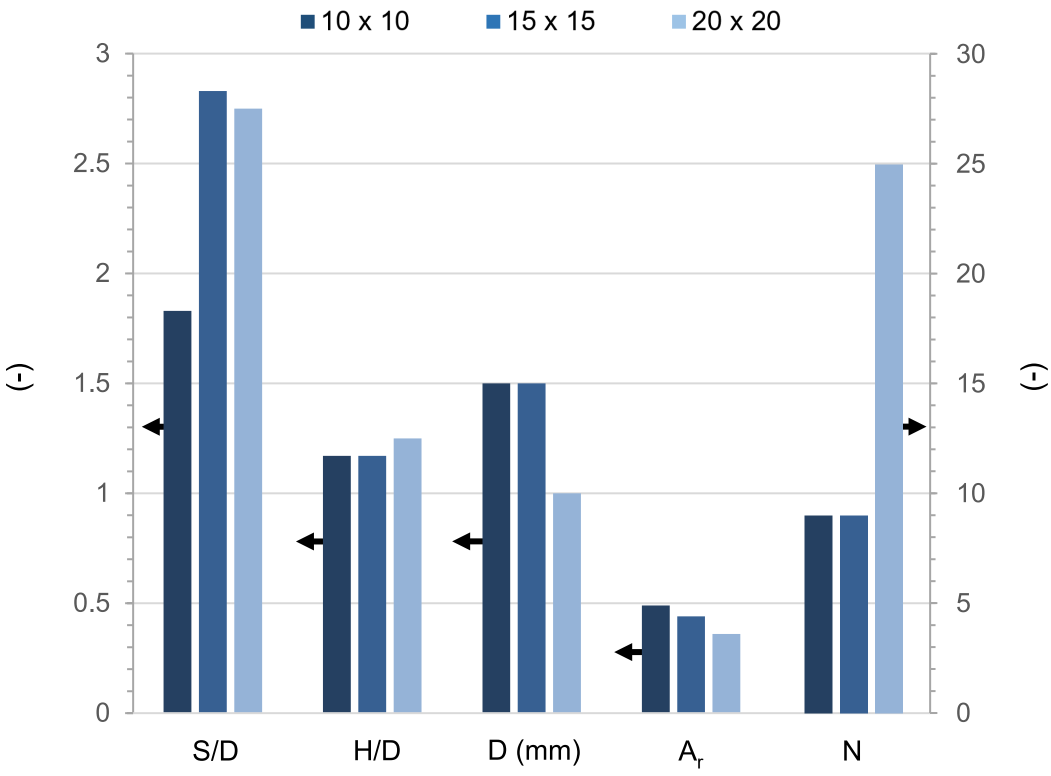

Figure 3.21: Comparison of optimum geometry parameters for SOO orifice designs for different heat source sizes.

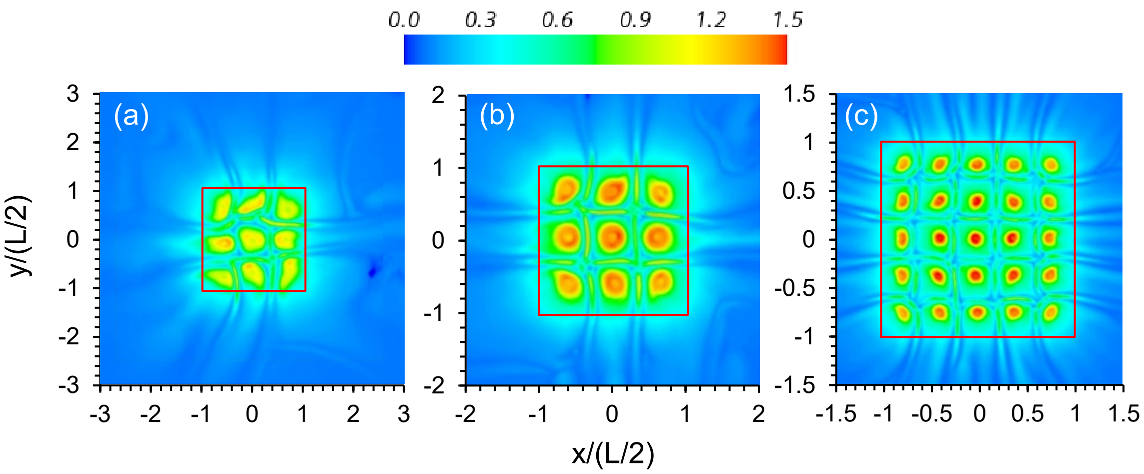

Figure 3.22: SOO surface heat flux ratio plots for (a) A_{hs} = 10 x 10 mm^2, (Q''_{hs} = 250 W/cm^2), (b) A_{hs} = 15 x 15 mm^2, (Q''_{hs} = 111 W/cm^2), and (c) A_{hs} = 20 x 20 mm^2, (Q''_{hs} = 62.5 W/cm^2).

For the heat source size of A_{hs} = 20 x 20 mm^2, Figures 3.21 and 3.22 show an increase in the jet population is required to accommodate targeted cooling of the larger source, whilst still maintaining low S/D < 3 to sustain high convective intensity in the inter-jet regions. However, there are clear trade-offs in this optimised design compared with the other two more concentrated cases discussed. The necessary increase in the jet population escalates the overall open flow area across the orifice plate, which has the effect of reducing the jet velocity and associated jet Reynolds number (Table 3.10). This is of course detrimental to the cooling intensity as per Eq. (3.16). To oppose this, the design incorporates a lower jet diameter, at D = 1.0 mm, to (i) sustain relatively high jet velocity and Reynolds number for larger N, and (ii) to sustain a high average convective heat transfer coefficient, since $h = Nu_{jet}(k_f/D)$ i.e. the average convective heat transfer coefficient is inversely proportional to the jet diameter. The overall effect is that compared to the mid-source case, the increased size of the heat source results in a decrease in heat flux of 44%, with the thermal resistance, R, decreasing by a commensurate yet lower 32% (Table 3.10) due to a net reduction in U (Figure 3.20). It is also worth noting that, unlike the other two cases where the tightly packed larger diameter jets generated high convective intensity near to the edge of the heat source border, Figure 3.21 indicates that for this case the trade-off between D, N and S/D is such that a lower Area Ratio of $A_r = 0.36$ results. As depicted in Figure 3.22, the lower D and A_r results in the high convective intensity zones of the outer most jets being further in from the heat source border. This accounts for the lower value of U compared with h_{pred} in Table 3.10 and illustrates that, despite the lower cooling demand due to the lower heat flux of the larger heat source, it remains a complex optimisation problem that requires a design approach similar to that taken here.

Referring to Table 3.10, the smaller jet diameter of this design also results in a 35% increased pressure drop across the orifice, despite the lower jet velocity attributed to the increased jet population. This causes the operating point on the pump curve to shift to a lower volumetric flow rate, which is 20% lower. These partially offset each other to the degree that the overall hydraulic pumping power only increases by 7%. The key conclusions regarding varying levels of heat source concentration on the thermal-hydraulic performance of the SOO designs are that they consistently target the convective cooling area bordered by the heat source, with heat spreading in the IHS playing a secondary, if not minor role in the heat transfer. It is necessary to have a low enough jet-to-target spacing (H/D ~ 1.2) to avoid jet spreading and deflection, and the inter-jet spacing be kept low (S/D < 3) to sustain high convective intensity within this target region. Sub-unity $A_r < 0.5$ ensures that the high intensity convective heat transfer is approximately contained within the marked border of the heat source for each case. Overall, the increase in the junction temperature does not increase linearly with the heat flux since reducing the target area supports higher average heat transfer coefficients within the targeted zone of the heat source. In terms of the pumping power, there is no important influence of heat source concentration, though it is noted that they are all near the maximum hydraulic power of $P_{p,max}$ = 2.34 W for the chosen pump.

3.4.5.2. MOO Design Comparison

In contrast to the SOO optimum designs, which tend to leverage the maximum hydraulic power of the pump, Figure 3.19 shows that the MOO designs operate at significantly lowered pumping power. These designs operate at approximately 3.6 to 4-fold reduced pumping power, though the increase in T_j is not nearly as severe. The pertinent design and thermal hydraulic performance data for all three heat source concentrations for the MOO portion of this study are listed in Table 3.11, with the geometric design features plotted in Figure 3.23. Comparing against the SOO design parameters in Figure 3.21, the most notable difference is the increase in the jet population, N, for each heater size, noting that S/D < 3 is still maintained to promote high cooling intensity between neighbouring jets. Consistent with what was discussed earlier, higher jet population has the end effect of reducing the volumetric flow rate and results in a significant reduction in the overall pressure drop, and this is the main contributor to the pumping power reduction for each MOO design. This has a detrimental effect on the Reynolds number, which is between 2.6 and 3.6 times lower than the respective SOO design.

Table 3.11: MOO optima for different heat source concentrations

Parameter	10 x 10 mm^2	15 x 15 mm^2	20 x 20 mm^2
Orifice layout	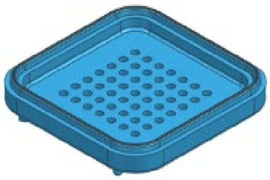	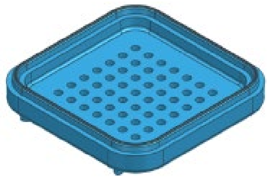	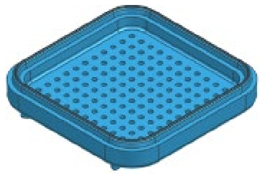
Q''_{hs} (W/cm^2)	250.0	111.1	62.5
S/D	1.83	2.17	2.25
H/D	1.17	1.83	1.75
N	49	49	121
D (mm)	1.50	1.50	1.00
V_{jet} (m/s)	1.41	1.42	1.30
Re_{jet}	2,929	2,938	1,790
A_r	3.24	1.96	1.38
T_j (°C)	79.26	60.15	51.95
ΔP (Pa)	4,974	4,773	4,536
$\dot{V}$ (L/min)	7.35	7.37	7.39
P_p (W)	0.61	0.59	0.56
U (W/m^{2}K)	56,480	44,179	36,863
R (K/W)	0.18	0.10	0.07
h_{pred} (W/m^{2}K)	34,174	31,637	37,200

In terms of the MOO designs and the overall influence of heat source concentration, a similar result to that of the SOO design is observed, though for a different reason. Compared with the mid-source case, the A_{hs} = 10 x 10 mm^2 case only experiences a 76% reduction in the source-to-sink thermal resistance, R, for a 125% increase in the source heat flux, again owing to the increase of the overall heat transfer coefficient, U, as shown in Figure 3.20. For this case, the increase in U is not due to an increase in the convective heat transfer coefficient, as it was for the SOO case, nor would this be expected since Re_{jet} is much lower; in fact h_{pred} is expectedly lower than U (Table 3.11). Here, the increase in U is mainly due to the higher Area Ratio ($A_r > 3$) which activates high convective heat flux over a larger area of the IHS, as seen in Figure 3.24. Similarly, for the largest A_{hs} = 20 x 20 mm^2 heater case, the reduced intensity of the convective heat transfer is countered by a greater active area for heat transfer on the convective side of the IHS. For the same reasons as with the SOO case discussed, a lower jet diameter is used for the much higher jet population whilst maintaining S/D < 3. Here however, the overhanging region is smaller in proportion to the heat source size, with A_r closer to unity and thus h_{pred} ~ U (Table 3.11). Resultingly, the 44% drop in heat flux only results in a 32% decrease in thermal resistance, R, the same as observed for the SOO case.

The key conclusions regarding varying levels of heat source concentration on the thermal-hydraulic performance of the MOO designs are that, compared with the SOO designs, they consistently implement higher jet populations to decrease the pressure drop and associated pumping power. Here, similarly low S/D < 3 is maintained such that the IHS plays a key role in sustaining a low thermal resistance despite the drop in flow velocity, Reynold's number and convective heat transfer intensity compared with the SOO designs. Comparatively, the thermal resistance is between 16% to 18% higher than the SOO designs, which results in moderate increase in T_j. However, this must be considered in the context that the hydraulic pumping power consumption reduction is in the region of 4-fold.

When considering the application of this design methodology to industrial contexts, the relative power consumed by cooling systems is minimal in smaller setups, such as PCs with single CPUs, where the cooling power constitutes a minor fraction of the CPU's input power. However, in large-scale industrial environments, such as data centres, even slight reductions in cooling power can significantly impact overall energy consumption. Therefore, the emphasis on minimising pumping power becomes contingent on the specific requirements of the application and user priorities. For users focused on energy efficiency, particularly in high power scenarios, optimising the energy distributed to the cooling system is paramount. This is demonstrated in the aforementioned fourfold difference in pumping power between SOO and MOO orifice configurations. When extended to industrial scale operations, such savings in pumping power translate into substantial reductions in energy use, underscoring the critical importance of this factor in the design of efficient larger scale cooling systems.

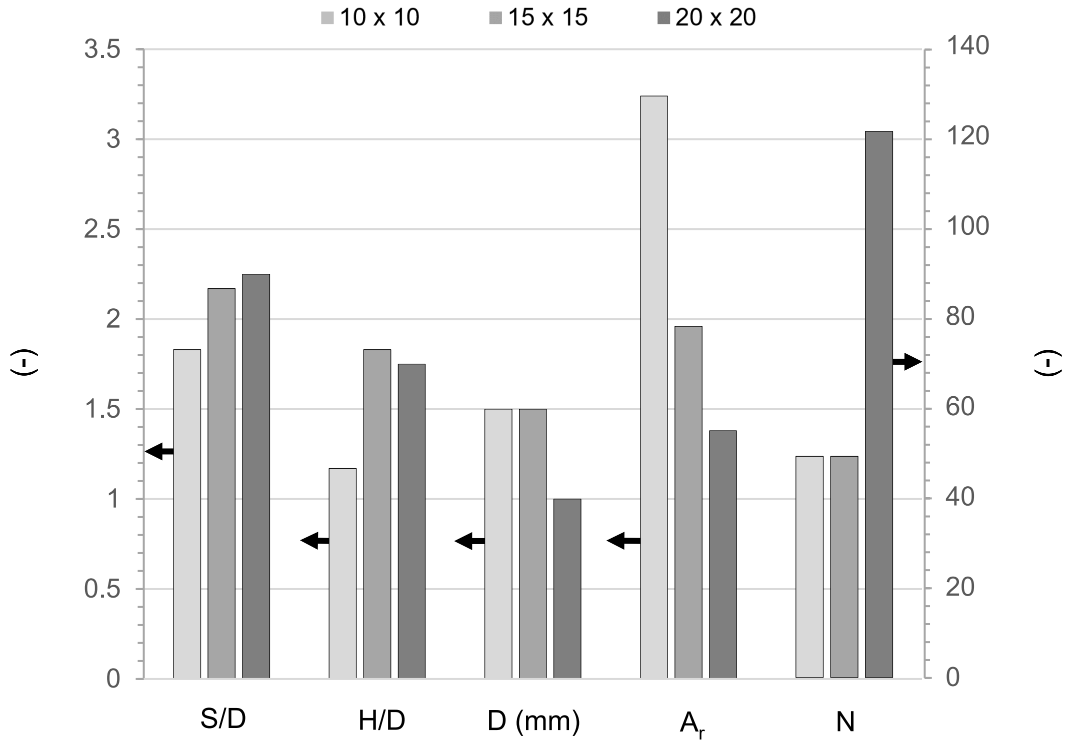

Figure 3.23: Comparison of optimum geometry parameters for MOO orifice designs for different heat source sizes.

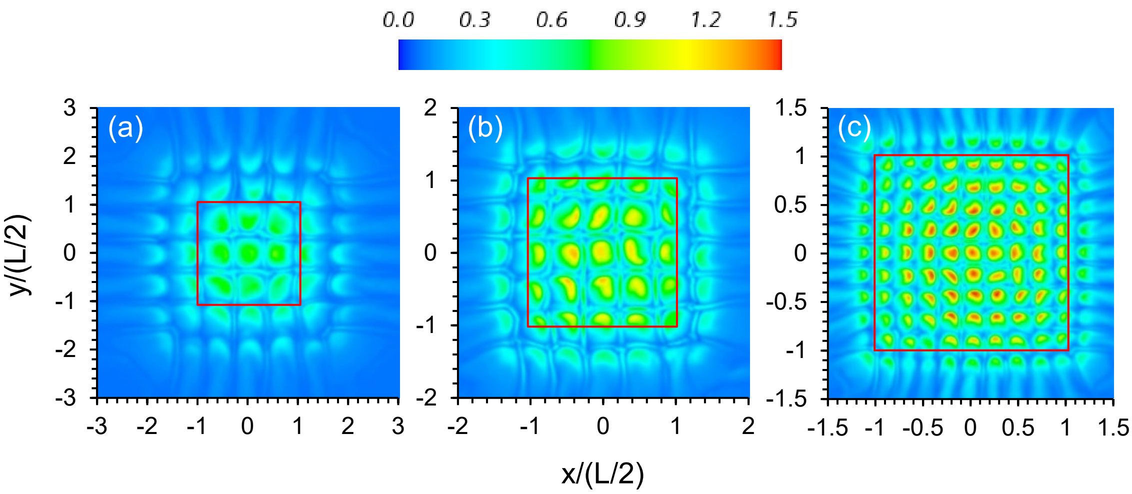

Figure 3.24: MOO surface heat flux ratio plots for (a) A_{hs} = 10 x 10 mm^2, (Q''_{hs} = 250 W/cm^2), (b) A_{hs} = 15 x 15 mm^2, (Q''_{hs} = 111 W/cm^2), and (c) A_{hs} = 20 x 20 mm^2, (Q''_{hs} = 62.5 W/cm^2).

3.5. Conclusions

This study investigates the influence of different geometric design parameters on the overall heat transfer and hydraulic performance of a liquid impinging jet array coldplate heat sink for centralised concentrated heat sources of different sizes, each with an Integrated Heat Spreader (IHS), mimicking a typical high-powered CPU package. A key aim of the study was to implement a simulation workflow by integrating multiple design software tools in such a way that heat exchanger optimisation is fully automated. The objective functions chosen for the optimisation study were the pumping power and/or the junction temperature, since these address the energy consumption and overall cooling performance. Based on the conducted investigation, the main conclusions are as follows:

1. Jet array impingement thermal-hydraulics are sensitive to a number of geometric design parameters, and there are cross-dependencies between them. This is complicated further when conjugate heat transfer associated with a heat spreader influences the overall system performance. Automation of the design processes is a powerful approach to optimise the heat exchanger design, whether single or multiple objective functions are considered.
2. The jet array heat exchanger designs which maximised cooling and minimised energy consumption (MOO optimums) leveraged a higher population of jets of low relative inter-jet spacing into the design. In doing so, a very low overall pressure drop was achieved owing to lower jet velocities. Despite this, high overall heat transfer coefficients were achieved by sustaining a high convective heat transfer intensity over a comparatively large area of the exposed IHS surface, with the jet array to heat source Area Ratio, A_r, being greater than unity. Decreasing heat source size allowed a higher proportion of the IHS to be actively cooled, escalating A_r, which curbs the rise in source temperature with increased heat flux.
3. For the jet array designs that maximised cooling (SOO optimums), the trade-off is that higher pumping power is required, being around four times that of the MOO

optimal designs. The higher pumping power and higher cooling effectiveness were achieved with jets of notably higher velocity compared with the MOO design. For the SOO designs considered, the higher jet velocities were a result of reduced jet population. Furthermore, the Area Ratio between the jet array and the heat source are consistently sub-unity, indicating that maximising cooling requires targeting the hot-spot region of the IHS created by the concentrated heat source. Decreasing heat source size allowed a higher packing density of jets within the target heat source region on the IHS, which moderates the rise in source temperature with increased heat flux.

There exists a wide range of commercial CPU packages with different die sizes, core counts and core architectures. Considering this, the subsequent chapter will first seek to apply the simulation-based optimisation strategy developed in this chapter to a commercial CPU package, where it is envisaged that once validated, it can be deployed as an engineering design tool for the full range of commercial CPUs.

References

[1] J. W. Elliott and A. J. Robinson, "Optimised Liquid Impinging Jet Arrays for Cooling CPU Packages," *IEEE Transactions on Components, Packaging and Manufacturing Technology,* vol. 15, no. 3, pp. 488-505, 2025, doi: 10.1109/TCPMT.2024.3485478.

[2] T. J. Chainer, M. D. Schultz, P. R. Parida, and M. A. Gaynes, "Improving Data Center Energy Efficiency With Advanced Thermal Management," *IEEE Transactions on Components, Packaging and Manufacturing Technology,* vol. 7, no. 8, pp. 1228-1239, 2017, doi: 10.1109/TCPMT.2017.2661700.

[3] H. Lee, Y. Jeong, J. Shin, J. Baek, M. Kang, and K. Chun, "Package embedded heat exchanger for stacked multi-chip module," *Sensors and Actuators A: Physical,* vol. 114, no. 2, pp. 204-211, 2004, doi: 10.1016/j.sna.2003.12.026.

[4] H. Zhang, S. Shao, H. Xu, H. Zou, and C. Tian, "Free cooling of data centers: A review," *Renewable and Sustainable Energy Reviews,* vol. 35, pp. 171-182, 2014, doi: 10.1016/j.rser.2014.04.017.

[5] Z. Jian-Hui and Y. Chun-Xin, "Design and Simulation of the CPU Fan and Heat Sinks," *IEEE Transactions on Components and Packaging Technologies,* vol. 31, no. 4, pp. 890-903, 2008, doi: 10.1109/TCAPT.2008.2006188.

[6] G. Laguna *et al.*, "Numerical parametric study of a hotspot-targeted microfluidic cooling array for microelectronics," *Applied Thermal Engineering,* vol. 144, pp. 71-80, 2018, doi: 10.1016/j.applthermaleng.2018.08.030.

[7] A. L. Moore and L. Shi, "Emerging challenges and materials for thermal management of electronics," *Materials Today,* vol. 17, no. 4, pp. 163-174, 2014, doi: 10.1016/j.mattod.2014.04.003.

[8] I. Mudawar, "Assessment of high-heat-flux thermal management schemes," *IEEE Transactions on Components and Packaging Technologies,* vol. 24, no. 2, pp. 122-141, 2001, doi: 10.1109/6144.926375.

[9] M. Saini and R. L. Webb, "Heat rejection limits of air cooled plane fin heat sinks for computer cooling," *IEEE Transactions on Components and Packaging Technologies,* vol. 26, no. 1, pp. 71-79, 2003, doi: 10.1109/TCAPT.2003.811465.

[10] F. M. Naduvilakath-Mohammed, R. Jenkins, G. Byrne, and A. J. Robinson, "Closed loop liquid cooling of high-powered CPUs: A case study on cooling performance and energy optimization," *Case Studies in Thermal Engineering,* vol. 50, p. 103472, 2023, doi: 10.1016/j.csite.2023.103472.

[11] J. W. Elliott, M. T. Lebon, and A. J. Robinson, "Optimising integrated heat spreaders with distributed heat transfer coefficients: A case study for CPU cooling," *Case Studies in Thermal Engineering,* vol. 38, p. 102354, 2022, doi: 10.1016/j.csite.2022.102354.

[12] P. Rodgers, V. Eveloy, and M. G. Pecht, "Limits of air-cooling: status and challenges," in *Semiconductor Thermal Measurement and Management IEEE Twenty First Annual IEEE Symposium, 2005.*, 15-17 March 2005, pp. 116-124, doi: 10.1109/STHERM.2005.1412167.

[13] S. Lee. "Calculating Spreading Resistance in Heat Sinks." https://cir.nii.ac.jp/crid/1573105975288257408 (accessed 11/07/2024).

[14] E. Ozturk and I. Tari, "Forced Air Cooling of CPUs With Heat Sinks: A Numerical Study," *Components and Packaging Technologies, IEEE Transactions on,* vol. 31, pp. 650-660, 2008, doi: 10.1109/TCAPT.2008.2001840.

[15] F. M. Naduvilakath-Mohammed, M. Lebon, G. Byrne, and A. J. Robinson, "An experimental investigation of vapor compression refrigeration cooling and energy performance for CPU thermal management," *Case Studies in Thermal Engineering,* vol. 54, p. 103963, 2024, doi: 10.1016/j.csite.2023.103963.

[16] Y. Han, B. L. Lau, G. Tang, H. Chen, and X. Zhang, "Si Microfluid Cooler With Jet-Slot Array for Server Processor Direct Liquid Cooling," *IEEE Transactions on Components, Packaging and Manufacturing Technology,* vol. 10, no. 2, pp. 255-262, 2020, doi: 10.1109/TCPMT.2019.2933864.

[17] P. Shen, S. Aliabadi, and J. Abedi, "A Review of Single-Phase Liquid Flow and Heat Transfer in Microchannels," in *Proceedings of the Second International Conference on Microchannels and Minichannels*, 2004, vol. 2, pp. 213-220, doi: 10.1115/ICMM2004-2337.

[18] M. Khan and A. Fartaj, "A review on microchannel heat exchangers and potential applications," *International Journal of Energy Research,* vol. 35, pp. 553-582, 2011, doi: 10.1002/er.1720.

[19] R. Dey, T. Das, and S. Chakraborty, "Frictional and Heat Transfer Characteristics of Single-Phase Microchannel Liquid Flows," *Heat Transfer Engineering,* vol. 33, pp. 425-446, 2012, doi: 10.1080/01457632.2012.614153.

[20] T. Coşkun and E. Cetkin, "A review of heat and fluid flow characteristics in microchannel heat sinks," *Heat Transfer,* vol. 49, pp. 1-25, 2020, doi: 10.1002/htj.21819.

[21] M. Fabbri and V. K. Dhir, "Optimized Heat Transfer for High Power Electronic Cooling Using Arrays of Microjets," *Journal of Heat Transfer,* vol. 127, no. 7, pp. 760-769, 2004, doi: 10.1115/1.1924624.

[22] F. Bode, C. Patrascu, and I. Nastase, "Heat and mass transfer enhancement strategies by impinging jets: A literature review," *Thermal Science,* vol. 25, pp. 227-227, 2020, doi: 10.2298/TSCI200713227B.

[23] H. Martin, "Heat and Mass Transfer between Impinging Gas Jets and Solid Surfaces," *Advances in Heat Transfer,* vol. 13, pp. 1-60, 1977, doi: 10.1016/S0065-2717(08)70221-1.

[24] S. V. Garimella and R. A. Rice, "Confined and Submerged Liquid Jet Impingement Heat Transfer," *Journal of Heat Transfer,* vol. 117, no. 4, pp. 871-877, 1995, doi: 10.1115/1.2836304.

[25] N. Gao and D. Ewing, "Investigation of the effect of confinement on the heat transfer to round impinging jets exiting a long pipe," *International Journal of Heat and Fluid Flow,* vol. 27, no. 1, pp. 33-41, 2006, doi: 10.1016/j.ijheatfluidflow.2005.06.002.

[26] A. J. Robinson and E. Schnitzler, "An experimental investigation of free and submerged miniature liquid jet array impingement heat transfer," *Experimental Thermal and Fluid Science,* vol. 32, no. 1, pp. 1-13, 2007, doi: 10.1016/j.expthermflusci.2006.12.006.

[27] A. J. Robinson, "A Thermal–Hydraulic Comparison of Liquid Microchannel and Impinging Liquid Jet Array Heat Sinks for High-Power Electronics Cooling," *IEEE Transactions on Components and Packaging Technologies,* vol. 32, no. 2, pp. 347-357, 2009, doi: 10.1109/TCAPT.2008.2010408.

[28] Y. Fan and I. Hassan, "Numerical Simulation of a Novel Jet-Impingement Micro Heat Sink With Cross Flow Under Non Uniform Heating Condition," in *ASME 2011 9th International Conference on Nanochannels, Microchannels, and Minichannels*, 2011, vol. ASME 2011 9th International Conference on Nanochannels, Microchannels, and Minichannels, Volume 1, pp. 441-449, doi: 10.1115/icnmm2011-58002.

[29] M. R. Hajmohammadi, M. Mohammadifar, and M. Ahmadian-Elmi, "Optimal placement and sizing of heat sink attachments on a heat-generating piece for minimization of peak temperature," *Thermochimica Acta,* vol. 689, p. 178645, 2020, doi: 10.1016/j.tca.2020.178645.

[30] M. O. Qidwai, I. A. Badruddin, N. Z. Khan, M. A. Khan, and S. Alshahrani, "Optimization of Microjet Location Using Surrogate Model Coupled with Particle Swarm Optimization Algorithm," *Mathematics,* vol. 9, no. 17, p. 2167, 2021, doi: 10.3390/math9172167.

[31] R. Kempers and A. Robinson, "Heated Meter Bar Techniques, What You Should Know and Why," in *The Art of Measuring in the Thermal Sciences*: CRC Press, Florida, United States, 2020, pp. 313-335.

[32] R. L. Webb, "Heat Exchanger Design Methodology for Electronic Heat Sinks," *Journal of Heat Transfer,* vol. 129, no. 7, pp. 899-901, 2006, doi: 10.1115/1.2717249.

[33] S. J. Kline and F. A. McClintock, "Describing Uncertainties in Single-Sample Experiments," *Mechanical Engineering,* vol. 75, pp. 3-8, 1953.

[34] Cd-adapco. STAR CCM+ 3.04 User Manual, file:///C:/Program%20Files/Siemens/15.06.007/STAR-CCM+15.06.007/doc/en/online/index.html#page/connect%2Fsplash.html (accessed 28/05/2024).

[35] R. Zhang, Z. Chen, G. Xie, and B. Sunden, "Numerical Analysis of Constructal Water-Cooled Microchannel Heat Sinks with Multiple Bifurcations in the Entrance Region," *Numerical Heat Transfer, Part A: Applications,* vol. 67, no. 6, pp. 632-650, 2015, doi: 10.1080/10407782.2014.937286.

[36] C. G. Ferro, F. Pietrangelo, and P. Maggiore, "Heat exchange performance evaluation inside a lattice panel using CFD analysis for an innovative aerospace anti-icing system," *Aerospace Science and Technology,* vol. 141, p. 108565, 2023, doi: 10.1016/j.ast.2023.108565.

[37] P. M. Coelho and J. C. Faria, "On the Generalized Brinkman Number Definition and Its Importance for Bingham Fluids," *Journal of Heat Transfer,* vol. 133, no. 5, 2011, doi: 10.1115/1.4003169.

[38] R. Lanzafame, S. Mauro, and M. Messina, "Wind turbine CFD modeling using a correlation-based transitional model," *Renewable Energy,* vol. 52, pp. 31-39, 2013, doi: 10.1016/j.renene.2012.10.007.

[39] O. Sahni, K. E. Jansen, M. S. Shephard, C. A. Taylor, and M. W. Beall, "Adaptive boundary layer meshing for viscous flow simulations," *Eng. with Comput.,* vol. 24, no. 3, pp. 267–285, 2008, doi: 10.1007/s00366-008-0095-0.

[40] P. J. Roache, "Quantification of Uncertainty in Computational Fluid Dynamics," *Annual Review of Fluid Mechanics,* vol. 29, no. 1, pp. 123-160, 1997, doi: 10.1146/annurev.fluid.29.1.123.

[41] Y. Yang, J. Mao, P. Chen, F. Wang, and Z. Tu, "Numerical investigation of impingement heat transfer on the crossflow channel with vortex generators," *Applied*

Thermal Engineering, vol. 201, p. 117780, 2022, doi: 10.1016/j.applthermaleng.2021.117780.

[42] R. J. Goldstein and A. I. Behbahani, "Impingement of a circular jet with and without cross flow," *International Journal of Heat and Mass Transfer,* vol. 25, no. 9, pp. 1377-1382, 1982, doi: 10.1016/0017-9310(82)90131-4.

[43] M. A. R. Sharif and K. K. Mothe, "Evaluation of Turbulence Models in the Prediction of Heat Transfer Due to Slot Jet Impingement on Plane and Concave Surfaces," *Numerical Heat Transfer, Part B: Fundamentals,* vol. 55, no. 4, pp. 273-294, 2009, doi: 10.1080/10407790902724602.

[44] H. M. Hofmann, R. Kaiser, M. Kind, and H. Martin, "Calculations of Steady and Pulsating Impinging Jets—An Assessment of 13 Widely used Turbulence Models," *Numerical Heat Transfer, Part B: Fundamentals,* vol. 51, no. 6, pp. 565-583, 2007, doi: 10.1080/10407790701227328.

[45] B. T. Kannan and S. Sundararaj, "Steady State Jet Impingement Heat Transfer from Axisymmetric Plates with and without Grooves," *Procedia Engineering,* vol. 127, pp. 25-32, 2015, doi: 10.1016/j.proeng.2015.11.320.

[46] O. Enearu, Y. K. Chen, and C. Kalyvas, "A new approach to modelling of PEMFC flow field," in *2017 9th International Conference on Modelling, Identification and Control (ICMIC)*, 10-12 July 2017, pp. 958-964, doi: 10.1109/ICMIC.2017.8321594.

[47] T. Davis, R. Kumar, and F. Alvi, "Shear Layer Characteristics of the Supersonic Free and Impinging Jets," vol. 25, 2012, doi: 10.2514/6.2012-3138.

[48] M. L. Hosain, R. Bel Fdhila, and A. Daneryd, "Heat transfer by liquid jets impinging on a hot flat surface," *Applied Energy,* vol. 164, pp. 934-943, 2016, doi: 10.1016/j.apenergy.2015.08.038.

[49] B. N. Pamadi and I. A. Belov, "A note on the heat transfer characteristics of circular impinging jet," *International Journal of Heat and Mass Transfer,* vol. 23, no. 6, pp. 783-787, 1980, doi: 10.1016/0017-9310(80)90032-0.

[50] J. L. S.-J. Lee, "Stagnation Region Heat Transfer of a Turbulent Axisymmetric Jet Impingement," *Experimental Heat Transfer,* vol. 12, no. 2, pp. 137-156, 1999, doi: 10.1080/089161599269753.

[51] J. Lee and S.-J. Lee, "The effect of nozzle configuration on stagnation region heat transfer enhancement of axisymmetric jet impingement," *International Journal of Heat and Mass Transfer,* vol. 43, no. 18, pp. 3497-3509, 2000, doi: 10.1016/S0017-9310(99)00349-X.

[52] T. S. O'Donovan and D. B. Murray, "Jet impingement heat transfer – Part I: Mean and root-mean-square heat transfer and velocity distributions," *International Journal of Heat and Mass Transfer,* vol. 50, no. 17, pp. 3291-3301, 2007, doi: 10.1016/j.ijheatmasstransfer.2007.01.044.

[53] S. Beltaos, "Oblique Impingement of Circular Turbulent Jets," *Journal of Hydraulic Research,* vol. 14, no. 1, pp. 17-36, 1976, doi: 10.1080/00221687609499685.

[54] R. J. Goldstein and M. E. Franchett, "Heat Transfer From a Flat Surface to an Oblique Impinging Jet," *Journal of Heat Transfer,* vol. 110, no. 1, pp. 84-90, 1988, doi: 10.1115/1.3250477.

Chapter 4

Optimisation of Liquid Jet Impingement Coldplate for an Overclocked CPU with Multiple Discrete Cores

Abstract

This study details the development of an automated, multi-objective optimisation framework for liquid jet impingement cooling of commercial Central Processing Units (CPUs). Integrating Computer Aided Design (CAD), Computational Fluid Dynamics (CFD), and geometric optimisation software tools, optimised jet array configurations were tailored for cooling of a commercial CPU with multiple, heat-generating, high heat flux cores. Experiments were performed on a live test CPU under highly overclocked compute workload and the measurements used to verify the accuracy of the simulation model both pre and post optimisation. A comparative analysis of both single and multi-objective optimisation design strategies illustrated trade-offs depending on the choice of objective functions, which were chosen to be the average core junction temperature and the hydraulic pumping power in this study. When maximised cooling of the cores was considered, the optimum jet design aggressively targeted the concentrated heat source region of the CPU cores, achieving a core junction temperature 10 K below the throttling limit, even under highly overclocked workload conditions. Conversely, the multi-objective design that equally weighted cooling performance and hydraulic power penalty produced a design with a significantly larger population of lower-velocity jets, leveraging a larger effective surface area of the heat spreader to compensate for the lower jet impingement convective heat transfer coefficients. Despite the higher core junction temperature, it still remained below the throttling temperature whilst achieving a fourfold reduction in pumping power. Analysis

of the CPU thermal stack identified significant temperature gradients across the silicon die owing to the very high localised heat fluxes at the discrete cores. This contributed approximately 30% of the total core-to-coolant thermal budget, which is significant. This highlights the importance of applying realistic thermal boundary conditions when designing coldplate heat exchangers for practical CPU packages.

4.1. Introduction

The nonstop advancement in microelectronic device development introduces new thermal challenges, particularly in maintaining safe operating temperatures as the power and heat flux levels continue to increase. Effective heat dissipation from the Integrated Circuit (IC) components and devices has become a critical challenge, to the point where it can impede progress of the industry. For example, it is projected that the Thermal Design Power (TDP) for Central Processing Units (CPU) could exceed 400 W in the coming years [1]. Effective thermal management of these emerging high-powered processors is essential for ensuring product performance and reliability, to the extent that the development of high-performance heat sinks is crucial [2]. Since it is now well established that conventional air-cooled heat sink technologies are reaching their physical limits in managing the heat flux generated by modern processors [3, 4], the industry is now transitioning to liquid cooling. Liquid-based approaches to thermal management in applications such as data centres can not only manage the higher processor powers and heat fluxes, but facilitate higher overall server and rack power levels, and do so at much lower operating expense in terms of the energy consumption required for thermal management [5, 6].

Some previous works in this field of developing liquid heat exchangers for electronics cooling have used the die footprint to represent the electronic component as a concentrated heat source [7-9]. Historically however, it is more typical to distribute the heat load uniformly across the full base of the heat sink [10-12]. Although important in the context of heat exchanger technology development, these approaches do not account for the fact that CPU architectures contain multiple, discrete heat-generating cores that create concentrated thermal loads on the underside of the semiconductor die. The degree of heat concentration often necessitates that in practical application, an Integrated Heat Spreader (IHS) must be positioned between the die and the convective heat sink to create a sufficiently large heat transfer surface area. However, for the same reason fin efficiency of extended surfaces decreases with increasing convective heat transfer coefficient, the spreading efficiency of IHSs decreases as the intensity of convective heat transfer escalates [13]. In the context of transitioning from air to liquid cooling of CPUs, the full benefit of liquid cooling of the IHS is never fully realised, since the higher intensity of liquid convective heat transfer causes the heat to become more concentrated within the IHS, thus diminishing the effective area for convective heat transfer. This is a classical conjugate heat transfer problem, and for CPU-type arrangements, Elliott and Robinson [14] showed that compared with uniform convective cooling of the IHS, optimised non-uniform convective cooling can improve the overall thermal performance by targeting the higher cooling intensity in the region of heat concentration. Although the investigation proved that targeted cooling approaches can improve overall thermal performance, it did not address the practicalities associated with hydraulic penalties, such as pressure drop and pumping power. In practice, a heat sink design should seek to increase the cooling intensity and decrease the hydraulic penalties, and this requires careful balancing of performance objectives, since they are generally antagonistic to one another [15, 16].

Liquid jet array impingement offers a compelling solution for delivering high intensity and targeted convective cooling of CPUs [7, 17]. When simple circular jets are arranged in arrays, the average convective heat transfer coefficient for a given net flow rate is sensitive to a manageable set of geometric design parameters, such as jet-to-target distance [18], inter-jet spacing [19, 20], and nozzle size [21]. Conversely, for a given flow rate, the pressure drop is primarily sensitive to the nozzle size, making jet arrays well-suited for simultaneous heat transfer and hydraulic optimisation [22]. This was recently demonstrated by the present author's work [7], which described the development of an automated, simulation-based optimisation framework for impinging liquid jet array heat exchanger designs for CPU cooling applications. Although the work was limited to the use of uniform heat loading over assumed die sizes of typical CPUs fitted with IHSs, it showed that tailored jet arrays could be produced that either maximised the heat transfer or balanced both thermal and hydraulic performance. Consistent with the earlier work of Elliott et al. [13], the findings of this work indicated that for concentrated heat sources, the best thermal performance was achieved with a densely packed array of high velocity jets that targeted the high heat flux regions of the IHS, though at comparatively high pressure drop and pumping power. For balanced thermal-hydraulic performance, the optimisation procedure produced lower velocity jets in arrays of much higher population, leveraging a larger effective surface area of the IHS to offset the lower convective intensity of the slower jets, though resulting in significantly lower hydraulic penalties.

The primary objective of this study is to develop and test an automated optimisation design methodology for cooling of the cores of commercial CPU packages with liquid jet array type heat exchangers. This study builds upon the work of Elliott and Robinson [7] by adapting the previously developed optimisation framework to a commercially available CPU with multiple, discrete, and high heat flux cores on the underside of a silicon die. Both Single-Objective Optimisation (SOO) and Multi-Objective Optimisation (MOO) strategies are considered, providing insight into design trade-offs based on the specified objective functions. To the best of knowledge, this study is among the first to apply a comprehensive optimisation framework specifically tailored for liquid cooling of complete CPU packages, down to individual cores.

4.2. Experimental Study

4.2.1. The Case Study

This investigation focuses on the thermal-hydraulic optimisation of a liquid jet array impingement coldplate heat exchanger for high-performance computing of a commercial CPU package. A Computational Fluid Dynamics (CFD) based approach was developed to achieve this, with the numerical model applied to the configuration depicted in Figure 4.1(a). This figure illustrates the physical coldplate assembly, highlighting the swapable orifice plate, which is sandwiched between the manifold and the copper baseplate, with compressed O-rings providing fluid-tight seals between both the orifice plate and the manifold and the manifold and the copper base, thus allowing for straight-forward testing of different orifice plate designs. Figure 4.1(b) shows the idealised coldplate heat exchanger used for simulation purposes. Coolant enters via an inlet port to an upper plenum chamber after which it is forced through the nozzles of the orifice plate forming discrete jets which issue into the confined gap and impinge on the lower copper base. The coolant exits the confined gap into a skirt-type plenum chamber that frames the orifice plate and exits through the outlet port.

The Intel i5-12600K CPU, shown in Figure 4.2(a), was selected as the test CPU for this investigation and will be discussed in more detail later. The selection is somewhat arbitrary, though was partially motivated by the relatively high Thermal Design Power (TDP), high core-level heat flux, capability of being overclocked, and there being information available in terms of the core size and layout. Modifications were made to the commercial CPU package by removing the stock Integrated Heat Spreader (IHS) and solder-based Thermal Interface Material (TIM) (Figure 4.2(b)). Figure 4.1(c) depicts the digitised Intel i5-12600K assembled to the base of the coldplate heat exchanger, which now acts as the IHS.

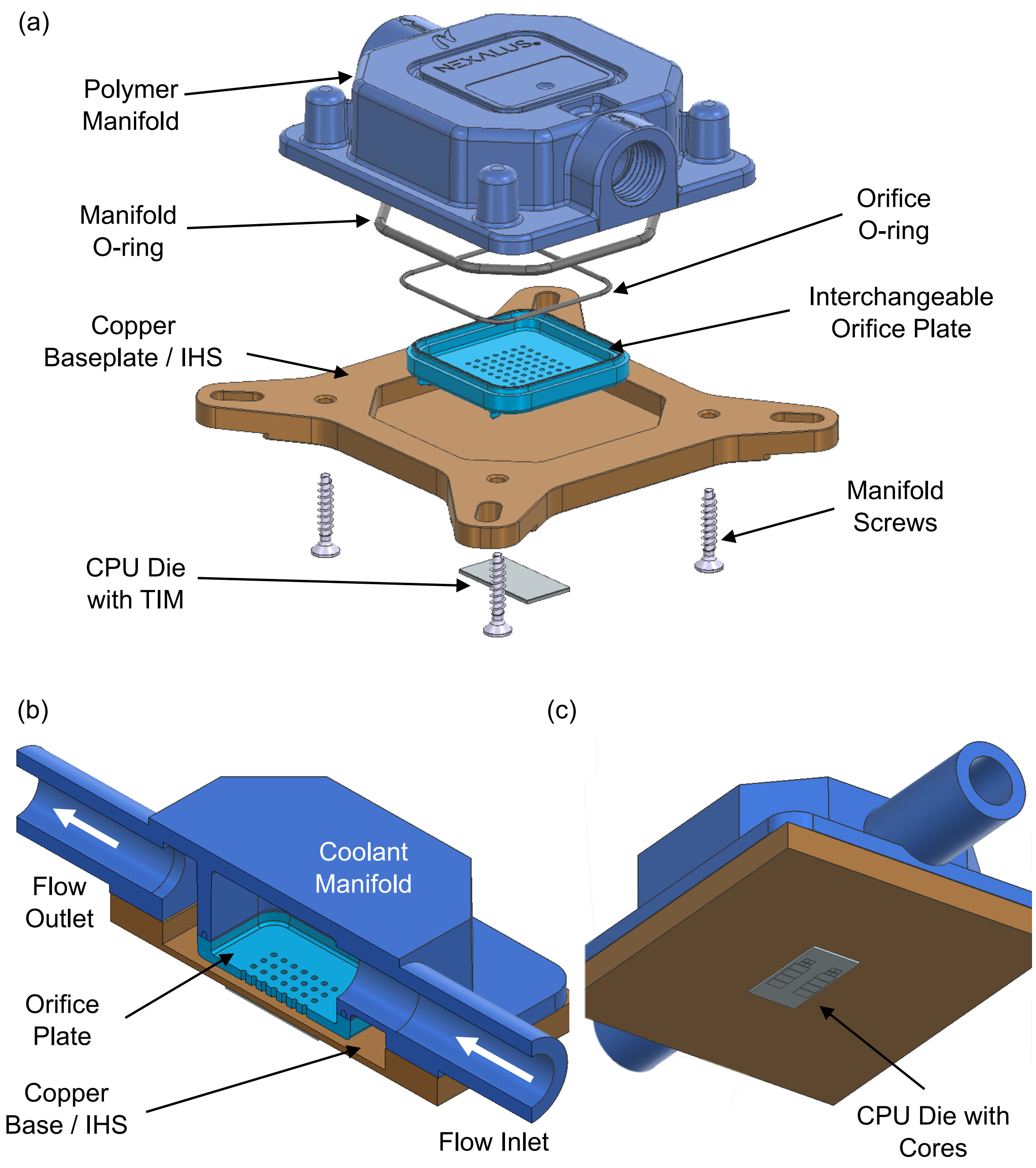

Figure 4.1: (a) Exploded view of physical coldplate assembly, (b) sectioned CAD assembly of coldplate heat exchanger and CPU die, and (c) underside of heat exchanger showing attached CPU die and core placements.

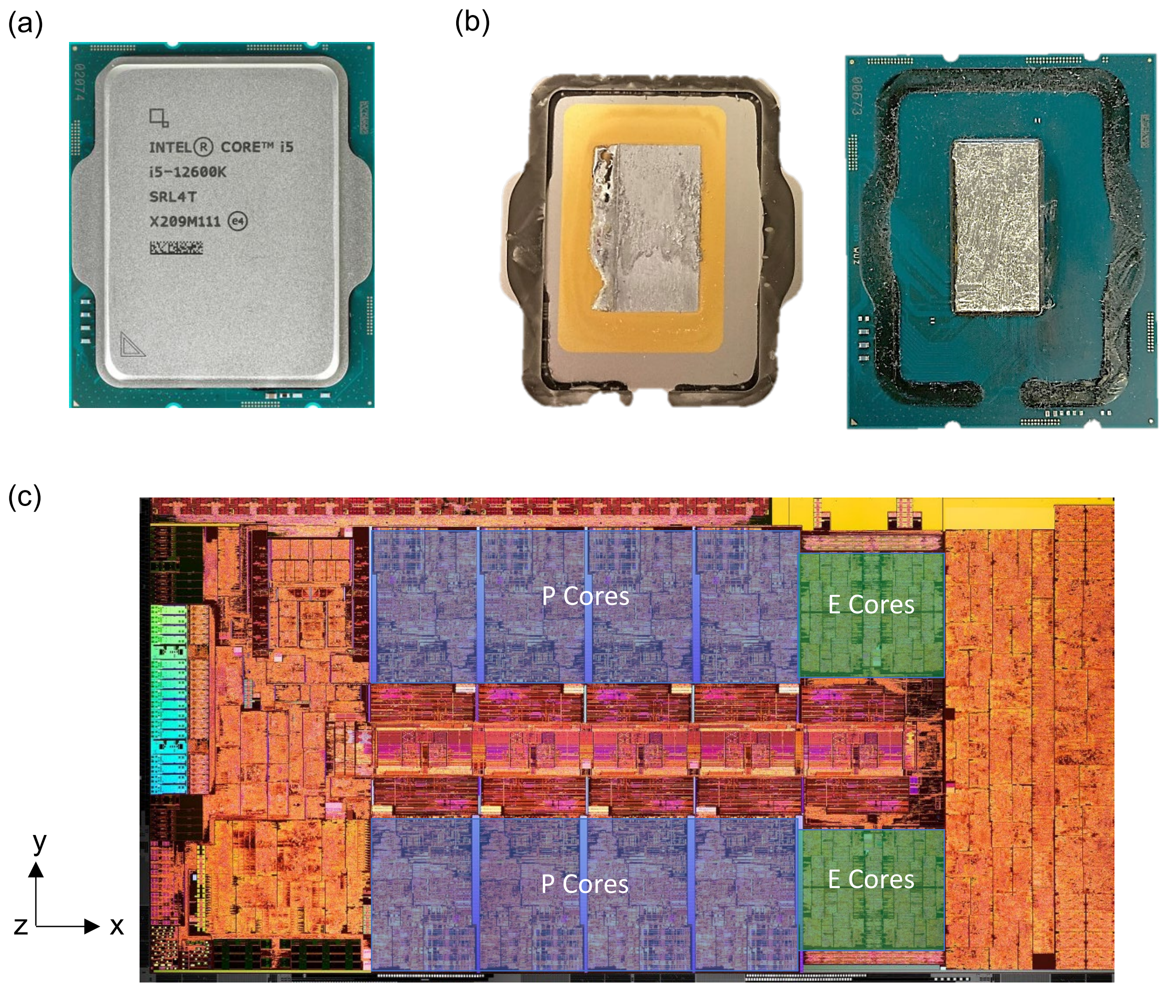

Figure 4.2: (a) Intel i5-12600K CPU in commercially available state, (b) CPU with IHS removed and die exposed, and (c) CPU circuit architecture illustrating location and types of cores.

4.2.2. Experimental Test Facility

An experimental test facility was constructed to generate and measure both the CPU computing data and heat exchanger thermal-hydraulic performance data used to verify the CFD model for both pre and post optimisation designs. The main components of the test facility are the CPU-motherboard assembly, the coldplate heat exchanger, and the coolant flow loop. Each will now be discussed in turn.

4.2.2.1. CPU and Motherboard

As mentioned, the Intel i5-12600K was selected as the test CPU and a list of key specifications is provided in Table 4.1 [23]. The Intel i5-12600K is part of the Alder Lake-S generation of CPUs. This family of Intel CPUs uses a common die architecture, shown in Figure 4.2(c), that contains up to 16 cores, with 8 designated performance cores (P-cores) and 8 efficiency cores (E-cores). The specific i5-12600K version of this CPU has only 10 cores active, including the 6 rightmost P-cores and 4 of the E-cores. Under high compute workload conditions, such as high-performance gaming and overclocking, the E-cores are disabled to maximise system performance, resulting in peak achievable temperatures by concentrating all power to the 6 active P-cores.

The suggested TDP of this CPU is 125 W, with an overall die size of 20.5 x 10.5 mm^2. The maximum specified design power, or Turbo TDP, for this CPU is ~150 W. CPU stress tests were conducted using the Y-cruncher software, with all data captured using the HWiNFO hardware monitoring tool. Overclocking was managed via the Intel Extreme Utility software, where the CPU achieved a maximum clock speed of 4.9 GHz and maintained an increased power draw of up to ~210 W, which is a 70% increase in power above the base TDP for a 1.2 GHz increase in clock speed. This was achieved by increasing the core voltage to 1.47 V, with an offset of -0.03 V.

Figure 4.3(a) shows the CPU mounted on the ASUS ROG Maximus Z790 Hero (LGA1700) DDR5 ATX Motherboard, paired with a Crucial PCIe 3.0 NVMe m.2 SSD and two Corsair Dominator Platinum RGB DDR5 32GB DRAMs. Power was supplied by a Super Flower SF-650P14XE (HX) power supply unit. This configuration facilitated CPU overclocking, with the core temperatures measured by the on-die Digital Thermal Sensors (DTS), with a stated accuracy of ±5 K [24]. Additionally, the power received by the CPU cores (SVI2 TFN) was monitored internally via telemetry of the core voltage. The CPU was housed within a socket of high-strength, heat-resistant thermoplastic polymer, which insulates the CPU and mitigates heat loss to the motherboard.

Table 4.1: Intel i5-12600K specifications [23]

Essentials	
Product Collection	12th Generation Intel® Core™ i5
Processor Number	i5-12600K
Lithography	Intel 7
CPU specifications	
Total Cores	10
Total Performance Cores	6
Total Efficient Cores	4
Performance-core Base Frequency	3.70 GHz
Processor Base Power	125 W
Maximum Turbo Power	150 W
Package Specifications	
Sockets Supported	FCLGA1700
Max CPU Configuration	1
Thermal Solution Specification	PCG 2020A
Max. Junction Temperature $T_{j,\,max}$	100 °C
P Core Size	3.4 x 2.2 mm^2
Die Size	20.5 x 10.5 mm^2
Package Size	45.0 x 37.5 mm^2

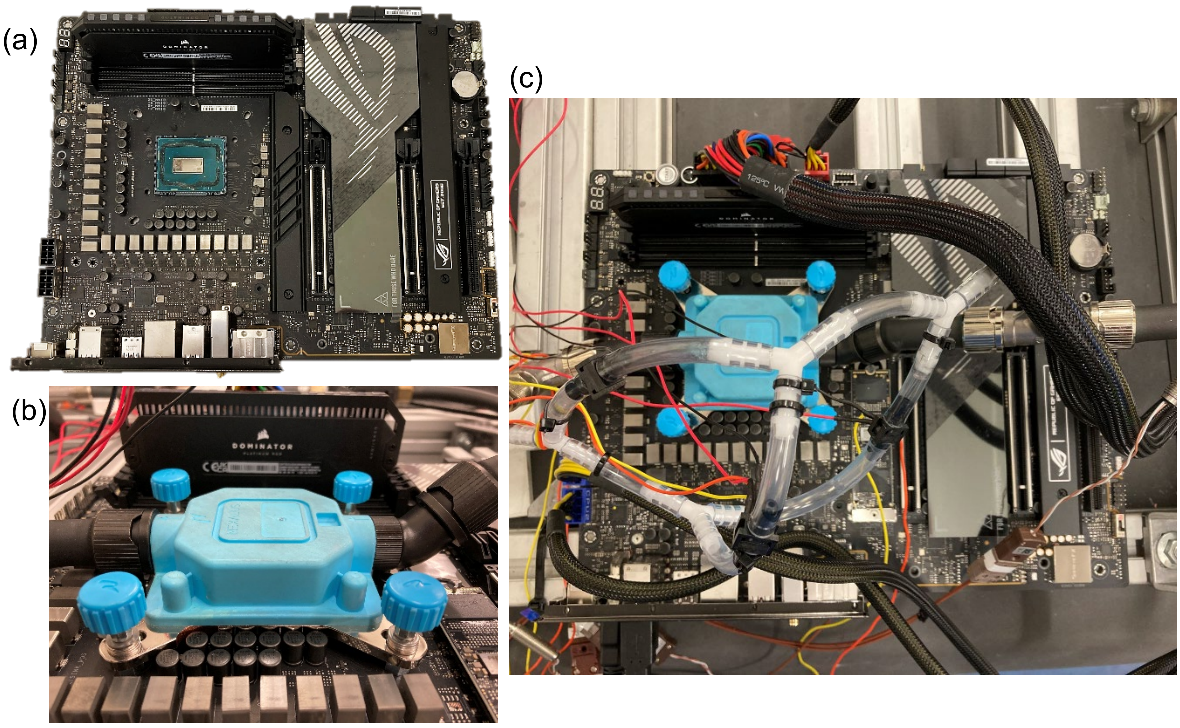

Figure 4.3: (a) Schematic of test motherboard with installed Intel i5-12600K CPU, (b) cold plate heat exchanger assembly mounted to motherboard CPU socket, and (c) live test motherboard-CPU assembly with coldplate heat exchanger integrated into experimental flow loop.

4.2.2.2. The Coldplate Heat Exchanger

The heat exchanger used in this study was a modified Nexalus Enflux^{TM} coldplate, as it allows swappable orifice plates for testing of different jet array designs (Figure 4.1(a)). The coldplate was constructed from an upper Trirex 3020U polycarbonate manifold and a lower 50 x 50 x 1.3 mm^3 nickel-plated copper base, which here doubled as the sole heat spreader for the system. Sandwiched between them was the test orifice plate, which for this investigation was 3D printed using an Elegoo Saturn 3 resin printer, with an x-y resolution of 19 x 24 μm^2 and z-axis accuracy of 20 μm, subsequent to curing under UV light. A baseline reference orifice plate was first tested in order to assess the overall impact of design optimisation. Consistent with the study by Elliott and Robinson [7], the baseline consisted of a square array of N = 49, D = 1.0 mm diameter circular nozzles, configured at a pitch-to-diameter ratio of S/D = 2.25 and dimensionless jet-to-target spacing of H/D = 1.7. Figure 4.4(a) is an image of the manufactured orifice plate produced for the baseline experimental tests, whilst Figure 4.4(b) shows it assembled in the manifold. To ensure an adequate level of accuracy, the orifice plate was examined under a microscope and measurements taken for a selection of jet nozzles across the full spread of the jet array. Figures 4.4(b) and (c) present microscope images of typical jet nozzles. For a sample of 25 measurements, the mean nozzle diameter was 0.986 mm with a standard deviation of 6.71 μm, representing dimensional error on the nozzle diameter of 14 μm (1.4%) compared to the D = 1.0 mm design point. The maximum under sizing of the jet diameter was 24 μm (2.4%), which is in-line with the stated accuracy for this 3D printer. Some residual roughness is also observed along the jet orifice edges, as visible in Figures 4.4(c) and (d)[6].

Figures 4.3(b) and (c) show the coldplate-motherboard-CPU assembly, noting that a layer of high thermal conductivity liquid metal TIM (Thermal Grizzly Conductonaut, k ≈ 75 W/mK) was applied between the copper base of the heat exchanger and the exposed CPU die. This enabled direct contact between the CPU die and the base of the heat exchanger which facilitated more accurate verification of the numerical simulations by reducing the

[6] For normal distribution of jet nozzle diameters across the baseline orifice plate, see Appendix E

uncertainties associated with the TIM layers between the heat source and the convective heat sink. Furthermore, torque screws, rated to 4 Nm, were used to secure the coldplate to the motherboard, ensuring an even pressure between the baseplate and the CPU die, and thus even distribution of the TIM.

In the original configuration of the CPU, a copper IHS, of approximate thickness 2.8 mm, was connected to the die using a solder-based thermal interface material (STIM), where k ≈ 50 - 87 W/mK [25]. The removal of both the IHS and the STIM significantly reduced the thermal resistance within the source-to-coolant thermal stack. Additionally, this modification eliminated uncertainties associated with the precise thermal properties and application of the STIM during the CPU's manufacturing process. By employing a liquid metal TIM and securing the components with torque screws, a higher degree of control over the thermal interface was achieved. While some uncertainty remains regarding the exact distribution of the liquid metal TIM, this is substantially reduced compared to the stock configuration of the i5-12600K in its commercial state.

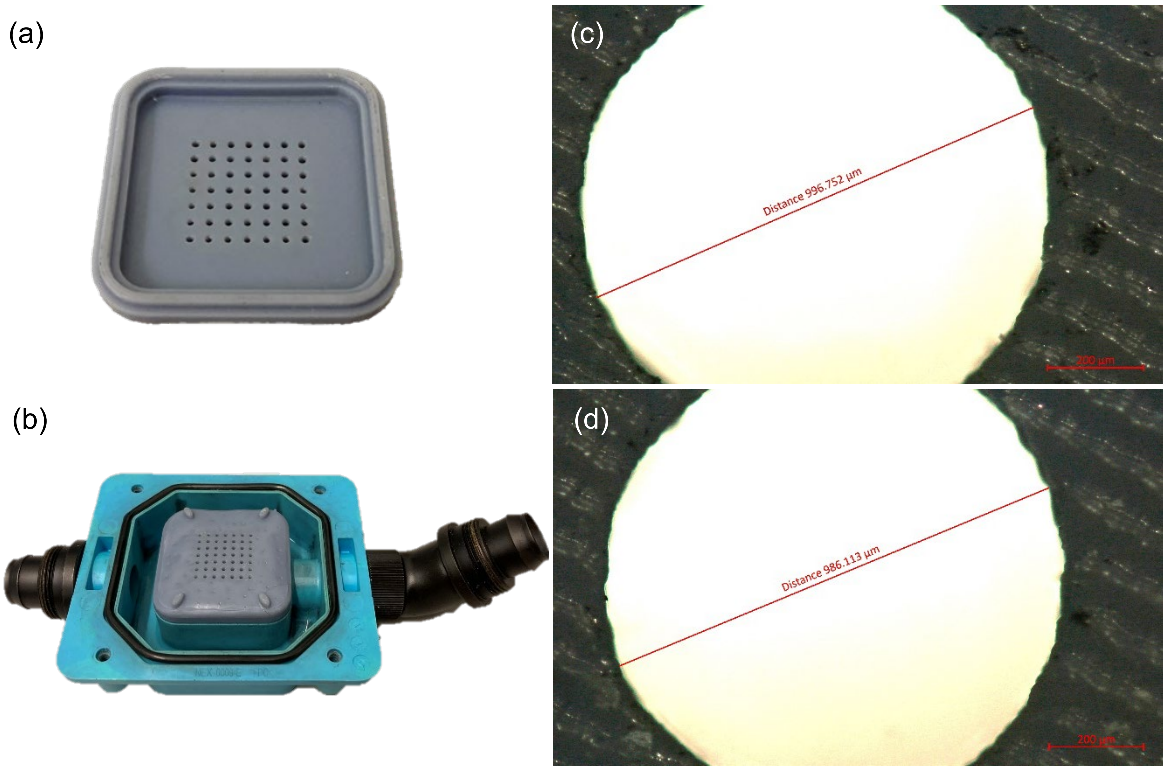

Figure 4.4: (a) 3D resin printed baseline orifice plate, (b) orifice plate positioned within coolant manifold, and (c)-(d) microscope images of single jet nozzles, highlighting dimensional accuracy.

4.2.2.3. The Flow Loop

The flow loop illustrated in Figure 4.5 included a 2-Litre coolant reservoir, a Polar Series Accel 500 LC recirculating chiller for temperature control, and a compact brazed heat exchanger for coolant inlet temperature regulation. Coolant flow was measured using a Sensata Cynergy3 UF series ultrasonic flow meter (10 L/min ± 3% RS). Temperature measurements were taken using 1.0 mm diameter sheathed T-type thermocouples inserted into the flow via compression fittings at key locations, such as the inlets and outlets of both heat exchangers. The thermocouples were calibrated to an uncertainty of ±0.5°C against an ASL F100 Precision Handheld RTD thermometer. Pressure measurements were recorded using Omega PX26 series wet/wet differential pressure sensors (100 kPa ± 0.25% FS), calibrated with a Digitron 2022P differential digital pressure meter. For all conducted tests, distilled water was used as the coolant, with an inlet temperature to the coldplate maintained at 35°C. The flow rate was controlled by adjusting the power to the TCS M3000 variable speed pump, with additional control via manual valves placed throughout the flow loop for finer adjustments at lower flow rates.

The measurement sensors were connected to a data acquisition (DAQ) system, utilising an NI 9211 DAQ Module for thermocouple input (±0.05°C) and a NI 9219 DAQ Module for pressure meter input (±0.1% RS). The output of the flow meter was recorded via direct voltage measurement using a IDM91E Handheld Digital Multimeter, with a resolution of 0.1 mV (±0.5%). National Instruments LabVIEW software was used for real-time monitoring and postprocessing of temperature and pressure data. Each stress test was allowed to reach steady-state conditions before recording data. Tests were conducted for flow rates between 1 and 7 L/min, with the total nominal power to the CPU cores at Q_{hs} ~ 150 W for Turbo TDP tests and Q_{hs} ~ 210 W under overclocking conditions. Slight variations in total power occurred between different tests, but did not vary by more than 0.76% for Turbo TDP and 1.8% for overclocking.

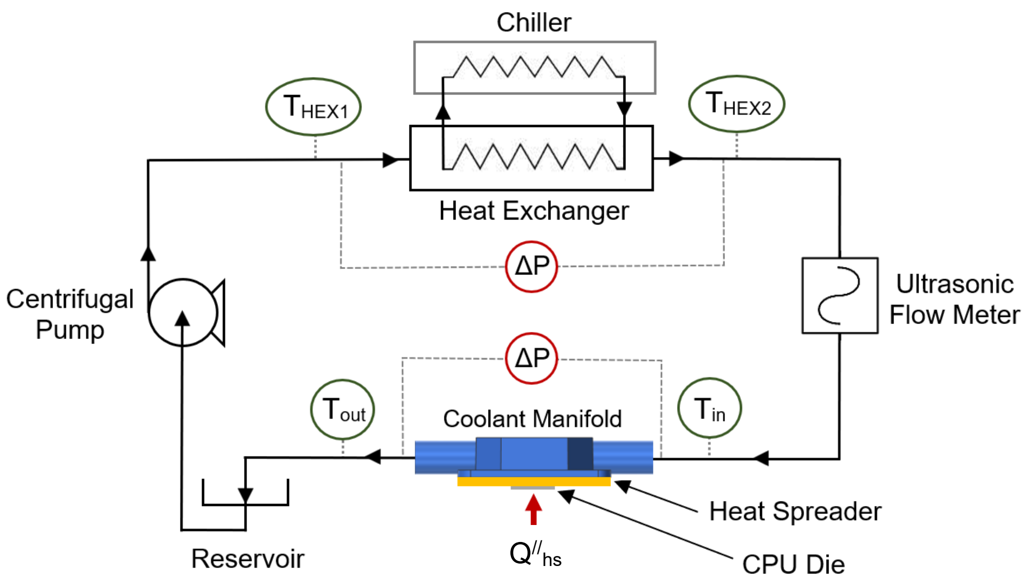

Figure 4.5: Schematic of flow loop test facility.

4.2.3. Performance Metrics and Data Reduction

A method of assessing the thermal-hydraulic performance of various heat exchanger designs is outlined below. The aim is to provide a means to not only assess the impact of heat exchanger design modifications, but also to provide data for adequate comparison and subsequent verification of the simulation model used for the heat exchanger design optimisation. Further to this, and different from what has been done previously in the literature, the thermal performance indicators are posed in the context of the CPU cores themselves, opposed to the overall region that the cores occupy, or the area of the die that interfaces with the heat exchanger.

For the physical testing of the Intel i5 12600K CPU, the power supplied to the CPU cores is recorded as a single, overall power to the cores, with no breakdown of the power to each individual core. This limitation, combined with the subsequent CFD verification requirements, necessitated that the experimental tests be conducted with the full load distributed across all active P-cores. The absence of core-specific power mapping complicated the identification of which cores were active during partial-load scenarios, making it impractical to run tests with fewer than the maximum core load. It is thus assumed that the overall CPU power is equally distributed across the 6 active P-cores, such that the power to each core is simply,

$$Q_{core} = \frac{Q_{hs}}{6} \tag{4.1}$$

The HWiNFO monitoring tool does, however, measure each individual active core junction temperature, $T_{core,j}$, though there is no mapping available of the individual measurements to the physical core location on the die. Furthermore, during testing some variation in $T_{core,j}$ resulted, though they were within the ±5 K uncertainty of the on-die sensors. It was thus not possible to assess if these differences were physical or simply due to measurement uncertainty. This puts some limits on the core-to-core comparison of the experimental measurements with the CFD predictions. Here, the average temperature across all six active CPU cores is used to quantify the junction temperature, T_j, performance metric, given by;

$$T_j = \frac{T_{core,1} + T_{core,2} + T_{core,3} + T_{core,4} + T_{core,5} + T_{core,6}}{6} \tag{4.2}$$

Considering the cores as discrete heat sources [26], Eqs. (4.1) and (4.2) can be combined to estimate the average core-to-coolant thermal resistance, R_{core},

$$R_{core} = \frac{(T_j - T_\infty)}{Q_{core}} \tag{4.3}$$

where $T_\infty = (T_{in} - T_{out})/2$ is the average of the inlet and outlet coolant temperature. Given the known dimensions of each core, and thus its surface area, A_{core}, a performance metric that gives a sense of the overall cooling intensity that the discrete cores experience can be defined as,

$$U_{core} = \frac{Q_{core}}{(T_j - T_\infty)A_{core}} = \frac{Q''_{core}}{(T_j - T_\infty)} = \frac{1}{R_{core}A_{core}} \tag{4.4}$$

where $Q''_{core} = Q_{core}/A_{core}$ is the core-level heat flux. This performance indicator, U_{core}, is similar to what is generally termed as a source-to-sink overall heat transfer coefficient, with units of W/m^2K, and takes into account the entire stack between the core and coolant (die, TIM, heat spreading, convection), though here it must be remembered that it is representative of the discrete heat sources (cores) on the CPU. Data was recorded during the experiments at a frequency of 1 Hz across a 10 minute window following temperature stabilisation, resulting in 600 samples being recorded for each CPU core. Thermal steady state was assumed when the variation in temperature measurements was no greater than 0.5°C after 50 readings, typically within 15 - 20 minutes following a cold start.

In terms of the hydraulic performance metrics, both for the setup / verification of the simulation model and the subsequent optimisation study, the average exit velocity of the flow through each jet, V_{jet}, and hence the jet Reynolds Number, Re_{jet}, are defined as [27]:

$$V_{jet} = \frac{4\dot{V}}{N\pi D^2} \tag{4.5}$$

$$Re_{jet} = \frac{V_{jet}D}{\nu} \tag{4.6}$$

where $\dot{V}$ is the volumetric flow rate of the fluid entering the cold plate manifold and v is the kinematic viscosity of the coolant. The hydraulic power of the coldplate heat exchanger is determined as,

$$P_p = \dot{V}\Delta P \tag{4.7}$$

where ΔP is the pressure drop across the heat exchanger.

4.2.4. Uncertainty Analysis

An uncertainty analysis was performed for the derived quantities described in Eqs. (4.3) - (4.7), using the using the root sum of squares (RSS) method as detailed by Kline and McClintock [28]; where x_i refers to the measurement value, Unc_i the uncertainty of said measurement and Unc_z is the uncertainty attributed to the derived parameter, Z, which can be calculated by,

$$Unc_z = \sqrt{\left(\sum_{i=1}^{n}\left[\frac{\partial Z}{\partial x_i}Unc_i\right]^2\right)} \tag{4.8}$$

Experimental uncertainties associated with the measured parameters are listed in Table 4.2, whilst Table 4.3 presents the uncertainties on derived parameters within the experimental test range of flow rates.

Table 4.2: Measurement error

Error (Absolute)	1 LPM	4 LPM	7 LPM
T_j [Turbo] (°C)	5.0	5.0	5.0
T_j [OC] (°C)	N/A	5.0	5.0
$\dot{V}$ (L/min)	0.03	0.09	0.18
ΔP (Pa)	17.5	85.0	250.0

Table 4.3: Uncertainty on derived parameters

Relative Error (%)	1 LPM	4 LPM	7 LPM
V_{jet}	3.7	3.7	3.7
Re_{jet}	4.1	4.1	4.1
P_p	6.8	3.5	3.5
R_{core} (Turbo)	5.9	6.9	7.2
R_{core} (OC)	N/A	5.3	5.6

4.3. Numerical Simulations

4.3.1. Computational Domain and Governing Equations

The CFD model, constructed within STAR-CCM+, was first developed for verification against experimental data. Noting that the same general features were used for the optimisation study, the imagery in the discussion below will use the baseline orifice plate design for conciseness.

Figures 4.6(a) and (b) depict the CAD representation of the Intel Alder Lake-S processor die. As mentioned earlier, the i5 12600K version and stress tests considered here only use the 6 rightmost P-cores, though the inactive cores are retained as they may be useful for future studies. Each P-core has a surface area of 3.4 x 2.2 mm², and as Figure

4.6 shows, the 6 active cores are not exactly centred on the geometric centre of the die. Additionally, the die itself is not centrally positioned on the geometric centre of the CPU base holder (Figure 4.2(b)). Therefore, when fully assembled to the motherboard, the CPU cores are not aligned with geometric centre of the heat exchanger base.

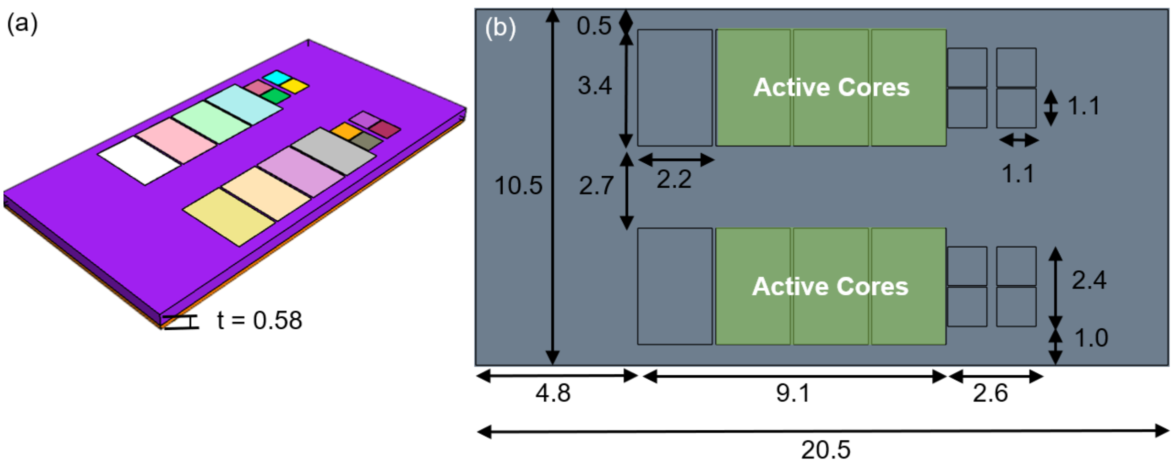

Figure 4.6: Intel Alder Lake-S processor die represented as, (a) an isometric CAD model with die thickness, t, specified, and (b) CAD model with die and core dimensions. All dimensions are in mm.

Figure 4.7(a) provides an illustration of the assembled computational domain including the CPU, TIM, and the coldplate heat exchanger, whereas Figure 4.7(b) illustrates the final mesh associated with the baseline design case. As it is illustrated, the fluid domain encompasses the flow path from the manifold inlet through the upper plenum chamber, orifice nozzles, lower plenum chamber, and exit port. The fluid domain geometry was subsequently imported into STAR-CCM+ and constrained by the non-variable geometry elements, including the coldplate base / IHS and CPU. A thermal interface material thickness of 0.2 mm was selected based on the typical range of thicknesses expected for an interface material, which is dependent on both material and application [29]. Due to this, the TIM is the largest source of uncertainty in the set-up of this CFD problem.

Similar to the study in the previous chapter, the STAR-CCM+ model developed for simulation utilised a steady-state, coupled implicit solver with a second-order upwind discretisation scheme to accurately capture flow gradients. The convergence criterion for the iterative solver was defined by a residual threshold of 10^{-6}, with automatic initialisation to establish consistent starting conditions for the solver, streamlining the simulation process and promoting efficient convergence.

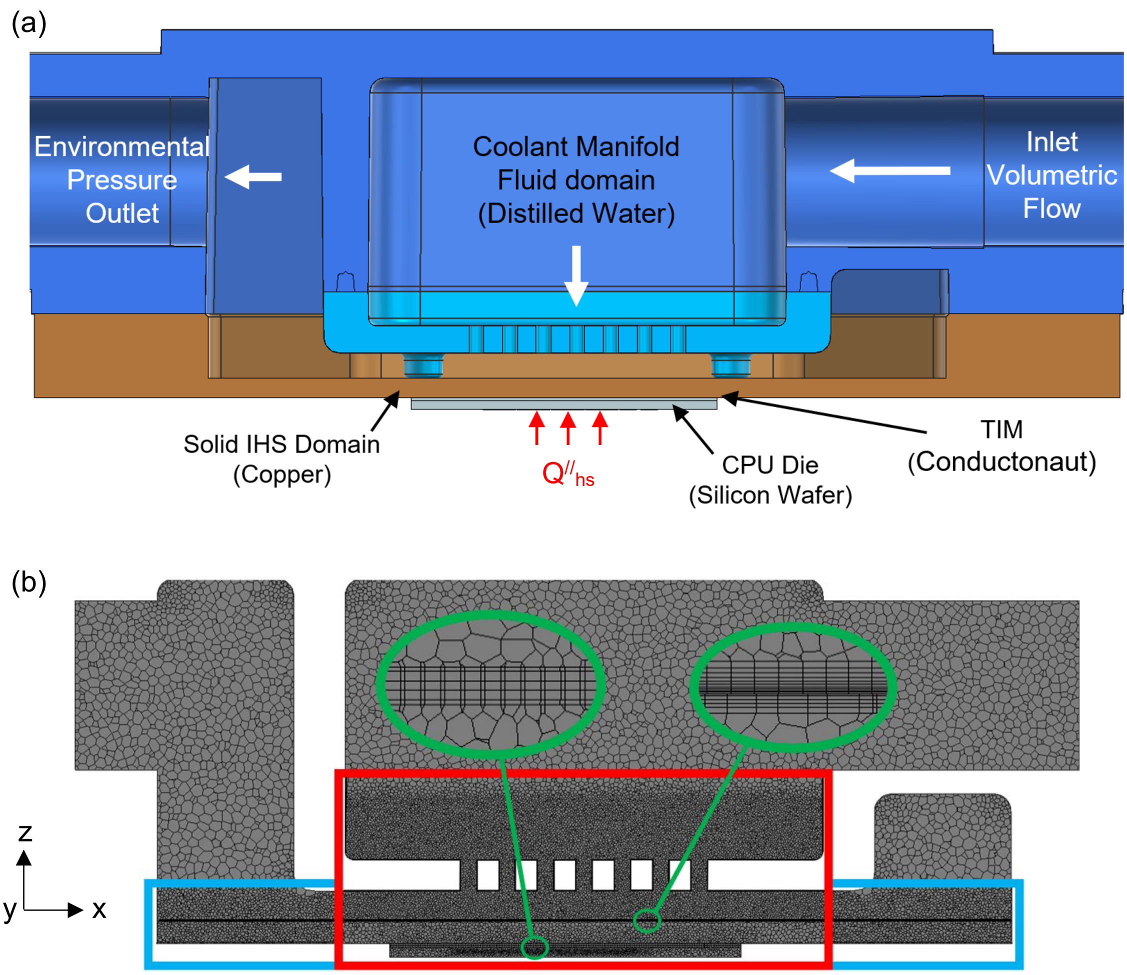

Figure 4.7: Sectioned view of (a) CAD model of computational domain, and (b) STAR-CCM+ domain mesh with localised mesh regions. Insert images show increased mesh density near interfaces.

Although not entirely negligible, thermal losses via conduction through the bottom of the CPU package and subsequent spreading into the motherboard were excluded from this study. These losses, estimated to account for approximately 5% of the total heat dissipation, were considered sufficiently minor to be omitted from the CFD optimisation. This decision was made to streamline the thermal analysis process, particularly given the substantial number of design points expected to be simulated during the multi-objective optimisation.

The study prioritises the dominant heat dissipation pathway through the cooling solution, that being the source-to-coolant route. Furthermore, accurately quantifying these losses experimentally would present significant challenges due to the configuration of the motherboard-CPU-heat exchanger assembly. The expected small magnitude of these losses, relative to the overall thermal budget, ensures they would not meaningfully impact the results of the impinging jet array optimisation. By focusing on the primary heat transfer mechanisms, the study maintains a clear emphasis on the most critical thermal performance factors.

For the CFD simulations solved within STAR-CCM+, the steady-state incompressible conservation equations for mass, momentum, and energy are as follows:

Conservation of mass:

$$\nabla . u = 0 \tag{4.9}$$

Conservation of Momentum:

$$u \cdot \nabla \mathrm{u} = -\frac{\nabla \mathrm{P}}{\rho} + \frac{1}{\rho}(\nabla \cdot \mu \nabla u) - (\overline{u'} \cdot \nabla \overline{u'}) \tag{4.10}$$

Conservation of Energy (Fluid):

$$\mathrm{u} \, . \nabla \mathrm{T} = \frac{1}{\rho}\left[\nabla \cdot \left(\frac{k_f \nabla T}{C_{pf}}\right)\right] \tag{4.11}$$

Conservation of Energy (Solid):

$$\nabla \cdot \left(\frac{k_s \nabla T}{C_{ps}}\right) = 0 \tag{4.12}$$

where u is the velocity of the fluid, u’ is the velocity fluctuation component due to turbulence, ρ is the fluid density, P is the pressure, μ is the dynamic viscosity, and T is the temperature. Additionally, k_i is the thermal conductivity and C_{pi} is specific heat capacity, with subscripts i = *f* & *s* representing the coolant fluid and solid respectively. Given the expected turbulence of the impinging jet flow, use of an adequately accurate turbulence model when applying the Reynolds-Averaged Navier-Stokes (RANS) approximation is imperative. As detailed recently in Elliott and Robinson [7], the SST (Shear-Stress Transport) k-ω was found to be the most appropriate turbulence model for the present problem, which aligns with the findings from existing literature [30-32].

Since the monitoring software limited the CPU core power measurement to the sum total across all cores, the heat input boundary condition in the simulations was applied in the same way, with the total measured power divided equally across all of the cores. For the verification process, simulations were conducted under two CPU power conditions: the maximum Turbo thermal design power of 150 W and the maximum overclocking (OC) power of 210 W, which were determined from the experimental measurements. An environmental (atmospheric) pressure boundary condition was set at the outlet port, while a set volumetric flow rate was applied at the inlet port. Additionally, no-slip boundary conditions were imposed on all fluid regions in contact with solid surfaces. Consistent with the experimental study, the verification simulations were caried out over a flow rate range of 1 - 7 L/min with the inlet temperature of 35°C.

From a practical point of view, coldplate heat exchangers will typically be deployed either in a pumped flow loop or in a scenario where a controlled pressure drop exists, say between a distribution and collection manifold. Either way, the net flow rate through the coldplate, and thus its heat transfer performance, will be influenced by its flow resistance. For the optimisation study performed in this work, the former scenario was selected, such that the flow rate for a given design was determined by the operating point on a specific pump curve, chosen here to be the TCS M500 series micropump. To achieve this, the inlet flow condition was set to the TCS M500 pump curve and the converged flow rate is an output of the overall iteration routine of the simulation. In this way, each jet array design configuration results in a unique operating point on the pump curve, and thus unique flow rate, pressure drop, pumping power and junction temperature, with the latter two being the main hydraulic and thermal performance indicators used when comparing different designs. For specific details of the pump and associated pump curve, the reader is directed to Elliott and Robinson [7].

Finally, it should be noted that for the baseline case, the jet array area was centred on the coldplate base opposed to the area enclosed by the cores. However, for the optimisation study, which will be shown to produce very targeted cooling designs, the jet array was centred on the area of the cores.

4.3.2. Meshing, Mesh Independence, and Convergence

The CFD simulation model required a mesh of sufficient density to ensure convergence of the flow simulations while maintaining a balance between accuracy and computational time, given the large number of design points anticipated for the optimisation study. The mesh, depicted in Figure 4.7(b), was constructed using polyhedral cells over a base tetrahedral mesh. The advantage of polyhedral cells lies in their ability to reduce maximum cell skewness, allowing for better flow alignment with cell faces and minimising interpolation errors [33].

To capture the boundary layers effectively, particularly in the jet impingement regions near the solid base, an advanced layer meshing strategy was employed. This approach generated layers of prismatic cells near boundaries, improving the resolution of the boundary layer interactions at domain interfaces [34]. The region surrounding the impingement area maintained a y^+ value of unity. This localised meshing was performed in two stages: the first stage covered the channel between the orifice plate and the heat spreader to ensure accurate resolution of the fluid boundary layers downstream of the jet impingement; the second, more refined stage focused on the orifice plate region. This allowed the mesh to accommodate jet diameters from as small as 0.5 mm, the smallest used in the optimisation study. Enhanced mesh density was also applied to the CPU die and cores to ensure mesh resolution for capturing of junction temperatures (see Figure 4.7(b)).

A mesh independence study was conducted by progressively increasing the number of mesh cells to determine the point at which changes in tracked parameters were less than 1% between successive meshes. Table 4.4 gives examples of the influence of mesh count on the two most relevant parameters, junction temperature and pressure drop, showing adequate mesh independence at approximately 3 million cells. For each simulation, convergence criteria were set to root mean square (RMS) residual levels of 1 $x10^{-6}$. As with the previous investigation covered in Chapter 3, the Grid Convergence Index is included here, as defined by [35], supporting solution convergence with a consistent decrease across mesh levels.

Table 4.4: Mesh independence study

Parameter	I	II	III	IV	V	VI
No. of elements ($x10^6$)	0.51	1.01	1.81	2.48	3.07	3.76
T_j diff. (%)	-	5.21	5.58	3.81	1.22	0.32
ΔP diff. (%)	-	14.59	7.87	3.32	1.57	-0.55
GCI	-	-	84.48	7.02	0.14	3.19 $x10^{-12}$

4.3.3. Simulation Model Verification

Elliott and Robinson [7] verified the accuracy of a similar CFD simulation model, though for a simplified case of uniform heat sources with an IHS. This model did not include a CPU processor with multiple discrete cores, so the main task here is to verify the efficacy of the present model, which includes the idealised CPU architecture and associated assumptions so that it can be used with confidence in the ensuing optimisation study. To achieve this, the experimental apparatus described previously was used to generate a set of experimental results for the selected CPU configuration to verify the numerical model. Experimental data was compared with the simulation predictions under two power conditions: Turbo TDP of total power Q_{hs} = 150 W representing a core heat flux of Q''_{core} = 334 W/cm^2, and maximum overclocking power of Q_{hs} = 210 W representing a core heat flux of Q''_{core} = 468 W/cm^2. Flow rates between 1 - 7 L/min were tested, though for the overclocking scenario, flow rates below 4 L/min were not possible because they resulted in junction temperatures approaching the maximum allowable temperature of T_{j_max} = 100°C, where throttling occurs to safeguard the CPU.

Plots illustrating the thermal-hydraulic comparison between the simulation predictions and experimental results are presented in Figure 4.8. The results show that the simulations accurately predicted both the magnitude and trends of the junction temperature, T_j, (Figure 4.8(a)) and core thermal resistance, R_{core}, and source-to-sink overall heat transfer coefficient, U_{core}, (Figure 4.8(b)), with both increasing flow rates and power. Notably, Figure 4.8(b) shows a non-negligible difference in the experimental R_{core} and U_{core} values for the two core heat flux levels, and this too is accurately captured by the simulation model. As will be discussed later, the small area of the cores results in non-negligible thermal resistance across the silicon die. Silicon thermal conductivity is also quite sensitive to temperature, with a temperature coefficient of about 0.42 (W/mK)/K over the range of temperatures measured here [36]. The increase in R_{core} and U_{core} with applied heat flux is thus primarily a temperature effect owing to the decrease in the silicon thermal conductivity, which is of the order of 10% lower at the higher heat flux temperatures. This illustrates an important nuance of the present work compared with the simplified treatment of the heat loading for representing semiconductor electronics typically used in the past, including recent work by the present authors [7].

The CFD simulations predict the experimental thermal data within the associated experimental uncertainty ranges. Similarly, comparison of the predicted and measured hydraulic parameters are acceptable, with the pressure drop (Figure 4.8(c)) and pumping power (Figure 4.8(d)) trends correctly captured, with discrepancies consistently around 10%. This is outside of measurement error, and predominantly due to the slight under sizing of the orifices and the residual roughness produced during the manufacturing process. Despite this, the comparison is more than adequate for the purposes here, and the simulation model is deemed sufficiently accurate for the simulation-driven optimisation design study.

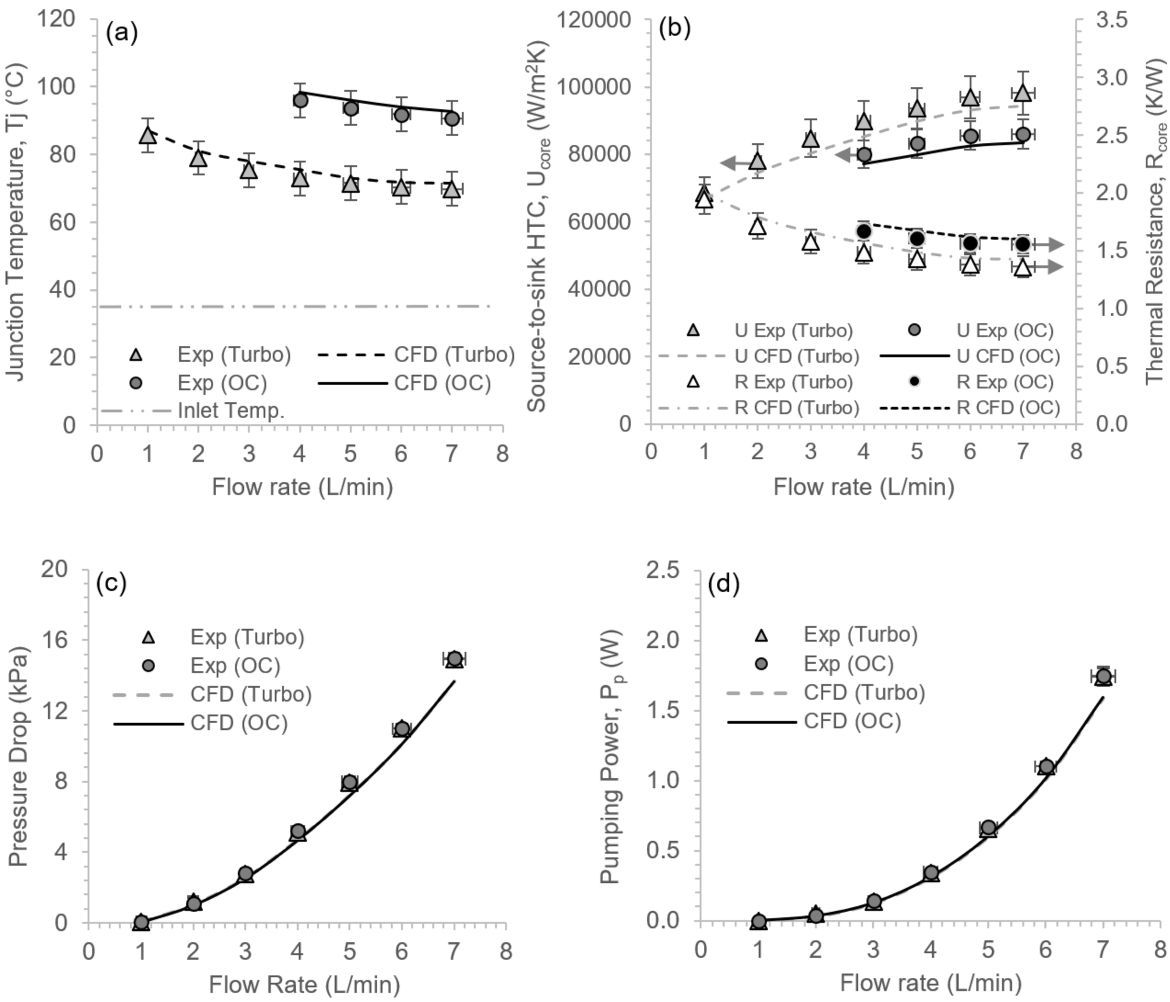

Figure 4.8: Comparison between numerical and experimental data for the Intel i5-12600K CPU with varying coolant flow rate: (a) Junction temperature, (b) core thermal resistance and source-to-sink overall heat transfer coefficient, (c) pressure drop, and (d) hydraulic power. All tests were carried out with an inlet coolant temperature of T_{in} = 35°C, for heating loads of Q_{hs} = 150W (Turbo, Q''_{core} = 334 W/cm^2) and Q_{hs} = 210W (OC, Q''_{core} = 468 W/cm^2).

4.3.4. Optimisation Workflow

The automated optimisation workflow developed in this study builds upon the methodology established by Elliott and Robinson [7], modified to accommodate the Intel i5-12600K CPU architecture. As detailed in Elliott and Robinson [7], the optimisation strategy integrates three separate commercial software packages operating within a feedback-type loop, driving each design iteration towards a global optimum. Siemens NX was used as the

CAD modelling platform to generate the variable heat exchanger geometries, specifically focusing on the orifice plate, which was the primary component undergoing optimisation. Figure 4.9 illustrates the key geometric design variables used to optimise the heat exchanger, namely the jet-to-jet spacing ratio (S/D), jet-to-target distance ratio (H/D), total jet population (N), and jet diameter (D). The range studied for each parameter is given in Table 4.5. For a given set of design parameters, the geometry was then auto-imported into STAR-CCM+ for the CFD simulations, and this is facilitated by the CAD-embedded feature of Siemens NX. Other essential solid components, such as the heat exchanger manifold & base, CPU die & cores, and the TIM were modelled directly within STAR-CCM+ since they did not involve variable geometries, thus simplifying the CFD domain setup for successive design points.

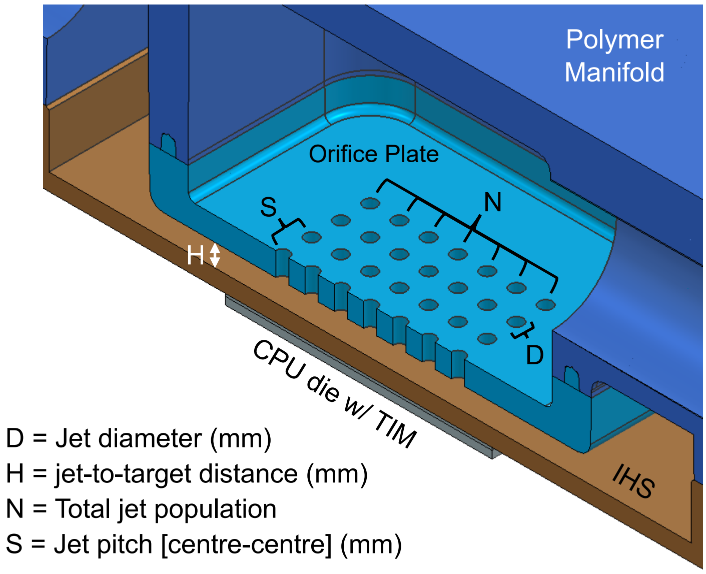

Figure 4.9: Sectioned isometric model geometry, highlighting geometric variables for optimisation.

The optimisation itself was managed through the Hierarchical Evolutionary Engineering Design System (HEEDS) software, which interfaced with STAR-CCM+ to import simulation results and evaluate them against predefined objective functions. For each successive design point, HEEDS updated the geometry in NX CAD, which was then auto-imported into STAR-CCM+, triggering the next CFD simulation. This cycle continued until a targeted number of feasible design iterations was reached. For this investigation, 175 design variations was found to be sufficient.

The primary objective of this study was to develop an automated design process capable of executing Multi-Objective Optimisations (MOO) for a jet array impingement coldplate heat exchanger. For this study, the optimisation sought to balance two key targets; the maximising of the cooling intensity while minimising overall hydraulic energy consumption. To achieve these goals, two objective functions were chosen for the automated process; the CPU core junction temperature, T_j, and the pumping power, P_p. The overarching aim was to minimise both T_j and P_p to optimise thermal performance and system efficiency. Within the HEEDS optimisation platform, the SHERPA hybrid adaptive algorithm was employed to coordinate the optimisation of each design parameter. This algorithm adapts its approach with each design iteration, allowing the process to efficiently navigate the design space in search of global optima. By continuously refining its methodology, SHERPA facilitated the discovery of converged solutions while reducing computational time and effort.

Table 4.5: Geometric variable ranges for optimisation

Parameter	Description	Unit	Range
S/D	Jet spacing ratio	-	1.17 - 6.5
H/D	Jet-target ratio	-	0.17 - 5.5
N	Jet population	-	9 - 169
D	Jet diameter	mm	0.5 - 1.5

4.4. Results

4.4.1. Optimisation Pareto Plot

Figure 4.10 presents the Pareto Plot associated with the 175 feasible design solutions simulated across the multi-parameter design space. The vertical and horizontal coordinates are the pumping power, P_p, and the junction temperature, T_j, respectively, as they are the two objective functions considered in this study. The plot reveals a well-defined Pareto

Front, which delineates between the regions of feasible and non-feasible solutions. As discussed, the range of pumping power across the design space was determined by the operating point on the selected pump curve for each design iteration, which varied in response to the pressure drop characteristics inherent to the jet array configuration at each design point. Consistent with the study of Elliott and Robinson [7], some clustering is observed along the Pareto front, and this is indicative of the adaptive capabilities of the HEEDS MO-SHERPA algorithm. The feasible solution space encompasses a junction temperature range of 88.67°C to 108.6°C, remembering that the throttling temperature of the CPU is $T_{j,max}$ = 100°C, which is marked in the figure. The hydraulic pumping power ranged between 0.37 W and 2.33 W, with the later approximately that of the maximum pumping power of the selected pump, $P_{p,max}$ = 2.34 W [7].

Also marked on the Pareto Plot is the baseline orifice design point which, while close to the Pareto Front, was not optimised towards either objective, along with the designs which minimise the junction temperature (SOO optimum, closest to the vertical axis), and simultaneously minimise both the junction temperature and pumping power (MOO optimum, closest to the origin). Both the SOO and MOO designs will now be discussed in more detail.

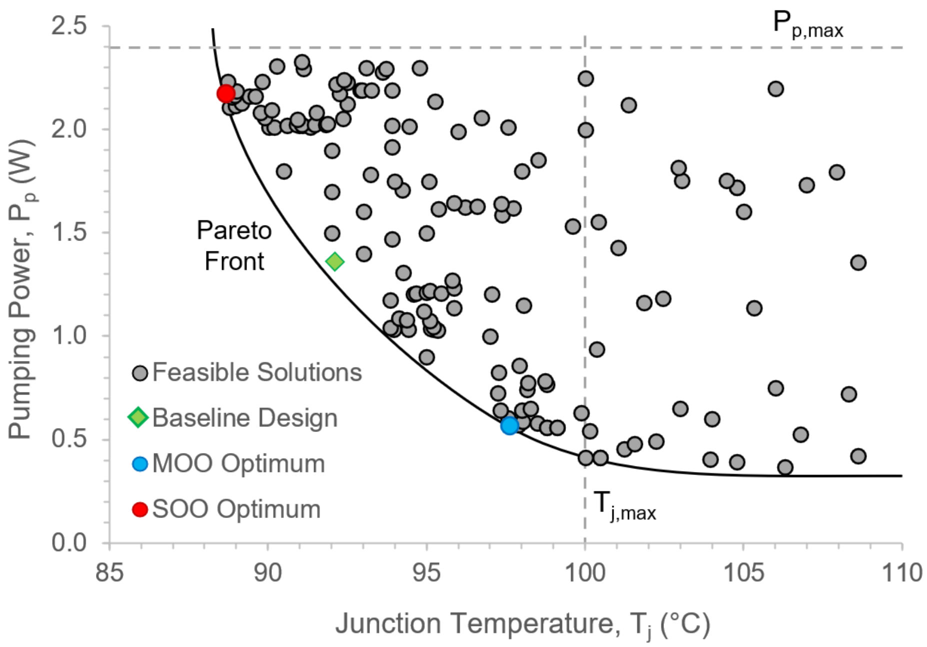

Figure 4.10: Pareto plot containing all 175 feasible design solutions for an input power condition of Q_{hs} = 210 W (Q''_{hs} = 468 W/cm^2) for inlet coolant temperature of T_{in} = 35°C.

4.4.2. Single Objective Optimum Orifice Design

Table 4.6 lists the relevant design parameters and thermal-hydraulic performance data for the SOO optimal design configuration. This design generates a net core-to-coolant thermal resistance of R_{core} = 1.52 K/W which results in an average junction temperature of T_j = 88.6°C for an orifice design with N = 9 jets of D = 1.5 mm diameter, S/D = 2.17 and H/D = 0.83. The volumetric flow rate is $\dot{V}$ = 4.9 L/min with a net pressure drop of ΔP = 26.7 kPa and associated pumping power of P_p = 2.18 W, as dictated by the operating point on the chosen pump curve. Compared with the baseline, the SOO optimum design features fewer jets of larger diameter which are more concentrated on the projected region that encloses the array of cores, and results in a 3.5 K drop in average junction temperature with a 0.9 W increase in pumping power.

This design architecture confirms earlier findings of Elliott and Robinson [7] for maximum cooling of concentrated heat sources. Despite the presence of a heat spreader, the SOO design favours fewer larger diameter jets with low inter-jet spacing, such that the impinging flow is focussed on the heat source zone, as depicted in Figures 4.11(a) and (b). Elliott et al. [13] provide the reasoning underpinning this concentrated cooling result as being related to conjugate heat transfer effects, whereby increasing the aggressiveness of the convective cooling causes the spreading efficiency of the IHS to reduce, which is antagonistic to the aim of reducing the convective-side thermal resistance. In response, the optimal design favours concentration of as much available coolant supply to a region commensurate with that of the heat source. This is demonstrated in this SOO design which, as depicted in Figures 4.11(a) and (b), produces high velocity (~5 m/s) jets that are arranged in a focussed array inside the region enclosed by the CPU cores. Additionally, some specific design features influence the fluid dynamics and associated forced convective cooling effectiveness. These have been detailed in Elliott and Robinson [7], and for conciseness only the most relevant features will be overviewed here.

As Figures 4.11(a) and (c) depict, the flow directly above the orifice plate is almost stagnant and of uniform pressure, which has an equalising effect of the flow across the array. Subsequent to accelerating into and through the nozzles, inertia-dominated (Re_{jet} = 10,646) jets are issued into the lower gap region and subsequently impinge on the heated interior base of the coldplate. Figure 4.4(c) shows that the constriction of the flow into the nozzles is the dominant pressure drop region, and a high vorticity shear layer is formed along the interior walls of the nozzles owing to the sharp leading edges (Figure 4.11(d)). The high jet inertia combined with the low inter-jet spacing of S/D ~ 2 and low jet-to-target spacing of H/D < 1, create close to ideal perpendicular jet profiles.

Table 4.6: SOO optimum orifice design and thermal hydraulic data

Parameter	Value	Orifice CAD
S/D	2.17	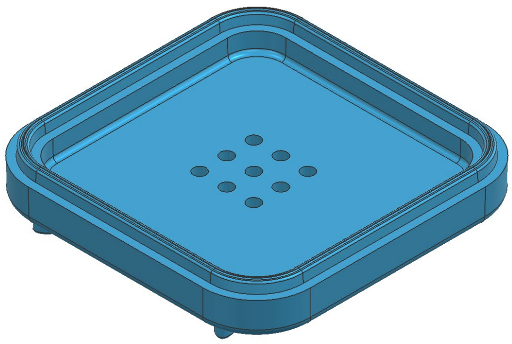
H/D	0.83	
N	9	
D (mm)	1.50	
V_{jet} (m/s)	5.14	
Re_{jet}	10,646	
T_j (°C)	88.60	
ΔP (Pa)	26,679	
$\dot{V}$ (L/min)	4.90	
P_p (W)	2.18	
R_{core} (K/W)	1.52	
U_{core} (W/m^{2}K)	87,765	

As is clear in Figure 4.11(a), the jets are of sufficient inertia and proximity to the target surface that crossflow effects do not cause significant jet deflection at the impact sites. As a result, their potential cores remain relatively intact up to the point of impingement with the surface. This produces a region of high stagnation pressure (Figure 4.11(c)), as well as a high local convective heat transfer coefficient (Figure 4.11(e)), that extends the approximate diameter of the jets. Notably, the convective heat transfer coefficient in these stagnation zone regions achieve magnitude levels in the region of approximately 70,000 - 90,000 W/m^{2}K, and is fairly consistent across all of the jets in the array owing to the similarity in their fluid dynamics behaviour.

The stagnation pressure region on the surface directly below the nozzles creates a horizontal pressure gradient in the lower channel, and this leads to the formation of horizontal wall jets which flow radially outwards from the stagnation zones. Notably, the rapid directional change of the wall jets along the surface produces high near-wall vorticity, indicative of intense fluid mixing. In between neighbouring jets, the inter-jet spacing is small enough that wall jet collisions occur with sufficient inertia to produce up-washing of the fluid near the approximate midpoint between adjacent jets. This creates an additional peak of the convective heat transfer coefficient, revealing increased convective cooling intensity, as evident in Figure 4.11(e). Overall, Figures 4.11(a) and (e) illustrate that this SOO jet array design sustains high convective cooling intensity over the approximate region of the cores, and does so by a combination of high Reynolds number jets with relatively large jet impingement zones (i.e. large diameter) which are in close proximity to the surface and to one another. The main penalty is that the hydraulic power is close to the maximum that the pump can produce, though this must be taken in the context that it is almost 100 times smaller than the net power to the cores.

Along with the convective heat transfer coefficient, Figure 4.11(e) also plots the convective heat flux at the solid-fluid interface. Their respective distributions over the full IHS surface are further visualised in Figures 4.12(a) and 4.12(b), where a clear similarity between the two is evident. Regions of high convective heat transfer intensity align closely with those of high convective heat flux over the entire IHS domain, and are predominantly concentrated over the geometric footprint of the CPU cores. The close correlation of the convective heat transfer coefficient and convective heat flux, with each being highly elevated over the region directly above the heat sources, clearly illustrates the targeted cooling nature of the SOO design. It is however noted that the heat spreading is by no means negligible, with Figure 4.11(e) and Figure 4.12 showing elevated convective heat transfer beyond the immediate core footprint. Though convection intensity and heat flux diminish outside the core region, the area of heat transfer escalates.

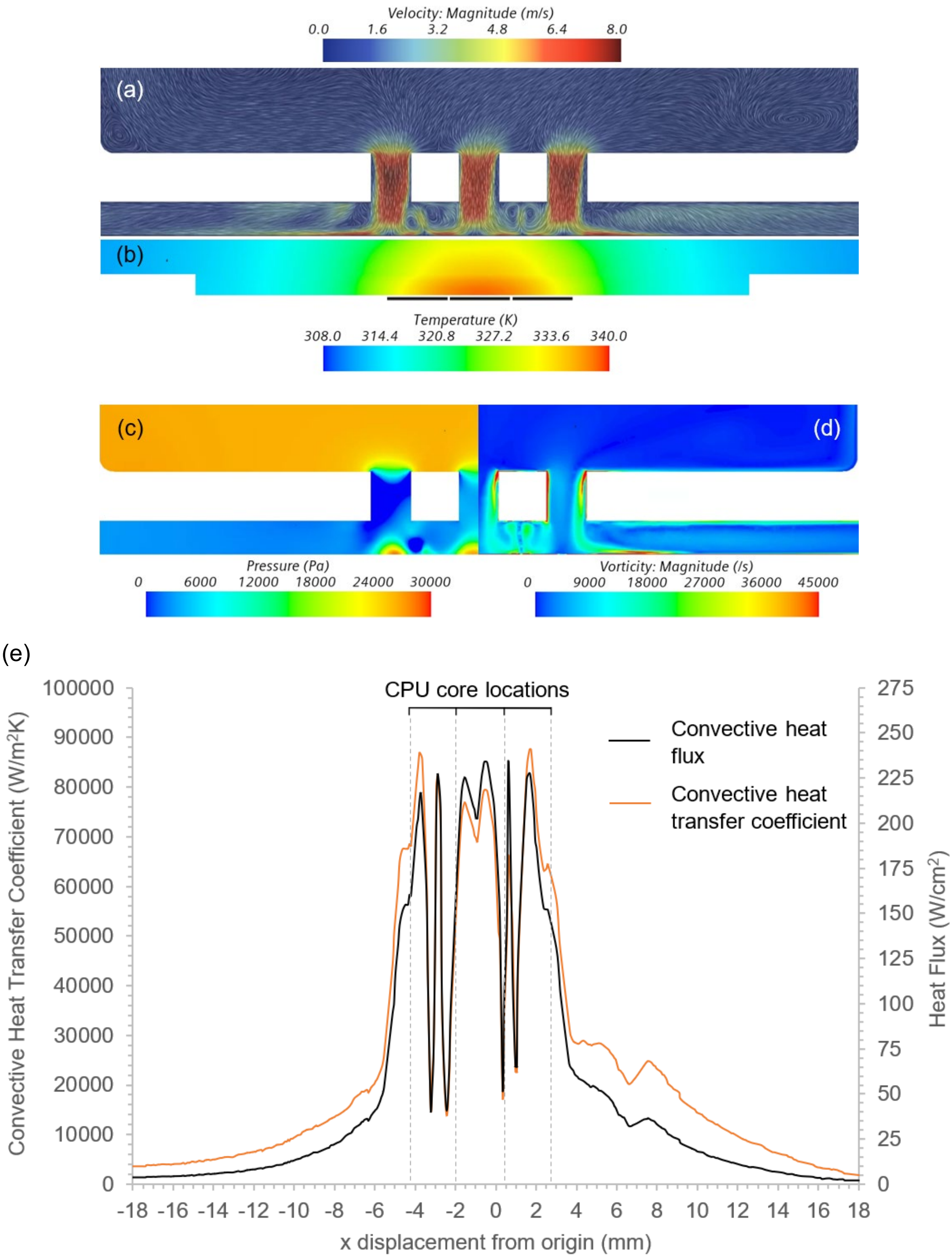

Figure 4.11: Sectioned SOO design cross-section plots through centre row of jets showing (a) velocity, (b) temperature, with active core locations highlighted, (c) pressure, and (d) vorticity fields, as well as (e) convective heat transfer coefficient and heat flux profiles with active core locations highlighted. Q_{hs} = 210 W, Q''_{core} = 470 W/cm^2, T_{in} = 35°C.

Overall, the design aimed at maximising heat transfer performance configures the jet array to aggressively target the heat-producing core region, with the heat spreading playing a secondary yet not insignificant role. From the hydraulic perspective, close to the maximum achievable pumping power is necessary to create the high velocity and highly turbulent jets to achieve the impressively high local convective heat transfer coefficients over a region that targets the cores.

An important contribution of this study is the consideration of a full CPU stacked package, which includes the discrete cores, semiconductor die, TIM layer, IHS, and forced convection. Compared with simplified scenarios typically considered previously, this is not as straight-forward a system to analyse in terms of the contribution of each component in the stack to the overall source-to-sink thermal resistance. Figure 4.13(a) is an attempt to demonstrate this, showing the CPU package stack with exposed cores and IHS surface (coloured by heat flux) that sandwich the solid components (coloured by temperature). As it is shown, the temperature profiles change both axially and laterally throughout the different solid materials in the stack, and this influences changes in the heat flux between the sources and the convective surface.

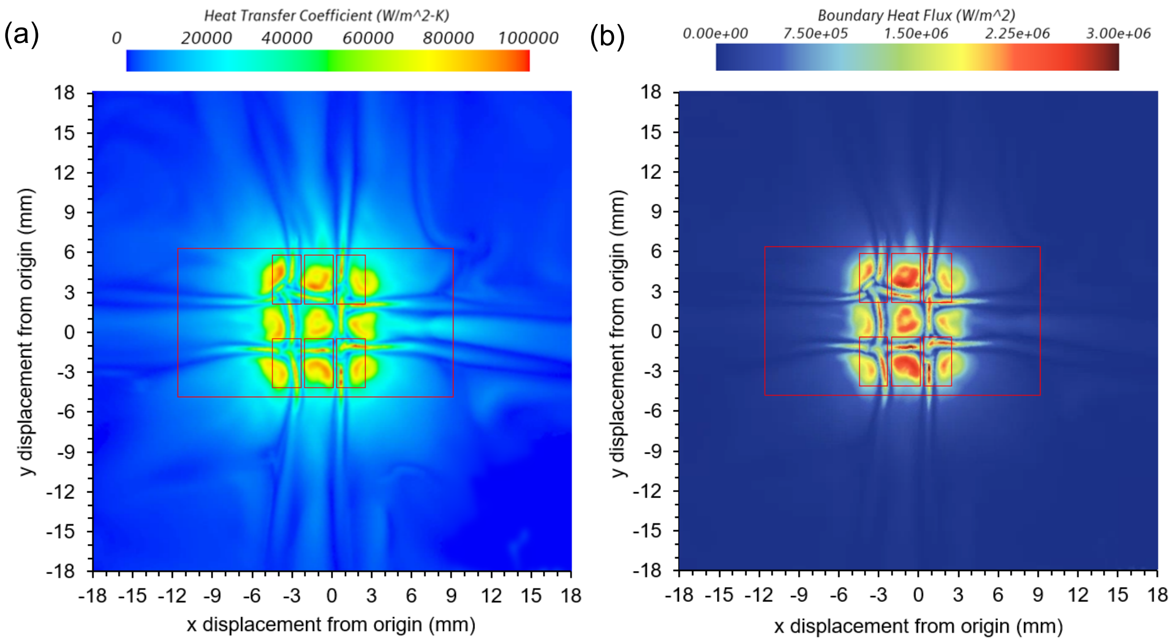

Figure 4.12: SOO design IHS-fluid interface: (a) convective transfer coefficient, and (b) convective heat flux distributions with CPU die with active core positions highlighted.

To get a practical sense of the heat transfer and associated thermal resistance contribution of each the die, TIM and coldplate heat exchanger (including spreading and convection), Figure 4.13(b) provides images of the surface temperature distributions on either side of each of the solid element in the stack. Additionally, Figure 4.13(c) plots the average temperature progression vertically through the solid and fluid domains above a single core area, along with the associated average heat flux at each solid-solid and solid-fluid interface. For reference, the total source-to-sink temperature drop, which is indicative of the total thermal resistance budget, is $\Delta T_{tot} = T_j - T_{in} = 53.6$ K. Hereafter, ΔT_{tot} will be referred to as the thermal budget.

Figures 4.13(b) and (c) show that a significant temperature drop occurs across the die, being in the region of 16 K, which is about 30% of ΔT_{tot}. The high contribution of the die to the overall thermal budget highlights an important take-away from this study. Notwithstanding the die being thin (t = 0.58 mm) and of reasonably high thermal conductivity (k_{Si} ~ 110 W/mK), the source heat flux at the cores is very high, being in the region of 470 W/cm^2. Furthermore, there is limited heat spreading in the die material, as visually apparent from the surface temperatures in Figure 4.13(b), and noted in Figure 4.13(c) from the moderate drop in surface heat flux (~20%) between the core and the adjacent region at the die-TIM interface. Therefore, despite the high thermal conductance of the silicon, which can be roughly estimated as k_{Si}/t ~ 190,000 W/m^{2}K, the high localised heat flux causes the temperature drop to be a considerable portion of ΔT_{tot}. The TIM material transfers a similarly high heat flux with minimal heat spreading, though owing to its low thickness (0.2 mm), incurs a lower yet not insignificant temperature drop of ~6 K, being in the region of 11% of ΔT_{tot}. The coldplate heat exchanger, which is here considered in its entirety (IHS & fluid domain), experiences the largest relative temperature drop of ~30 K, which is approximately 58% of ΔT_{tot}. Different from the die and TIM, the effect of heat spreading is apparent, both by visual observation of the temperature distribution on the top surface on the IHS (Figure 4.13(b)), and by the reduction of the convective heat flux above the selected core to ~180 W/cm^2, plotted in Figure 4.13(c), which is around 60% lower than that of the source

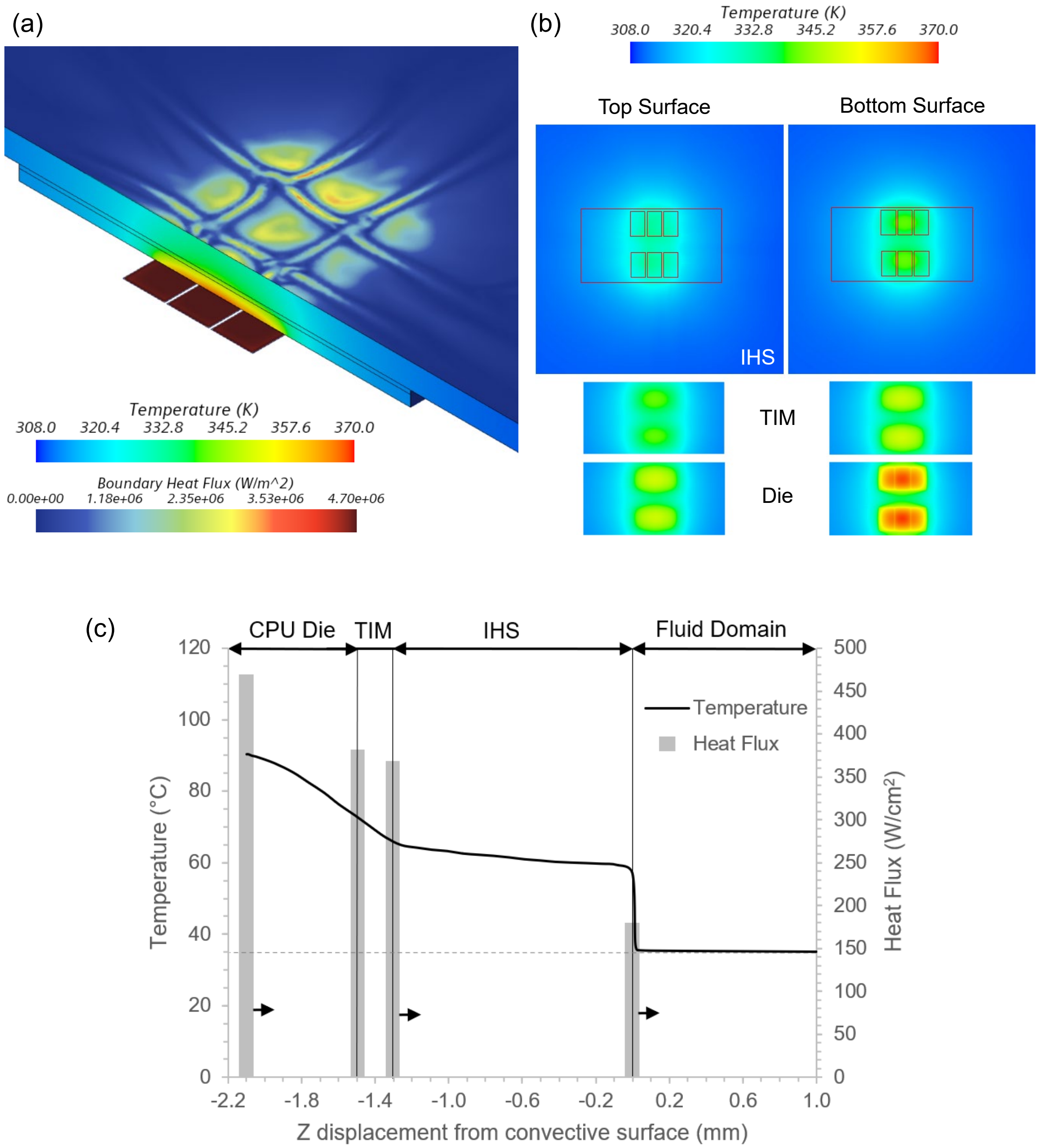

Figure 4.13: (a) Sectioned 3D contour of SOO solid domain geometry through centre of CPU core illustrating internal temperature distribution and surface heat fluxes, (b) temperature profile across contact surfaces of IHS, TIM and CPU die, and (c) line plot illustrating change in temperature through solid domain in z direction from centre of a CPU core to the convective surface, with associated heat flux at the contact interfaces between solid elements.

4.4.3. Multi-Objective Optimum Orifice Design

Table 4.7 details the relevant design parameters and the thermal-hydraulic performance of the MOO optimum design, which achieved a core-to-coolant thermal resistance of R_{core} = 1.78 K/W, a 17% increase compared to the SOO design. This resistance corresponds to an average MOO junction temperature of 97.5°C for a jet array configuration of N = 49 jets, with a diameter D = 1.5 mm, S/D = 2.5, and H/D = 1.5. As is clear from the image in Table 4.7, the higher population of jets and associated spacing results in a design that forces coolant over the full area afforded by the orifice plate. The larger total flow area has the effect of reducing the jet velocity and associated Reynolds number by just over 70%, which is considerable. However, the lower velocity jets incur a much lower pressure drop of ΔP = 4.7 kPa, which shifts the operating point on the pump curve to a marginally higher volumetric flow rate of $\dot{V}$ = 7.23 L/min, together yielding a very low pumping power of P_p = 0.56 W. This reflects a nearly 4-fold reduction in pumping power relative to the SOO optimum, though with a 9 K increase in junction temperature.

As with the SOO optimum, the general features of the MOO design for the discrete heat sources considered here align with those found by Elliott and Robinson [7]. As seen in Figure 4.14, comparatively the MOO and SOO jet profiles share some similarities. Particularly, they both induce high vorticity at the nozzle entry due to sharp flow constriction (Figure 4.14(c)), with the preponderance of the pressure drop occurring at the nozzle entrance (Figure 4.14(c)). In both designs, similar flow features such as the wall jet interaction creating the upwash effects between neighbouring jets are also evident (Figure 4.14(a)). Comparing Figure 4.11(a) with Figure 4.14(a), what is notably different relates to the lower jet velocities making them susceptible to influences from the flow in the upper manifold as well as crossflow within the channel. These effects are detailed in Elliott and Robinson [7], and overall result in some notable deflection of the jet profiles, particularly for those jets in the peripheral regions of the orifice plate. The lower impingement velocities and non-ideal jets negatively influence the convective heat transfer, which is depicted in Figures 4.14(e) and Figure 4.15. The first most notable difference compared with the SOO design is the much lower peak convective heat transfer coefficients, now ranging between 20,000 - 42,000 W/m^{2}K, with a clear tendency to diminish as the jet profiles become less ideal with increased distance from the centre. Secondly, the MOO design provides jet impingement convective cooling across a much larger area of the IHS. Therefore, despite the lower intensity of convective heat transfer, the MOO design leverages more of the available area of the heat spreader to sustain low thermal resistance with the lower velocity jets. This is clearly demonstrated when comparing Figures 4.11(e) and 4.12, with Figures 4.15(e) and 4.16, with the latter two showing elevated convective heat transfer coefficients and convective heat fluxes towards the near edge of the heat spreader. Simply put, minimising the hydraulic penalty fundamentally requires a reduction in the pressure drop, which is facilitated by a decrease in jet velocity. The knock-on effect is a reduction in the intensity of convective heat transfer. To compensate, the MOO design incorporates a higher population of jets to use more of the available heat spreader effective surface area, and thus sustain an overall low convective-side thermal resistance.

Table 4.7: MOO optimum orifice design and thermal hydraulic data

Parameter	Value	Orifice CAD
S/D	2.50	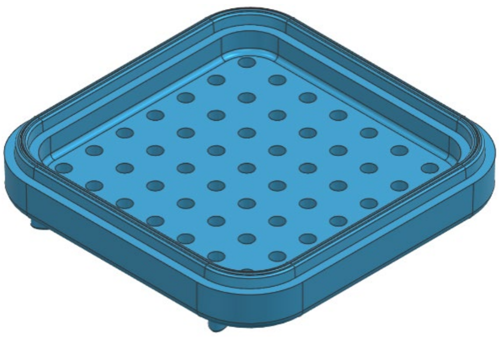
H/D	1.50	
N	49	
D (mm)	1.50	
V_{jet} (m/s)	1.39	
Re_{jet}	2883	
T_j (°C)	97.51	
ΔP (Pa)	4755	
$\dot{V}$ (L/min)	7.23	
P_p (W)	0.56	
R_{core} (K/W)	1.78	
U_{core} (W/m^{2}K)	75,052	

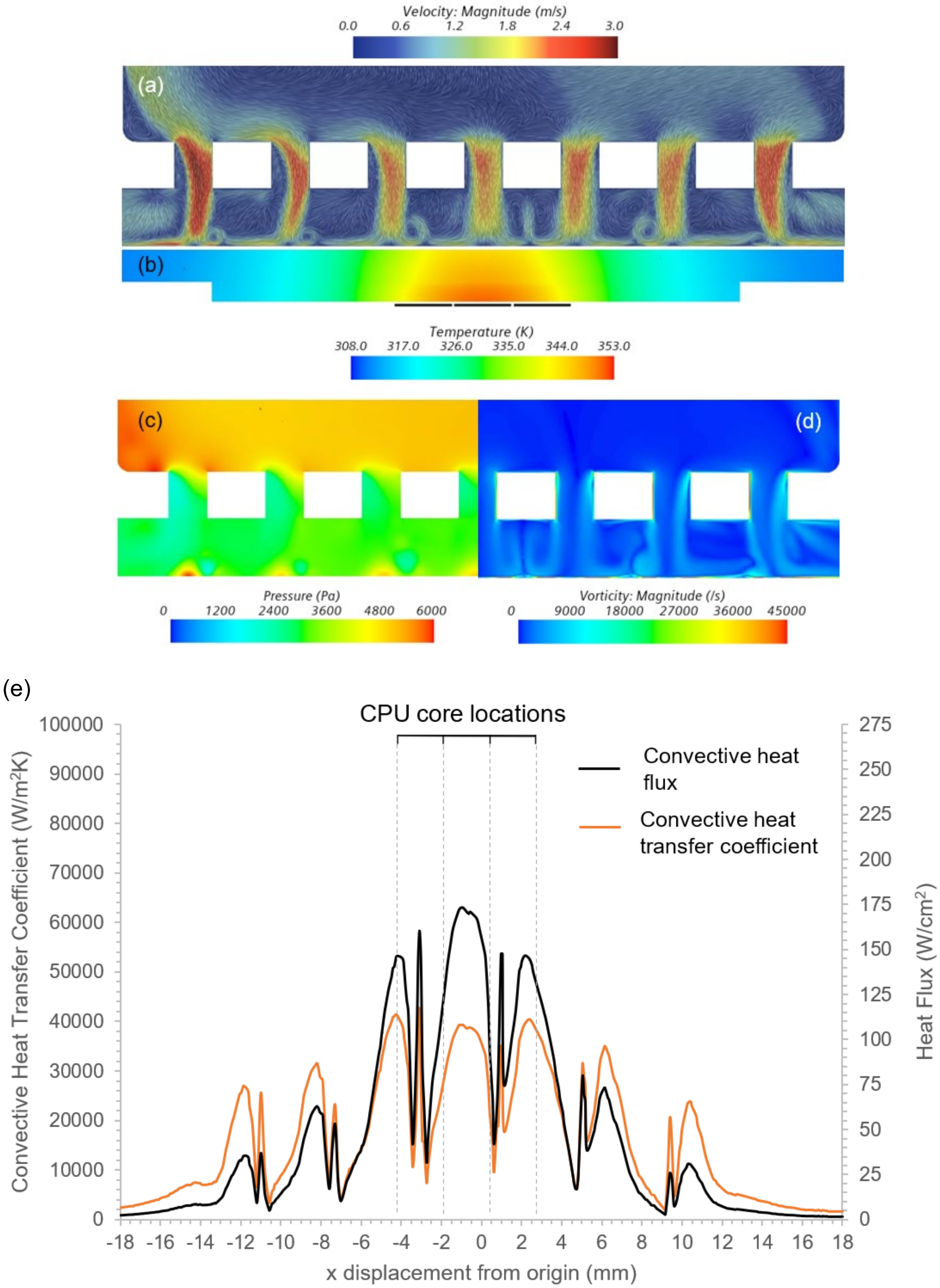

Figure 4.14: Sectioned MOO design cross-section plots through centre row of jets showing (a) velocity, (b) temperature, with active core locations highlighted, (c) pressure, and (d) vorticity fields, as well as (e) convective heat transfer and heat flux profiles. Q_{hs} = 210 W, Q''_{core} = 470 W/cm^2, T_{in} = 35°C.

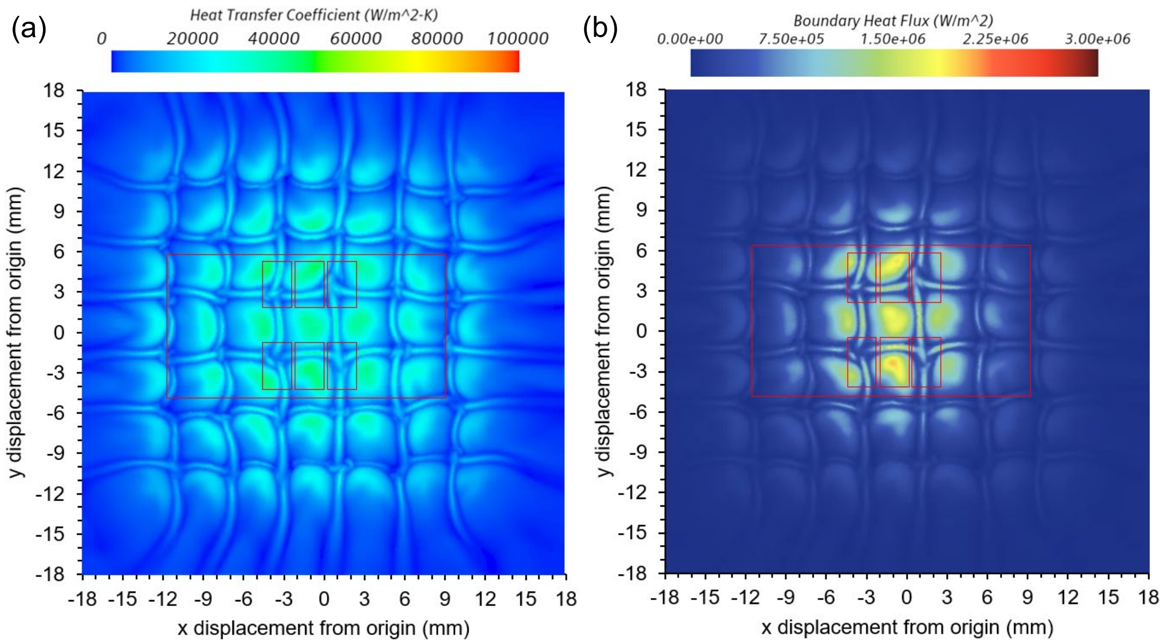

Figure 4.15: MOO IHS-fluid interface (a) convective transfer coefficient, and (b) convective heat flux distributions with CPU die and active core positions highlighted.

In a similar fashion as outlined for the SOO design case, Figure 4.16 presents the simplified breakdown of the heat transfer across the full CPU package stack. For reference, the total source-to-sink temperature drop, which is again indicative of the total thermal budget, is ΔT_{tot} = 62.6 K, compared with the 53.6 K for the SOO design.

Focussing on Figure 4.16(c), it is first clear that the overall thermal behaviour of the die and TIM for the MOO case are nearly identical to that of the SOO case, and this is unsurprising. However, due to the larger thermal budget, their relative contributions to ΔT_{tot} decrease by a few percentage points. A slight increase in the temperature drop (~1 K) and top-side heat flux across the die is noted, and this is due to the aforementioned higher die temperature causing a slight decrease in thermal conductivity of the silicon and increasing thermal resistance. The main difference in the MOO design is related to the coldplate. Comparatively, the temperature drop has increased by 8 K, contributing over 60% of the already larger thermal budget compared with the SOO design. However, this can be considered a marginal heat transfer penalty, in the context that the convective heat transfer intensity has approximately halved, and the pumping power has dropped by a factor of four. Reiterating, to mitigate the overall decrease in convective cooling intensity, the heat spreader area is used more effectively which is clearly represented by the convective heat flux above the core shown in Figure 4.16(c) dropping to ~120 W/cm^2, a 74% reduction compared to the source and indicative of the fact that the majority of the heat is now transferred to the fluid in the outer region away from the cores.

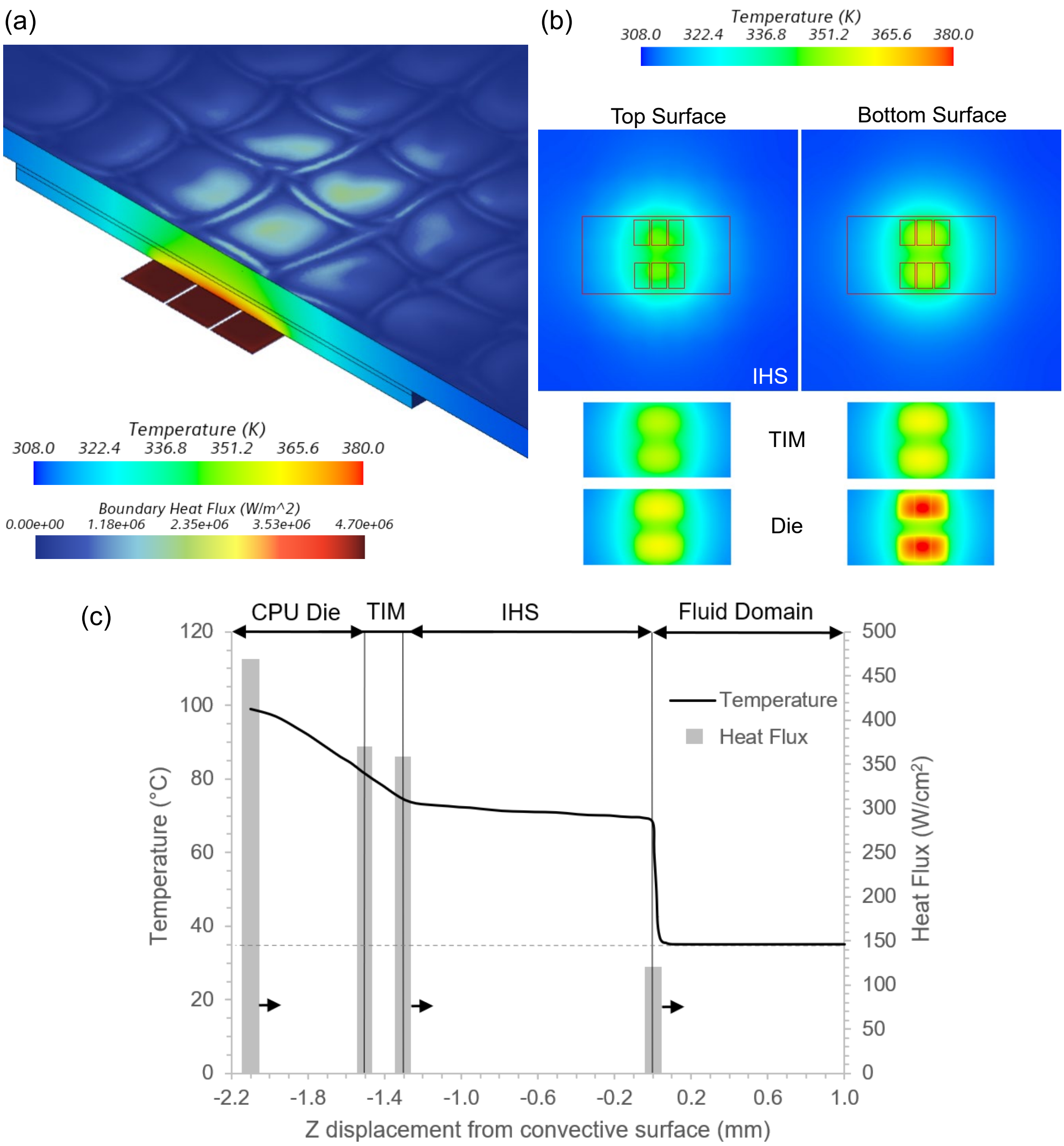

Figure 4.16: (a) Sectioned 3D contour of MOO solid domain geometry through centre of CPU core illustrating internal temperature distribution and surface heat fluxes, (b) temperature profile across contact surfaces of IHS, TIM and CPU die, and (c) line plot illustrating change in temperature through solid domain in z direction from centre of a CPU core to the convective surface, with associated heat flux at the contact interfaces between solid elements.

4.4.4. Overall Comparison of Optimised Designs

Figure 4.17(a) compares and contrasts the geometric design parameters of the two optimum jet array heat exchangers. For the range of parameters tested, they both use large diameter (D = 1.5 mm), closely spaced (S/D < 2.5) jets that are issued close to the target surface (H/D < 2). These ensure area coverage dominated by stagnation zones for jets that impinge within their potential core regions. The greatest variation is clearly the jet population, N, which differentiates between the targeted cooling of the SOO design and the more global cooling of the lower energy consumption MOO design. Figure 4.17(b) compares the selected thermal-hydraulic performance outputs for the two optimum orifice designs, showing the disproportionate difference in the hydraulic pumping power relative to that of the core junction temperature. Importantly, both designs are capable of maintaining a junction temperature below the 100°C throttling limit, so the most suitable design choice depends on the importance of energy consumption in application. This being said, the MOO design discussed above puts equal weight on the two objective functions, whereas the Pareto Front shown in Figure 4.10 clearly indicates that optimal design options exist between the SOO and MOO extremes that can involve different weighting on the objective functions.

Figure 4.18 illustrates the total thermal budget for the SOO and MOO designs, with an indicative breakdown of the thermal contribution attributed to each component in the stack between the heat source and coolant. The thermal budget depicted in the figure is for a representative single CPU core and should be taken as semi-quantitative, and is presented to highlight that despite the dominance of the coldplate thermal resistance, the die resistance is non-negligible, being in the range of 28 - 31% of the total thermal budgets. Including the TIM resistance of the order of 10% means that a significant portion (~40%) of the thermal budgets are taken up by non-coldplate heat exchanger components in the stack. As such, larger percentage improvements in the coldplate thermal resistance have a lower overall impact on the total core-to-coolant thermal resistance. Notably here, the SOO coldplate performs about 20% better than the MOO coldplate, though results in a lower 14% improvement in the overall thermal budget.

The convective intensity profiles observed for the two optimisation scenarios, depicted in Figures 4.11(e) and 4.14(e), highlight the successful realisation of the targeted convective intensity distributions initially outlined in both Chapter 2 of this thesis and Elliott et al. [13]. These results demonstrate two distinct strategies for thermal management optimisation; the sharply concentrated distribution achieved with the SOO orifice geometry, which proved highly effective for localised heat transfer, and the broader, less intense distribution produced by the MOO optimum, utilising an increased jet population and reduced jet velocities to deliver a more uniform, global cooling approach. These contrasting approaches underscore the efficacy of the methodologies employed in this investigation and capability of the developed framework in advancing optimised thermal management solutions tailored to specific objectives.

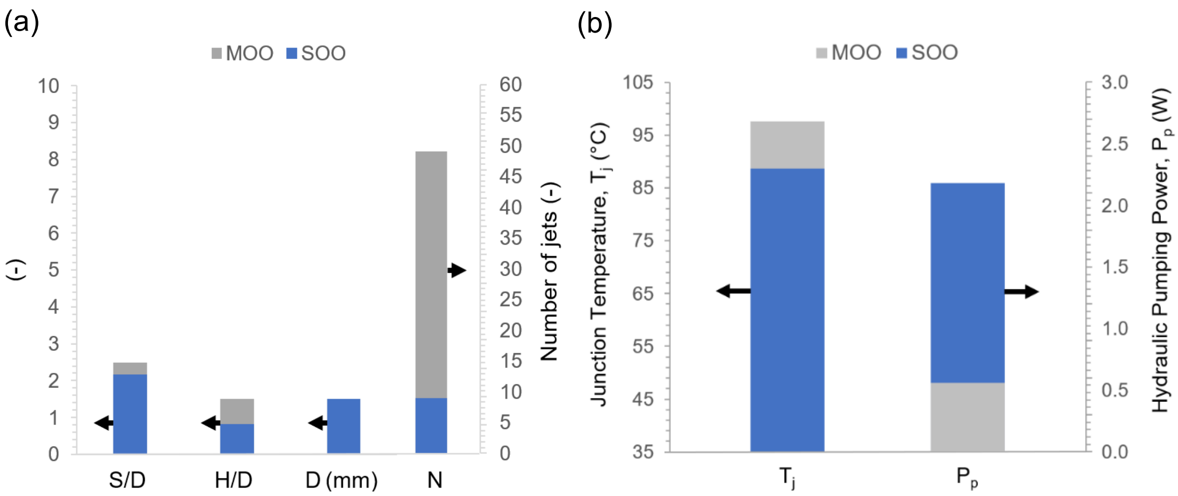

Figure 4.17: Comparison between SOO and MOO optima showing summaries of (a) geometric design parameter, and (b) thermal-hydraulic performance metrics.

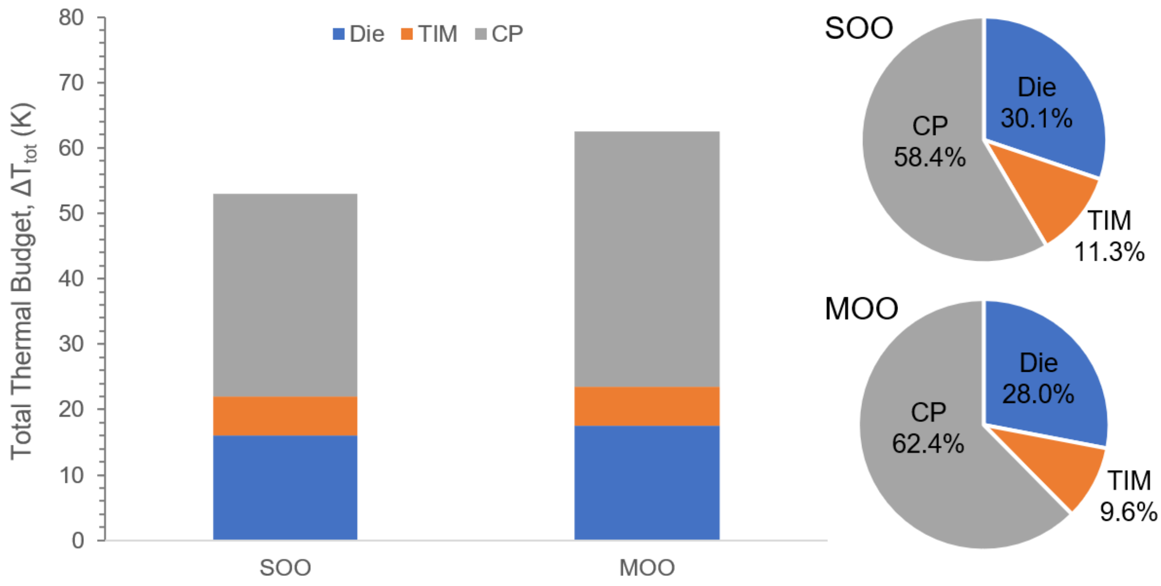

Figure 4.18: Approximate thermal budgets of MOO and SOO designs including breakdown into die, TIM and coldplate.

4.4.5. Optimised Experimental Validation

As a final proof-of-concept test of the developed design optimisation methodology, both optimised heat exchangers were manufactured and tested experimentally using the same procedure outlined earlier. Since there is a high uncertainty on the core temperature measurement with the on-die sensors, together with some small variations in the total core power between tests ($\bar{Q}_{hs}$ = 210.5 W, σ = 2.3 W), each coldplate was tested 10 times from a cold start, and the means ($\bar{T}_j$ & $\Delta\bar{P}$) and standard deviations, σ, used for comparison against the CFD simulations.

The results listed in Table 4.8 demonstrate the efficacy of the automated optimisation methodology developed in this work, with manufactured and tested optimised heat exchangers reproducing the thermal and hydraulic performance predicted by the CFD simulations, within or sufficiently close to 2σ from the respective means.

Table 4.8: Experimental verses CFD data

Study	Parameter	CFD	Experimental (Mean ± 2σ)	Absolute Difference
Baseline (6.6 L/min)	$\overline{T}_j$ (°C)	92.1	93.3 ± 1.1	1.2
	$\Delta\overline{P}$ (kPa)	11.1	12.4 ± 1.0	1.4
SOO (4.9 L/min)	$\overline{T}_j$ (°C)	88.6	89.7 ± 1.2	1.1
	$\Delta\overline{P}$ (kPa)	26.7	28.3 ± 1.7	1.6
MOO (7.2 L/min)	$\overline{T}_j$ (°C)	97.5	97.7 ± 0.7	0.2
	$\Delta\overline{P}$ (kPa)	4.8	5.1 ± 0.5	0.4

Figure 4.19: 3D printed orifice plates for (a) baseline, (b) SOO and (c) MOO designs.

4.5. Conclusions

The primary objective of this study was to develop and test an automated optimisation methodology for cooling of the cores of commercial CPU packages with liquid jet array type heat exchangers. To achieve this, a commercial CPU package, the Intel i5-12600K, was chosen as a demonstrator and a comprehensive optimisation workflow was developed across three distinct commercial software platforms within Siemens NX. The impact of the chosen heat exchanger design parameters was assessed by evaluating their influence on the average core temperature as well as the hydraulic pumping power penalty. Along with the automated simulation-based optimisation methodology, a key contribution of this study is the evaluation of the heat transfer associated with a typical commercial CPU stack, which includes the influence of the cores, die, TIM and coldplate, including conjugate heat transfer effects. The main conclusions from this investigation are:

1. Although seldomly implemented for CPUs, it is established here that carefully constructed experiments for live tests on commercial CPUs can be used to adequately verify the efficacy of related CFD simulations, and include details down to the level of the distributed cores on the CPU die.
2. Integrating CAD, CFD, and optimisation software packages is a viable approach for automated geometric optimisation of jet array impingement heat exchangers for commercial CPU packages, including both single and multi-objective optimisation.
3. The Single-Objective Optimisation (SOO) design, focused on maximising the cooling of the CPU cores, resulted in average junction temperatures more than 10 K below the throttling temperature limit under high stress overclocking workload conditions. This design used a small number of closely spaced high velocity jets to target the convective cooling to the impinging jets over the projected area of the CPU cores, whist requiring close to the maximum hydraulic power afforded by the pump to do so.
4. The Multi-Objective Optimisation (MOO) design, which sought to maximise the cooling of the cores whilst simultaneously minimising the hydraulic pumping power penalty, resulted in 9 K hotter average core temperatures compared with the SOO design, though with a near 4-fold decrease in required hydraulic power consumption. Despite the overall decrease in cooling performance, it was still safely below the throttling temperature for the same overclocking compute workload of this CPU. The MOO heat exchanger design used a significantly higher population of lower velocity jets to better leverage the available effective surface area for convective heat transfer from the Integrated Heat Spreader, thus compensating for the much lower intensity of convective heat transfer relative to the SOO design.
5. The net core-to-coolant thermal budget was estimated by considering the temperature differences across the solid and fluid mediums above a single CPU core. In doing so, it has been determined that the high heat flux levels associated with heat transfer from the discrete cores (~470 W/cm^2) result in a significant

temperature drop across the silicon die, to the extent that about 30% of the total thermal budget is associated with the heat transfer across the die. The implication is that improvements to the coldplate heat exchanger have a diminished overall impact on the net core-to-coolant performance.

Although the work here was carried out for the Intel i5-12600K, the developed optimisation procedure is by no means limited to this specific CPU. Thus, future research should aim to extend the developed optimisation workflow and test procedure to commercial CPUs with different die and core configurations. Depending on the CPU architecture and target power levels, future work may need to investigate incorporating enhancing surface structures on the coolant-exposed side of the IHS, ostensibly expanding the range of geometric design parameters compared with the present work. This could include adding additional objective functions to the MOO strategy, such as minimising temperature gradients in order to reduce thermal stresses, in particular those brough about by differential thermal expansion of the solid materials in the stack.

References

[1] "International Roadmap for Devices and Systems 2020: Systems and Architectures." IEEE. https://irds.ieee.org/editions/2020/systems-and-architectures (accessed 28/11/2024).

[2] S. Qiu, P. Xu, L. Geng, A. Mujumdar, Z. Jiang, and J. Yang, "Enhanced heat transfer characteristics of conjugated air jet impingement on a finned heat sink," *Thermal Science,* vol. 21, pp. 279-288, 2017, doi: 10.2298/TSCI141229030Q.

[3] H. E. Ahmed, B. H. Salman, A. S. Kherbeet, and M. I. Ahmed, "Optimization of thermal design of heat sinks: A review," *International Journal of Heat and Mass Transfer,* vol. 118, pp. 129-153, 2018, doi: 10.1016/j.ijheatmasstransfer.2017.10.099.

[4] F. M. Naduvilakath-Mohammed, R. Jenkins, G. Byrne, and A. J. Robinson, "Closed loop liquid cooling of high-powered CPUs: A case study on cooling performance and energy optimization," *Case Studies in Thermal Engineering,* vol. 50, p. 103472, 2023, doi: 10.1016/j.csite.2023.103472.

[5] A. Husain, M. Zunaid, K. Oufi, H. Gheilani, and M. Z. Ansari, "Heat Transfer Characteristics of Microjet Impingements with Flow Extraction," *SSRN Electronic Journal,* 2020, doi: 10.2139/ssrn.3567653.

[6] B. Ramakrishnan *et al.*, "CPU Overclocking: A Performance Assessment of Air, Cold Plates, and Two-Phase Immersion Cooling," *IEEE Transactions on Components, Packaging and Manufacturing Technology,* vol. 11, no. 10, pp. 1703-1715, 2021, doi: 10.1109/TCPMT.2021.3106026.

[7] J. W. Elliott and A. J. Robinson, "Optimised Liquid Impinging Jet Arrays for Cooling CPU Packages," *IEEE Transactions on Components, Packaging and Manufacturing Technology,* vol. 15, no. 3, pp. 488-505, 2025, doi: 10.1109/TCPMT.2024.3485478.

[8] T. Chen, C. Qi, J. Tang, G. Wang, and Y. Yan, "Numerical and experimental study on optimization of CPU system cooled by nanofluids," *Case Studies in Thermal Engineering,* vol. 24, p. 100848, 2021, doi: 10.1016/j.csite.2021.100848.

[9] U. Khan, H. Ullah, and A. Nawaz, "Design and Optimization of Heatsink for an Active CPU Cooler using Numerical Simulations," *Journal of Advanced Research in Fluid Mechanics and Thermal Sciences,* vol. 111, pp. 214-224, 2024, doi: 10.37934/arfmts.111.2.214224.

[10] Y. Cai, D. Liu, J.-J. Yang, Y. Wang, and F.-Y. Zhao, "Optimization of Thermoelectric Cooling System for Application in CPU Cooler," *Energy Procedia,* vol. 105, pp. 1644-1650, 2017, doi: 10.1016/j.egypro.2017.03.535.

[11] S. Siahchehrehghadikolaei, M. Gholinia, S. S. Ghadikolaei, and C.-X. Lin, "A CFD modeling of CPU cooling by eco-friendly nanofluid and fin heat sink passive cooling techniques," *Advanced Powder Technology,* vol. 33, no. 11, p. 103813, 2022, doi: 10.1016/j.apt.2022.103813.

[12] G. Ai, Y. Luo, and W. Su, "Investigation of Liquid Cooling Plate for Server CPUs Based on Topology Optimization," *Journal of Electronics Cooling and Thermal Control,* vol. 13, pp. 1-34, 2024, doi: 10.4236/jectc.2024.131001.

[13] J. W. Elliott, M. T. Lebon, and A. J. Robinson, "Optimising integrated heat spreaders with distributed heat transfer coefficients: A case study for CPU cooling," *Case Studies in Thermal Engineering,* vol. 38, p. 102354, 2022, doi: 10.1016/j.csite.2022.102354.

[14] G. Murray, J. W. Elliott, R. Jenkins, M. T. Lebon, G. Byrne, and A. J. Robinson, "Thermal-Hydraulic Characterisation of Electronics Cooling Liquids: A Case Study of Jet Impingement Coldplate on Emulated CPU," in *2022 28th International Workshop on Thermal Investigations of ICs and Systems (THERMINIC)*, 28-30 Sept. 2022 2022, pp. 1-4, doi: 10.1109/THERMINIC57263.2022.9950634.

[15] J. S. Lee, S. Y. Yoon, B. Kim, H. Lee, M. Y. Ha, and J. K. Min, "A topology optimization based design of a liquid-cooled heat sink with cylindrical pin fins having

varying pitch," *International Journal of Heat and Mass Transfer,* vol. 172, p. 121172, 2021, doi: 10.1016/j.ijheatmasstransfer.2021.121172.

[16] Y. Li, S. Roux, C. Castelain, Y. Fan, and L. Luo, "Design and Optimization of Heat Sinks for the Liquid Cooling of Electronics with Multiple Heat Sources: A Literature Review," *Energies,* vol. 16, no. 22, p. 7468, 2023, doi: 10.3390/en16227468.

[17] A. J. Robinson, "A Thermal–Hydraulic Comparison of Liquid Microchannel and Impinging Liquid Jet Array Heat Sinks for High-Power Electronics Cooling," *IEEE Transactions on Components and Packaging Technologies,* vol. 32, no. 2, pp. 347-357, 2009, doi: 10.1109/TCAPT.2008.2010408.

[18] P. Łapka, A. Ciepliński, and A. Rusowicz, "Numerical model and analysis of heat transfer during microjets array impingement," *Energy,* vol. 203, p. 117879, 2020, doi: 10.1016/j.energy.2020.117879.

[19] K. R. Saripalli, "Visualization of multijet impingement flow," *AIAA Journal,* vol. 21, pp. 483-484, 1983, doi: 10.2514/3.8102.

[20] L. Thielen, H. J. J. Jonker, and K. Hanjalić, "Symmetry breaking of flow and heat transfer in multiple impinging jets," *International Journal of Heat and Fluid Flow,* vol. 24, no. 4, pp. 444-453, 2003, doi: 10.1016/S0142-727X(03)00042-0.

[21] B. Končar, P. Norajitra, and K. Oblak, "Effect of nozzle sizes on jet impingement heat transfer in He-cooled divertor," *Applied Thermal Engineering,* vol. 30, no. 6, pp. 697-705, 2010, doi: 10.1016/j.applthermaleng.2009.11.018.

[22] A. Royne and C. J. Dey, "Effect of nozzle geometry on pressure drop and heat transfer in submerged jet arrays," *International Journal of Heat and Mass Transfer,* vol. 49, no. 3, pp. 800-804, 2006, doi: 10.1016/j.ijheatmasstransfer.2005.11.014.

[23] "Alder Lake - Microarchitectures - Intel." https://en.wikichip.org/wiki/intel/microarchitectures/alder_lake (accessed 15/08/2024).

[24] "AN 943: Thermal Modeling for Intel® Stratix® 10 FPGAs with the Intel® FPGA Power and Thermal Calculator." Intel.

https://www.intel.com/content/www/us/en/docs/programmable/683387/21-1/list-of-abbreviations.html. (accessed 05/03/2024).

[25] J. Bilek, J. K. Atkinson, and W. A. Wakeham, "Thermal Conductivity of Molten Lead-Free Solders," *International Journal of Thermophysics,* vol. 27, no. 1, pp. 92-102, 2006, doi: 10.1007/s10765-006-0035-4.

[26] T. J. Heindel, F. P. Incropera, and S. Ramadhyani, "Enhancement of natural convection heat transfer from an array of discrete heat sources," *International Journal of Heat and Mass Transfer,* vol. 39, no. 3, pp. 479-490, 1996, doi: 10.1016/0017-9310(95)00153-Z.

[27] A. J. Robinson and E. Schnitzler, "An experimental investigation of free and submerged miniature liquid jet array impingement heat transfer," *Experimental Thermal and Fluid Science,* vol. 32, no. 1, pp. 1-13, 2007, doi: 10.1016/j.expthermflusci.2006.12.006.

[28] S. J. Kline and F. A. McClintock, "Describing Uncertainties in Single-Sample Experiments," *Mechanical Engineering,* vol. 75, pp. 3-8, 1953.

[29] D. P. R. Thanu, B. Liu, and M. A. Cartas, "Thermal Interface Materials and Cooling Technologies in Microelectronic Packaging—A Critical Review," *Journal of Microelectronics and Electronic Packaging,* vol. 15, no. 2, pp. 63-74, 2018, doi: 10.4071/imaps.654289.

[30] F. R. Menter, "Zonal Two Equation k-w Turbulence Models For Aerodynamic Flows," in *23rd Fluid Dynamics, Plasmadynamics, and Lasers Conference*, Orlando, U.S.A., 1993, doi: 10.2514/6.1993-2906.

[31] C. W. Hirt and B. D. Nichols, "Volume of fluid (VOF) method for the dynamics of free boundaries," *Journal of Computational Physics,* vol. 39, no. 1, pp. 201-225, 1981, doi: 10.1016/0021-9991(81)90145-5.

[32] B. Basara and S. Jakirlić, "A new hybrid turbulence modelling strategy for industrial CFD," *International Journal for Numerical Methods in Fluids,* vol. 42, pp. 89-116, 2003, doi: 10.1002/fld.492.

[33] J. H. Ferziger and M. Peric, *Computational Methods for Fluid Dynamics*. Springer Berlin Heidelberg, 2012.

[34] O. Sahni, K. E. Jansen, M. S. Shephard, C. A. Taylor, and M. W. Beall, "Adaptive boundary layer meshing for viscous flow simulations," *Eng. with Comput.,* vol. 24, no. 3, pp. 267–285, 2008, doi: 10.1007/s00366-008-0095-0.

[35] P. J. Roache, "Quantification of Uncertainty in Computational Fluid Dynamics," *Annual Review of Fluid Mechanics,* vol. 29, no. 1, pp. 123-160, 1997, doi: 10.1146/annurev.fluid.29.1.123.

[36] E. Yamasue, M. Susa, H. Fukuyama, and K. Nagata, "Thermal conductivities of silicon and germanium in solid and liquid states measured by non-stationary hot wire method with silica coated probe," *Journal of Crystal Growth,* vol. 234, no. 1, pp. 121-131, 2002, doi: 10.1016/S0022-0248(01)01673-6.

Chapter 5

Conclusions and Future Work

5.1. Conclusions

This research systematically identified and addressed critical gaps in the knowledge associated with thermal management solutions for concentrated heat sources, with a specific focus on advanced CPU package architectures. Through the hypotheses and research results presented, this thesis provides a new understanding of the interplay between the heat transfer, hydraulic penalties, and optimisation strategies, culminating in the development of an automated simulation-based optimisation methodology for liquid jet impingement heat exchangers. This new simulation workflow demonstrates the capacity to generate optimal designs for electronics cooling, particularly CPUs. This chapter consolidates the key conclusions, linking them to the identified gaps in knowledge and assessing the validity of the proposed hypotheses.

The first identified knowledge gap pertained to the behaviour of heat spreaders in managing concentrated heat sources, particularly the interplay between heat spreading efficiency and convective cooling performance. A key question was whether uniform or distributed cooling strategies are more effective when heat spreading efficiency is limited. While heat spreading efficiency shares conceptual parallels with fin efficiency, its application to heat spreaders, particularly when aggressively cooled, has remained largely underexplored. This research advanced the theoretical understanding of liquid-cooled heat spreader performance by investigating the impact of non-uniform heat transfer coefficient distributions on the thermal behaviour of an Integrated Heat Spreader (IHS). Chapter 2 validated the hypothesis that optimising the convective heat transfer coefficient distribution across the IHS convective surface can enhance thermal performance relative to a uniform distribution. Using a Genetic Algorithm-based code developed in MATLAB, it was demonstrated that imposing an optimised Gaussian distribution significantly improved performance, reducing maximum temperature and thermal gradients of the concentrated heat source. Improvements were achieved by aligning the convective cooling intensity with localised heat flux regions, thereby taking advantage of the lateral heat spreading within the IHS. These findings highlight the potential of leveraging conjugate heat transfer principles for improving heat spreader effectiveness.

With it now established that distributed cooling of the IHS, tailored to mitigate localised heat flux peaks at the source, could outperform uniform cooling strategies, Chapter 3 investigated liquid impinging jet arrays as a practical means to implement this type of cooling strategy. Specifically, the question to be answered was whether distributed cooling strategies could be effectively applied to heat exchanger designs for idealised CPU packages. The hypothesis posited that while hydraulic performance would dictate practical limits of these solutions, distributed cooling would remain advantageous. Chapter 3 details a new simulation-based optimisation scheme, verified against experiments, that applied both single and multi-objective optimisation strategies to idealised, single, centralised heat sources that were representative of CPU semiconductor dies. These strategies yielded markedly different design solutions depending on whether hydraulic and/or heat transfer performance were considered as the objective functions, underscoring the adaptability of the optimisation framework. Although the findings proved the hypothesis that heat spreader efficiency and associated conjugate heat transfer effects could be leveraged to improve liquid cooling of concentrated heat sources, and further emphasised the inherent trade-offs between cooling intensity and hydraulic penalties, it did so in scenarios which were idealised in terms of actual commercial CPU packages.

To bridge the gap between ideal and real-world CPU thermal management, Chapter 4 extended the automated simulation-based design methodology to a commercial CPU package, specifically the Intel i5-12600K CPU. The results confirmed the aforementioned hypothesis, demonstrating that distributed cooling strategies could be effectively tailored to a commercial CPU architecture which included discrete heat producing cores on the underside of the die, achieving high-performance cooling while managing hydraulic penalties. The findings confirmed that the insights derived from addressing the earlier gaps in knowledge could be translated into practical real-world application, provided that hydraulic considerations were appropriately accounted for. Furthermore, the work conclusively established the superiority of distributed cooling over uniform cooling when aggressive convective intensity results in low heat spreader efficiency.

Importantly, Chapter 4 also investigated the influence of CPU die architecture on the overall source-to-sink heat transfer. It was hypothesised that the principles developed for the simplified heat source configurations considered in Chapter 3 would remain applicable, though the overall influence of the discrete and very high heat flux CPU cores was unknown. The results highlighted that the heat transfer from the high heat flux cores across the CPU die accounted for approximately 30% of the total core-to-coolant thermal budget, which is significant. This finding provides new insight and practical understanding related to the importance of CPU design architecture on the overall thermal management strategy. While the overarching optimisation principles held, the study revealed unique challenges posed by the heat flux levels and layout of the CPU cores on the semiconductor die. These findings emphasise the advantages of tailored heat exchanger designs that take into account the full CPU stacked package from the cores to the coolant.

The research presented in this thesis addresses critical gaps in the knowledge related to CPU thermal management, offering both theoretical advancements and practical contributions. The development of the automated simulation-based optimisation methodology for liquid impinging jet array heat exchangers as part of the full CPU stacked package represents a significant advancement, providing a robust, versatile and adaptable engineering tool for tackling the complex thermal challenges of modern CPUs. Through the comprehensive consideration of conjugate heat transfer, hydraulic penalties, and architectural nuances, this work paves the way for the development of high-performance, energy-efficient cooling solutions tailored to the evolving demands of the electronics industry.

5.2. Future Work

This research successfully developed an experimentally verified automated simulation-based optimisation design methodology tailored for liquid-cooled heat exchangers used in CPU thermal management. In the context of progressing the work further, additional geometric parameters that were outside the scope of the present thesis should be explored, including but not limited to orifice plate thickness, nozzle geometry variations, manifold configuration, and heat spreader material and dimensions etc. These design features are well-documented to influence both heat transfer and hydraulic performance significantly, though the manufacturing and cost implications need to be weighed against any potential performance improvements. This does, however, highlight the adaptability of the developed engineering tool, in the sense that expanding the design parameter range is straight forward and not limited to the selected range of parameters investigated thus far.

Additionally, further experimental and simulation work could seek to explore enhanced surface structures on the coolant-exposed side of the IHS, again expanding the range of geometric design parameters compared with the present work. Incorporating surface texturing, such as fins, dimples, wells, or other structured geometries, could improve the convective heat transfer by enhanced fluid mixing intensity, additional surface area, or even smoother Gaussian-type heat transfer profiles centred on regions of higher heat flux, as identified in Chapter 2. Once again, these surface enhancement features could be integrated into the multi-objective optimisation strategy in a relatively straight forward manner, and even include additional objective functions such as minimising temperature gradients to reduce thermal stresses.

Although the optimisation strategy in Chapter 4 was validated using the Intel i5-12600K CPU, the workflow is easily adaptable to other CPU architectures. Future work should aim to expand the optimisation and experimental verification processes to include additional commercial CPU packages with varying core sizes, configurations, power and heat flux levels. This would demonstrate the broader applicability of the developed design process and bring it to the point where it becomes reliable for use as an engineering tool for industry.

Appendix A

MATLAB Numerical Model Addendum

A.1. Gaussian HTC Function Derivation

The following addendum details the derivation of the numerical function produced for the Gaussian distribution function as described in Chapter 2, beginning with the base form of Eq. (2.14),

$$f(x) = \left[Z \left(e^{-\frac{1}{2}\left(\frac{x^2+y^2}{a^2}\right)} \right) \right] + m \tag{2.14}$$

The function was constrained by the desired average value of the heat transfer coefficient across the convective surface of the heat spreader which, for a Gaussian function, correlates to the area between the Gaussian function and the x-axis. The area under a Gaussian curve is defined as,

$$Area = \frac{1}{b-a} \int_a^b f(x)\, d(x) \tag{A.1}$$

The expression for Z is derived from the function for the average heat transfer coefficient, h_{avg}, which corresponds to the area underneath the Gaussian curve. Given the nature of the distribution of the heat transfer coefficient on the spreader surface, Z is derived as a 1D case varying only in the x direction. This parameter can then be substituted into Eq. 2.10, which applies it across both x and y directions as a 2D distribution across the full heat spreader convective surface. Therefore, assuming that *a* and *b* are the outer geometric limits of the heat spreader and are equally displaced from the origin, they can be denoted by a single variable, *r*. The final form of *Z,* as described in Eq. (2.15), can be found via the following derivation,

$$h_{avg} = \frac{1}{r-(-r)} \int_{-r}^{r} f(x)\, dx$$

$$h_{avg} = \frac{1}{2r} \int_{-r}^{r} \left(\left[Ze^{-\frac{1}{2}\left(\frac{x}{a}\right)^2} \right] + m \right) dx$$

$$2rh_{avg} = \int_{-r}^{r} \left(Ze^{-\frac{1}{2}\left(\frac{x}{a}\right)^2} + m \right) dx$$

$$2rh_{avg} = \left[\frac{\sqrt{\pi} a\, Z \left(erf\left(\frac{x}{\sqrt{2}\, a} \right) \right)}{\sqrt{2}} + mx \right]_{-r}^{r}$$

$$2rh_{avg} = \left(\frac{\sqrt{\pi} a\, Z \left(erf\left(\frac{r}{\sqrt{2}\, a} \right) \right)}{\sqrt{2}} + mr \right) - \left(\frac{\sqrt{\pi} a\, Z \left(erf\left(\frac{-r}{\sqrt{2}\, a} \right) \right)}{\sqrt{2}} - mr \right)$$

$$2rh_{avg} = 2mr + \frac{\sqrt{\pi} a\, Z \left(erf\left(\frac{r}{\sqrt{2}\, a} \right) \right)}{\sqrt{2}} - \frac{\sqrt{\pi} a\, Z \left(erf\left(\frac{-r}{\sqrt{2}\, a} \right) \right)}{\sqrt{2}}$$

$$2rh_{avg} - 2mr = Z \left(\frac{\sqrt{\pi} a \left(erf\left(\frac{r}{\sqrt{2}\, a} \right) \right)}{\sqrt{2}} - \frac{\sqrt{\pi} a \left(erf\left(\frac{-r}{\sqrt{2}\, a} \right) \right)}{\sqrt{2}} \right)$$

$$Z = \left(\frac{2rh_{avg} - 2mr}{\frac{\sqrt{\pi} a \left(erf\left(\frac{r}{\sqrt{2}\, a} \right) \right)}{\sqrt{2}} - \frac{\sqrt{\pi} a \left(erf\left(\frac{-r}{\sqrt{2}\, a} \right) \right)}{\sqrt{2}}} \right)$$

$$Z = \left(\frac{2\sqrt{2}\, r \left(h_{avg} - m \right)}{\sqrt{\pi} a \left(erf\left(\frac{r}{\sqrt{2}\, a} \right) - erf\left(\frac{-r}{\sqrt{2}\, a} \right) \right)} \right) \tag{2.15}$$

A.2. Optimisation Code

The optimisation code developed using the Gaussian function detailed in Chapter 2 was constructed as two separate sections. The primary model function, fully outlined in Figure A.1 below, details the implementation of the Gaussian function as well as model generation and the relevant objective functions and primary boundary conditions required for the design problem. There were three possible objective functions for which the problem could be optimised for; the average temperature across the contact face between source and spreader, T_{avg}, the maximum temperature across this face, T_{max}, and the maximum temperature difference T_{max} - T_{min}. All three of these objectives were defined at the end of the function, but were only considered active objective functions when called upon in the first line of the code. In the example given, the Genetic Algorithm is only optimising the heat transfer coefficient distribution for the average temperature, T_{avg}, with all three objectives defined in lines 52 - 54.

```
1  function Tavg = HTC_Curve_GA(x)
2  model=createpde('thermal');
3  %Function Inputs
4  d=0.0025;
5  Lsource=0.013;
6  Lspreader=0.04;
7  k=400;
8  Tinf=293;
9  Qin=169;
10 Asource=Lsource*Lsource;
11 Aspread=Lspreader*Lspreader;
12 %GA Requirements
13 Av=35000;
14 m=x(1);
15 a=x(2);
16 rad=Lspreader/2;
17 Z=(2*sqrt(2)*rad*(Av-m))/(sqrt(pi)*a*((erf(rad/((sqrt(2))*a)))-...
18     (erf(-rad/((sqrt(2))*a)))));
19 %Initial Model Set-up and Geometry
```

```
geo=multicuboid([Lsource,Lspreader],[Lsource,Lspreader],d);
model.Geometry=geo;
pdegplot(model,'FaceLabels','on')
generateMesh(model,'Hmax',0.0015);
pdemesh(model);
%Thermal Properties and Boundary Layers
thermalProperties(model,'ThermalConductivity',k);
thermalBC(model,'Face',1,'HeatFlux',Qin/Asource);
outerCC = @(location,~) ((Z*exp(-...
    0.5*(((location.x)^2)+((location.y)^2))/(a^2)))+m);
thermalBC(model,'Face',[2,12],"ConvectionCoefficient",outerCC,...
    "AmbientTemperature",Tinf);
%Result
result=solve(model);
%Information Extraction - IHS Contact Area
r=result.Mesh.Nodes;
Height=r(3,:);
TopFace = find(Height==0);
TTF=transpose(TopFace);
Contact=r([1,2],TopFace);
Temp1=result.Temperature(TTF);
Temp1avg=mean(Temp1);
%Part 2 (Y)
Dispy=Contact(2,:);
TFY=find(Dispy<=(Lsource/2) & Dispy>=-(Lsource/2));
TTFY=transpose(TFY);
Temp2=Temp1(TTFY,:);
%Part 3 (X)
Dispx=Contact(1,TFY);
HSContactFace=find(Dispx<=(Lsource/2) & Dispx>=-(Lsource/2));
THSCF=transpose(HSContactFace);
TempContact=Temp2(THSCF,:);
Tavg=mean(TempContact);
Tmax=max(TempContact);
Tdiff=max(TempContact)-min(TempContact);
```

Figure A.1: MATLAB optimisation model function.

The second element of code was the Genetic Algorithm, responsible for running the optimisation of the objective functions and specifying the limits of the two variable optimisation parameters, *a* and *m*. This optimisation code is specified in Figure A.2 below.

```
ObjFun=@HTC_Curve_GA;
nvars=2;
LB=[0 0.001];
UB=[30000 0.01];
options = optimoptions('ga','Display','iter',...
    'PlotFcn',@gaplotbestf, 'MutationFcn',...
    @mutationadaptfeasible, 'MaxGenerations',1000);
[x,fval]=ga(ObjFun,nvars,[],[],[],[],LB,UB,[],options);
```

Figure A.2: MATLAB genetic algorithm optimisation function.

For this example, h_{avg} = 35,000 W/m^2K and *m* is given in the range of 0 - 30,000 W/m^2K. Upon completion of the optimisation, the matrix 'x' can be called, which provides a 1 x 2 matrix detailing the optimum values for *m* and *a* respectively for the minimised objective function(s). In this case, the optimum values were given as x = [4798.1, $4.7x10^{-3}$]. Therefore, for a 40 x 40 x 2.5 mm^3 heat spreader with a 13 x 13 mm^2 heat source contact surface area and applied heat flux of 100 W/cm^2, the optimum heat transfer coefficient distribution function for minimising average surface temperature can be approximated as,

$$f(x) = \left[\left(\frac{205086210.4}{(erf(3009.0) - erf(-3009.0))} \right) \left(e^{-\frac{1}{2}\left(\frac{x^2+y^2}{2.2x10^{-5}}\right)} \right) \right] + 4798.1 \qquad (A.2)$$

Appendix B

Experimental Apparatus Calibration

B.1. Thermocouple Calibration

The following figure presents the calibration curves illustrating the predicted vs measured data recorded across all seven thermocouples compared to the reference probe with the associated curve equation. All probes were calibrated against a ASL F100 Precision Handheld RTD thermometer.

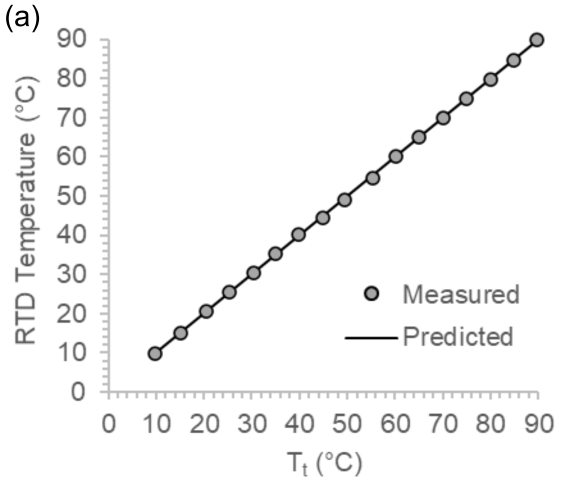

$T_{RTD} = 0.9992T_t - 0.2375$

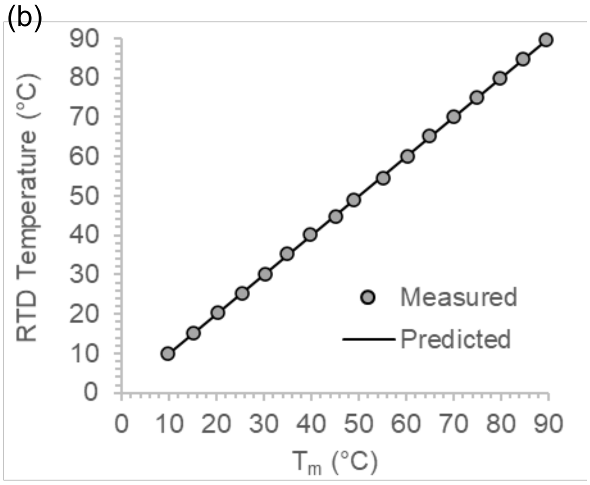

$T_{RTD} = 0.9992T_m - 0.2668$

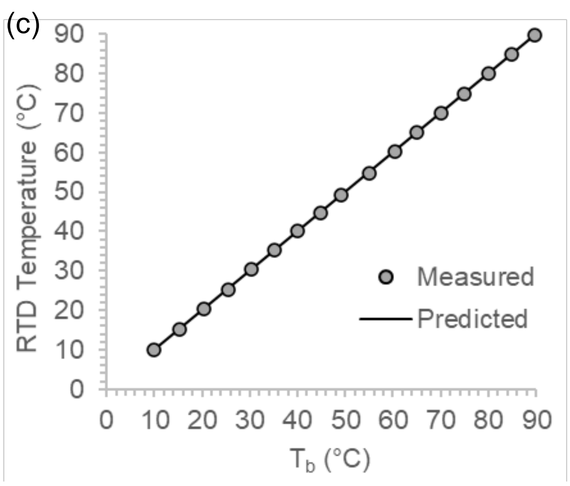

$T_{RTD} = 0.9958T_b - 0.3640$

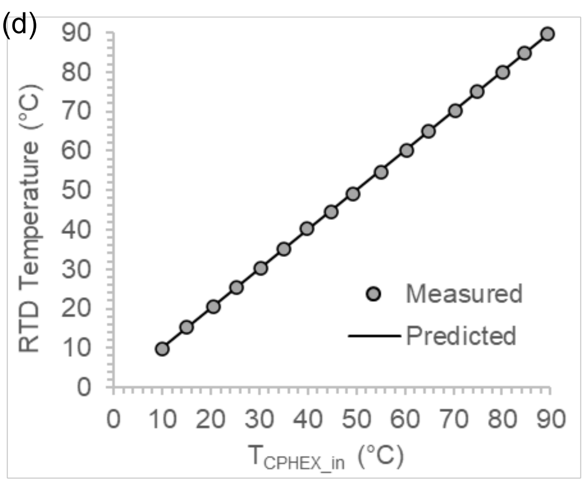

$T_{RTD} = 1.0058T_{CPHEX\_in} - 0.2013$

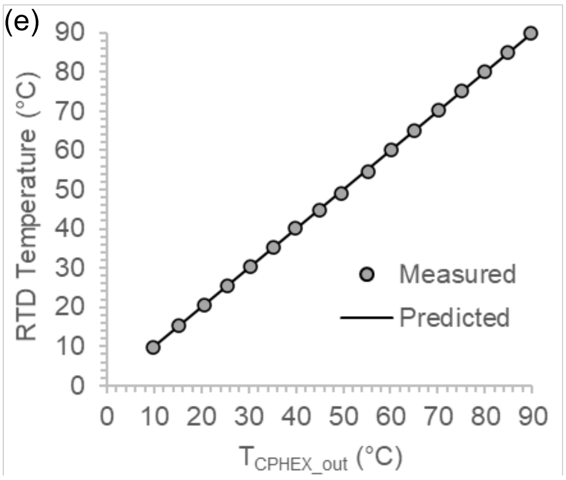

$T_{RTD} = 1.0005T_{CPHEX\_out} – 0.2040$

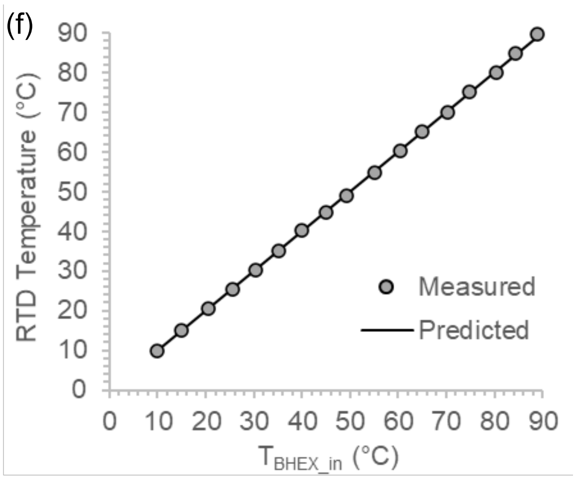

$T_{RTD} = 1.0029T_{BHEX\_in} – 0.1559$

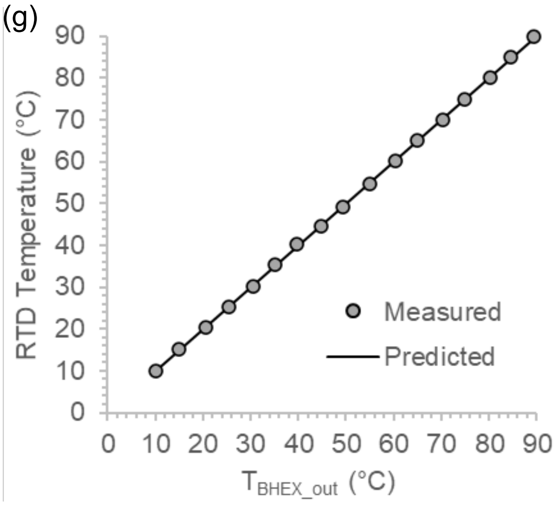

$T_{RTD} = 0.9987T_{BHEX\_out} – 0.0020$

Figure B.1: Thermocouple calibration plots for (a) top, (b) middle and (c) bottom TTV thermocouple, thermocouple at (d) inlet and (e) outlet to cold plate heat exchanger, and (f) inlet and (g) outlet to brazed heat exchanger.

B.2. Pressure Meter Calibration

A total of four Omega PX26 wet/wet differential pressure meters were used across the experimental test apparatus, calibrated against a Digitron 2022P differential digital pressure meter. Three different meters were used across the cold plate heat exchanger on account of their pressure range capabilities, as the expected variation in orifice plate designs produced by the optimisation workflow would likely produce a wide range of pressures across the fluid manifold within the tested range of flow rates. The maximum range of the three meters placed across the cold plate heat exchanger are as follows; PX26-015DV = 100 kPa, PX26-005DV = 35 kPa, and PX26-001DV = 7 kPa. An additional PX26-015DV sensor was placed across the brazed heat exchanger as a precautionary measure to monitor for any flow irregularities. The following calibration plots present the predicted vs measured data recorded across the pressure meters.

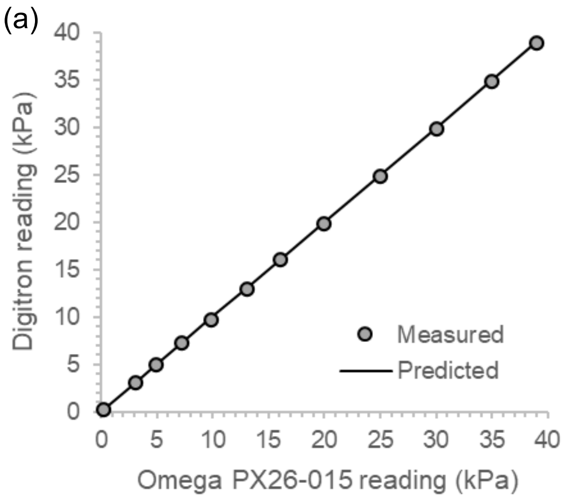

$P_{Ref} = 0.9885P_{015} – 0.0319$

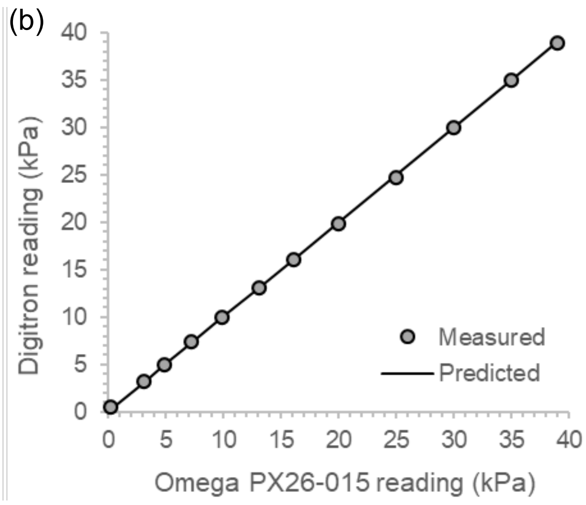

$P_{Ref} = 0.9856P_{015} – 0.0499$

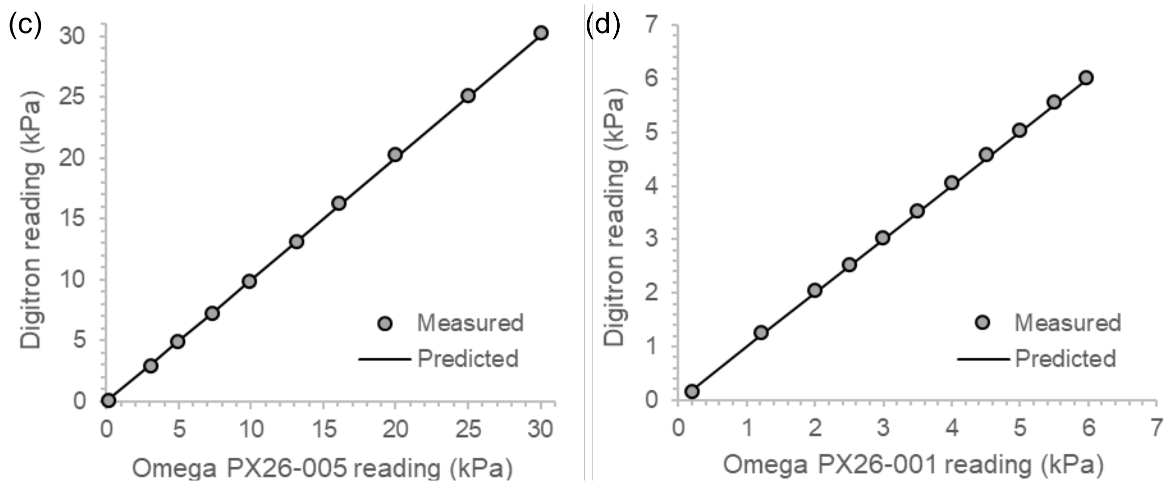

$P_{Ref} = 1.0169P_{005} - 0.1586$ $\qquad$ $P_{Ref} = 1.0079P_{001} - 0.0931$

Figure B.2: Pressure calibration plots for (a) Omega PX26-015$_{Brazed}$, (d) Omega PX26-015$_{Cold\ Plate}$, (c) Omega PX26-005 and (d) Omega PX26-001 sensors.

B.3. Flow Meter Check

The Sensata Cynergy3 UF series ultrasonic (US) flow meter has its own stated error from the manufacturer, though for an extra layer of comfort was checked against a rotameter (1 - 10 L/min ±1.5% FS) between flow rates of 1 - 8 L/min for both ambient temperautre (20°C) and the inlet temperature required for the optimisation simulations (35°C). The comparison plots for both inlet temperatures are presented below.

(a)

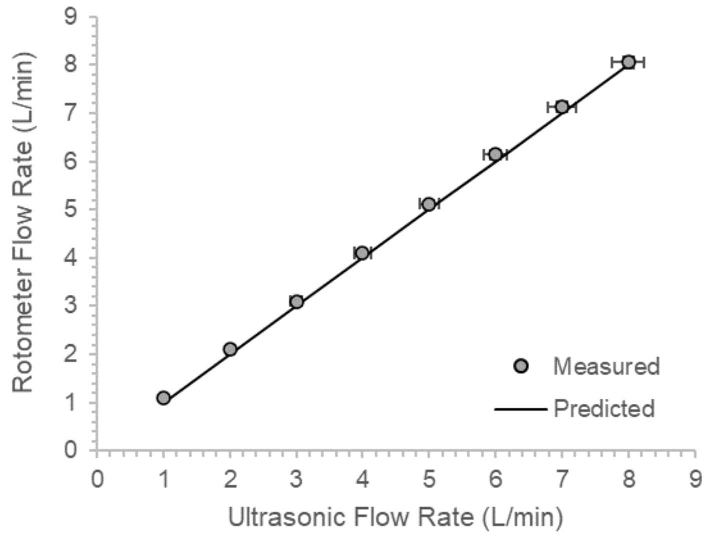

$$\dot{V}_{Rot} = 1.0095\dot{V}_{US} + 0.0821$$

(b)

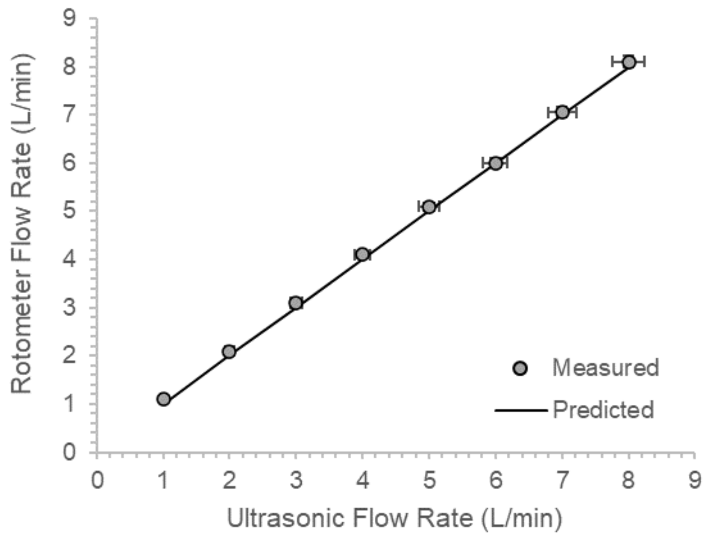

$$\dot{V}_{Rot} = 0.9911\dot{V}_{US} + 0.1714$$

Figure B.3: Flow meter cross-check curvies for (a) 20°C and (b) 35°C fluid temperatures.

B.4. Calibration Certification

The calibration certification corresponding to the ASL F100 Precision Handheld RTD thermometer and the Digitron 2022P differential digital pressure meter respectively, utilised in the calibration of the appropriate experimental apparatus, are presented below.

Industrial Temperature Sensors Ltd.
Unit W4J,Ladystown,Toughers Business Park, Naas, Co. Kildare
Tel: 045-408164 Fax: 045-408165 Web: www.itsirl.com email: info@itsirl.com

CERTIFICATE OF CALIBRATION

Certificate No: C226857A1 — 1 OF 2

Customer: Trinity College Dublin

Instrument: Temperature Meter

Model: ASL F100 — S/N: 016219/92

Range: 0°C + 200°C

Calibration Method: Comparison — Temperature Scale: ITS 90

Test Equipment:
(1) DDM 900 Precision Thermometer S/N. 005100200191 Cert No. 2662
(1a) Reference PRT Probe S/N.09AS118 Cert No. 2662
(2) Fluke 9172 Metrology Well S/N. B12342
(3) Fluke 7380 High Precision Bath S/N. B14489
(4) Lauda UB20 High Precision Bath S/N. B02001

	Reference Temperature °C	Measured Reading °C	Error °C	Measurement Uncertainty °K
CH A	-0.0014	0.1220	0.1234	0.020
CH A	20.0026	20.0060	0.0034	0.020
CH A	39.9831	40.0100	0.0269	0.020
CH A	59.9780	60.0270	0.0490	0.020
CH A	79.9826	80.0370	0.0544	0.020
CH A	99.9717	100.0240	0.0523	0.020
CH A	119.9817	120.0260	0.0443	0.020
CH A	139.9935	140.0270	0.0335	0.020
CH A	160.9776	159.9910	-0.9866	0.020
CH A	179.9628	179.9500	-0.0128	0.020
CH A	199.9648	199.9260	-0.0388	0.020

TESTED BY: Stephen Ralph DATE: 30/09/2020

Stephen Ralph

The reported expanded uncertainty is based on a standard uncertainty multiplied by a coverage factor k=2, providing a level of confidence of approximately 95%. The uncertainty evaluation has been carried out in accordance with national standards requirements. This certificate is issued in accordance with the national standards & provides traceability of measurement to recognised national standards, & to units of measurement realised at the national physical laboratory or other recognised standards laboratories.

Industrial Temperature Sensors Ltd.

Unit W4J,Ladystown,Toughers Business Park, Naas, Co. Kildare
Tel: 045-408164 Fax: 045-408165 Web: www.itsirl.com email: info@itsirl.com

CERTIFICATE OF CALIBRATION

Certificate No: C226857A1 2 OF 2

Customer: Trinity College Dublin

Instrument: Temperature Meter

Model: ASL F100 S/N: 016219/92

Range: 0°C + 200°C

Calibration Method: Simulation Temperature Scale: ITS 90

Test Equipment:
(1) DDM 900 Precision Thermometer S/N. 005100200191 Cert No. 2662
(1a) Reference PRT Probe S/N.09AS118 Cert No. 2662
(2) Fluke 9172 Metrology Well S/N. B12342
(3) Fluke 7380 High Precision Bath S/N. B14489
(4) Lauda UB20 High Precision Bath S/N. B02001

	Reference Temperature °C	Measured Reading °C	Error °C	Measurement Uncertainty °K
CH B	0.0000	0.0430	0.0430	0.020
CH B	20.0000	19.9270	-0.0730	0.020
CH B	40.0000	39.9480	-0.0520	0.020
CH B	60.0000	59.9480	-0.0520	0.020
CH B	80.0000	79.8950	-0.1050	0.020
CH B	100.0000	99.8750	-0.1250	0.020
CH B	120.0000	119.9100	-0.0900	0.020
CH B	140.0000	139.8700	-0.1300	0.020
CH B	160.0000	159.9150	-0.0850	0.020
CH B	180.0000	179.8860	-0.1140	0.020
CH B	200.0000	199.7450	-0.2550	0.020

TESTED BY: Stephen Ralph DATE: 30/09/2020

Stephen Ralph

The reported expanded uncertainty is based on a standard uncertainty multiplied by a coverage factor k=2, providing a level of confidence of approximately 95%. The uncertainty evaluation has been carried out in accordance with national standards requirements. This certificate is issued in accordance with the national standards & provides traceability of measurement to recognised national standards, & to units of measurement realised at the national physical laboratory or other recognised standards laboratories.

Digitron part of Rototherm Group	**Calibration Certificate - 2000 Pressure**	Form 05 Rev. 2 04/04/2017 Page 1 of 1

Registered Address:	Rototherm Group Kenfig Industrial Estate Margam, Port Talbot, SA13 2PW, United Kingdom Tel: +44 (0) 1656 740 551 Registered in Wales No. 2570730 W: www.digitron.com	Customer Address:	TRINITY COLLEGE DUBLIN SARA DOHERTY - DEPT MECH ENG. PARSONS BUILDING TRINITY COLLEGE DUBLIN IRELAND
Date of Issue	22 April 2021	Certificate Number	41349

Customer Details

Company:	TRINITY COLLEGE DUBLIN	Customer/ Works Order No.:	E12949
Customer PO Number:	PC140421GByr		

Instrument Details

Product Code:	2082P7	Description:	2000 Series Differential Manometer
Serial Number:	4605110532	Range:	0 - 2 Bar
Customer ID No. (If req'd):	N/A	System Accuracy:	20°C to 30°C 0.1% rdg +0.1%fs +1 digit, -10°C to 50°C 0.15% rdg +0.15% fs +1 digit
Condition of UUT:	Good.		

Traceability

Measurements were taken in these conditions:	
Temperature (°C)	21.5
Atmospheric Pressure (Mbar)	1012

Measurements were taken using listed test equipment in table below:		
Test Equipment Description	Test Equipment ID	UKAS Certificate No.
MENSOR CPC 6000	EQ.3299	20461 & N28162 to N28169

Test Results

Ref mbar/bar	UUT Rdg mbar/bar	PASS/FAIL	Allowable Tolerance mbar/bar
0.0	0.0	PASS	2.1
30.0	29.8	PASS	2.1
190.0	189.7	PASS	2.3
1000	999	PASS	4
1950	1949	PASS	5

The calibration was conducted in a temperature controlled environment maintained at 21 ± 2°C in accordance with the applicable calibration procedures of Rototherm Group using UKAS certified test equipment

Tested By:	H SPAIN	Calibration Date	22 April 2021
Signature:	H SPAIN	Postion Held	Calibration Technician
Checked by Competent Person Supervisor, Line Manger, QA, etc.	M Jones		

Template No TP 005 | Template Rev 02 | Template Rev Date 4/04/2017

Company Proprietary Information

Appendix C

Propagation of Errors Example

In continuation of the uncertainty analysis detailed in Chapter 3, an example is provided here to illustrate the propagation of uncertainty errors for the derived parameter U, the overall heat transfer coefficient of the system. The coefficient is calculated using the relationship $U = Q/A\Delta T$, for input conditions of 250 W of heater power for a 15 x 15 mm^2 heat source at a maximum flow rate of 6 L/min with an inlet temperature of 35°C. The temperature difference, ΔT, represents the temperature difference between the junction temperature, T_j, and the average fluid temperature, calculated as the mean of inlet (T_{in}) and outlet (T_{out}), temperatures of the cold plate heat exchanger.

To calculate T_j, a Monte Carlo method was employed, using measurements from three thermocouples embedded in the heated meter bar neck of the Thermal Test Vehicle. The thermocouples used had a measurement uncertainty of ± 0.5°C, with a positional accuracy of approximately 0.127 mm. The least squares method was applied to extrapolate the temperature gradient, dT/dx, across the TTV neck height, with uncertainties distributed across 10,000 data points using a Gaussian normal distribution and a 95% confidence interval. The resulting average uncertainty in the temperature gradient was approximately 1.11%.

Using the temperature gradient, the junction temperature could be determined via linear regression by incorporating the vertical displacement between the junction position, x_j, and the top thermocouple position, x_{top}, and adding it to the temperature of the top thermocouple on the TTV, T_{top}. Therefore, $T_j = T_{top} + \frac{dT}{dx}(x_j - x_{top})$ = 57.9 ± 0.6 °C, with the error taking into account the confidence level and standard deviation of the Monte Carlo dataset for the temperature difference, with the thermocouple temperature and position uncertainty. The heat transfer rate, Q, was calculated using the thermal conductivity of OFE copper, k, along with the cross-sectional area of the TTV neck, A, and the temperature gradient dT/dx, so that $\mathrm{Q = kA/(dT/dx)}$. For this example, Q = 232.7 ± 5.8 W, where the uncertainty primarily arises from the calculated temperature gradient. The heat source area was determined to be A = 2.25 x10^{-4} ± 1.80 x10^{-7} m^2 and the temperature difference ∆T = 21.5 ± 0.9°C.

As highlighted in Chapter 3, the propagation of errors is dictated by the following equation,

$$Unc_z = \sqrt{\left(\sum_{i=1}^{n}\left[\frac{\partial Z}{\partial x_i}Unc_i\right]^2\right)} \tag{3.8}$$

Hence, the uncertainty for the overall heat transfer coefficient, U, based on both the measuring apparatus errors and the standard errors on both T_j and the temperature gradient found using the Monte Carlo method, can be given as,

$$Unc_U = \sqrt{\left(\left[\frac{\partial U}{\partial Q}Unc_Q\right]^2 + \left[\frac{\partial U}{\partial A}Unc_A\right]^2 + \left[\frac{\partial U}{\partial \Delta T}Unc_{\Delta T}\right]^2\right)}$$

$$Unc_U = \sqrt{\left(\left[\frac{Unc_Q}{A\Delta T}\right]^2 + \left[\frac{Q\ Unc_A}{A^2\Delta T}\right]^2 + \left[\frac{Q\ Unc_{\Delta T}}{A\Delta T^2}\right]^2\right)}$$

$$Unc_U = \sqrt{\left(\left[\frac{5.8}{21.5(2.3\text{x}10^{-4})}\right]^2 + \left[\frac{233.1(1.8\text{x}10^{-7})}{21.5(2.3\text{x}10^{-4})^2}\right]^2 + \left[\frac{233.1\ (0.9)}{21.5^2(2.3\text{x}10^{-4})}\right]^2\right)}$$

$$Unc_U \approx 2415.0$$

Therefore, for this example, the approximate heat transfer coefficient U = 48308.8 ± 2415.0 W/m^{2}K, which equates to an uncertainty of approximately 5.0%.

Appendix D

Additional Numerical Verification

In addition to the STAR-CCM+ verification conducted in Chapter 3, further analysis on the accuracy of the numerical model was conducted using the Factor of Safety (FoS) method. Having deemed STAR-CCM+ a suitable software with which to model turbulent flow behaviour of an impinging jet system, a numerical model was constructed within the software that was representative of the experimental apparatus, i.e. the full TTV was modelled with the heated meter bar neck present on the heat spreader as detailed in Chapter 3. The aim here is two-fold; to verify that the simplified heat source assumption used in Chapter 3 is appropriate, and to estimate the numerical uncertainty associated with the CFD simulations. This model, depicted in Figure D.1, was compared directly to the experimental data for model verification against the three temperature readings taken at different intervals along the length of the TTV. The coldplate assembly remained unchanged, using the Nexalus Enflux^{TM} CPU heat exchanger assembly as the base model with the baseline orifice plate jet configuration, with an inlet flow rate of 6 L/min at 35°C and a maximum heat source power of 250 W.

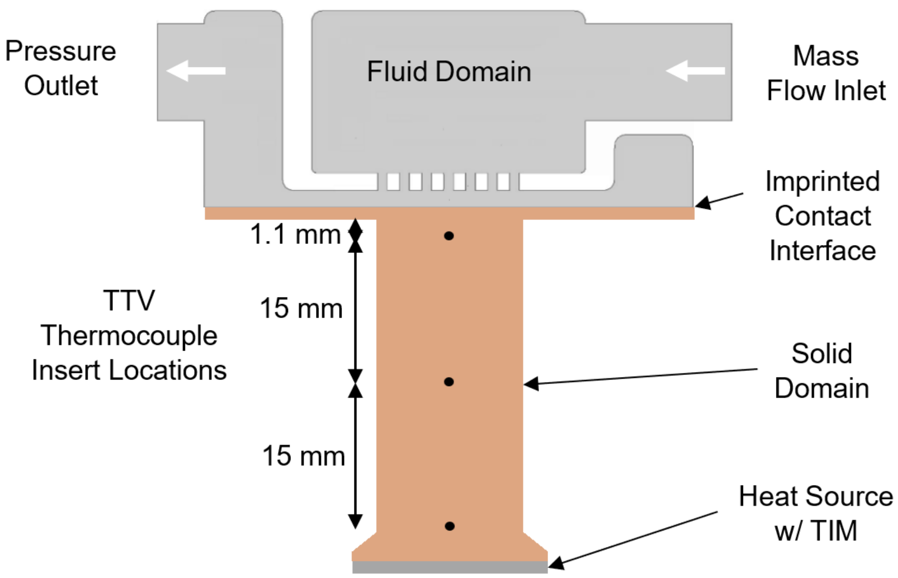

Figure D.1: Numerical model of experimental apparatus.

Verification of the numerical model involved assessing the numerical uncertainties within the simulations performed. Aside from computational round-off errors, spatial and temporal discretisation are the primary source of numerical error. Discretisation error can be estimated using the Richardson Extrapolation in its generalised form [1]. This provides an approximation of the exact solution for the discretisation error, f_{exact}, which is stated as,

$$f_{exact} = f - \delta \tag{D.1}$$

where,

$$\delta = \frac{\varepsilon_{21}}{{r_r}^{p} - 1} \tag{D.2}$$

Here, f is the initial solution, δ is the pth order error coefficient, ε_{21} is the difference between the medium and fine meshes for the parameter of interest, r_r is the arbitrary grid refinement ratio, which in this instance is the cubic root of 2 as the mesh density approximately doubled with successive iterations. Additionally, p is the observed order of accuracy, a function of the natural log of r_r. The solution can be said to be validated if the normalised error falls within the limits established by the Factor of Safety method. This method uses the values from the Richardson Extrapolation, specifically the error coefficient, to determine the uncertainty limits within which numerical validation lies [2]. The Factor of Safety method specifically is used to provide an indication on how far the solution is from asymptotic convergence. This simulation uncertainty estimate, defined as $Unc._{FS}$, is given as;

$$Unc._{FS} = \begin{cases} \left(FS_1 p' + FS_0(1 - p')\right) \times |\delta| \; for \; 0 < p' \leq 1 \\ \left(FS_1 p' + FS_2(p' - 1)\right) \times |\delta| \; for \; p' \geq 1 \end{cases} \tag{D.3}$$

where FS_0 = 2.45, FS_1 = 1.6 and FS_2 = 14.8. Also, p' is the ratio of observed order of accuracy of the mesh grid to the theoretical order of accuracy, defined as p/p_{th}, where the theoretical order of accuracy p_{th} is 2 for second order schemes. Tables D.1 and D.2 show how for three successive mesh iterations, varying from a course (C) mesh of 0.99 million cells to a fine (F) mesh of approximately 4.5 million cells, the numerical model achieves validation of the experimental data through monotonically converging values that fall within the limits established by the Factor of Safety method. Validation is achieved when the normalised comparison error, E', is less than the normalised validation uncertainty. The normalised validation uncertainty $Unc._V'$ is given by,

$$Unc._V' = \sqrt{Unc._{FS}'^2 + Unc._{EXP}'^2} \quad (D.4)$$

where $Unc._{FS}'$ is the normalised uncertainty estimate and $Unc._{EXP}'$ is the normalised experimental uncertainty. The parameter r_g is the grid convergence ratio, defined as $\varepsilon_{21}/\ \varepsilon_{32}$. The Grid Convergence Index is also included, as defined in Chapter 2, with the decreasing value with increasing mesh density confirming solution convergence.

Table D.1: STAR-CCM+ mesh convergence check

Z (mm)	Experiment (°C)	f_1 (F) (°C)	f_2 (M) (°C)	f_3 (C) (°C)	E	E'	ε_{21}	ε_{32}	r_g	Convergence
0.0	57.2	58.1	59.5	64.1	-0.92	-0.02	1.38	4.60	0.30	Monotonic
1.1	60.72	62.0	64.3	68.0	-1.30	-0.02	2.26	3.69	0.61	Monotonic
16.1	106.8	107.9	109.4	113.0	-1.08	-0.02	1.97	3.17	0.62	Monotonic
31.1	154.0	115.6	157.3	160.1	-1.52	-0.03	1.79	2.76	0.65	Monotonic

Table D.2: STAR-CCM+ validation

Z (mm)	p	δ	p'	$Unc._{FS}$	$Unc._{FS}'$	$Unc._{EXP}'$	$Unc._V'$	GCI (fine)	GCI (course)
0.0	5.20	0.59	2.60	16.55	0.29	0.0087	± 0.29	0.05	0.54
1.1	2.13	3.55	1.07	9.51	0.17	0.0087	± 0.17	0.84	1.36
16.1	2.06	3.23	1.03	6.74	0.12	0.0087	± 0.12	0.78	1.25
31.1	1.87	3.30	0.94	5.46	0.10	0.0087	± 0.10	0.84	1.29

References

[1] P. J. Roache, "Quantification of Uncertainty in Computational Fluid Dynamics," *Annual Review of Fluid Mechanics,* vol. 29, no. 1, pp. 123-160, 1997, doi: 10.1146/annurev.fluid.29.1.123.

[2] T. Xing and F. Stern, "Factors of Safety for Richardson Extrapolation," *Journal of Fluids Engineering,* vol. 132, no. 6, 2010, doi: 10.1115/1.4001771.

Appendix E

Orifice Nozzle Diameter Uncertainty

The below figure illustrates the normal distribution of nozzle diameters recorded across the range of jets present on the baseline orifice configuration, as detailed in Chapter 4. For a total of 25 samples taken, the mean diameter was 0.986 mm, with the smallest recorded diameter being 0.976 mm. This resulted in a mean error of 14 μm, a 1.4 % deviation compared to the 1 mm design point, and a dataset standard deviation of 6.71 μm.

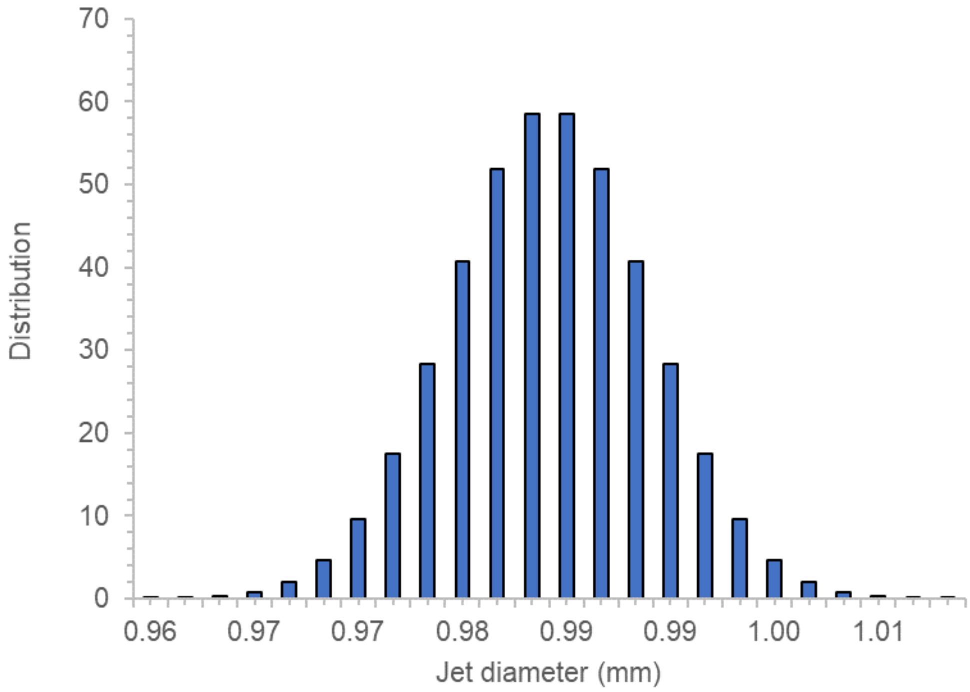

Figure E.1: Normal distribution of jet nozzle diameters across baseline orifice plate.